MONASH University

The observational signatures of nascent neutron stars

Author:
Nikhil SARIN

Supervisors:
Assoc. Prof. Paul
D. LASKY & Dr Gregory
ASHTON

*A thesis submitted in fulfillment of the requirements
for the degree of Doctor of Philosophy*

in the

School of Physics and Astronomy

September 30, 2021

Copyright Notice

Publications

Listed below are publications where I have made significant contributions. I am an author on several other publications as a member of the LIGO Scientific Collaboration.

1. LIGO/Virgo Collaboration inc. **N. Sarin** (2017), *Search for post-merger gravitational waves from the remnant of the binary neutron star merger GW170817*, ApJL, 851, L16., arXiv:1710.09320

2. **N. Sarin**, P. D. Lasky, L. Sammut, G. Ashton (2018), *X-ray guided gravitational-wave search for binary neutron star merger remnants* Phys. Rev. D 98, 043011, arXiv:1805.01481

3. LIGO/Virgo Collaboration inc. **N. Sarin** (2019), *Search for Gravitational Waves from a Long-lived Remnant of the Binary Neutron Star Merger GW170817.*, ApJ, 875:2, arXiv:1810.02581

4. G. Ashton, M. Hübner, P. D. Lasky, C. Talbot, et al. inc. **N. Sarin** (2019), *Bilby: A user-friendly Bayesian inference library for gravitational-wave astronomy*, ApJS., 241, 27, arXiv:1811.02042

5. **N. Sarin**, P. D. Lasky, G. Ashton (2019), *X-ray afterglows of short gamma-ray bursts: Magnetar or Fireball?* ApJ 872 114, arXiv:1812.08176

6. **N. Sarin**, P. D. Lasky, G. Ashton (2020), *Gravitational waves or deconfined quarks: What causes the premature collapse of neutron stars born in short gamma-ray bursts?* Phys. Rev. D 101, 063021, arXiv:2001.06102

7. I. Romero-Shaw et al. inc. **N. Sarin** (2020), *Bayesian inference for compact binary coalescences with BILBY: Validation and application to the first LIGO–Virgo gravitational-wave transient catalogue.* MNRAS, 499 3, arXiv:2006.00714

8. K. Ackley et al. inc. **N. Sarin** (2020), *Neutron Star Extreme Matter Observatory: A kilohertz-band gravitational-wave detector in the global network.* PASA 37:e047, arXiv:2007.03128

9. **N. Sarin**, P. D. Lasky, G. Ashton (2020), *Interpreting the X-ray afterglows of gamma-ray bursts with radiative losses and millisecond magnetars.* MNRAS, 499:4, arXiv:2008.05745

10. **N. Sarin**, P. D. Lasky (2021), *The evolution of binary neutron star post-merger remnants: a review.* Published in General Relativity and Gravitation, arXiv:2012.08172

11. L. Strang, A. Melatos, **N. Sarin**, P. D. Lasky (2021), *Exploring properties of neutron stars born in short gamma-ray bursts with a plerion-like X-ray plateau* MNRAS, 507:2, arXiv:2107.13787

12. **N. Sarin**, G. Ashton, P. D. Lasky et al. (2021), *CDF-S XT1: The off-axis afterglow of a neutron star merger at z = 2.23.* Submitted to ApJL, arXiv:2105.10108

13. **N. Sarin**, R. Hamburg, E. Burns et al. (2021), *A new class of low-efficiency long gamma-ray bursts.* Submitted to ApJ, arXiv:2106.01556

Declaration of Authorship

I, Nikhil Sarin, hereby declare that this thesis contains no material which has been accepted for the award of any other degree or diploma at any university or equivalent institution and that, to the best of my knowledge and belief, this thesis contains no material previously published or written by another person, except where due reference is made in the text of the thesis.

This thesis revolves around understanding the different multi-messenger observational signatures associated with nascent neutron stars. In particular, focusing on the impact and signature of binary neutron star merger remnants and how such signatures can shed light on several fundamental questions in astrophysics. This thesis includes seven papers led by me which have been previously published or submitted to peer-reviewed journals. These papers appear verbatim in Chapters 2, 3, 4, 5, 6, 7, and 8. The ideas, development and writing up of Chapters 3, 4, 5, 6, 7, and 8 in the thesis were the principal responsibility of myself, the student, working within the School of Physics and Astronomy under the supervision of Assoc. Prof. Paul Lasky and Dr Gregory Ashton. Chapter 2 was prepared as an invited review in the topical collection on binary neutron stars in the journal General Relativity and Gravitation.

I note that where possible, the material in Chapters 2-8 is identical to the published/submitted version of the manuscript. However, in Chapter 7 some tables have been compressed to preserve the thesis formatting. For the full version of these tables, I refer the reader to the arXiv version of this manuscript.

The inclusion of co-authors reflects the fact that the work came from active collaboration between researchers and acknowledges input into team-based research. My contribution to each chapter published separately is summarised below. Co-authors are not Monash students unless stated.

- Chapter 2
  Title: The evolution of binary neutron star post-merger remnants: a review.
  Status: Published in General Relativity and Gravitation, (2021)
  Contribution: Writing (60%)
  Co-authors: P. D. Lasky- writing (40%).

- Chapter 3
  Title: X-ray afterglows of short gamma-ray bursts: Magnetar or Fireball?
  Status: Published in ApJ, (2019)
  Contribution: Project idea, development and writing - (75%)
  Co-authors: P. D. Lasky - project idea, development and manuscript input (15%), G. Ashton - project development and manuscript input (10%).

- Chapter 4
  Title: X-ray guided gravitational-wave search for binary neutron star merger remnants
  Status: Published in PRD, (2018)
  Contribution: Project development and writing (70%)
  Co-authors: P. D. Lasky - project idea, development and manuscript input (15%), L. Sammut - project idea, development and manuscript input (10%), G. Ashton - manuscript input (5%).

- Chapter 5
  Title: Interpreting the X-ray afterglows of gamma-ray bursts with radiative losses and millisecond magnetars.
  Status: Published in MNRAS, (2020)
  Contribution: Project idea, development and writing (80%)
  Co-authors: P. D. Lasky - project development and manuscript input (10%), G. Ashton - project development and manuscript input (10%).

- Chapter 6
  Title: Gravitational waves or deconfined quarks: What causes the premature collapse of neutron stars born in short gamma-ray bursts?
  Status: Published in PRD, (2020)
  Contribution: Project idea, development and writing (70%)
  Co-authors: P. D. Lasky - project development and manuscript input (15%), G. Ashton - project development and manuscript input (15%).

- Chapter 7
  Title: CDF-S XT1: The off-axis afterglow of a neutron star merger at z=2.23.
  Status: Submitted to ApJL, (2021)
  Contribution: Project idea, development and writing (70%).
  Co-authors: G. Ashton - project development and manuscript input (10%) , P. D. Lasky - writing, project development and manuscript input (10%), K. Ackley - manuscript input (5%) , Y. Mong (Monash student) - data processing (2%), D. K. Galloway - project development, data processing and manuscript input (3%).

- Chapter 8
  Title: Low-efficiency long gamma-ray bursts: A case study with AT2020blt
  Status: Submitted to ApJ, (2021)
  Contribution: Project idea, development and writing (75%)
  Co-authors: R. Hamburg - project development (5%), E. Burns - project development and manuscript input (5%), G. Ashton - manuscript input (5%), P. D. Lasky - project development and manuscript input

(5%), G. Lamb - project development and manuscript input (5%).

Signed:

_____

Date: September 30, 2021

I, Assoc. Prof. Paul Lasky, hereby certify that the above declaration correctly reflects the nature and extent of the student's and co-authors' contributions to this work. In instances where I am not the responsible author I have consulted with the responsible author to agree on the respective contributions of the authors.

Signed:

_____

Date: September 30, 2021

Our lives are defined by opportunities, even the ones we miss.

Eric Roth, *The Curious Case of Benjamin Button*

Abstract

Faculty of Science
School of Physics and Astronomy

Doctor of Philosophy

The observational signatures of nascent neutron stars

by Nikhil SARIN

Two neutron stars merge somewhere in the Universe approximately every 10 to 100 seconds, creating explosions potentially observable in gravitational waves and across the electromagnetic spectrum. These observations are intrinsically connected to the fate of the merger. This thesis focuses on using these different signatures to shed light on the aftermath of these explosions and several fundamental questions in astrophysics. I begin by reviewing the different signatures expected from a binary neutron star merger, describing the impact of different merger outcomes in detail. In particular, I examine the X-ray afterglows of gamma-ray bursts and their connection to nascent neutron stars. I describe work introducing a new method to study the behaviour of nuclear matter in a previously unexplored regime. This work has led to tentative evidence for the presence of temperature-dependent phase transitions. I introduce a new model incorporating radiative losses with energy injection from a nascent neutron star that self-consistently explains X-ray flares seen in gamma-ray bursts, plateau diversity, and X-ray afterglow data. I describe a Bayesian framework for identifying the mechanism responsible for powering the X-ray afterglow of gamma-ray bursts. I apply this method to GRB140903A, demonstrating that GRB140903A definitively produced an infinitely stable neutron star. I also describe work introducing a new waveform model for the gravitational-wave signature of such a neutron star and how we can use X-ray observations to guide our searches for gravitational waves. I also include work on interpreting the nature of two transients, CDF-S XT1 and AT2020blt. The latter likely being the afterglow of a low-efficiency long gamma-ray burst, with prompt emission potentially weaker than $\lesssim 98.4\%$ of the gamma-ray burst population hinting at a sub-population of very-low efficiency gamma-ray bursts. On the other hand, I show that CDF-S XT1 is likely the X-ray afterglow of an off-axis short gamma-ray burst. As potentially the first orphan afterglow observed in X-rays, and at $z = 2.23$, one of the most distant binary neutron star merger ever observed this event has several implications. I discuss these implications alongside the prospect of identifying other off-axis afterglows. The works presented in this thesis are shedding significant insight into the presence and dynamics of nascent neutron stars and improving our understanding of the biggest explosions in the Universe. I conclude by discussing these insights, some closing thoughts and the next big questions in this field.

Acknowledgements

Firstly, I would like to thank my supervisors, Paul and Greg, for allowing me to pursue a PhD and for all your help guiding me through it. This thesis would not be possible without your endless advice, feedback, encouragement, patience and mentoring. I have grown significantly as a researcher and person, and you have both played a significant part in that growth. Thank you for being incredibly fun to work with. You have set the bar remarkably high for all future collaborators, and I hope we can continue working together and keep in touch.

I also thank Duncan and Eric, who have mentored me throughout my PhD, especially during the latter stages where I had to make the tough decisions that will shape my career. I also acknowledge other scientists in the department and, more widely, the members of OzGrav for creating an inclusive, healthy environment that has been a joy to work in and allowed me to thrive.

To my fellow PhD students, especially Paul E, Shanika, and Moritz, you made the bad times enjoyable and the good times great. The banter, the walks, and the general sensible and nonsensical conversations were invaluable, and especially with the Pandemic, crucial for my mental well-being.

Beyond the workplace, I must acknowledge the role of my family and friends. To my parents, Alka and Pradeep, whose constant support, love and sacrifice have shaped who I am and led me here. To my brother, Himanshu, for his unique support and ability, only an older brother could have that makes me strive to always do better, personally and professionally. To Liz, for her guidance on where I should do a postdoc and for becoming an integral part of the family. To baby Norah, for being a constant and wonderful reminder of *joie de vivre*. To Cedar, who cannot understand this but deserves all the treats for being the loving goofball he is.

To Caroline for all her love, support and companionship that has made this journey significantly easier than it otherwise would have been. For always being there to listen and for never letting me forget the things that matter.

To the friends from the infamous group chat - Arjun, Anish, Dillan, Jason and Rugved the bond fostered over the years (coming up close to a decade) is a fantastic memento of the simpler days when all we cared about was who brought the football and how long we could play. For that, I say thanks.

To the 'Soheb is at his sister's this weekend, gang', thank you for all the weekend pandemic therapy.

To my friends from hockey, for always being up for a game, and for never asking me when I will submit my thesis.

Contents

You can't fall if you don't climb,
but there is no joy in living your whole life on the
ground.

Chapter 1

Introduction

The joint electromagnetic and gravitational-wave observation of a binary neutron star merger, GW170817 (Abbott et al., 2017b,c,d) ushered in a new era of gravitational-wave and electromagnetic multi-messenger astronomy. This historical event and its ongoing observations continue to offer unprecedented insights into several fundamental questions in astrophysics (e.g., Abbott et al., 2017e; Kasen et al., 2017; Troja et al., 2017; Evans et al., 2017a; Hajela et al., 2020; Troja et al., 2020; Metzger & Fernandez, 2021). However, despite the wealth of observations, one question remains unanswered. What was the nature of the remnant of GW170817?

Among many things, GW170817 confirmed the long-held suspicion that binary neutron star mergers are the progenitors of at least some short gamma-ray bursts. Short gamma-ray burst afterglow observations (since the launch of *Swift*) have hinted towards nascent neutron stars, often referred to as millisecond magnetars, to be the central engine of some subset of explosions (e.g., Fan & Xu, 2006; Troja et al., 2007; Fan et al., 2013; Rowlinson et al., 2013; Lü et al., 2015). These rapidly rotating, highly magnetic neutron stars are also believed to be born in some long gamma-ray bursts and some superluminous supernovae (e.g., Cano et al., 2017; Nicholl et al., 2017b).

Observations of gamma-ray bursts (both long and short) and supernovae currently offer one of the only ways to probe these nascent, exotic objects that harbour the hottest and densest observable matter and the largest magnetic field fields in the Universe. However, to better understand what is at the heart of these explosions and probe the properties of the engine, one must better understand these explosions themselves. The primary aim of this thesis is to gain insight into the different observational signatures of nascent neutron stars, in particular their connection to gamma-ray bursts, to ultimately determine what is present in the aftermath of these explosions. Better understanding these explosions and the dynamics and nature of their central engine has far-reaching implications on several fundamental questions in astrophysics. In the following, I provide a brief historical overview of gamma-ray bursts, nascent neutron stars and binary neutron star mergers. For each topic, I highlight some open questions that subsequent chapters in this thesis attempt to address. I note that the bulk of the background into these topics is in the subsequent chapters, particularly Chapter 2 and the following sections serve as an overview of these topics.

1.1   Gamma-ray bursts

Gamma-ray bursts are aptly named highly energetic bursts of gamma-rays, historically split into two categories: short and long. Long gamma-ray bursts are known to be associated with the collapse of massive stars (e.g., Kulkarni et al., 1998; Greiner et al., 2015; Cano et al., 2017). Short gamma-ray bursts are now known to be due to the merger of a neutron star binary, i.e., a binary neutron star merger (e.g., Abbott et al., 2017d) or a neutron star black hole merger (e.g., Foucart, 2020). For a recent review into gamma-ray bursts see e.g., Zhang (2018). A subset of short gamma-ray bursts may also be from magnetar flares (e.g., Burns et al., 2021). However, for the rest of this thesis, this subpopulation will be ignored, and short gamma-ray bursts will be used synonymously with the merger of a neutron star binary.

Typically, classification between a long or a short gamma-ray burst is determined by considering T90 (i.e., the time duration where 90% of the gamma-ray energy is released). For short gamma-ray bursts, T90 $\lesssim$ 2 s, while long gamma-ray bursts have T90 $\gtrsim$ 2 s. This historical classification has shown several signs of strain (e.g., Levesque et al., 2010; Ahumada et al., 2021; Rossi et al., 2021). This stresses the need for new classification methods, such as those that consider the host-galaxy properties (Wang et al., 2015; Fong et al., 2015) or the gamma-ray emission energetics and spectra (e.g., Minaev & Pozanenko, 2020).

To further complicate matters, the process of how gamma-ray bursts generate gamma-ray emission is not well understood, and it is also unclear whether the engine is a neutron star, black hole or a combination. Several models for generating gamma-ray emission have been suggested in the literature, such as internal shocks (Kumar, 1999; Beloborodov, 2000), photospheric emission (Lazzati et al., 2013), and magnetic field dissipation (Zhang & Yan, 2011) among others. These models are all able to describe some (but not all) properties of the data. Given this uncertainty in the emission mechanism, typically, a radiative efficiency for the ratio between the gamma-ray to total energy is computed, which in principle can shed insight into the emission mechanism. This radiative efficiency ranges from $1 - 90\%$ for long and short gamma-ray bursts alike (Wang et al., 2015; Fong et al., 2015). However, this large range of efficiencies is puzzling and led to the so-called "efficiency crisis" of gamma-ray bursts (e.g., Fan & Piran, 2006) since no one mechanism can explain the vast range.

Perhaps our best understanding of gamma-ray burst physics comes from the broadband afterglow that follows these explosions (e.g., Piran, 1999). This afterglow is believed to be the product of the interaction of the relativistic jet with the surrounding interstellar medium (e.g., Piran, 1999; Sari et al., 1998, 1999). This model is also referred to as the fireball model (e.g., Mészáros et al., 1998; Sari et al., 1998, 1999). Predictions of an afterglow (e.g., Paczynski & Rhoads, 1993; Katz, 1994; Mészáros & Rees, 1997) predated and well described the first-ever observation of a gamma-ray burst afterglow (Costa et al., 1997). However, as more detailed afterglow observations arrived, problems started to emerge. These problems led to theorists reconsidering several

vanilla assumptions such as a negligible reverse shock, a constant density interstellar medium, shell thicknesses, etc (see Zhang & Mészáros (2004) for a review of the problems at the beginning of the *Swift* era). A detailed look into observations, particularly the temporal ("jet") breaks attributed to jet collimation, provided a measurement of the proper energetics of the burst. These observations indicate that there is a standard energy reservoir for gamma-ray bursts (Frail et al., 2001). This standard energy reservoir hints that gamma-ray burst jets might be structured (e.g., Rossi et al., 2002) i.e., the energy and Lorentz factor distributions have an angular dependence, and different gamma-ray bursts are viewed from different angles (e.g., Zhang & Mészáros, 2002; Kumar & Granot, 2003). More definitive evidence arrived in the spectacular form of GW170817, where the multi-wavelength afterglow is best described by structured jet models (e.g., Alexander et al., 2018; Troja et al., 2017; Lamb et al., 2018; Ryan et al., 2019) confirming that jets are likely structured. In light of GW170817, other gamma-ray bursts have also been reinterpreted and show evidence for a structured jet (e.g., Troja et al., 2018; Cunningham et al., 2020). Some of these may have also been viewed from outside the ultra-relativistic jet, i.e., observed off-axis. While several phenomenological structured jet models have been used to fit the data, the true jet structure is unknown.

Swift observations of the early afterglow also produced some surprising features not expected theoretically. First, *Swift* often detected X-ray flares of varying sizes and durations in the afterglow (e.g., Fan & Wei, 2005; Burrows et al., 2005; Giannios, 2006; Bernardini et al., 2011) requiring an engine that suddenly restarts or is active for long timescales. Second, a significant fraction of afterglows showed an extended plateau in X-rays up to $10^5 - 10^6$ s in duration (e.g., Burrows et al., 2006; Fan & Xu, 2006; Rowlinson et al., 2013). Perhaps even more puzzlingly, a subset of gamma-ray bursts showed a short plateau phase followed by a rapid decay segment (e.g., Troja et al., 2007; Rowlinson et al., 2010). These latter features, dubbed the external and internal plateau respectively, are remarkably well explained by the spin-down energy of a rapidly rotating, highly magnetic, nascent neutron star (Zhang & Mészáros, 2001; Fan & Xu, 2006; Dai et al., 2006; Rowlinson et al., 2013). While the external plateau and the late-time flares could be explained without requiring a neutron star (e.g., Oganesyan et al., 2019; Beniamini et al., 2020b), the internal plateaus are incredibly difficult (e.g., Zhang, 2014). This suggests that some (if not all) internal and external plateaus indicate a neutron star was born in the gamma-ray burst.

1.2 Nascent neutron stars

Neutron stars are born in the collapse of some massive stars and (depending on the nuclear equation of state) some fraction of binary neutron star mergers. Newly born neutron stars were first proposed as an engine for long gamma-ray bursts by Usov (1992). A nascent neutron star can naturally explain the rapid variability observed in gamma-ray bursts, and their

spin energy reservoir if efficiently tapped, is a large enough reservoir to explain the luminosity of gamma-ray bursts (e.g., Dai & Lu, 1998). However, it is not fully understood how these young neutron stars launch a jet that can power the gamma-ray burst. A range of numerical simulations of the collapse of massive stars or binary neutron star mergers show the initial stages of jet formation given sufficiently strong neutron star magnetic fields ($B \gtrsim 10^{14}$ G) (e.g., Giacomazzo & Perna, 2013; Mösta et al., 2015; Ciolfi, 2018; Raynaud et al., 2020). This is easy to achieve for most progenitor properties through processes like the magneto-rotational instability, the $\alpha - \Omega$ dynamo, the Kelvin-Helmholtz instability and others which amplify magnetic fields by several orders of magnitude (e.g., Mösta et al., 2015; Aguilera-Miret et al., 2020; Bernuzzi, 2020). It is important to note that no numerical simulation of supernovae or binary neutron star mergers resolves all these magnetic field amplification mechanisms. Therefore, the amplification seen in simulations are only a lower limit. Typically, numerical simulations mitigate this issue by starting with relatively high seed magnetic fields $B \sim 10^{12-14}$ G. Although the early stages of jet-formation are seen in these simulations with a neutron star engine, none of these simulations produce jets that reach the required Lorentz factor that could explain gamma-ray bursts. This may be a limitation of the numerical simulations or hint at problems with the neutron star engine model (e.g., Ciolfi, 2018; Mösta et al., 2020).

As mentioned above, internal and external X-ray plateaus of gamma-ray bursts are well described with the spin-down energy of a nascent neutron star (e.g., Rowlinson et al., 2013; Lü et al., 2015). Their spin-down energy is also invoked to explain some superluminous supernovae (e.g., Greiner et al., 2015; Nicholl et al., 2017a). Fits to the internal and external plateaus and superluminous supernovae observations with simplified models all show great agreement with the data. However, the models describing how this spin energy is extracted and turned into radiation are in their infancy. Moreover, these models often ignore the complicated interplay between the spin-down energy, ejecta and the jet, and where these models exist, they have not been confronted with the data.

The X-ray afterglows of several gamma-ray bursts have been fit with the spin-down energy of nascent neutron stars (e.g., Rowlinson et al., 2013; Lü et al., 2015). However, some subset of these observations (particularly the external plateaus) can be explained by modifications to the fireball model (e.g., Troja et al., 2016; Beniamini et al., 2020b), high-latitude emission (Oganesyan et al., 2019), or fallback accretion onto a newborn black-hole (Desai et al., 2019). This raises the question of whether a neutron star engine is necessary to explain some or all external and internal plateau observations.

Early models for the spin-down of a nascent neutron star assumed that the neutron star spun down solely through magnetic dipole radiation (Zhang & Mészáros, 2001; Rowlinson et al., 2013), fixing the braking index to $n = 3$. This assumption is almost certainly flawed as realistic calculations of the braking index show $n \lesssim 3$ (Melatos, 1997). Furthermore, most measurements of braking indices of neutron stars in our Galaxy are significantly different from $n = 3$ (e.g., Archibald et al., 2016). More recently, the assumption

of solely magnetic-dipole spin down has been relaxed (Lasky et al., 2017; Lü et al., 2018; Xiao & Dai, 2019), see also Sarin et al. (2020a) and Chapter 5. These works are leading to measurements of the braking index of a large fraction of putative neutron stars born in gamma-ray bursts. Unsurprisingly, these braking indices have a broad range and are often inconsistent with $n = 3$. Moreover, in some cases, they hint towards spin down through gravitational waves (Fan et al., 2013; Gao et al., 2016) and evolution of the braking index through time (e.g., Şaşmaz Muş et al., 2019). All these features have important implications for the dynamics of these young neutron stars (e.g., Dall'Osso et al., 2015a; Lander & Jones, 2018, 2020). These insights are essential to understanding how these objects evolve into the old isolated neutron stars we see in our Galaxy today.

1.3 Binary neutron star mergers

Most neutron stars are born in binaries and are potentially observable in gravitational waves and in radio. In total, we have potentially observed 20 binary neutron star systems in the Universe, 18 in our Galaxy (e.g., Farrow et al., 2019; Andrews & Mandel, 2019) and two extra-galactic binaries observed with gravitational waves (Abbott et al., 2017b, 2020a).

Binary neutron stars are predominately formed through isolated binary evolution (e.g., Tauris et al., 2017) and offer a playground to probe several fundamental questions in physics such as testing general relativity (e.g., Kramer et al., 2006), the expansion of the Universe (e.g., Abbott et al., 2017e; Hotokezaka et al., 2019), the behaviour of nuclear matter (e.g., Abbott et al., 2019b; Margalit & Metzger, 2017) and the source of r-process elements in the Universe (e.g., Kasen et al., 2017; Watson et al., 2019). Their lives and deaths can and have already been used to provide a myriad of insights into stellar evolution, binary interactions and short gamma-ray bursts, among others (e.g., Ferdman et al., 2013; Fong & Berger, 2013; Nakar, 2019; Chattopadhyay et al., 2020; Howitt et al., 2020). Long before GW170817 confirmed the link between binary neutron star mergers and short gamma-ray bursts, there was a strong belief these two events were connected (e.g., Eichler et al., 1989; Narayan et al., 1992; Paczynski & Rhoads, 1993). This connection was reinforced when a detailed look into the offsets and host galaxies matched theoretical expectations of binary neutron star formation (Nakar, 2007; Fong & Berger, 2013; Berger, 2014). Similarly, excess emission observed in some gamma-ray bursts (Metzger et al., 2010; Tanvir et al., 2013) hinted at the presence of a kilonova alongside the gamma-ray burst, providing a tentative link between the origin of the heaviest elements in the Universe and binary neutron star mergers.

This all came together in the remarkable multi-messenger discovery of GW170817 (Abbott et al., 2017b,c,d). This historic event definitively connected binary neutron star mergers with kilonovae (e.g., Abbott et al., 2017c; Evans et al., 2017a; Smartt et al., 2017; Cowperthwaite et al., 2017; Villar et al., 2017; Kasen et al., 2017) and short gamma-ray bursts (e.g., Abbott

et al., 2017d; Goldstein et al., 2017a; Savchenko et al., 2017). Although not without its share of surprises, it is truly amazing how several features of the gravitational-wave signal and electromagnetic emission matched theoretical expectations (e.g., Metzger, 2017a). The broad features and colour of the kilonova lightcurve matched qualitative predictions (Metzger et al., 2010). Similarly, the afterglow qualitatively matched the theoretical expectation for an off-axis observer (Granot et al., 2002). The masses of the binary were also wholly consistent with binary neutron stars in our Galaxy.

The multi-messenger observations of GW170817 perhaps created a warped perception of what to expect in the multi-messenger era. This expectation likely came crashing back to reality with the observation of GW190425 (Abbott et al., 2020a). Observed with a single gravitational-wave detector, the sky localisation region was roughly half the sky (cf. $\sim 20\text{deg}^2$ for GW170817). This large region, combined with the greater distance, meant that no electromagnetic counterpart was detected, and upper limits were mainly uninteresting (e.g., Coughlin et al., 2019; Nicholl et al., 2021). Perhaps most interesting was the progenitor masses of GW190425, which were a 5σ outlier from the Galactic double neutron star population (Abbott et al., 2020a) throwing into question our understanding of binary neutron star formation.

In the near future, most gravitational-wave observations will likely be without a gamma-ray counterpart since most mergers will be observed off-axis (e.g., Howell et al., 2019). However, this leaves the opportunity to detect the kilonova, which is quasi-spherical and observable for a wide range of viewing angles (e.g., Chase et al., 2021). One also has the opportunity to observe the afterglow emission, which is observable for a broader range of viewing angles and longer lasting. Several features of these observations will depend directly on what remains behind in the aftermath of these mergers, and answering this question has implications on several fundamental questions in Astrophysics.

1.4 Thesis layout

The following chapters in the thesis address particular aspects related to nascent neutron stars and gamma-ray bursts more broadly.

Chapter 2 is an in-depth review into the different merger remnants of a binary neutron star merger. In particular, the review discusses the evolution of the post-merger remnant and the different electromagnetic and gravitational-wave signatures expected in each scenario. This introduction and Chapter 2 together serve as the introductory material for this thesis, reflecting the state of the field and our understanding at the time of writing.

The first four science Chapters (3-6) focus on nascent neutron stars and the X-ray afterglows of gamma-ray bursts. Chapter 3 introduces a Bayesian method for determining whether a nascent neutron star was born in a gamma-ray burst. We apply this Bayesian method to GRB140903A and GRB130603B, finding that GRB140903A likely produced an infinitely stable

neutron star for all possible equations of state. Having established evidence that neutron stars are likely born in short gamma-ray bursts, I then turn to their gravitational-wave signature. In Chapter 4, I introduce a waveform model for the gravitational-wave signature of a nascent neutron star. This waveform model has since been used in searches for gravitational-wave transients and for the remnant of GW170817 by the LIGO Scientific Collaboration (LSC) (Abbott et al., 2017f, 2019c,a). I also demonstrate a detection pipeline that improves the sensitivity of these gravitational-wave searches by $\sim 50\%$ utilising coincident X-ray observations. Utilising our method, third-generation gravitational-wave detectors may detect gravitational waves out to the distance of GW170817.

The model used to fit the X-ray data described in Chapters 3-4, while being an extension to what came before in the literature, is still in many respects simplified. In Chapter 5, I describe a new model for the X-ray afterglow of gamma-ray bursts incorporating radiative losses with the spin-down of a nascent neutron star. This model builds a better picture of how nascent neutron stars can power the X-ray afterglow of gamma-ray bursts. Moreover, the model provides a natural way to explain X-ray flares seen in some gamma-ray bursts and explain the diversity of X-ray plateaus. I test this model on a subset of gamma-ray bursts, finding that the model is a better fit for the data than previously used in the literature. I measure the braking index of GRB061121 as $n = 4.85^{+0.11}_{-0.15}$ suggesting the neutron star born in this gamma-ray burst spins down predominantly through gravitational-wave emission.

Having studied individual gamma-ray bursts, I then consider what clues a large population of gamma-ray bursts provide. In Chapter 6, I identify 18 putative neutron stars born in the entire catalogue of short gamma-ray bursts observed by *Swift*, including 5 that were previously not identified in the literature. I measured the collapse time of these putative neutron stars and performed Bayesian hierarchical inference on the population of collapse times. Together, this population offers several tantalising insights into these objects. Firstly, most nascent neutron stars that collapse do so on timescales $\lesssim 100\,$s. This is significant as this is approximately the time it takes *Swift* to slew, implying that *Swift* may be missing a non-negligible fraction of internal plateaus. Secondly, I measure the maximum neutron star mass as $M_{\mathrm{max}} = 2.31^{+0.36}_{-0.21} M_{\odot}$, which indicates that a significant fraction of binary neutron star mergers will form neutron stars. I also found that these neutron stars spin down predominantly through gravitational-wave emission, which has important implications for the dynamics of these objects. Lastly, I found tentative evidence that these nascent neutron stars are composed of freely moving deconfined quarks, hinting at temperature-dependent phase transitions.

In Chapters 7-8, I turn my attention to transients more broadly, firstly CDF-S XT1 and later AT2020blt. CDF-S XT1 (Chapter 7) is an enigmatic fast X-ray transient identified in the Chandra Deep-Field South Survey. I find that the X-ray data are best interpreted as the afterglow from an off-axis gamma-ray burst similar to GRB170817A. By combining the multi-wavelength data,

spectra and host galaxy properties, I build a cohesive picture for this transient being the orphan afterglow of a short gamma-ray burst at a redshift $z = 2.23$. As one of the most distant binary neutron star mergers observed, this has important implications on binary stellar evolution and the chemical enrichment of the Universe. AT2020blt (Chapter 8) is an afterglow-like transient at $z = 2.9$ detected by the Zwicky Transient Facility. However, unlike most detected afterglows, there is no prompt gamma-ray emission detection. Through detailed afterglow analysis, I find that AT2020blt belongs to the low-efficiency tail of long gamma-ray bursts that were previously missed due to the selection bias of gamma-ray detectors.

In Chapter 9, I examine the implications of the works presented in this thesis. I also discuss the big questions remaining in this field and what is necessary to address these questions both from a theoretical and observational perspective. I conclude by mentioning some of my planned future work and presenting some closing thoughts.

Chapter 2

The evolution of binary neutron star post-merger remnants: a review

Abstract

Two neutron stars merge somewhere in the Universe approximately every 10 to 100 seconds, creating violent explosions potentially observable in gravitational waves and across the electromagnetic spectrum. The transformative coincident gravitational-wave and electromagnetic observations of the binary neutron star merger GW170817 gave invaluable insights into these cataclysmic collisions, probing bulk nuclear matter at supranuclear densities, the jet structure of gamma-ray bursts, the speed of gravity, and the cosmological evolution of the local Universe, among other things. Despite the wealth of information, it is still unclear when the remnant of GW170817 collapsed to form a black hole. Evidence from other short gamma-ray bursts indicates a large fraction of mergers may form long-lived neutron stars. We review what is known observationally and theoretically about binary neutron star post-merger remnants. From a theoretical perspective, we review our understanding of the evolution of short- and long-lived merger remnants, including fluid, magnetic-field, and temperature evolution. These considerations impact prospects of detection of gravitational waves from either short- or long-lived neutron star remnants which potentially allows for new probes into the hot nuclear equation of state in conditions inaccessible in terrestrial experiments. We also review prospects for determining post-merger physics from current and future electromagnetic observations, including kilonovae and late-time x-ray and radio afterglow observations.

2.1 Introduction

The coincident gravitational-wave and electromagnetic observations of binary neutron star merger GW170817/GRB170817A (Abbott et al., 2017b,c,d)

was a watershed moment, signaling the beginning of a new field of multi-messenger gravitational-wave astronomy. Gravitational-wave emission from the inspiral phase was detected by the Advanced LIGO (Aasi et al., 2015) and Advanced Virgo (Acernese et al., 2015) interferometers (Abbott et al., 2017b). No gravitational-wave signal from the merger or post-merger phase was observed (Abbott et al., 2017f, 2019c). Approximately 1.7 s after the inferred merger time, GRB 170817A was observed by the *Fermi* Gamma-ray Burst Monitor (von Kienlin et al., 2017; Meegan et al., 2009a) and *Integral* (Savchenko et al., 2017), with an optical/UV counterpart detected by an array of instruments less than eleven hours later (Abbott et al., 2017c; Arcavi et al., 2017; Coulter et al., 2017; Lipunov et al., 2017; Soares-Santos et al., 2017; Tanvir et al., 2017; Valenti et al., 2017). Subsequent observations across a majority of the electromagnetic spectrum have continued for more than 1000 days (e.g., Fong et al., 2019; Hajela et al., 2019, 2020; Troja et al., 2020).

Gravitational-wave observations of the inspiral phase of binary neutron star mergers such as GW170817 and the more-recent GW190425 (Abbott et al., 2020a) provide valuable insight into the progenitor neutron stars, including their masses and spins, as well as the *cold* equation of state of nuclear matter (Abbott et al., 2017b,d, 2019b, 2020a). The lack of gravitational-wave observations of the merger and post-merger phase limits our inference of the remnant's evolution. We rely instead on indirect observations of the post-merger remnant derived from electromagnetic observations of ejected and stripped material. Understanding the post-merger evolution has the potential to provide valuable, complementary insights into the *hot* nuclear equation of state, as well as details about short gamma-ray bursts and kilonovae hitherto unknown.

This review is dedicated to understanding what we know about binary neutron star post-merger remnants from both an observational and theoretical perspective, and what we hope to learn in the near future as both gravitational-wave and electromagnetic observations increase in both number and detail.

There are four possible evolutionary pathways for a neutron star post-merger remnant. These depend primarily on the remnant mass and the unknown neutron star equation of state. The latter dictates the Tolman-Oppenheimer-Volkoff mass $M_{\rm TOV}$, which is the maximum mass a non-rotating neutron star can sustain (Tolman, 1939; Oppenheimer & Volkoff, 1939). Observations of pulsars in binary systems indicate $M_{\rm TOV} \gtrsim 2.0\,M_\odot$ (Demorest et al., 2010; Antoniadis et al., 2013; Cromartie et al., 2019). Determining the evolutionary pathway of both individual binary neutron star mergers and populations will therefore provide insights into the nuclear equation of state.

Given a remnant mass M, the four evolutionary pathways (shown schematically in Fig. 2.1) are:

- $M \gtrsim \chi M_{\rm TOV}$: the system promptly collapses to a black hole. Here χ is the threshold for prompt collapse which is dependent on the equation of state. Most equations of states predict $1.3 \lesssim \chi \lesssim 1.6$ (e.g., Shibata
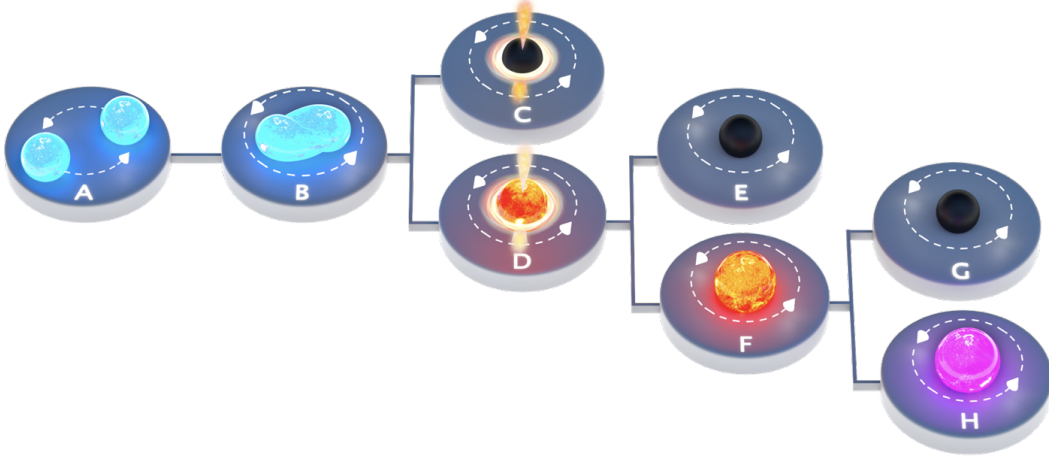
FIGURE 2.1: The fate of binary neutron star merger remnants. Two neutron stars coalesce, losing orbital angular momentum through the emission of gravitational waves until they eventually merge (panels A→B). Depending on the mass of the remnant, it will either promptly collapse to form a black hole with an accretion torus and jet (panels B→C), or form a rapidly differentially-rotating neutron star (panels B →D). Depending on the mass of this neutron star, it will either be *hypermassive*, in which case it will collapse to form a black hole in $\mathcal{O}(1\,\mathrm{s})$ (panels D→E), it will be *supramassive,* collapsing to form a black hole in $\lesssim 10^5\,\mathrm{s}$ (panels F→G), or it will form an infinitely stable neutron star (panels F→H).

et al., 2000, 2006; Baiotti & Rezzolla, 2017; Agathos et al., 2020; Bauswein et al., 2020). See path A→B→C of Fig. 2.1 and Sec. 2.3.

- $1.2\,M_{\mathrm{TOV}} \lesssim M \lesssim \chi\,M_{\mathrm{TOV}}$: a *hypermassive* neutron star survives the collision, but collapses to form a black hole on dynamical timescales. See path A→B→D→E of Fig. 2.1 and Sec. 2.4.

- $M_{\mathrm{TOV}} < M \lesssim 1.2\,M_{\mathrm{TOV}}$: a *supramassive* neutron star will survive the collision and will collapse to form a black hole on secular timescales. See path A→B→D→F→G of Fig. 2.1 and Sec. 2.5.

- $M \leq M_{\mathrm{TOV}}$: a stable neutron star will survive the merger. See path A→B→D→F→H of Fig. 2.1 and Sec. 2.5

Neutron stars can sustain more mass than their non-rotating limit M_{TOV} only when rapidly rotating (e.g., Friedman & Ipser, 1987; Baumgarte et al., 2000) or extremely hot (e.g., Bauswein et al., 2010; Kaplan et al., 2014), in which case either centrifugal support or thermal gradients provide an extra term in the force-balance equation of hydrodynamic equilibrium. As the star spins down and/or cools, this extra support is lost and the star eventually reaches a point where it can no longer support its own mass and collapses to form a black hole. In the case of hypermassive stars where $M \gtrsim 1.2M_{\mathrm{TOV}}$, uniform rotation cannot provide enough centrifugal support to prevent collapse, implying the star collapses as soon as enough differential

rotation is quenched. While this necessarily happens on the system's dynamical timescale i.e., the free-fall timescale the exact timescale is unknown. We discuss this in detail in Sec. 2.4.

In the supramassive case, even once differential rotation ceases and the star is uniformly rotating, it can still have enough centrifugal support to prevent gravitational collapse. Secular timescales associated with magnetic dipole radiation and gravitational-wave emission become relevant to establish the timescale for collapse in this case. It was previously believed that collapse would necessarily happen on a timescale of $\lesssim 10^5$ s (Ravi & Lasky, 2014), but this is dependent on the strength of the external dipole magnetic field. Recent afterglow observations of GW170817 may controversially shed new light on this topic (e.g Yu et al., 2018; Li et al., 2018; Piro et al., 2019; Ai et al., 2020; Troja et al., 2020). We discuss this in detail in Sec. 2.2.1.

Each of the pathways shown in Fig. 2.1 has different gravitational-wave and electromagnetic signatures, providing hope that one will be able to use such observations to make measurements of the nuclear equation of state. For example, the specific kilonova color depends on the survival time of merger remnants (e.g., Li & Paczyński, 1998; Metzger et al., 2010; Metzger & Fernández, 2014). In this article, we review theoretical and observational aspects of each of the pathways shown in Fig. 2.1.

The article is set out as follows. In Sec. 2.2, we review observational features of GW170817/GRB170817A that potentially allow us to discriminate the post-merger evolutionary pathway. We detail conflicting reports that independently suggest either a short- or long-lived neutron star survived the merger. There is compelling evidence that we have observed electromagnetic emission from numerous other binary neutron star mergers seen as short gamma-ray bursts. In Sec. 2.2.2, we review observational features of short gamma-ray bursts that potentially hint at long-lived neutron star remnants. Following the observational review, we discuss more theoretical aspects of post-merger remnant dynamics, separating the discussion into the different pathways outlined in Fig. 2.1. In Sec. 2.3 we discuss the prompt formation of black holes, in Sec. 2.4 we discuss dynamics and evolution of short-lived hypermassive remnants, and in Sec. 2.5 we discuss the evolution of longer-lived supramassive and stable neutron star remnants.

2.2 Observational evidence for post-merger remnants

2.2.1 The fate of GW170817

The smoking-gun observation to determine the nature of a post-merger remnant are gravitational waves from the hot, differentially rotating nascent neutron star. Searches for gravitational waves from possible post-merger remnants of GW170817 or GW190425 have not detected a signal (Abbott et al.,

2017f, 2019c, 2020a)[1]. This lack of detection was expected given current detector sensitivities and theoretical models (e.g., Clark et al., 2016b; Sarin et al., 2018; Zappa et al., 2018, and references therein). In the following, we concentrate on GW170817 for three primary reasons: first, given GW170817's relative proximity and loudness compared to GW190425; second the fact that the former has a plethora of electromagnetic observations, whereas the latter had no counterpart detections; and third, because of the larger total mass for GW190425, implying it likely promptly collapsed to form a black hole (i.e., path A→B→C in Fig. 2.1) (Abbott et al., 2020a).

Although the non-detection of gravitational waves means we are unable to definitively confirm the fate of the post-merger remnant of GW170817, much can be inferred through the various electromagnetic observations, albeit with somewhat conflicting conclusions. Here we elaborate on the possible fates of the post-merger remnant of GW170817[2], the observations that support and contradict each scenario.

Parameter estimation of the gravitational-wave inspiral signal constrained the total mass of the system to $2.74^{+0.04}_{-0.01}M_\odot$ (Abbott et al., 2019b). A small fraction of this total mass $\approx 0.07\,M_\odot$ was ejected and powered the optical kilonova AT2017gfo (Cowperthwaite et al., 2017; Coulter et al., 2017; Soares-Santos et al., 2017; Arcavi et al., 2017; Smartt et al., 2017; Chornock et al., 2017; Abbott et al., 2017c; Troja et al., 2017). AT2017gfo was first detected as a luminous blue source with a thermal spectrum peaking in optical and ultraviolet frequencies (e.g., Evans et al., 2017a), evolving over the course of a few days to become dominated by emission in the near-infrared (e.g., Tanvir et al., 2017; Pian et al., 2017). The late-time near-infrared observations agree well with "red" kilonova models predicted by the radioactive decay of heavy r-process nuclei (Li & Paczyński, 1998; Metzger et al., 2010). Similarly, the early-time "blue" observations are well explained by lower-opacity radioactive material (Metzger et al., 2010) as would be expected if the outer layers of the ejecta are composed exclusively of light r-process nuclei formed from matter with relatively high electron fractions (Metzger & Fernández, 2014). We point the interested reader to Fernández & Metzger (2016); Metzger (2017b) for detailed reviews of kilonovae and Sec. 2.4.2, where we discuss the theoretical impact of merger remnants on kilonovae.

Different neutron-richness of the material implies different ejecta sources. Two possible sources are the dynamical ejecta launched by tidal forces (Rosswog et al., 1999; Radice et al., 2016), and matter launched from shock heating at the contact boundary of the merger (Bauswein et al., 2013; Hotokezaka et al., 2013a; Margalit & Metzger, 2017). The former is ejected along the equatorial plane with typically lower electron fractions than the latter, which is

---

[1]van Putten & Della Valle (2019) claim a detection of gravitational waves following GW170817, although see Oliver et al. (2019a) for a rebuttal of this work.

[2]It is worth noting that the electromagnetic observations of GW170817 are consistent with a neutron star black hole merger, which would produce a black hole remnant. However, to claim GW170817 was a neutron star black hole merger, one must be able to explain the existence of black holes less massive than $2M_\odot$.

launched along a broad range of directions (e.g., Sekiguchi et al., 2016; Metzger, 2017b). Another source of ejecta are outflows from the accretion torus of a central engine (Metzger et al., 2008; Siegel & Ciolfi, 2016; Siegel & Metzger, 2018), typically with broad electron-fraction distributions that can increase with time due to constant neutrino irradiation from a central neutron-star engine.

As mentioned, observations of AT2017gfo showed evidence for at least two distinctive components: an early-time "blue" component and a late-time "red" component. There are also hints at a third "purple" component (Villar et al., 2017), a point we discuss in more detail below. Common interpretations of these observations suggest that the two dominant components of the kilonova were powered by two distinct ejecta components. The early blue component by a lanthanide-poor $\approx 0.02 M_\odot$ of material with electron fraction $Y_e \gtrsim 0.25$ from accretion-disk outflows along the binary polar axis (e.g., Smartt et al., 2017; Evans et al., 2017a; Tanvir et al., 2017; Pian et al., 2017), or alternatively from dynamical ejecta launched through shock heating. On the other hand, the late-time red component was likely powered by lanthanide-rich $\approx 0.05 M_\odot$ ejecta with electron fraction $Y_e \lesssim 0.25$ (e.g., Cowperthwaite et al., 2017). The total amount of ejecta and the blue component in particular, offers the first clue into the nature of the post-merger remnant. The amount of ejecta required to produce these observations is incompatible for a remnant that promptly collapsed into a black hole (e.g., Radice et al., 2018b). Prompt collapse would have resulted in a primarily red and dimmer kilonova (e.g., Margalit & Metzger, 2017; Piro et al., 2019).

The merger was accompanied by a gamma-ray burst jet that was most-likely structured and off axis (Troja et al., 2017; Alexander et al., 2018; Mooley et al., 2018b,a; Troja et al., 2019). In classical gamma-ray burst models, the jet is launched through accretion onto a black hole, leading to interpretations of the 1.7 s delay between the gravitational-wave signal and gamma-ray burst (Goldstein et al., 2017a; Savchenko et al., 2017) as the maximum lifetime of a putative neutron star before it collapses into a black hole (e.g., Metzger et al., 2018). This is further necessitated by claims that the region around the poles needs to be relatively free of ejecta to efficiently launch an ultra-relativistic jet (e.g., Ciolfi et al., 2019), a point we return to in Sec. 2.5.1. This interpretation is contentious. There are numerous short and long gamma-ray burst observations with evidence of neutron-star central engines (e.g., Rowlinson et al., 2010, 2013; Lü et al., 2015; Sarin et al., 2020b), providing observational evidence jets are not only launched from accretion tori around black holes. In addition, numerical-relativity simulations show short gamma-ray burst jets could potentially be launched given sufficiently large, but realistic, magnetic field strengths of the remnant neutron star ($B \gtrsim 10^{14}$ G) (e.g., Ruiz et al., 2016; Ciolfi, 2018; Mösta et al., 2020; Ruiz et al., 2021). We discuss these points in greater detail in Sec. 2.5.1. These observations and simulations disfavour the hypothesis that the remnant of GW170817 *must* have collapsed into a black hole in order to launch the jet, opening the possibility for the remnant to be a long-lived supramassive or an infinitely stable neutron star.

With the above caveats in mind, *if* the remnant collapsed to a black hole

before launching the jet, strong constraints on the non-rotating neutron star maximum mass can be derived, indicating $M_{\text{TOV}} \lesssim 2.2\,M_\odot$ (e.g., Margalit & Metzger, 2017; Rezzolla et al., 2018a; Ai et al., 2020). Although other analyses derive a more conservative estimate, $M_{\text{TOV}} \lesssim 2.3\,M_\odot$ by relaxing some of the assumptions on energy emitted in gravitational-wave and neutrinos indirectly imposed by other analyses (e.g., Shibata et al., 2019; Ruiz et al., 2018).

While the blue color and total ejecta mass are helpful in ruling out prompt collapse, the exact source of the ejecta mass is unclear. Observations suggest an ejecta mass of $\approx 0.02 M_\odot$ with a mean velocity and electron fraction of $\approx 0.25c$ and $Y_e \gtrsim 0.25$, respectively (Smartt et al., 2017; Evans et al., 2017a; Tanvir et al., 2017; Pian et al., 2017). Although the velocity and high electron fraction agree with a shock-heated dynamical ejecta source, the quantity of material is difficult to explain. Relativistic hydrodynamics simulations of equal-mass progenitor systems typically only show ejecta mass $\lesssim 0.01 M_\odot$ for soft equations of state that have small neutron star radii $R \lesssim 11$ km (e.g., Hotokezaka et al., 2013a; Bauswein et al., 2013; Radice et al., 2016). However, such compact progenitors have less ejecta in the tidal tails, and less mass in the resultant torus, which is inconsistent with the observations of the red component of the kilonova discussed above (Radice et al., 2018b; Metzger et al., 2018). This raises doubt about the dynamical source of the blue component of the kilonova. An alternate explanation for the origin of this ejecta posits that it is a magnetized neutrino-irradiated wind from a hypermassive neutron star that survived ~ 1 s before collapsing into a black hole and had a strong poloidal magnetic field $B_p \approx 1 - 3 \times 10^{14}$ G (Metzger et al., 2018). Kilonova observations a few hours after the merger, had they existed, could have provided observational support for this hypothesis.

There are other interpretations of the kilonova observations that imply a different fate of the post-merger remnant. For example, there is speculation that observations are best fit by a three-component model (Villar et al., 2017). Here, the early-time blue kilonova is of similar mass as inferred by other groups, but the late-time observations are dominated by an intermediate-opacity purple component with a significantly weaker red component. These purple/red components may be sourced by the accretion disk around a central engine, however it is difficult to interpret why there is a large variation in the opacity of these components, especially if they are coming from the same source. The purple component may be naturally supported by a long-lived remnant neutron star (Yu et al., 2018), where the high-energy emission from the remnant's wind ionizes the surrounding material (Metzger & Fernández, 2014). Li et al. (2018) compared models that could account for both the peak luminosity and time of the kilonova observation, concluding that the observations are best fit with a long-lived neutron star.

A long-lived remnant supports the low-significance x-ray flare 155 d following the merger (Piro et al., 2019), potentially due to untwisting toroidal magnetic field similar to x-ray flares from older magnetars (Thompson & Duncan, 1995, 1996; Piro et al., 2019) (although, see Lin et al. (2019) for an alternate explanation). Energetic arguments imply the toroidal component

of the magnetic field must be $B_t \gtrsim 10^{14}$ G, albeit with a relatively low $\approx$ 10^{12} G poloidal field such that gravitational-wave emission dominates the spin down for long times (Piro et al., 2019). Such a low poloidal but high toroidal magnetic field structure is perhaps concerning but not dissimilar to the soft gamma-ray repeater SGR 0418+5729 (Rea et al., 2013) (although one should treat such measurements cautiously; see (e.g., Mastrano et al., 2013)). Prolonged x-ray excess almost 1,000 d after the merger is still consistent with a long-lived central engine driving the emission (Troja et al., 2020). If indeed this excess is due to a long-lived neutron star, it is almost certainly not supramassive, but likely has a mass below the TOV mass, i.e., it follows path A→B→D→F→H in Fig. 2.1. Although the above interpretations suggest a long-lived neutron star may have formed in the aftermath of GW170817, there are also problems with this interpretation. For example, if long-lived, the surface poloidal component of the magnetic field must be $B_p \lesssim 10^{11} - 10^{12}$ G (Yu et al., 2018; Piro et al., 2019; Ai et al., 2018). This constraint is problematic as it is energetically difficult to launch a Poynting-flux-dominated jet with $B_p \lesssim 10^{14}$ G (e.g., Ciolfi, 2018, and references therein). Moreover, Kelvin-Helmholtz and magneto-rotational instabilities dramatically amplify the seed magnetic fields to values greater than $B_p \gtrsim 10^{15}$ G (e.g., Kiuchi et al., 2014, 2015; Aguilera-Miret et al., 2020). Furthermore, the lack of signature of the rotational energy of the stable neutron star on the kilonova Margalit & Metzger (2017) and radio (e.g., Ricci et al., 2020; Schroeder et al., 2020) implies a considerable amount of energy emitted in gravitational waves, which requires a large ellipticity (Ai et al., 2020). If the remnant of GW170817 was long-lived, it perhaps provides the most interesting constraints on the maximum mass of neutron stars $M_{\mathrm{TOV}} \gtrsim 2.4\,M_\odot$ (Ai et al., 2020).

If, dear reader, you are not yet confused enough about the nature of the remnant of GW170817, there is one final scenario consistent with all observations. Namely, the remnant was a supramassive neutron star that spun-down primarily through gravitational waves, collapsing into a black hole after losing centrifugal support approximately 300 s after the merger (e.g., Ai et al., 2020). We note that one can impose longer collapse times for different magnetic field configurations. Such a scenario supports the kilonova observations and the potential lack of observational signature of a rapidly spinning neutron star in other electromagnetic bands at later times. In general, one may expect to see the signature of such a remnant on the x-ray afterglow of the short gamma-ray burst (e.g., Rowlinson et al., 2010, 2013, and Sec. 2.2.2). However, *Swift* did not observe the region until ~ 0.039 d after the gamma-ray burst trigger (Evans et al., 2017a), placing an upper limit on the collapse time $t_{\mathrm{col}} \lesssim 0.039$ d of such a supramassive neutron star. If supramassive and collapsing in less than ~ 0.039 d, the maximum neutron star mass $2.1 \lesssim M_{\mathrm{TOV}}/M_\odot \lesssim 2.4$ (Ai et al., 2020).

The first multimessenger binary neutron star merger GW170817 offered an unprecedented opportunity for a detailed study into the the aftermath of such a collision. Unfortunately, while electromagnetic observations were

plentiful and extensive, they remain inconclusive. The lack of a smoking-gun observation of gravitational waves from a post-merger remnant make inferring the nature of the remnant difficult. In practice, the only scenario everyone seems to agree can be ruled out is of prompt collapse into a black hole.

2.2.2 The fate of other binary neutron star merger remnants

The coincident detection of gravitational waves from a binary neutron star merger GW170817 and the short gamma-ray burst GRB170817A confirmed that at least some of the latter are caused by the former. While sensitivity improvements in gravitational-wave detectors will see increased numbers and regularity of binary neutron star merger detections, it will remain true that most observed gravitational-wave signals will *not* be accompanied with electromagnetic signatures. Likewise, the foreseeable future will see most short gamma-ray burst observations *not* accompanied by gravitational-wave detections. But there is already a wealth of short gamma-ray burst observational data at our disposal that can, and is, used to understand the remnants of binary neutron star mergers.

The x-ray afterglows of some short gamma-ray bursts exhibit extended plateaus that indicate energy injection from rapidly rotating neutron star central engines (e.g., Rowlinson et al., 2013; Lü et al., 2015). This even includes the observations of a putative off-axis gamma-ray burst seen only as an x-ray transient CDF-S XT2 that is consistent with these other x-ray afterglows (Xue et al., 2019; Xiao et al., 2019). Such observations are difficult to interpret in the standard afterglow model of synchrotron radiation from shocks produced by a jet interacting with the surrounding interstellar medium. The first such observation consistent with energy injection from a short gamma-ray burst was GRB051221A (Fan & Xu, 2006), which was followed by a catalogue of bursts (Rowlinson et al., 2013). These were shown to be consistent with models of energy injection where the spin down of the nascent neutron star is driven by magnetic dipole radiation (Dai & Lu, 1998; Zhang & Mészáros, 2001), a model that has further been extended to include spin down with arbitrary braking indices (Lasky et al., 2017), akin to what is seen in the spin down of radio pulsars.

For the majority of short gamma-ray bursts with extended x-ray plateaus, debate continues to rage about the origin of the x-ray flux. For example, evidence for an achromatic jet break in the broadband observations of GRB140903A. This achromatic break has been used to argue that the long-lived emission is due to a combination of jet geometry and dynamics of the fireball (Troja et al., 2016), in stark contrast to other works that showed the afterglow is consistent with the spin down of a long-lived central engine (Lasky et al., 2017; Zhang et al., 2017). Systematic Bayesian model comparison between the two scenarios using only x-ray observations overwhelmingly favours the latter explanation (Sarin et al., 2019).

Model comparison between fireball dynamics and a long-lived central engine for another gamma ray-burst GRB130603B yields intriguingly different

results (Sarin et al., 2019). The discriminator between the two models is a quantity called the odds ratio, but this itself depends on the unknown equation of state. The punch line is that, if the maximum neutron star mass is $M_{TOV} \lesssim 2.3\,M_\odot$, the data favours the fireball-shock model. Conversely, if $M_{TOV} \gtrsim 2.3\,M_\odot$, the data favours the existence of a long-lived neutron star central engine. It is worth mentioning the above conclusion relies on knowing the underlying binary neutron star mass distribution, which in light of GW190425, we do not. Moreover, more detailed modeling for each scenario is required, which may further discriminate and potentially yield different conclusions.

The evolution of the x-ray luminosity in these afterglows does allow us to understand somewhat the dynamical evolution of the central engine. For example, gamma-ray bursts GRB130603B and GRB140903A, are spinning down with braking index $n = 2.9 \pm 0.1$ and $n = 2.6 \pm 0.1$, respectively (Lasky et al., 2017), where a braking index of $n = 3$ is dipole magnetic spin down in vacuum. It is worth stressing that all but one radio pulsar with accurately measured braking index falls below $n = 3$ where magnetic torques are believed to dominate spindown (Archibald et al., 2016; Clark et al., 2016a; Marshall et al., 2016), although see Parthasarathy et al. (2019) for a census of the highly uncertain nature of braking indices in *young* pulsars. Moreover, it is also worth emphasising that calculations of realistic braking indices for pulsars predicts they fall below 3 (e.g., Melatos, 1997)—we discuss theoretical expectations for the dynamics of neutron-star spin down on these relatively long timescales in Sec. 2.5.

The highly dynamic nature of the newly-born neutron star implies the assumed constant braking index and smooth spin-down evolution are almost certainly naive assumptions. For example, the magnetic field's inclination angle will likely evolve as a function of time, leading to a changing inferred braking index (see Şaşmaz Muş et al. (2019) for interpretations of long gamma-ray bursts in this context and Sec. 2.5 for details of the relevant physics), or the triaxial nature of the remnant may cause precession and a flux-modulated amplitude of the light curve (Melatos, 2000; Suvorov & Kokkotas, 2020). In addition, the radiative efficiency is likely not constant throughout the spin down and may, for example, depend on the luminosity of the central engine itself (Xiao & Dai, 2019). This radiative efficiency likely changes as the shock front decelerates as it ploughs into the interstellar medium (Cohen & Piran, 1999; Dall'Osso et al., 2011; Stratta et al., 2018; Sarin et al., 2020a), and may evolve through plerionic-like emission as electrons fill the cavity within the gamma-ray burst blast wave (Strang & Melatos, 2019). In reality, the dynamical evolution of the remnant and the resultant emission that eventually reaches the observer will be affected by all of these physical processes and more, although which are truly the most dominant is still an open question.

In all, approximately 70% of short gamma-ray bursts exhibit behaviour consistent with long-lived remnants, split into $\approx 30\%$ with supramassive, and $\approx 30\%$ stable neutron stars (Gao et al., 2016), although these numbers

are highly uncertain (e.g., Margalit & Metzger, 2019). In principle, understanding these fractions together with the progenitor mass distribution has the ability to provide strong constraints on the neutron star equation of state through the maximum mass. In practice, our understanding of the numbers are not yet mature enough to make quantifiably-reliable estimates for three reasons. First, determining the nature of the remnant from the x-ray data alone is fraught with difficulties, as highlighted by the various analyses of GRB130603B and GRB140903A mentioned above. Second, while we previously thought we understood the mass distribution of binary neutron stars from galactic radio observations of double neutron star systems (e.g., Kiziltan et al., 2013; Alsing et al., 2018; Farrow et al., 2019), only one of the two extragalactic neutron star mergers has progenitor masses consistent with that distribution (Abbott et al., 2020a). Third, it is possible that some short gamma-ray bursts may be misidentified as long gamma-ray bursts caused by the collapse of massive stars, or that they are caused not by merging neutron stars, but by a neutron star-black hole merger, or that they represent a biased sample of neutron star mergers only including ones that produced a black hole which could launch an ultra-relativistic jet. All of these effects would cause systematic problems with measuring the maximum mass. Understanding both these systematic effects by collecting more gravitational-wave observations to ameliorate the former issue, and more x-ray plateau observations the latter, will eventually provide interesting and stringent constraints on M_{TOV}.

Perhaps our best understanding of post-merger behaviour comes from a subset of eighteen short gamma-ray bursts that not only exhibit x-ray plateaus, but also show sudden drops in the x-ray luminosity tens to thousands of seconds after the prompt emission (e.g., Troja et al., 2007; Rowlinson et al., 2013; Sarin et al., 2020b). Such dramatic changes in flux are particularly difficult to explain in the standard fireball-shock scenario, but fit well the premise that a *supramassive* neutron star was born in a neutron star merger and collapses to form a black hole simultaneously shutting of the energy injection.

The supramassive neutron star observations again provide a tantalising way of developing our understanding of the dynamics of the nascent neutron star and the equation of state of nuclear matter (e.g., Fan et al., 2013; Lasky et al., 2014; Ravi & Lasky, 2014; Li et al., 2016; Gao et al., 2016; Drago et al., 2016; Drago & Pagliara, 2018). The procedure is straight forward: if we understand the progenitor mass distribution (which we do not), as well as the dominant spin down mechanism (we do not understand that either), and the spin-down rate/braking index (not really), then we can rearrange the set of equations governing the system's evolution to find that the time of collapse is a function of the unknown maximum neutron star mass, which we can therefore infer. This procedure has been performed a number of times in different works, each arriving at different answers depending on the underlying assumptions at each of the step. The vanilla assumptions of dipole vacuum spin down of hadronic stars does not well fit the data (Fan et al., 2013; Ravi & Lasky, 2014), leading some authors to infer that quark stars, rather than

hadronic stars, best explain the data (e.g., Li et al., 2016; Drago et al., 2016), while others infer that gravitational radiation dominates the star's angular momentum loss rather than magnetic dipole radiation (e.g Fan et al., 2013; Gao et al., 2016).

The correct way to do the above procedure rigorously is to include all sources of uncertainty and marginalise over the unknown parameters such as those describing the progenitor mass distribution, the braking index, the equation of state, etc (for details, see Sarin et al., 2020b). Hierarchical Bayesian inference then allows posterior probability distributions to be calculated for each of these parameters, including those that describe the population as a whole, rather than individual gamma-ray burst afterglows. As one would expect, including all uncertainties implies less-well constrained parameters. Ultimately, the eighteen-known short gamma-ray bursts allow us to constrain $M_{\mathrm{TOV}} = 2.31^{+0.36}_{-0.21}\,\mathrm{M_\odot}$, with 68% uncertainties. Perhaps more interestingly, $69^{+21}_{-39}\%$ of remnants are inferred to be spinning down predominantly through gravitational-wave emission, potentially providing interesting consequences for gravitational-wave detection of a post-merger remnant, or indirectly through a stochastic gravitational-wave background. Furthermore, the observations show tentative evidence for these neutron stars to be composed of deconfined quark matter, suggesting a phase transition in the course of merger that may be visible through gravitational-wave measurements of the inspiral (e.g., Chatziioannou et al., 2017; Bauswein et al., 2019).

Having reviewed the observational aspects of short gamma-ray bursts and what can be learned about the remnants of the binary neutron star mergers that power them, we now move onto more theoretical aspects, following the evolutionary scenarios discussed alongside Fig. 2.1d.

2.3 Prompt formation of black holes
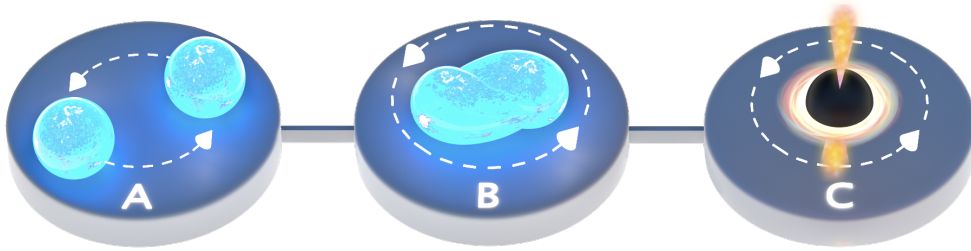
FIGURE 2.2: A post-merger remnant of mass $M \gtrsim 1.5\,M_{\mathrm{TOV}}$ will immediately collapse to form a black hole with an accretion torus and jet.

Perhaps the least interesting of outcomes of a binary neutron star merger is the prompt collapse to a black hole (Fig 2.2; panels B→C). Upon collapse, a thick accretion torus forms in the black hole's equatorial plane, potentially driving a Blandford-Znajek jet (Blandford & Znajek, 1977) that is seen as the

short gamma-ray burst. Such a scenario likely leaves an undetectable post-merger gravitational-wave signal, and little direct electromagnetic signal that can be used to infer properties of the central engine,unless the binary has significantly unequal masses, where the tidal disruption of the secondary neutron star can power significant electromagnetic counterparts (e.g., Bernuzzi et al., 2020).

Prompt black hole formation implies that, following coalescence, the gravitational-wave signal simply shuts down, with nearly spherical collapse generating comparatively minimal gravitational-wave emission. We can approximate the lowest quasi-normal mode ringdown frequency for a remnant black hole as (Echeverria, 1989)

$$f_{\text{gw}}^{\text{qnm}} \approx 11\,\text{kHz} \left(\frac{M}{3M_\odot} \right)^{-1} \left[1 - 0.63\,(1-a)^{3/10} \right], \qquad (2.1)$$

where M is the remnant mass and a the dimensionless spin. Faster rotating black holes emit higher frequency gravitational-wave signals; a non-rotating ($a = 0$) black hole of $M \approx 3\,M_\odot$ emits its lowest quasinormal mode signal at $f_{\text{gw}}^{\text{qnm}} \approx 4\,\text{kHz}$. Prompt collapse will more typically result in a remnant with $a \sim 0.7$–0.8 for which $f_{\text{gw}}^{\text{qnm}} \gtrsim 6\,\text{kHz}$. In these regimes, the sensitivity of current interferometers (Abbott et al., 2016; Aasi et al., 2015; Acernese et al., 2015) and even proposed future detectors (e.g., Miller et al., 2015; Punturo et al., 2010; Abbott et al., 2017a; Martynov et al., 2019; Ackley et al., 2020) is not sufficient to detect such a signal at relevant distances.

Potentially, the prompt formation of a black hole can have implications for electromagnetic emission, in particular through a lack of sustained energy injection into the x-ray and optical afterglow signal and in the amount of ejecta both dynamical and from an accretion disk. For example, kilonova observations would likely differ from those of GW170817/AT2017gfo in that they would be primarily red due to the lack of neutrino irradiation of the ejected material and inferred to have less mass (e.g., Margalit & Metzger, 2017; Piro et al., 2019). If observations can concretely say no remnant survived the collisions, tight constraints could be placed on the equation of state of nuclear matter. We return to this in subsequent sections.

2.4 Short-lived, hypermassive neutron stars

A dominant fraction of binary neutron star mergers likely form post-merger neutron star remnants that are either hypermassive, supramassive, or long-lived (e.g., Gao et al., 2016; Margalit & Metzger, 2019). In all these cases, the remnant will undergo a short period of highly-dynamic activity (Fig. 2.3; panels B→D) before either settling down into rigid-body rotation (Fig. 2.1; panels D→F), or collapsing to form a black hole (Fig. 2.3; panels D→E). The latter scenario describes that of a hypermassive neutron star. We review those dynamics in Sec. 2.4.1, and consequences for electromagnetic and gravitational-wave observations in Secs. 2.4.2 and 2.4.3, respectively.
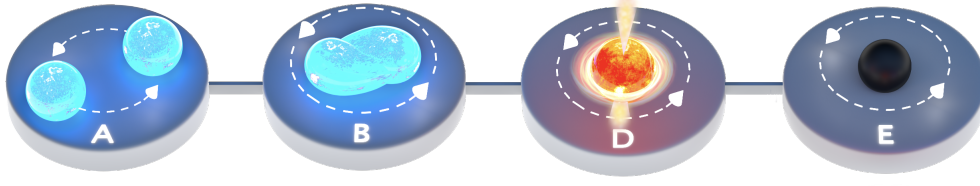
FIGURE 2.3: A post-merger remnant of mass $1.2\,M_{\mathrm{TOV}} \gtrsim M \gtrsim 1.5\,M_{\mathrm{TOV}}$ will form a hypermassive neutron star which will collapse to a black hole on a timescale $\mathcal{O}(1\,\mathrm{s})$.

We note that the dynamics and emission scenarios outlined in this section are also relevant for the early evolution of a supramassive (Fig. 1: panels D→F→G) and an eternally-stable neutron star (panels D→F→H).

2.4.1   Dynamics and the Collapse Time

The short-term dynamics of binary neutron star merger remnants in the first tens of milliseconds and up to a few seconds depends on physics as yet not completely understood. Immediately following the merger, the rotational profile of the remnant and the amount of mass in the disk depend principally on the mass ratio of the progenitor (e.g., Oechslin & Janka, 2006; Fernández & Metzger, 2013; Metzger & Fernández, 2014; Bernuzzi, 2020) and the equation of state (e.g., Shibata & Taniguchi, 2006; Shibata et al., 2006; Kastaun & Galeazzi, 2015). The hot remnant is rotating differentially, has an incredibly strong magnetic field, several large-amplitude oscillation modes, and cools primarily through neutrino emission. If the mass of the remnant is above the supramassive limit, then it will collapse within a few seconds of formation. General relativistic magnetohydrodynamic simulations are currently inadequate to robustly and reliably determine that lifetime for several reasons. First, not all of the aforementioned physics is adequately resolved (Kiuchi et al., 2018, and see below), and second, the simulations generally only last $\lesssim 50\,\mathrm{ms}$ Ciolfi et al. (2017) (although (see e.g., Ciolfi et al., 2019; Ciolfi, 2020a; Shibata et al., 2021) for recent, long-lived simulations lasting up to $1\,\mathrm{s}$ post merger).

Differential rotation of the remnant and thermal pressure are expected to provide extra centrifugal support to sustain the remnant above the maximum rigidly-rotating mass limit. When either of these is sufficiently quenched, the remnant will collapse rapidly to form a black hole. Conventional wisdom (e.g., Baumgarte et al., 2000; Shapiro, 2000) states that differential rotation is suppressed on an Alfvén timescale, which can be approximately written as

$$\tau_{\mathrm{A}} \approx 0.3\,\mathrm{s} \left(\frac{\langle B \rangle}{10^{15}\,\mathrm{G}} \right) \left(\frac{M}{2M_\odot} \right)^{1/2} \left(\frac{R}{10\,\mathrm{km}} \right)^{-1/2}, \qquad (2.2)$$

where $\langle B \rangle$ is the volume-averaged magnetic field inside the star, and R is the star's radius. Below we argue that magnetic-field quenching should occur

on a longer timescale than expressed in Eq. 2.2. Clearly, not all of the differential rotation must be suppressed for the remnant to collapse, but only the critical threshold must be reached which will depend ultimately on a number of factors, including how much more massive the remnant is than the supramassive-mass threshold.

The speed with which the internal magnetic field grows, its saturation strength, and the role of magnetic-field instabilities are potentially the most significant unknowns when considering the suppression of differential rotation (e.g., Ferrario et al., 2015). General relativistic, three-dimensional magnetohydrodynamic simulations of mergers show the magnetic field at the shock interface between the two stars grows rapidly at initial times (e.g., Giacomazzo & Perna, 2013; Kiuchi et al., 2014, 2015; Ruiz et al., 2016; Ciolfi et al., 2017; Kiuchi et al., 2018; Ciolfi et al., 2019; Aguilera-Miret et al., 2020). This field growth is primarily due to the Kelvin-Helmholtz instability that develops at the shear boundary between the two stars. The highest-resolution simulations show amplification of the average field up to $\sim 10^3$ times the seed field (Kiuchi et al., 2018), although this is still under-resolved and considered a lower limit on the potential of the Kelvin-Helmholtz instability (Kiuchi et al., 2018; Duez & Zlochower, 2019). Recently, numerical simulations with a resolution ~ 37 m (cf. typical resolutions $\gtrsim 120$ m) show amplifications up to 10^5 times the seed field (Aguilera-Miret et al., 2020). This resolution is considered adequate for resolving the Kelvin-Helmholtz instability. Magnetic winding, the magneto-rotational instability, and turbulence can subsequently amplify the field to $\gtrsim 10^{16}$ G on short timescales (e.g., Duez et al., 2006a,b; Zrake & MacFadyen, 2013; Siegel et al., 2013). It is worth noting that these latter effects are beyond the resolution limit of current numerical simulations Baiotti & Rezzolla (2017); Kiuchi et al. (2018), in particular with respect to MRI-driven turbulence, implying quantitative evolution of the star's magnetic-field growth should not be trusted.

Most numerical-relativity simulations are performed under the assumption of ideal magnetohydrodynamics, where infinite conductivity of the fluid implies the magnetic field is frozen into the dynamic fluid. However, the hot remnant should almost certainly have regions of finite conductivity, implying flux freezing is not the correct assumption. The scarce numerical-relativity simulations of post-merger remnants that *include* the effects of resistive magnetohydrodynamics in the core indeed show the expected result that the magnetic field lags behind the fluid (Dionysopoulou et al., 2015). This implies that magnetic winding is less efficient than previously believed, and the Alfvén timescale of Eq. 2.2 should be taken as a rough *lower* bound for the quenching of differential rotation through magnetic-field winding.

In addition to differential rotation, the nascent star is supported through thermal pressures. Merger simulations ubiquitously show temperatures at the shock interface in excess of 3×10^{11} K, and the majority of the star above 10^{11} K (e.g., Sekiguchi et al., 2011a,b; Foucart et al., 2016; Perego et al., 2019). Simulations that take cooling into account show the remnant may not collapse for a few cooling timescales (Paschalidis et al., 2012), which may be as long as a few seconds (Duez & Zlochower, 2019). We return to the cooling

of the nascent neutron star in Sec. 2.5.3, but the above argument suggests the dominant physical processes dictating the collapse time of the remnant is magnetic winding rather than thermal dissipation.

Quite clearly there is complicated physics dictating the collapse time of a hypermassive remnant. If one believes that the collapse of the hypermassive star is required to launch the gamma-ray burst, then 1.74 s delay between the gravitational-wave inferred merger time of GW170817 and the gamma-ray detection could be partially explained by the collapse time of the hypermassive star. This is complicated by the additional unknown time it takes for the jet to launch from the black hole, and for the jet to break out from the merger ejecta. It would therefore be nice to be able to directly measure the collapse time of the hypermassive star, which may be done with future gravitational-wave detections—see Sec. 2.4.3.

Ultimately, when the remnant collapses to form a black hole, it will do so approximately on a dynamical timescale (Stark & Piran, 1985). The dynamics and timescale of the collapse depend heavily on the system's angular momentum (Baiotti et al., 2005, 2007) and the degree of differential rotation (Giacomazzo et al., 2011). Although the free-fall timescale of a massive neutron star is $\lesssim 0.01$ ms, the collapse timescale for a rapidly, differentially rotating neutron star is ~ 1 ms (Giacomazzo et al., 2011). Whether the collapse time can be measured upon a successful detection of post-merger gravitational waves is an open question (see Sec. 2.4.3), however the lifetime of the remnant is believed to indirectly impact the spectral evolution of the electromagnetic signature; a point to which we now turn.

2.4.2 Electromagnetic consequences

Kilonova emission is a direct result of radioactive decay of heavy elements produced by the merger ejecta. As this review deals specifically with the merger remnant, rather than the merger itself, we do not review the physics of kilonovae emission directly. Instead, we focus on the effects the hypermassive remnant's lifetime, dynamics, and evolution have on the kilonova and other electromagnetic emission channels. For reviews of kilonova itself (see e.g., Fernández & Metzger, 2016; Metzger, 2017b).

The ejecta in a neutron star merger can be broadly split into two categories: dynamical ejecta produced in the merger itself, and the (secular) outflow from the accretion disk formed around the remnant object. We note that there may be additional sub-dominant channels that contribute to the total ejecta. Both the amount of ejecta and its properties (velocity and electron fraction) are intrinsically connected to binary parameters and the fate of the merger remnant, with the electron fraction being perhaps the most critical as it directly impacts what elements can be synthesised and therefore the color of the kilonova.

Dynamical ejecta usually constitutes two sources: shock-heated ejecta from the contact interface between the two merging neutron stars and spiral arms from the tidal interactions in the merger. The former following a $\sin^2 \theta$ distribution with respect to the polar angle (e.g., Perego et al., 2017a), while

the latter is launched predominantly in the equatorial plane (e.g., Bernuzzi, 2020). The total quantity of dynamical ejecta depends sensitively on the fate of the merger remnant and the binary mass ratio (e.g., Bauswein et al., 2013; Lehner et al., 2016), if the remnant promptly collapses into a black hole, there will be little shock-heated ejecta, as the region is promptly swallowed up (Bauswein et al., 2013; Ciolfi et al., 2017; Radice et al., 2018a). In general, asymmetric binaries tend to produce more ejecta (Rezzolla et al., 2010; Bauswein et al., 2013). However, we emphasise that this relationship is not well understood quantitatively. Numerical simulations suggest that the total dynamical ejecta in a merger is in the range of $10^{-4} - 10^{-2} M_\odot$ with velocities in the range $0.1 - 0.3c$ (see e.g., Hotokezaka et al., 2013a) and a broad electron fraction distribution, $Y_e \sim 0.1 - 0.4$ (Radice et al., 2016) which dictates what elements can be synthesised from this ejecta, potentially up to an atomic mass number, $A \sim 195$ (Wanajo et al., 2014; Martin et al., 2015). We note that this is an area of active research, with significant uncertainties in many critical nuclear reaction quantities (Zhu et al., 2020).

The other source of ejecta in a neutron star merger is the outflow from the accretion disk that forms around the remnant object. The quantity of mass in the accretion disk range from $\sim 0.01 - 0.3 M_\odot$ depending on the binary parameters (e.g., Oechslin & Janka, 2006) and the fate of the merger remnant, with prompt formation likely resulting in less mass around the remnant object (e.g., Perego et al., 2014; Metzger & Fernández, 2014; Martin et al., 2015; Metzger, 2017b). Depending on the lifetime of the remnant neutron star (as we discuss below), outflows from this disk likely contribute more mass to the ejecta than the dynamical ejecta launched in the merger itself (Perego et al., 2014; Fernández & Metzger, 2016; Siegel & Metzger, 2018), a statement seemingly verified by the inferred properties of the kilonova, AT2017gfo (e.g., Smartt et al., 2017; Kasen et al., 2017; Metzger et al., 2018). It is the properties of this outflow that are most affected by the nature and lifetime of the remnant and make the biggest impact on the kilonova. In particular, the cooling of the nascent neutron star through neutrino losses. We discuss the thermal evolution of neutron stars in detail in Sec 2.5.3.

The accretion disk itself evolves viscously and cools through neutrino emission, driving a wind similar to proto-neutron stars born in supernovae (e.g., Beloborodov, 2008; Metzger et al., 2008). The mass loss through this channel is dependent on the neutrino flux, which as we elaborate below is connected to the fate of the remnant. Depending on the merger outcome, this process results in a mass loss of up to $10^{-3} M_\odot$ either from the disk, remnant neutron star or a combination of the two. Further evolution of the disk is dictated by angular momentum transport, either through turbulence generated by the magneto-rotational instability (e.g., Metzger & Fernández, 2014; Siegel & Metzger, 2017, 2018) or by spiral density waves excited by oscillations of a neutron star remnant which expand the disk outwards (e.g., Nedora et al., 2019; Metzger, 2017b). Initially, the disk accretes matter at a relatively high rate, but once this rate drops below a critical threshold, cooling through neutrinos is ineffective and the disk thermally expands. In this process, free nucleons recombine into $\alpha-$particles which releases

enough energy to unbind a significant fraction of the disk (e.g., Beloborodov, 2008; Metzger et al., 2008, 2010; Fernández & Metzger, 2013; Perego et al., 2014; Martin et al., 2015; Metzger & Fernández, 2014; Siegel & Metzger, 2017; Fernández et al., 2019). The amount of ejecta this process unbinds is again connected to the fate of the remnant, with numerical simulations suggesting prompt black hole formation unbinds up to $\sim 40\%$ of the disk (e.g., Fernández & Metzger, 2016) while a neutron star remnant unbinds potentially up to $\sim 90\%$ (e.g., Siegel & Metzger, 2017) due in large part to the additional neutrino flux from the remnant neutron star.

In principle, the quantity of ejecta driven by the outflow of the accretion disk is closely linked to the fate of the remnant and can principle be used to infer the fate of the remnant. However, there are substantial quantitative uncertainties (e.g., Bernuzzi, 2020) due to simplified neutrino treatments, numerical artifacts from limited resolution, and additional unmodelled processes such as a magnetised neutrino driven wind (e.g., Metzger et al., 2018). Moreover, there are significant systematic uncertainties associated with nuclear reaction networks, opacities, etc., that can led to substantial bias in inferring properties of the kilonova from observations (Zhu et al., 2020; Barnes et al., 2020).

Ignoring the aforementioned complications, a more reliable discriminator of the fate of the remnant is to consider the impact of neutrino radiation on the electron fraction of the ejecta. As we discuss in more detail in Sec 2.5.3, nascent neutron stars cool by emitting neutrinos. The additional neutrino flux increases the electron fraction with time through $\nu_e + n \rightarrow p + e^-$. The electron fraction continues to increase with longer remnant lifetimes making it increasingly difficult to synthesize heavier r-process elements (e.g., Metzger & Fernández, 2014; Kasen et al., 2015; Lippuner et al., 2017; Kawaguchi et al., 2020), which directly affects the colour of the kilonova. For $Y_e \lesssim 0.25$, a predominantly red kilonova is expected with elements greater than atomic mass $A \gtrsim 140$, while for electron fractions $Y_e \gtrsim 0.25$, lighter elements are expected and the colour of the kilonova is predominantly blue (e.g., Metzger, 2017b). Numerical calculations suggest that a remnant lifetime longer than ~ 300 ms will make $Y_e \gtrsim 0.25$ in the ejecta from the disk outflow (Lippuner et al., 2017), although other calculations suggest a larger lifetime of ~ 1s for a similar electron fraction (Sekiguchi et al., 2016; Kawaguchi et al., 2020).

2.4.3   Gravitational-wave emission and detection

Gravitational-wave emission from the first second post-merger is expected to have a relatively large strain amplitude, possibly comparable to the peak amplitude of the inspiral phase, albeit with frequencies in the kHz range. This makes them an interesting target for current and future ground-based gravitational-wave observatories. In the following two subsections we review state-of-the-art predictions for gravitational-wave emission and detection, respectively.

Gravitational-wave emission

Numerical-relativity simulations of binary neutron star mergers and their subsequent post-merger evolution show that gravitational-wave emission from a hypermassive remnant is dominated by the quadrupolar f-mode (e.g., Xing et al., 1994; Ruffert et al., 1996). Depending on the equation of state, this occurs anywhere from $\sim$ 2 to 4 kHz (e.g., Takami et al., 2015), and is strongly correlated with the star's compactness and tidal deformability (e.g., Bauswein et al., 2012; Bauswein & Janka, 2012; Hotokezaka et al., 2013a; Read et al., 2013; Takami et al., 2014; Bauswein & Stergioulas, 2019). It is actually somewhat surprising that the frequency of the dominant f-mode post-merger correlates so well with the tidal deformability and compactness—these are quantities calculated for *cold, non-rotating* neutron stars, whereas the hypermassive post-merger remnant is rapidly rotating and has a temperature $\gtrsim$ few $\times 10^{10}$ K (e.g., Sekiguchi et al., 2011a,b; Foucart et al., 2016). This suggests rotational and temperature effects play a minor role in the dominant properties of the gravitational-wave signal, and broadly implies that a successful measurement of the dominant post-merger gravitational-wave frequency is a robust measurement of the nuclear equation of state. Importantly, if the gravitational-wave frequency of the post-merger oscillations do *not* match up to the tidal deformation measured from the inspiral phase, this could be the signature of a first-order hadron-quark phase transition occurring in the core of neutron stars at high temperatures and pressures (e.g., Most et al., 2019; Bauswein et al., 2019).

In Fig. 2.4 we plot an example gravitational waveform from a hypermassive post-merger remnant (Bernuzzi et al., 2015)[3]. This shows the merger of two 1.35 M$_\odot$ neutron stars with the H4 equation of state (Lackey et al., 2006) at a distance of 40 Mpc. The strain amplitude is maximal at time $t = 0$, which we take as a proxy for the merger time (other definitions are often used, including the first contact between the two stars). For this simulation, the neutron star collapsed after time $t \approx 14$ ms, although we reiterate this collapse time is not a reliable prediction for all of the reasons given in Sec. 2.4.1.

In Fig. 2.5 we plot the gravitational-wave amplitude spectral density for the waveform shown in Fig. 2.4. The amplitude spectra of the full waveform, which includes almost ten full orbits of the binary prior to merger, is shown as the solid black curve, whereas the dashed black curve includes only the post-merger component. For comparison, we also plot the design amplitude noise spectral densities for three instruments; Advanced LIGO (solid blue curve; Aasi et al., 2015), the Einstein Telescope (red dashed curve; Punturo et al., 2010) and Cosmic Explorer (dot-dashed green curve; Abbott et al., 2017a).

For the three sensitivity curves shown alongside the predicted gravitational-wave spectrum in Fig. 2.5 we can calculate the expectation

---

[3]This waveform is publicly available through the CoRe database of binary neutron star merger waveforms (waveform ID BAM:0035; Dietrich et al., 2018)
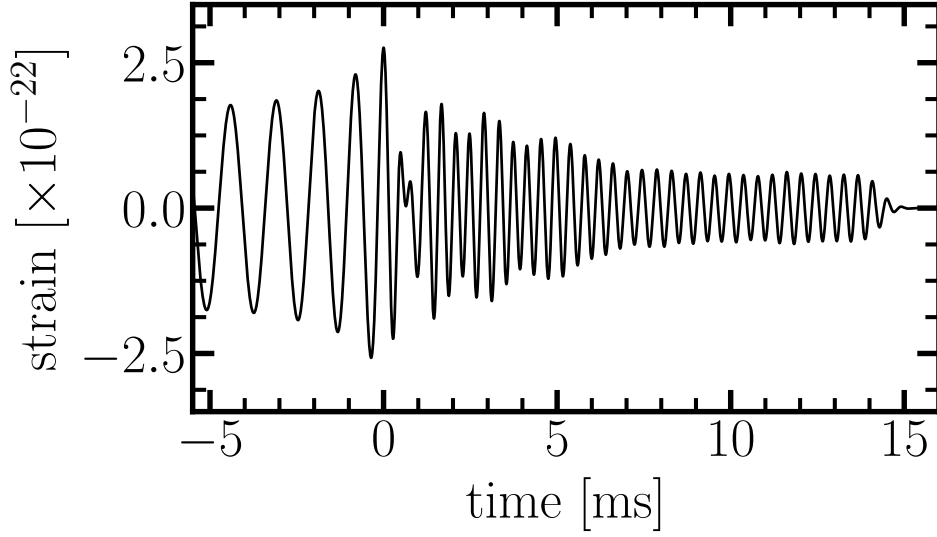
FIGURE 2.4: Gravitational-wave strain from a numerical relativity simulation of a binary neutron star merger. Gravitational-waves from the hypermassive post-merger remnant can have amplitudes comparable to that of the peak of the inspiral. In this example, the gravitational-wave signal shuts off rapidly approximately 14 ms after the merger, signifying the collapse of the hypermassive neutron star to a black hole. This simulation (Bernuzzi et al., 2015; Dietrich et al., 2018) is of an equal-mass binary with $M = 1.35\,\mathrm{M}_\odot$ component masses using the H4 equation of state at a distance of 40 Mpc.

value of the single-detector, optimal matched filter

$$\langle S/N \rangle^2 = 4\mathrm{Re} \int df \frac{|\tilde{h}(f)^2|}{S_h(f)}, \tag{2.3}$$

where $\tilde{h}(f)$ is the Fourier transform of the gravitational-wave time series, and $S_h(f)$ is the noise power spectral density. We calculate this for the post-merger signal only (i.e., for time $t > 0$) and find $\langle S/N \rangle = 1.0, 9.0$, and 12.7, for Advanced LIGO, Einstein Telescope, and Cosmic Explorer, respectively.

Together with the latest prediction for the merger rates derived from the first gravitational-wave observation of a binary neutron star merger (Abbott et al., 2017b), one can estimate the expected event rates for post-merger gravitational-wave detection. Marginalising over a range of equations of state, Martynov et al. (2019) predicted $\lesssim 2$, S/N > 5 detections of a post-merger remnant per year with Einstein Telescope, and $\lesssim 10$ such detections per year with Cosmic Explorer (see also Clark et al., 2016b). According to these calculations, the pay-off is likely to only come with third-generation detectors where the high-frequency ($\gtrsim$kHz) sensitivity is increased by a factor of at least ten over Advanced LIGO design sensitivity. This has prompted many to also think about the potential for stacking multiple sub-threshold post-merger signals with second- or third-generation inteferometers (Yang et al., 2018), or to build dedicated high-frequency gravitational-wave instruments with the primary science goal to detect tidal effects during the inspiral

of binary neutron star mergers as well as their post-merger remnants (e.g., Miao et al., 2018; Martynov et al., 2019; Ackley et al., 2020).
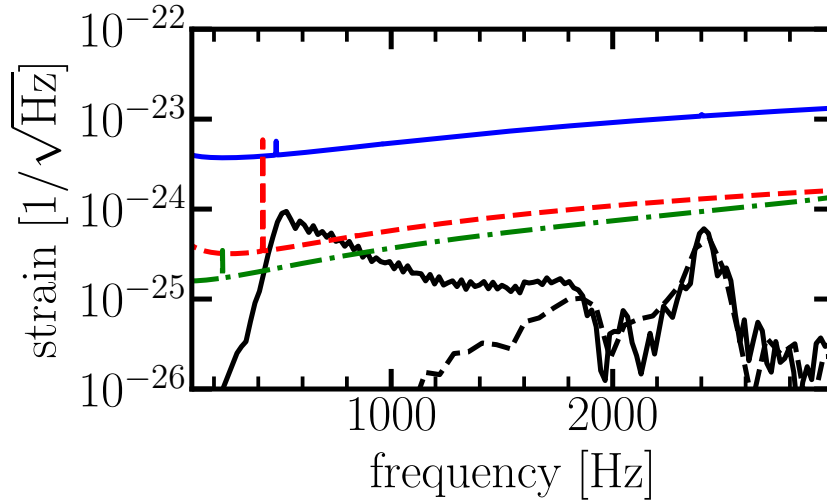

FIGURE 2.5: Gravitational-wave amplitude spectrum from the hypermassive post-merger remnant shown in Fig. 2.4. The solid black curve shows the full spectral density including almost 30 ms if inspiral, whereas the dashed black curve shows the spectral density of just the post-merger remnant (i.e., truncating the time series at the merger). The solid blue, dashed red, and dot-dashed green curves are the projected amplitude spectral densities of Advanced LIGO at design sensitivity, the Einstein Telescope, and Cosmic Explorer, respectively. This post-merger signal has a single-detector signal-to-noise ratio of 1.0, 9.0 and 12.7 for the three detectors, respectively.

When the hypermassive star collapses to form a black hole, it does so on a relatively short timescale ($\sim$ ms; see Sec. 2.4.1 and Fig. 2.4), implying the signal is potentially upward of $\sim 1\,$kHz. However, the amplitude of the signal is weak; optimistic estimates from simulations of collapsing, differentially-rotating stars suggest they may be detectable at a distance of up to 10 Mpc with third-generation detectors such as the Einstein Telescope or Cosmic Explorer (Giacomazzo et al., 2011). Numerical relativity simulations of binary neutron star mergers with subsequent hypermassive star formation and collapse seem to show no discernible burst of radiation above that seen from the star's oscillations immediately prior to collapse.

It is currently an open question as to whether gravitational-wave parameter estimation methods targeting hypermassive neutron star signals—see next section—can infer the collapse time with a successful gravitational-wave detection. If they can, this would allow us to probe the complex physics that governs the quenching of differential rotation discussed in Sec. 2.4.1.

Gravitational-wave detection methods

The LIGO/Virgo collaborations have a number of methods in place to search for and characterise gravitational waves in the immediate aftermath of a neutron-star merger. Two algorithms were used to search for short-lived

gravitational-wave signals following GW170817 (Abbott et al., 2017f, 2019b): Coherent Wave Burst (cWB; Klimenko et al., 2016) and BayesWave (Cornish & Littenberg, 2015; Littenberg & Cornish, 2015; Chatziioannou et al., 2017). The cWB algorithm searches for coherent excess power in multi-resolution wavelet transformations, while BayesWave uses Bayesian inference, modelling the gravitational-wave signal itself as a linear superposition of wavelets; see Abbott et al. (2017f) and Abbott et al. (2019b), respectively, for details of the specific implementation and setup of the two algorithms searching for gravitational waves following GW170817. Neither methods found any hint of a signal, but placed upper limits on the total energy emitted in gravitational waves.

The two methods described above do not rely on waveform models to search for the gravitational-wave signal. While they are therefore more robust than modelled searches that use template waveforms, they are also less sensitive (Tsang et al., 2019; Easter et al., 2020). However, modelled searches are in their infancy due to a paucity of enough reliable gravitational-wave templates to perform matched-filter searches. This is rapidly changing, with analytic approximations (Bauswein et al., 2016; Bose et al., 2018), principal component decompositions (Clark et al., 2016b), and machine-learning algorithms (Easter et al., 2019) showing promising results fitting to numerical-relativity waveforms.

Two recent Bayesian methods have been independently developed that use analytic waveforms. Using only a single oscillation mode modelled as a damped sinusoid (or Lorentzian function in the frequency domain), Tsang et al. (2019) showed an average mismatch between numerical-relativity injections and recovered signals of 0.15. A single damped sinusoid allows the main f_2 peak to be measured, which is the key peak for determining the equation of state. This method is therefore capable of distinguishing inspiral and post-merger inferences of the equation of state (Tsang et al., 2019) to, for example, determine potential quark deconfinement in the stellar core that only occurs at high temperatures (Bauswein et al., 2019).

Instead of a single damped sinusoid, Easter et al. (2020) modelled the full waveform as a linear sum of three damped sinusoids (inspired by Bauswein et al., 2016; Bose et al., 2018), also allowing all three frequencies to drift linearly in time. They found an average mismatch of only 0.03, implying the method is $\approx$ 15% more sensitive than Tsang et al. (2019). The addition of the extra mode oscillations in the analytic waveform approximations is unlikely to improve equation of state estimates, however realistic modelling of the frequency drift of the fundamental f_2 mode may have some, as yet undetermined effects.

In reality, given the potential inaccuracies of gravitational waveforms from numerical-relativity simulations (see previous section), both modelled and unmodelled searches will be needed as this field hopefully moves from the development to the observational stage.

Of course, many binary neutron star coalescences will likely be detected before a bona fide post-merger detection. This opens the possibility to effectively *stack* sub-threshold events by either multiplying Bayes factors from

individual events or by coherent summation of signals relying on pre-merger phase information (Yang et al., 2018).
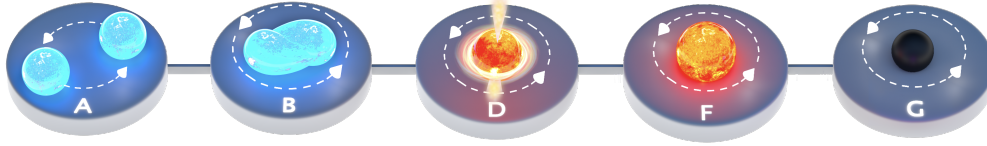
2.5 Long-lived neutron star remnants

FIGURE 2.6: A post-merger remnant of mass $1.0\,M_{\text{TOV}} \leq M \gtrsim 1.2\,M_{\text{TOV}}$ will form a supramassive neutron star, which will collapse to a black hole on a timescale $\lesssim 10^5\,\text{s}$
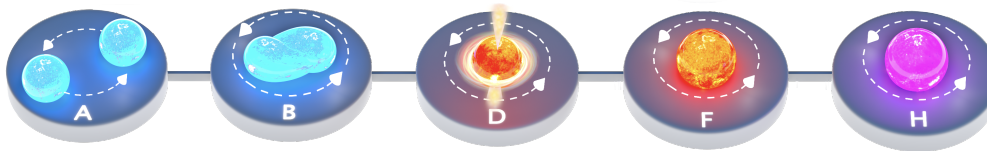

FIGURE 2.7: A post-merger remnant of mass $M \leq 1\,M_{\text{TOV}}$ will form an infinitely-stable neutron star.

Post-merger remnants less massive than $\sim 1.2 M_{\text{TOV}}$ will survive for more than one second. They are deemed supramassive if their mass is greater than the non-rotating limit M_{TOV}—Fig. 2.6—or infinitely stable if their mass is less than M_{TOV}—Fig. 2.7. Observational evidence from the x-ray afterglow of short gamma-ray bursts suggests a non-negligible fraction of binary neutron star mergers may result in these outcomes (e.g., Rowlinson et al., 2013; Lü et al., 2015).

Figures 2.6 and 2.7 emphasise an important point: even supramassive and stable remnants will still undergo a period of strong differential rotation immediately after the merger (panel B), implying the gravitational-wave emission and detection discussion from Secs. 2.4.1 and 2.4.3 are still relevant. However, electromagnetic emission due to r-process nucleosynthesis discussed in Sec. 2.4.2 may be different depending on the lifetime of the remnant; a point we return to in Sec. 2.5.5.

2.5.1 Can a long-lived neutron star launch a jet?

The question whether a neutron star can launch an ultra-relativistic jet that can produce a short gamma-ray burst continues to engage theorists and observers. Before we review our more recent understanding of this question, it is intriguing to start near the beginning and briefly review our understanding of short gamma-ray bursts themselves. We refer the interested reader

to more detailed reviews of gamma-ray bursts (e.g., Nakar, 2007; Kumar & Zhang, 2015; Nakar, 2019).

Several lines of evidence of short gamma-ray bursts suggest that the central engine must be able to launch an ultra-relativistic outflow (e.g., Ackermann et al., 2010), a constraint demanded by the compactness problem (Ruderman, 1975). Constraints on the total energy requires that the outflow is collimated into a narrow jet (e.g., Nakar, 2007), while rapid variability of the prompt emission implies the engine must be a compact object (e.g., Nakar, 2007; Berger, 2014). Immediately, these constraints imply two potential central engines, a black hole or a neutron star. Moreover, one of the implicit requirements imposed by an ultra-relativistic outflow is having a relatively baryon-free environment where the jet is launched (e.g., Nakar, 2007; Ciolfi, 2018), such that the ultra-relativistic jet can launch efficiently, break out of the environment and stay relativistic. It is this constraint of having a clean environment, sometimes refereed to as the baryon-loading problem (Shemi & Piran, 1990), that has led to debate about whether long-lived neutron stars can launch jets and power short gamma-ray bursts.

Assuming the central engine is a black hole, there are two main mechanisms for generating an ultra-relativistic jet that can produce a short gamma-ray burst: neutrino-antineutrino annihilation along the black hole spin axis (Eichler et al., 1989; Ruffert & Janka, 1998), and the Blandford-Znajek mechanism (Blandford & Znajek, 1977). Although both processes may be responsible for launching jets, the Blandford-Znajek mechanism is more favoured due to energetic constraints, with the neutrino-antineutrino annihilation unable to produce high energy gamma-ray bursts (e.g., Kyutoku et al., 2018; Ciolfi, 2018), although we note that neutrino luminosity on long timescales is far from certain. In the case of a long-lived neutron star the mechanism for launching the jet is far from certain, although it is clear that if a jet is launched, it is likely through magnetic processes that tap into the large rotational-energy reservoir (e.g., Bucciantini et al., 2012; Ciolfi et al., 2019) or a combination of a neutrino-annihilation and magnetic processes (e.g., Perego et al., 2017b; Fujibayashi et al., 2017). However, the problem as we alluded to above is the baryon-load of the environment. We refer the interested reader to more detailed reviews of gamma-ray burst jet launching (e.g., Ciolfi, 2018).

As we discussed earlier in Sec 2.4.2, neutrino radiation from the nascent neutron star unbinds a non-negligible (potentially $\gtrsim 10^{-2} M_\odot$) amount of matter (e.g., Fernández & Metzger, 2016; Metzger, 2017b). This additional ejecta pollutes the surrounding environment, particularly along the spin axis (e.g., Ciolfi et al., 2017). This pollution means that even tapping into the entire $\approx 10^{52}$ erg of rotational energy, the maximum Lorentz factor of a jet that forms is $\mathcal{O}(10)$, an order of magnitude smaller than required to alleviate the compactness problem (Nakar, 2007; Murguia-Berthier et al., 2014, 2017), and two orders of magnitude smaller than measurements from short gamma-ray bursts (e.g., Ackermann et al., 2010). This led Murguia-Berthier et al. (2017) to argue that the formation of an ultra-relativistic jet has to wait until the formation of a black hole. One may think this opens up

the possibility of a supramassive neutron star producing a short gamma-ray burst, however detailed analysis by Margalit et al. (2015) showed that for a range of equations of state, accretion disk and therefore jet formation is unlikely after the collapse of a supramassive neutron star. Given our current constraints on the maximum mass of neutron stars, this suggests up to 80% of binary neutron star mergers will not produce a short gamma-ray burst.

Beniamini et al. (2017) showed that to efficiently launch an ultra-relativistic jet, the energy per baryon ($\eta \propto \dot{E}/\dot{M}$) at the base of the jet must exceed a critical threshold ($\eta \gtrsim 100$). Following this result, one can derive a critical timescale for when this threshold is exceeded Beniamini et al. (2020c). For $B \sim 3 \times 10^{16}$ G this timescale is ≈ 0.2 s, short enough to be consistent with the delay seen in GRB170817A. Alternatively, for more typical parameters, this timescale is $\gtrsim 3$ s, inconsistent with the delay of GRB170817A. This suggests that typical magnetars are unable to produce short gamma-ray bursts with a delay consistent with GRB170817A, although it is important to emphasise that it is not necessary for all short gamma-ray bursts to have the same delay from merger, implying a timescale $\gtrsim 3$ s is not necessarily problematic. Furthermore, given the complicated physics at play for launching a jet, it is worth questioning how reliably these scalings can distinguish between timescales within an order of magnitude. More importantly however is the dependency of this timescale on the magnetic field. As discussed in earlier sections, numerical simulations do not resolve the magneto-rotational and Kelvin-Helmholtz instabilities, underestimating the amplification of the magnetic field. If the magnetic field amplification is higher this will naturally alleviate this problem with the timescale for efficiently launching ultra-relativistic jets.

Several numerical simulations have shown the formation of a relativistic outflow from a long-lived neutron star (e.g., Giacomazzo & Perna, 2013; Ciolfi et al., 2017, 2019; Ciolfi, 2020a). However, these outflows do not have high-enough Lorentz factors (i.e., $\Gamma \gtrsim 100$) to produce gamma-ray emission, and therefore explain short gamma-ray burst observations. The corollary is that long-lived neutron stars are not viable candidates for producing short gamma-ray bursts. However, recent numerical simulations have changed this conclusion (Mösta et al., 2020). Including detailed physics of neutrinos in their simulation, Mösta et al. (2020) showed that neutrinos emitted by the nascent neutron star predominantly around the polar region end up preventing baryon pollution, which are therefore likely to aid the formation of a relativistic jet. It is worth noting that the Mösta et al. (2020) simulations still do not have outflows with sufficiently high Γ, however they propose this could be because they are still not including full neutrino transport, whereby pair annihilation could still substantially boost Γ to the relevant regime.

While theoretical support is slowly arriving, there is considerable, although perhaps subjective, observational evidence for long-lived neutron stars being viable engines of short gamma-ray bursts. The 1.74 s delay between the gravitational-wave signal, GW170817 and gamma-ray burst, GRB170817A has been calculated to be dominated by the timescale for the relativistic jet to reach the γ-ray emitting radius (Ren et al., 2020; Beniamini

et al., 2020c). Independently, kilonova observations have been suggested to require a magnetised wind from a hypermassive neutron star that survived for up to 1 s (Metzger et al., 2018). In combination, these two independent arguments suggest that the relativistic jet in GRB170817A is likely launched by the differentially rotating neutron star before it collapsed into a black hole. If a differentially rotating neutron star can launch such a jet then long-lived neutron stars which also go through this evolutionary phase must be able to launch a jet as well.

Another more tentative observational evidence for a neutron star engine is the recent detection of a luminous kilonova from short GRB200522A (Fong et al., 2020). The kilonova is significantly brighter than expected from r-process nucleosynthesis alone and the characteristic features of the emission suggest additional energy from a neutron star. If true, this neutron star is most definitely stable and given the kilonova is detected as a counterpart to a short gamma-ray burst, the neutron star engine must have launched the jet that powered this gamma-ray burst. We note that given there are large systematic uncertainties with kilonova modelling (e.g., Zhu et al., 2020) and there may be alternative explanations for this exceptionally bright kilonova. Moreover, Gemini observations of GRB200522A only find a weak counterpart, contrary to expectations if a magnetar was present (O'Connor et al., 2021).

Perhaps the best observational evidence for long-lived neutron stars being able to launch relativistic jets and power short gamma-ray bursts are x-ray afterglow observations. The observations of a plateau (e.g., Fan & Xu, 2006; Dall'Osso et al., 2011; Rowlinson et al., 2013; Lü et al., 2015), a sharp drop in luminosity (e.g., Rowlinson et al., 2010, 2013; Sarin et al., 2020b) and late-time x-ray flares (e.g., Fan & Xu, 2006) are all best interpreted by invoking the spin-down energy of a long-lived neutron star (Zhang & Mészáros, 2001; Lasky et al., 2017). If long-lived neutron stars are powering the x-ray afterglows they must by definition also be responsible for launching the ultra-relativistic jet and producing prompt emission.

Although these observational lines of evidence are not definitive, they do strongly suggest long-lived neutron stars can launch jets that produce short gamma-ray bursts, with more recent numerical simulations (e.g., Mösta et al., 2020) backing up this claim.

2.5.2 Supramassive or stable

Back-of-the-envelope calculations suggest supramassive stars born from neutron-star mergers are expected to survive for anywhere between $\sim 10\,\text{s}$ to $\sim 4 \times 10^4\,\text{s}$ (Ravi & Lasky, 2014), which is broadly consistent with observationally-inferred collapse times from short gamma-ray burst x-ray afterglows (Rowlinson et al., 2013). However, a detailed look at the expected and observed distributions show the stars tend to collapse on shorter timescales than one might expect (Fan et al., 2013; Ravi & Lasky, 2014; Sarin et al., 2020b). Suggestions for the resolution of this discrepancy include excess gravitational-wave emission at early times (Fan et al., 2013; Gao

et al., 2016; Lü et al., 2017; Lin & Lu, 2019), or deconfined quark matter changing the star's moment of inertia from that with normal matter (Li et al., 2016, 2017a; Drago & Pagliara, 2018). Hierarchical Bayesian inference of the population of collapse times for 18 supramassive neutron stars identified by the 72 *Swift* x-ray afterglow observations suggest the story may be some combination of these two effects (Sarin et al., 2020b).

These constraints have important consequences. Firstly, if these nascent neutron stars are really composed of deconfined quarks, then it suggests there is a temperature dependent hadron-quark phase transition. Understanding where in the nuclear phase diagram such a transition occurs is critical to our understanding of the behaviour of nuclear matter (e.g., Bauswein et al., 2019; Chatziioannou & Han, 2020). An unexplored consequence of this phase transition is on the kilonova; additional neutrino flux from the cooling of a hybrid star cf. a purely hadronic star may mean that the electron fraction in the accretion disk outflow is higher than expected. In turn, this could make it difficult to infer the time the remnant collapsed based on the r-process elements synthesised (e.g., see Lippuner et al., 2017; Kawaguchi et al., 2020). We discuss the cooling of nascent neutron stars in more detail in Sec. 2.5.3.

The implication that supramassive neutron stars are spinning down predominantly through gravitational waves has important consequences for the dynamics of these neutron stars, a point we discuss in more detail in later sections. More immediately relevant is the implication significant gravitational-wave spin down has on the electromagnetic observations. As discussed in Sec 2.2.1, energetic constraints on GW170817 from kilonova (e.g., Margalit & Metzger, 2017) and radio (e.g., Ricci et al., 2020; Schroeder et al., 2020) observations put strong limits on the total energy of the ejecta. It has been proposed that this energy constraint indirectly rules out a long-lived neutron star in GW170817 (Margalit & Metzger, 2017). However, if the supramassive star spins down predominantly through gravitational-wave emission and therefore collapses earlier than expected, then these constraints are weakened significantly. This also implies that future analyses utilising energy constraints to infer the nature of the remnant need to carefully consider energy losses through gravitational waves. However, it is worth stressing we have an incomplete, quantitative understanding of how much energy is radiated in gravitational waves.

Finally, it is worth mentioning that the hierarchical analysis of collapse times (Sarin et al., 2020b) predict a large fraction of supramassive stars collapse in $\lesssim 100\,\mathrm{s}$. This is significant, because this is also approximately the time it takes *Swift* to slew, implying a number of post-merger remnants may be observationally misidentified as being hypermassive because *Swift* is not able to slew in time to see the result of the energy injection from the central engine.

2.5.3 Thermal evolution

The thermal evolution and history of a newly born neutron star has important consequences on several aspects of its evolution, including, for example,

neutrino emission, the role of viscosity in dynamical and secular instabilities, the freezing out of the crust, and the transformation of the core to neutron superfluidity and proton superconductivity.

At very early times the star cools through neutrino emission (e.g., Shapiro & Teukolsky, 1983; Perego et al., 2019). In general, the neutrinos do not free stream, implying the cooling timescale is set by the time it takes for the neutrinos to diffuse out of the star (e.g., Rosswog & Liebendörfer, 2003). It is these neutrinos that affect the electron fraction of the ejecta, and hence alter the colour of the kilonova (see Sec. 2.4.2). An approximate cooling timescale given by the neutrino diffusion timescale is (Paschalidis et al., 2012)

$$t_{\rm cool} \approx 1200 \left(\frac{M}{2.8\,M_\odot} \right) \left(\frac{R}{15\,{\rm km}} \right) \left(\frac{E_\nu}{10\,{\rm MeV}} \right)^2 {\rm ms}, \qquad (2.4)$$

where $E_\nu = 10\,{\rm MeV}$ is the root-mean-square value of the neutrino energy found in simulations (Rosswog & Liebendörfer, 2003).

During the cooling of the remnant, the first major structural change is the formation of the crystalline lattice crust. This typically takes $\mathcal{O}({\rm days})$ for the base of the crust to begin forming, with a complete crust not forming for up to a year following birth (e.g., Krüger et al., 2015, and references therein). In the stellar core, neutron superfluidity and proton superconductivity are expected at temperatures $\lesssim (5-9) \times 10^8\,{\rm K}$ and $\lesssim (2-3) \times 10^8\,{\rm K}$, respectively (see Page et al., 2011; Shternin et al., 2011, and references therein). While the development for superfluidity and superconductivity are certainly relevant for late-time evolution of neutron stars, e.g., in understanding glitches in young radio pulsars, it is not clear what observational impact it has on the evolution of post-merger remnants.

2.5.4   Dynamical evolution

Nascent neutron stars born in binary neutron star mergers are differentially rotating with large poloidal magnetic fields in the range of $\sim 10^{14-16}\,{\rm G}$. This differential rotation winds up a toroidal component of the magnetic field roughly symmetrical to the rotation axis. One expects this toroidal component B_t to dominate over the poloidal component B_p deforming the neutron star into a prolate ellipsoid (e.g., Cutler, 2002; Lander & Jones, 2018). Misalignment between the rotation and magnetic axes result in precession (e.g., Dall'Osso et al., 2018; Lander & Jones, 2018). Internal dissipative processes drive the magnetic axis towards orthogonality with the spin axis (Mestel & Takhar, 1972; Jones, 1976a; Cutler, 2002), minimising the energy of the system and also making the system an optimal emitter of gravitational waves (e.g., Cutler, 2002; Lasky & Glampedakis, 2016; Dall'Osso et al., 2018). This instability is known as the "spin-flip instability".

In reality, the evolution of the misalignment angle χ between the star's magnetic and rotation axes is significantly more complicated. In general, for a star deformed by a dominantly toroidal field, viscous dissipation increases χ. Conversely, χ decreases for a star deformed predominantly through a

poloidal field. Early efforts to model the evolution of χ focused on determining the effects of this viscous dissipation. However, the evolution of χ is in fact a complex mixture of dissipation, neutrino cooling, and the effects of the external torque from spin-down which also acts to decrease χ (Lander & Jones, 2018).

The coupling between the spin-down and viscous effects proves to be critical in large parts of the neutron star parameter space and determining whether $\chi \to 0°$ (i.e., an aligned rotator that will not emit gravitational waves) or $\chi \to 90°$ (i.e., an orthogonal rotator, an optimal emitter of gravitational waves) (Lander & Jones, 2018). This coupling is ignored in Dall'Osso et al. (2018) by assuming that the timescale for spin flip is much faster than the spin down. This may not be true, and depends on the dissipation timescale, which is inversely proportional to the size of the deformation (Ipser & Lindblom, 1991). The dissipation timescale is closely related to the spin-flip time-scale, an approximation of which is (e.g., Lasky & Glampedakis, 2016),

$$\tau_{sf} \approx 8\,s \left(\frac{R}{15\,km} \right)^2 \left(\frac{\langle \rho \rangle}{10^{15}\,gcm^{-3}} \right) \left(\frac{\epsilon_B}{10^{-3}} \right)^{-1} \left(\frac{\epsilon_\Omega}{0.3} \right)^{-2} \left(\frac{\xi}{10^{30}\,g\,cm^{-1}\,s^{-1}} \right)^{-1}$$
(2.5)

Here, $\langle \rho \rangle$ is the volume-averaged density, R is the neutron star radius, ϵ_B is the magnetic-field induced ellipticity, ϵ_Ω is the rotational ellipticity, and ξ is the bulk viscosity coefficient. For these parameters, it is difficult to imagine the spin-flip timescale being much faster than the spin-down timescale especially considering there are short gamma-ray bursts with observations on significantly shorter timescales where the emission is potentially derived from spin-down. However, this timescale is extremely sensitive to the temperature $\xi \sim T^6$ and therefore the cooling history of the neutron star, which is not well understood.

The evolution of χ is critical for developing an understanding of what mechanism is responsible for radiating away the rotational energy of the long-lived neutron star (e.g., Margalit et al., 2018; Lander & Jones, 2020). In the context of magnetars born in long gamma-ray bursts, Margalit et al. (2018) showed that an aligned rotator will almost exclusively power a gamma-ray burst, while a misaligned rotator will deposit some fraction of its rotational energy onto the supernova. Similar behaviour is to be expected in a long-lived neutron star born in a binary neutron star merger. In the first several seconds while $\chi \to 0°$ the rotational energy will be lost in powering the gamma-ray burst (Lander & Jones, 2020). However once the system begins to orthogonalise i.e., $\chi \to 90°$ the energy will be lost in gravitational waves and in powering the kilonova.

For neutron stars born in long gamma-ray bursts, the evolution of the braking index through coupling of the spin and magnetic axes has potentially been measured directly (Şaşmaz Muş et al., 2019; Çıkıntoğlu et al., 2020). Such a model has not yet been fit to short gamma-ray burst observations. However, measurements of braking indices $n \lesssim 3$ of long-lived neutron stars from short gamma-ray bursts hint towards the evolution of χ for a number

of objects (Lasky et al., 2017; Sarin et al., 2020a), although it is worth noting there are other ways to explain such measurements (Lasky et al., 2017). If χ is evolving, it will be important to understand the timescales and the long-term evolution. This will provide important clues into the evolution of these objects into ordinary magnetars we see in our galaxy today. While more immediately, it will allow for more informed inferences about the radiation mechanisms that are tapping into the large rotational-energy reservoir of long-lived neutron stars.

2.5.5   Electromagnetic observations

In Sec 2.5.1 we discussed whether a neutron star could launch an ultra-relativistic jet and produce a short gamma-ray burst. Here, we discuss the broader electromagnetic imprints of a long-lived neutron star remnant.

The longest numerical simulations of binary neutron stars and their remnants last approximately 100 ms post merger (e.g., De Pietri et al., 2018; Ciolfi et al., 2019; De Pietri et al., 2020), significantly shorter than the time where they could be used to provide insight into the electromagnetic signature of a long-lived neutron star. Such insights therefore rely predominantly on analytical and semi-analytic models (e.g., Zhang & Mészáros, 2001; Dall'Osso et al., 2011; Metzger & Piro, 2014).

The diverse predictions of electromagnetic signatures from long-lived post-merger remnants can all be primarily attributed to the large reservoir of rotational energy of the long-lived neutron star. Unlike hypermassive neutron stars which can trap a significant amount of their spin-down energy as they collapse into black holes (e.g., Metzger, 2017b; Shibata et al., 2019), supramassive and infinitely stable neutron stars will radiate a large fraction of this energy away with several electromagnetic consequences.

One of the signatures of spin-down energy is on the kilonova itself (e.g., Yu et al., 2013). The injection of spin-down energy is either via a Poynting flux from a collimated jet (Bucciantini et al., 2012) or photons generated from dissipation of a magnetar wind (Thompson et al., 2004; Zhang, 2013). This increased energy creates a distinct impact on the kilonova lightcurve, altering the peak time and duration, while drastically increasing the luminosity of the kilonova compared to a kilonova only powered by radioactive decay. This latter characteristic implies the colour of the kilonova becomes bluer, simply due to higher luminosity translating to a higher effective temperature for a similar photospheric radius. Such effects are identical to the differences seen between ordinary and magnetar-driven supernovae (Kasen & Bildsten, 2010; Nicholl et al., 2020; Margalit et al., 2018). As mentioned in Sec. 2.2.1, this is one of the interpretations of the kilonova following GW170817 (Yu et al., 2018). The recent identification of an exceptionally bright kilonova following short GRB200522A (Fong et al., 2020) provides further tantalising evidence for this magnetar-driven kilonova scenario. An additional imprint of this increased ejecta energy will be seen on the synchrotron radio signal generated from the interaction of the ejecta with the interstellar medium (Hotokezaka & Piran, 2015; Horesh et al., 2016; Ricci et al., 2020; Schroeder et al., 2020). Such

constraints have been used to infer the fate of several gamma-ray bursts, suggesting that $< 50\%$ of binary neutron star mergers make a long-lived neutron star (Schroeder et al., 2020). However, we note that this may be overly constraining as they ignore rotational energy lost through other channels.

Even disregarding the impact of the spin-down luminosity, a long-lived remnant will show a distinctive characteristic feature on the kilonova. As discussed in Secs. 2.4.2 and 2.5.3, the nascent neutron star cools rapidly through neutrino cooling. This additional neutrino flux dramatically increases the electron fraction of the ejecta and suppresses the production of lanthanides (e.g., Lippuner et al., 2017; Metzger, 2017b; Kawaguchi et al., 2020). Such ejecta would naturally be less opaque than more lanthanide-rich ejecta making the resulting kilonova dominantly "blue" regardless of how much rotational energy is deposited into the kilonova ejecta.

Potentially some of the best electromagnetic observations of nascent neutron stars is the evidence of energy injection in the x-ray afterglows of gamma-ray bursts. A large fraction of x-ray afterglows have plateaus followed by sharp drops in luminosity (e.g., Rowlinson et al., 2013), which are challenging to explain with the canonical model for afterglows that model the interaction of a relativistic jet with the surrounding environment. The spin-down energy from a nascent neutron star can naturally explain both these features (e.g., Zhang & Mészáros, 2001; Rowlinson et al., 2013). However, the exact mechanism that extracts this rotational energy is still uncertain. Either the spin-down energy is extracted directly from the remnant itself (e.g., Zhang & Mészáros, 2001; Rowlinson et al., 2013; Lasky et al., 2017; Strang & Melatos, 2019) with a constant efficiency, or indirectly through energy injection at the afterglow shock interface (e.g., Cohen & Piran, 1999; Dall'Osso et al., 2011; Sarin et al., 2020a). Systematic model selection suggests the latter model, with a generalised braking index better explaining the observations (Sarin et al., 2020a), at least for the small subset (eight) of short and long gamma-ray bursts analysed. Such a model also self-consistently explains x-ray flares that are seen at the onset of the plateau phase, providing additional support for this model.

An alternative way to generate x-ray emission with a magnetar is through the interaction of a magnetar wind with the merger ejecta (e.g., Yu et al., 2013; Metzger & Piro, 2014; Siegel & Ciolfi, 2016; Strang & Melatos, 2019; Strang et al., 2021). Assuming the magnetar is completely enshrouded in the merger ejecta, the magnetar wind energy will be dissipated via shocks or magnetic re-connection creating a hot nebula behind the ejecta. This hot nebula will be comprised of photons and electron/positron pairs analogous to a pulsar wind nebula (e.g., Metzger & Piro, 2014). Initially, most of the spin-down energy will be lost in expanding the nebula and ejecta along with it. This expansion will eventually reduce the optical depth allowing photons at various wavelengths to diffuse out once the diffusion timescale becomes shorter than the expansion timescale (Metzger & Piro, 2014). While such a model explains several observational features of x-ray afterglows, it is problematic as this model cannot explain x-ray emission at early-times ($T \lesssim 10\,\mathrm{hr}$) as the ejecta is still optically thick. In this model, early-time x-ray observations must be

from synchrotron emission from the interaction of the relativistic jet with the surrounding environment, with the neutron star component becoming dominant after the ejecta becomes optically thin. Such a constraint is, however, problematic, given sharp drops in x-ray plateaus are seen as early as 100 s after the prompt (e.g., Sarin et al., 2020b). There are two ways to reconcile this issue. First, the timescale for the ejecta to become optically thin need not be as long as 10 hr, as this timescale is dependent on the opacity of r-process elements, which are far from certain (e.g., Tanaka et al., 2020; Barnes et al., 2020). Second, and perhaps more importantly, the simple assumption that a magnetar is wholly enshrouded in the merger ejecta may not be valid, with potential holes due to piercing by the ultra-relativistic jet that produced the gamma-ray burst or by Rayleigh-Taylor instabilities in the ejecta itself (e.g., Strang & Melatos, 2019; Strang et al., 2021).

An important question to consider with the spin-down energy is whether the radiation is emitted isotropically or beamed in a particular direction, perhaps along with the jet that produces the gamma-ray burst prompt emission itself. The answer to this question could shed critical insight into the emission mechanism. Observations and interpretations of CDF-S XT2 (Xue et al., 2019) as a magnetar seen off-axis suggests the magnetar spin-down energy is emitted isotropically. However, isotropic emission potentially leads to violations of the total energy budget for certain gamma-ray bursts believed to be powered by nascent neutron stars (e.g., Beniamini & Mochkovitch, 2017a). By contrast, if the spin-down energy is collimated, it must be through a mechanism that can be sustained for long timescales to explain the late-time x-ray observations. One explanation for the collimation originates from the interaction of the magnetar wind and the surrounding environment. Magnetohydrodynamic simulations suggest that the deceleration of the magnetar wind due to the dense environment of the merger ejecta may collimate the wind into a jet for sufficiently high spin-down luminosity (Bucciantini et al., 2012). However, such a mechanism seems unfeasible, as the jet will become unstable and susceptible to magnetohydrodynamic instabilities once the spin-down luminosity of the long-lived remnant drops (Porth et al., 2013; Metzger & Piro, 2014).

Ultimately, testing detailed models with better observations will allow us to determine what physical processes are relevant. Beyond these more immediate electromagnetic observations, long-lived neutron stars may also be responsible for fast radio bursts, to which we now turn our attention.

2.5.6   Fast radio bursts

Fast radio bursts are millisecond duration pulses of coherent radio emission. In general they come from cosmological distances, with dispersion measures significantly larger than galactic values. We refer the reader to Cordes & Chatterjee (2019); Zhang (2020a) for recent reviews on fast radio bursts.

Ever since the original discovery (Lorimer et al., 2007), subsequent identification of fast-radio burst repeaters (Spitler et al., 2014, 2016) and localisation

of its host galaxy (Chatterjee et al., 2017; Tendulkar et al., 2017), nascent magnetars have been invoked to explain these enigmatic astrophysical phenomena (e.g., Popov & Postnov, 2013; Lyubarsky, 2014; Kulkarni et al., 2014; Katz, 2016; Beloborodov, 2017; Metzger et al., 2017a, 2019; Katz, 2018; Lu & Kumar, 2018; Margalit et al., 2019; Lu et al., 2020). While it is possible that there are two distinct populations of fast radio bursts, characterised as repeaters and isolated bursts (e.g., Falcke & Rezzolla, 2014; Zhang, 2017, 2020b), a non-repeating population may be disfavoured on rate-based arguments (e.g., Nicholl et al., 2017b; Ravi, 2019). We note there are numerous other alternative progenitor models, in fact, as recently as 2019, theoretical models outnumbered the number of events themselves (Platts et al., 2019). However, this all changed with the recent watershed discovery of a fast radio burst from a galactic magnetar, SGR1935+2154, which provided the smoking-gun observation for the magnetar origin for fast radio bursts.

SGR1935+2154 is a galactic soft gamma repeater first identified by *Swift* as a potential gamma-ray burst candidate (Stamatikos et al., 2014), it is associated with a supernova remnant at a distance $d \approx 6$ kpc (Gaensler, 2014; Zhou et al., 2020), with an estimated surface magnetic field $B \approx 10^{14}$ G and age (based on the supernova remnant association) $\gtrsim 16$ kyr (Zhou et al., 2020). On April 28, 2020, a millisecond duration radio pulse was independently detected from this source by CHIME (The Chime/Frb Collaboration et al., 2020) and STARE2 (Bochenek et al., 2020) in coincidence with a bright X-ray burst (Zhang et al., 2020). Various analyses confirmed the analogous nature of the coherent radio emission with cosmological fast radio bursts albeit with significantly lower energy (at least ~ 25 times) than typical cosmological fast radio bursts. This observation provided unequivocal evidence that magnetars are the progenitors of at least some fast radio bursts (e.g., Margalit et al., 2020a), with the discrepancy in energies attributed to the old age of this magnetar, weaker magnetic field, and slower rotation (e.g., Lu et al., 2020; Beloborodov, 2020).

Observations of SGR1935+2154 provide evidence that young, rapidly rotating magnetars produce some fast radio bursts. However, it is unclear whether these magnetars are ones born in core-collapse supernovae or in binary neutron star mergers. The first repeating fast radio burst FRB121102 was localised to a low metallicity dwarf star-forming galaxy (Chatterjee et al., 2017; Tendulkar et al., 2017) and also associated with a persistent radio source (Marcote et al., 2017). The host galaxy properties and the persistent radio source are best interpreted as the emission from a young magnetar embedded in the expanding supernova ejecta (e.g., Omand et al., 2018; Margalit & Metzger, 2018) pointing towards a superluminous supernovae/long gamma-ray burst origin for FRB121102. The Australian Square Kilometer Array Pathfinder (ASKAP) has since localised another fast radio burst FRB180924 (Bannister et al., 2019), finding the host galaxy properties and offsets to be comparable to short gamma-ray bursts. FRB180924, therefore, provided the first possible evidence for a binary neutron star remnant merger origin for fast radio bursts. Since then, more fast radio bursts have been localised in host galaxies strongly suggestive of binary neutron star merger

remnant origins (e.g., Ravi et al., 2019). Rate-based arguments suggest all fast radio bursts are repeaters (e.g., Ravi, 2019), implicitly demanding long-lived sources, i.e., long-lived neutron star remnants. Moreover, as supramassive neutron stars have been shown to collapse on relatively short timescales (e.g., Sarin et al., 2020b) where the kilonova ejecta is still optically thick, implying fast radio bursts would not escape to an external observer (e.g., Margalit et al., 2019). The timescale for this ejecta to become optically thin ranges from weeks to months, implying any fast radio bursts associated with binary neutron star mergers must be from infinitely stable neutron stars (e.g., Margalit et al., 2019).

While the progenitor model of fast radio bursts can be confidently confirmed as a nascent magnetar, the exact mechanism that generates the coherent radio emission is unknown. The various models can be broadly divided into two categories: those for which the emission is close to magnetar i.e., a pulsar-like mechanism involving the magnetosphere (e.g., Katz, 2016; Lu et al., 2020), and those for which the emission mechanism involves relativistic shocks similar to gamma-ray bursts, where the coherent radio emission is generated far from the magnetar (e.g., Beloborodov, 2017; Metzger et al., 2019). Future observations of fast radio bursts will be able to shed light into which mechanism is correct.

2.5.7   Gravitational-wave emission and detection

Gravitational-wave emission

Long-lived neutron stars also emit gravitational waves, but we have an incomplete understanding of which mechanisms are relevant, how long they are active for, or how much energy is emitted. As we discuss later, this uncertainty weakens our ability to detect gravitational waves from a long-lived neutron star while also weakening our ability to infer the fate from indirect energetic constraints from electromagnetic observations (e.g., Shibata et al., 2019).

Three main instabilities are relevant for producing gravitational waves in long-lived post-merger remnants. These are the spin-flip, bar-mode and *r*-mode instabilities (e.g., Cutler, 2002; Lai & Shapiro, 1995; Shapiro, 2000; Shibata et al., 2000; Andersson & Kokkotas, 2001; Andersson, 2003). Note there are potentially other mechanisms, such as gravitational-wave emission due to the formation of mountains from fall-back accretion (Sur & Haskell, 2020). Here we briefly discuss these gravitational-wave emission mechanisms following on from the discussion in Sec 2.5.4. For a detailed review of gravitational waves from neutron stars we refer the reader to (e.g., Lasky, 2015, and references therein).

The precessional spin-flip instability drives a nascent neutron star to become an orthogonal rotator and therefore an optimal emitter of gravitational waves (Cutler, 2002). Past studies (e.g., Lander & Jones, 2018) have shown that once a system evolves to being near-aligned or near-orthogonal, it does not further evolve. However, more recent work (e.g., Lander & Jones, 2020)

has shown that including the effect of a neutrino-driven wind can change the late-time behaviour, with orthogonal rotators slowly decreasing the angle between magnetic and rotation axes over hundreds of years to become more aligned. Lander & Jones (2018) also showed that nascent neutron stars would become orthogonal rotators for sufficiently large toroidal magnetic fields $B_t \gtrsim 10^{14}$G. Such magnetic fields are naturally expected in binary neutron star mergers (e.g., Giacomazzo & Perna, 2013; Kiuchi et al., 2014; Ciolfi et al., 2019; Mösta et al., 2020), making it likely that long-lived neutron stars born in binary neutron star mergers become orthogonal rotators and stay that way for a long time.

As discussed in Sec 2.5.4, the timescale for orthogonalisation is far from certain, but is a critical component for building gravitational-wave waveform models for the spin-flip instability. An aligned rotator does not emit gravitational waves. As the angle between the magnetic and rotation axes increases, the star will emit gravitational waves dominantly at the spin frequency, or twice the spin frequency, with a host of other potential values that depend on the precession timescale (e.g., Jones & Andersson, 2002; Lasky & Melatos, 2013). Building gravitational-wave waveform models for this evolution requires careful modelling of the orthogonlisation timescale, including the evolution of the misalignment angle between the rotation and magnetic axes. If the orthogonlisation timescale is short compared to the overall gravitational-wave emission timescale, then the uncertainty associated with the evolution of the misalignment angle can be largely ignored. Such an assumption would be detrimental to detection prospects if the orthogonalisation timescale is comparable to the timescale for gravitational-wave emission.

Assuming orthogonalisation has already taken place, Sarin et al. (2018) built a model for the gravitational-wave signature of long-lived post-merger remnants. Unfortunately, detection prospects are not good with second-generation gravitational-wave interferometers; for detection at greater than a few Mpc, the amount of emitted gravitational-wave energy must exceed the rotational energy budget of the system.

The critical quantities determining the energy produced in gravitational waves for gravitational-wave dominated spin down (i.e., the most optimistic scenario cf. when the spin down is dominated by electromagnetic torques) are the initial spin period and ellipticity. The strong magnetic fields expected in a binary neutron star merger deform the nascent neutron star, with the size of this deformation dependent on the magnetic field and the internal geometry of the field. For simple stellar models, the ellipticity can be approximated as (Cutler, 2002)

$$\epsilon_B \approx 10^{-6} \left(\frac{\langle B_t \rangle}{10^{15}\text{G}} \right)^2 , \qquad (2.6)$$

where $\langle B_t \rangle$ is the volume-averaged toroidal magnetic field strength. Observational inferences based on the collapse times of supramassive neutron stars from short gamma-ray bursts suggests $\epsilon_B \sim 10^{-3}$ (Gao et al., 2016). Such large ellipticities require $\langle B_t \rangle \sim 10^{16}$–$10^{17}$ G, i.e., toroidal fields that are 1-2 orders of magnitude stronger than inferred values of the poloidal field. It is

an open question whether such magnetic fields are dynamically stable (e.g., Braithwaite, 2009; Lasky et al., 2011; Ciolfi & Rezzolla, 2012; Akgün et al., 2013; Herbrik & Kokkotas, 2017; Sur & Haskell, 2020).

Another mechanism to generate gravitational waves in a newly-born neutron star is through unstable f modes, also known as the bar-mode instability. This comes in two varieties: dynamical and secular. To activate the dynamical instability, the ratio of a star's rotational kinetic energy T to gravitational binding energy W must be $T/|W| \geq 0.24$ (Lai & Shapiro, 1995; Shapiro, 2000; Baiotti et al., 2007; Corsi & Mészáros, 2009, although note this number is dependant on the unknown equation of state), while the secular instability is active for $T/|W| \geq 0.14$. For realistic equations of state, the dynamical instability is only activated when the star is differentially rotating (e.g., Friedman & Schutz, 1978; Corsi & Mészáros, 2009; Ravi & Lasky, 2014; Lasky & Glampedakis, 2016). The growth of the dynamical instability is therefore halted when the magnetic field damps differential rotation, which is governed by the Alfvén timescale of $\mathcal{O}(1)$s (Shapiro, 2000). Therefore, the dynamical bar mode is only expected to be active in the first seconds of a neutron star's life.

More relevant for long-term gravitational-wave emission is the secular instability. It is worth noting that several equations of state that support masses $\gtrsim 2\,\mathrm{M}_\odot$ do not have rigidly-rotating equilibrium solutions with $T/|W| \geq 0.14$, implying the secular bar-mode instability cannot be active for those equations of state (Ravi & Lasky, 2014). However, if active, the secular bar mode grows to large non-linear amplitudes on timescales of $\mathcal{O}(10\text{--}100)\,\mathrm{s}$ (Doneva et al., 2015). For the instability to grow, the nascent neutron star has to cool to a temperature below $\sim 10^{10}\,\mathrm{K}$, such that bulk viscosity does not suppress the instability. As we have discussed in Sec 2.5.3, a newly-born neutron star is cooled to this temperature a few seconds after the merger, making the secular-bar mode a potentially-dominant mechanism for gravitational-wave emission (Corsi & Mészáros, 2009).

Another oscillation mode that will likely lead to the gravitational-wave radiation are the r modes; low-frequency toroidal oscillations for which the Coriolis force is the restoring force. These oscillations are retrograde in the co-moving frame and prograde in the inertial frame,(Andersson & Kokkotas, 2001; Andersson, 2003), making them always unstable to the Chandrasekhar-Friedman-Schutz (CFS) instability (Chandrasekhar, 1970; Friedman & Schutz, 1978). Whether this instability is active is dependent on a delicate balance between gravitational-wave radiation which drives up the size of the instability, and viscous processes that dampen the oscillations. For nascent neutron stars, the dominant viscous force is bulk viscosity, which in turn depends sensitively on neutron star microphysics, cooling history, and rotation (e.g., Andersson, 2003; Lasky, 2015).

Recently, an interpretation of the x-ray afterglow of GRB090510 suggests that the observations support gravitational-wave losses due to r-mode oscillations through the measurement of the braking index $n = 7$ (Lin & Lu, 2019). This interpretation is contentious, most notably because a braking index of $n = 7$ is not necessarily a reliable indicator of spin-down through r-mode

gravitational-wave emission (e.g., Alford & Schwenzer, 2014, 2015)

Long-lived neutron stars could also emit gravitational waves from mountains formed through fall-back accretion (e.g., Piro & Thrane, 2012; Melatos & Priymak, 2014; Sur & Haskell, 2020). However, given the relatively little amount of material ejecta in a binary neutron star merger, this mechanism is likely only relevant for neutron stars born in supernovae and long gamma-ray bursts.

All the different mechanisms described above suggest it is quite likely that long-lived neutron stars spin down, at least in some part, through gravitational wave emission. This is to an extent observationally verified by the observed collapse time distribution (Sarin et al., 2020b), which suggests $\sim 70\%$ of these neutron stars are spinning down predominantly through gravitational-wave radiation. However, knowing which mechanism is active and for how long can only be verified through the direct detection of gravitational waves from these objects, something to which we now turn.

Gravitational-wave detection methods

Searching for gravitational waves from long-lived neutron stars suffers from some of the same problems as traditional searches for continuous gravitational waves (see Riles, 2013, and references therein). The long-duration signals expected implies traditional matched-filtering approaches are computationally unfeasible (e.g., Brady et al., 1998) requiring semi-coherent methods that are less sensitive than fully coherent methods. Similarly, the uncertainty in the gravitational-wave modelling necessitates the use of unmodelled searches, which by design are not as sensitive as modelled searches.

The LIGO/Virgo Collaborations searched for gravitational waves from a potential long-lived post-merger remnant from GW170817 on intermediate ($\lesssim 500$ s; Abbott et al., 2017f) and long ($\lesssim 8$ d; Abbott et al., 2019c) timescales (the latter timescale being set by the length of data available following the merger). No viable candidate was found, however upper limits on the gravitational-wave strain and energy were derived.

A number of complementary pipelines were used in the LIGO/Virgo searches. The robustly-named Stochastic Transient Analysis Multi-detector Pipeline (STAMP; Thrane et al., 2011) looks for tracks of excess power in cross-correlated data from the two detectors using seedless clustering algorithms (Thrane & Coughlin, 2013, 2015). Coherent Wave Burst (cWB; Klimenko et al., 2016) was used with a similar setup as for the short-duration search; see Sec. 2.4.3. The Hidden Markov Tracking method using the Viterbi algorithm (Suvorova et al., 2016; Sun & Melatos, 2019) searches for quasichromatic signals with unknown frequency evolution and stochastic timing noise. The Adaptive Transient Hough (Krishnan et al., 2004; Oliver et al., 2019b) assumes the signal's frequency evolution can be modelled as a power law, with the amplitude and frequency described by the generalised millisecond magnetar model (Lasky et al., 2017; Sarin et al., 2018). Finally, the Generalized FrequencyHough algorithm (Antonucci et al., 2008; Astone

et al., 2014; Miller et al., 2018) is a pattern-recognition technique that maps time-frequency points to lines in frequency-spin down space.

Four of the aforementioned algorithms are unmodelled searches, and one is modelled. Upper limits for the unmodelled searches were derived using two theoretically-motivated signal models; the generalised millisecond magnetar model that describes a spinning-down neutron star with arbitrary braking index (Lasky et al., 2017; Sarin et al., 2018), and a waveform model (Corsi & Mészáros, 2009) where the star's spin evolution is dictated by the gravitational-wave driven secular Chandrasekhar-Friedman-Schutz instability (Chandrasekhar, 1970; Friedman & Schutz, 1978).

The derived upper limits from the searches do not necessarily bode well for future detections of gravitational waves from long-lived neutron star remnants. Throughout the entire explored parameter space, the distance at which a source could have been observed from the remnant of GW170817 was, at best, just $\sim 1\,\mathrm{Mpc}$, cf. the actual distance of $\sim 40\,\mathrm{Mpc}$.

Although aLIGO/Virgo's sensitivity is predicted to improve by a factor of a few over the sensitivity at the time GW170817 was detected, the prospect for detection with second-generation telescopes is still grim. From an observational perspective, aLIGO/Virgo could eventually be sensitive to mergers at best at $\sim 10\,\mathrm{Mpc}$. Theoretical estimates are consistent with this (see e.g., Corsi & Mészáros, 2009; Fan et al., 2013; Dall'Osso et al., 2015a; Doneva et al., 2015), although (see e.g., Dall'Osso et al., 2018; Lasky & Glampedakis, 2016; Sarin et al., 2018) for more pessimistic estimates. However, in practice, the most optimistic of these estimates may require nonphysical quantities of gravitational-wave energy, for example in excess of the total rotational energy budget of the system (Sarin et al., 2018). A successful detection of gravitational waves from a long-lived post-merger remnant may therefore have to wait until A+ (Miller et al., 2015), or even third-generation detectors such as Einstein Telescope (Punturo et al., 2010) or Cosmic Explorer (Abbott et al., 2017a).

2.6   Conclusions and Outlook

The era of gravitational-wave and electromagnetic multi-messenger astronomy began spectacularly with GW170817 (Abbott et al., 2017b,c,d), a watershed event that provided invaluable insights across several domains of high energy astrophysics. Observations of GW190425 transformed our understanding of the formation of binary neutron stars, highlighting the flaw in the simple assumption that the mass distribution of cosmological binary neutron stars follows the same mass distribution as ones observed locally in our galaxy (e.g., Abbott et al., 2020a). The future of electromagnetic and gravitational-wave multi-messenger astronomy looks bright, with upgrades to both gravitational-wave and electromagnetic detectors in progress (e.g., Abbott et al., 2016; Bellm et al., 2019) and proposed for the future (e.g., Ivezić et al., 2019; Punturo et al., 2010; Abbott et al., 2017a; Ackley et al., 2020).

Notwithstanding our limited understanding of the maximum mass of neutron stars and the binary neutron star mass distribution, we expect potentially up to $\sim 80\%$ of neutron star mergers to produce some form of neutron-star remnant (Margalit & Metzger, 2019). However, at least for the near future, the smoking gun observation of gravitational waves from short or long-lived remnants is unlikely. As such, the fate of the remnant will need to be inferred through the suite of electromagnetic observations.

In the near future, electromagnetic observations, in particular, the early x-ray afterglow and kilonova observations provide the best probe into the nature of the remnant. Late time radio limits on the energy of the ejecta will also provide clues into the nature of the remnant. The latter analyses will require a good understanding of the different channels of energy emission, in particular gravitational waves. If future research concludes that long-lived remnants cannot launch ultra-relativistic jets capable of producing short gamma-ray bursts. This would imply that short gamma-ray bursts are a biased and relatively small fraction of binary neutron star mergers, something that will become telling as the rate of binary neutron star mergers becomes better constrained. Furthermore, any discrepancy in binary neutron star merger and gamma-ray burst rates must therefore be explained by neutron star-black hole mergers, a statement which has significant implications on the properties of such binaries.

Although x-ray afterglow and kilonova observations are the best electromagnetic channels for determining the fate of the post-merger remnant, they alone may also not be definitive without further development and testing of models, requiring input from theorists, simulations and observers. In particular, the idea of using the colour of kilonova to probe the lifetime of the remnant is fraught with difficulties such as viewing angle dependence (e.g., Darbha & Kasen, 2020), and the uncertain impact of the jet-ejecta interaction (e.g., Nativi et al., 2020). These uncertainties, combined with our incomplete knowledge of nuclear reactions and opacities of r-process elements, implies significant systematic uncertainties for inferring the properties of kilonovae from observations (e.g., Zhu et al., 2020).

Inferring the fate of the remnant from the early-time x-ray afterglow observations may be more reliable, particularly if the emission from the long-lived neutron star is isotropic (as suggested by the observations of CDF-S XT2 (e.g., Xue et al., 2019)). This is different from the emission expected from the interaction of the jet with the interstellar medium (the physics known to be responsible for the afterglow in normal circumstances), which is strongly affected by relativistic beaming (e.g., Totani & Panaitescu, 2002; Granot et al., 2002). However, models for the emission from nascent neutron stars are in their infancy, with significant development required such that they accurately reflect all the critical physics (e.g., Metzger & Piro, 2014; Lasky et al., 2017; Şaşmaz Muş et al., 2019; Strang & Melatos, 2019; Sarin et al., 2020a). Jet structure could also explain such observations without requiring a neutron star remnant; in such a scenario, systematic model selection may provide the answer (see e.g., Sarin et al., 2019).

The observations of an x-ray plateau with a sharp drop in luminosity following a binary neutron star merger may provide the most definitive electromagnetic evidence for the fate of a binary neutron star merger. Here again there may be different emission mechanisms such as a reverse shock formed from the interaction of a relativistic jet with the surrounding interstellar medium (e.g., van Eerten, 2018; Lamb & Kobayashi, 2019), or radial stratification of the jet such that it is refreshed at late times (e.g., Lamb et al., 2020). High-latitude emission (e.g., Oganesyan et al., 2020; Ascenzi et al., 2020), or fall back accretion (Desai et al., 2019) that may also explain the sharp drop in luminosity without requiring a supramassive neutron star. Fortunately, if the gamma-ray burst is observed off-axis, several of these scenarios become less likely to be the cause (e.g., van Eerten, 2018). However, to ensure this sharp drop in luminosity is observed, the electromagnetic counterpart of a binary neutron star merger must be identified quickly, on timescales as short as 100s, which will be difficult in the near future. In light of these theoretical and observational issues, it is the combination of various electromagnetic phenomena and richer data confronted with more detailed models that can shed light into the nature of the remnant.

In this review, we have discussed the fate of binary neutron star mergers GW170817 and GW190425 and potential other neutron star mergers seen as short gamma-ray bursts. We have reviewed all possible outcomes of a binary neutron star merger from the prompt collapse into a black hole to the formation of an infinitely stable neutron star, discussing their observational signature, evolution, and prospects for gravitational-wave detection. As observations of binary neutron star mergers grow in number, understanding the fate of the remnant will become increasingly more important due to its far-reaching implications, such as on the nuclear equation of state, gamma-ray bursts, kilonovae, fast radio bursts, and beyond. At least in the near future, the lack of smoking-gun gravitational-wave observations means the fate must be inferred from electromagnetic observations. The promise of richer and more frequent observations confronted with better models ensures this will be an exciting endeavour.

Chapter 3

X-ray afterglows of short gamma-ray bursts: Magnetar or Fireball?

Abstract

The origin of the X-ray afterglows of gamma-ray bursts has regularly been debated. We fit both the fireball-shock and millisecond-magnetar models of gamma-ray bursts to the X-ray data of GRB 130603B and 140903A. We use Bayesian model selection to answer the question of which model best explains the data. This is dependent on the maximum allowed non-rotating neutron star mass M_{TOV}, which depends solely on the unknown nuclear equation of state. We show that the data for GRB140903A favours the millisecond-magnetar model for all possible equations of state, while the data for GRB130603B favours the millisecond-magnetar model if $M_{TOV} \gtrsim 2.3 M_{\odot}$. If $M_{TOV} \lesssim 2.3 M_{\odot}$, the data for GRB130603B supports the fireball-shock model. We discuss implications of this result in regards to the nuclear equation of state and the prospect of gravitational-wave emission from newly-born millisecond magnetars.

3.1 Introduction

The coincident observation of short gamma-ray burst GRB170817A (Goldstein et al., 2017b) and gravitational waves from a binary neutron star merger (Abbott et al., 2017b) confirmed the association between the compact object progenitor model and short gamma-ray bursts. Short gamma-ray bursts are often followed by an extended emission in lower energy electromagnetic bands referred to as an afterglow. The origin of the afterglow, particularly the X-ray afterglow, is a source of debate. Some models attribute it to an expanding fireball that emits X-ray photons through synchrotron emission once the jet hits the surrounding interstellar medium (Mészáros & Rees, 1993a; Piran, 1999; Meszaros, 1999; Zhang, 2007), while others attribute it to a combination

of an expanding fireball and a millisecond spin-period magnetar central engine (Dai & Lu, 1998; Zhang & Mészáros, 2001; Fan et al., 2006; Rowlinson et al., 2010, 2013). In this work, we consider the question of which model best explains the data for two short gamma-ray bursts: GRB130603B and GRB140903A. The component of the afterglow corresponding to the fireball-shock model is always believed to be present and produces an effect on the afterglow in several electromagnetic bands while the millisecond-magnetar model provides an additional dominant component to the X-ray afterglow.

GRB130603B is believed to be the first credible detection of a kilonova associated with a short gamma-ray burst (Tanvir et al., 2013; Berger et al., 2013) observed first by the Neil Gehrels *Swift* observatory and then with *XMM* up to 6.5 days after the initial burst (Fong et al., 2014). The millisecond magnetar model has been used extensively to explain the X-ray plateau observed in this gamma-ray burst (Fan et al., 2013; de Ugarte Postigo et al., 2014; Fong et al., 2014; Lü et al., 2015; Lasky et al., 2017).

GRB140903A was observed by *Swift* on the 3rd of September 2014 with follow-up observations with *Chandra* $\approx$ 3 and $\approx$ 15 days after the initial burst (Troja et al., 2016). This gamma-ray burst is especially intriguing from our perspective as both the fireball-shock and millisecond magnetar models have been successfully fit to the observations, with no conclusion available for which model best describes the data. Troja et al. (2016) fit the fireball model to this gamma-ray burst using the X-ray and other wavelength observations, inferring a narrow jet opening angle of $\theta \approx 5°$ among other physical quantities such as the jet-break times, suggesting that the observations could be a product of the jet geometry and dynamics within the fireball model. However, both Zhang et al. (2017) and Lasky et al. (2017) successfully fit the millisecond magnetar model to the same X-ray observations.

GRB140903A highlights the need for systematic model selection between the fireball and millisecond magnetar model. In this paper, we use Bayesian inference and model selection to show which of the two models best explain the data for the two aforementioned GRBs. In Secs. 3.2 and 3.3 we introduce the fireball and magnetar models, respectively. In Sec. 3.4 we compare our results for GRB130603B and GRB140903A and select between the fireball and millisecond-magnetar models with an *uninformed* and an *informed* prior odds. The latter being based on the probability that a long-lived millisecond magnetar is born in the gamma-ray burst. We discuss the implications of our result on the prospect of gravitational-wave detection and neutron star equation of state in Sec. 3.5.

3.2 Fireball model

The fireball-shock model has been successful in interpreting a large fraction of gamma-ray bursts. In this model, the ejecta is composed of several shells of matter with a distribution of Lorentz factors. The relativistic fireball sweeps

through the ambient interstellar medium which decelerates the fireball producing a pair of shocks; a long-lived forward shock and a short-lived reverse shock. The former shock produces the broadband afterglow (Piran, 1999; Mészáros & Rees, 1993b; Meszaros, 1999; Mészáros, 2001a). Sari et al. (1999) determined the light-curve signature for synchrotron emission from a power-law distribution of accelerated electrons produced by the long-lived shock. The shape and evolution of this light-curve strongly depends on the frequency of the synchrotron emission as well as the geometry of the fireball itself. At high frequencies above the self-absorption frequency of lower energy electrons, the flux density in a given frequency band ν, can be parameterized by the electron power-law distribution index p as $F_\nu \propto t^{-3(p-1)/4}$ for a spherical fireball. However, generally, a parameter-free description of the form

$$F_\nu \propto t^\alpha \nu^\beta, \tag{3.1}$$

is used (e.g., Sari et al., 1999; Zhang, 2007). Here, t is the time since burst, α is the temporal index, and β is the spectral index. The fireball model is characterized by a series of power laws of this form (e.g., Zhang, 2007).

In reality, there is a strong physical relationship between the temporal and spectral indices based on the properties of the surrounding environment, such as interstellar density. However, in this paper we only model the X-ray component in a single frequency band between 0.2 and 10 keV corresponding to the energy range of *Swift*, in which case Eq. (1) can be re-expressed in terms of the luminosity as

$$L(t) = At^\alpha. \tag{3.2}$$

Here, L is the luminosity, and A is an amplitude that incorporates the frequency-dependent scaling term from Eq. (3.1). Since we are only looking at the temporal evolution a change in temporal index alone may not be indicative of a jet-break. We focus solely on the X-ray observations in this paper to allow direct comparison with the millisecond-magnetar model. We elaborate on other frequency bands later but note here that a critical feature of the fireball-shock model is that the temporal index α is the same across all frequency bands.

We use a Bayesian framework to fit the fireball model to the X-ray afterglow data of GRB140903A and GRB130603B. The general form for N power laws is given by

$$L(t) = \begin{cases} A_1 t^{\alpha_1}, & t \leq t_1 \\ A_2 t^{\alpha_2}, & t_1 < t \leq t_2 \\ ..., & ... \\ A_N t^{\alpha_N}, & t > t_N \end{cases}, \tag{3.3}$$

where A_i, α_i, and t_i are the amplitude, temporal index and time since burst of the ith component-break. We note here that the first power law models the prompt emission. To compare directly with the millisecond-magnetar model, we reparameterize the series of broken power laws in terms of Δt_i, which is the time between successive breaks. We explain this point in more detail in Sec. 3.3. Bayesian inference requires us to define priors to allow fitting of

the model. For the amplitudes, we only require a prior on the first A_1 as the others are determined by demanding the light curve be continuous between any two component breaks. For A_1 we use a log-uniform prior between 10^{-1} and 10^5 L_{50}, where $L_{50} = 10^{50}$ erg s^{-1}. For each of the power-law exponents α_N, we set a uniform prior between -10 and 0. For the time between successive temporal breaks we use a log-uniform prior between 10^{-10} and 10^6 s except for Δt_2 where we set the minimum of the prior on Δt_2 to 10 s as the first power-law component models the prompt emission, which for short gamma-ray bursts can last up to this time. We can derive the rest of the parameters using these priors.

The number of power-law components is itself a free parameter to be fit for. In our analysis, we consider a maximum number of components of 6 as with the inclusion of the prompt emission power law, it is difficult to expect more than 4 temporal breaks (e.g., Sari et al., 1998). We find the addition of more components does not provide a better fit, a point we discuss further below. We fit our model using the nested sampling package MULTINEST (Feroz et al., 2009), which allows us to evaluate the evidence for our model given the data. Evidence and the basics of Bayesian inference and model selection are explained in Appendix 3.6. We iteratively fit power-law components, evaluating the evidence at each iteration. The number of components that best explains the data is given by that with the highest evidence. We find that the evidence is maximised with the four component fireball model for both GRB130603B and GRB140903A. In Fig. 3.1 we show our fits with the fireball model in the bottom panel, with the evidences $\mathcal{Z}$ shown in Table 3.1. For GRB140903A, our results for the temporal-break times and number of

TABLE 3.1: Evidences $\ln \mathcal{Z}$ for GRB130603B and GRB140903A for different power-law components in the fireball model. The subscript denotes the number of power-law components in the fireball model. The model in bold is the favoured number of power-law components for each gamma-ray burst. The evidences and the errors, the latter being the sampling error are both calculated by MULTINEST.

	GRB130603B	GRB140903A
$\ln \mathcal{Z}_{1,F}$	431 ± 0.02	57 ± 0.02
$\ln \mathcal{Z}_{2,F}$	1019 ± 0.03	434 ± 0.03
$\ln \mathcal{Z}_{3,F}$	1258 ± 0.03	620 ± 0.03
$\ln \mathcal{Z}_{4,F}$	$\mathbf{1280 \pm 0.03}$	$\mathbf{637 \pm 0.03}$
$\ln \mathcal{Z}_{5,F}$	1275 ± 0.03	637 ± 0.03
$\ln \mathcal{Z}_{6,F}$	1273 ± 0.04	634 ± 0.03

power-law components excluding the prompt emission and the power-law exponents are consistent with Troja et al. (2016) who analysed GRB140903A data across multiple wavelength bands. Our maximum posterior fit parameters for the four-component fireball model of GRB130603B and GRB140903A are shown in Table 3.2.

TABLE 3.2: Maximum posterior parameters of the four-component fireball model for GRB130603B and GRB140903A without the prompt emission power law.

	α_2	α_3	α_4	t_2 (s)	t_3 (s)
GRB130603B	-0.33	-1.28	-2.07	1459	12180
GRB140903A	-0.15	-1.02	-1.99	5907	45480

3.3 Magnetar model

The millisecond magnetar model was first introduced by Dai & Lu (1998) and Zhang & Mészáros (2001) as a model for the X-ray afterglow evolution through sustained energy injection from a millisecond magnetar central engine. Zhang & Mészáros (2001) derived a model for luminosity evolution from the spin down of this millisecond magnetar through magnetic dipole radiation producing the X-ray afterglow. Dall'Osso et al. (2011) extended this model to provide a full solution for energy injection from a magnetar central engine that spins down through magnetic dipole radiation while also including effects of radiative losses due to shocks in the interstellar medium. They also showed that this model allows for non-zero slopes in the plateau which is helpful in explaining the observations of several gamma-ray bursts. Rowlinson et al. (2010; 2013) successfully fit the millisecond magnetar model of Zhang & Mészáros (2001) to various short gamma-ray bursts. Dall'Osso et al. (2011) and Stratta et al. (2018) fit the model from Dall'Osso et al. (2011) to a sample of long and short gamma-ray bursts. Lasky et al. (2017) extended the millisecond magnetar model to include the spin down of magnetars with arbitrary braking indices n, and fit this model to the X-ray afterglows of GRB130603B and GRB140903A in a Bayesian framework. Lasky et al. (2017) measured the braking index for both GRB130603B and GRB140903A as $n = 2.9 \pm 0.1$ and $n = 2.6 \pm 0.1$ respectively; the former being consistent with the $n = 3$ value associated with a star spinning down predominantly through magnetic dipole radiation. The braking index was fixed as $n = 3$ in the fits of Rowlinson et al. (2013) and Zhang et al. (2017).

The generalised millisecond magnetar model is (Lasky et al., 2017),

$$L(t) = A_1 t^{\alpha_1} + L_0 \left(1 + \frac{t}{\tau} \right)^{\frac{1+n}{1-n}},$$ (3.4)

where the first term corresponds to the prompt emission, which is the same as the fireball model described in Sec. 3.2, L_0 is the initial luminosity at the onset of the plateau phase, τ is the spin-down timescale, and n is the braking index which parameterizes the dominant mode of radiation causing spin-down of the millisecond magnetar.

We reparameterize the millisecond magnetar model (Eq. 3.4) to allow direct comparison with the fireball model. This reparameterization is approximately similar as the first term is sub-dominant at later times by several

orders of magnitude. The reparameterized millisecond-magnetar is

$$L(t) = \begin{cases} A_1 t^{\alpha_1}, & t < t_1 \\ A_2 \left(1 + \frac{t}{\tau}\right)^{\alpha}, & t > t_1. \end{cases} \tag{3.5}$$

This implies two different α values for $t > t_1$. An $\alpha_2 \approx 0$ when $t < \tau$ and an $\alpha_3 = (1+n)/(1-n)$ for $t > \tau$. The reparameterization allows us to define priors for the magnetar model which are equivalent to those used in the fireball model. We can then use our previously defined priors on Δt_2 and α and construct the parameters τ and n via

$$\tau = \Delta t_1 + \Delta t_2, \tag{3.6}$$

and

$$n = \frac{\alpha - 1}{\alpha + 1}. \tag{3.7}$$

With this reparameterization, the three component fireball model and millisecond magnetar model have the same parameters. Implicitly, the two models have the parameters,

$$\{A_1, \alpha_1, \Delta t_1, \alpha_2, \Delta t_2, \alpha_3\}. \tag{3.8}$$

We note that the millisecond magnetar model does not explicitly have three power-law exponents, however mathematically for $t < \tau$ the millisecond magnetar model has an $\alpha_2 \approx 0$ power-law exponent, while α_3 is the power-law exponent for $t > \tau$. We fit this reparameterized millisecond magnetar to the X-ray afterglow of GRB130603B and GRB140903A, our resulting fit to both gamma-ray burst light curves are shown in Fig. 3.1. For both gamma-ray bursts, our reparameterized millisecond magnetar model produces similar posteriors for τ and n as Lasky et al. (2017).

3.4 Model Selection

In Fig. 3.1 we show X-ray lightcurves of GRB130603B (left panels) and GRB140903A (right panels) with the millisecond magnetar model (top row) and the four-component fireball model (bottom row).

We calculate the Bayes factor (see Appendix 3.6) to compare between the two models. We find that the Bayes factor $\mathrm{BF_{M/F}} = 19$ and 2271 for GRB130603B and GRB140903A, respectively. If we assume both hypotheses are equally likely *a priori* by setting the prior odds $\Pi_\mathrm{M}/\Pi_\mathrm{F} = 1$, then this tells us that the data prefers the millisecond magnetar model by 19 and 2271 times over a four-component fireball model for GRB130603B and GRB140903A, respectively. Although both models are mathematically similar, the magnetar model is preferred by the data as it provides a smooth transition between power laws compared to the fireball model that has sharp transitions.
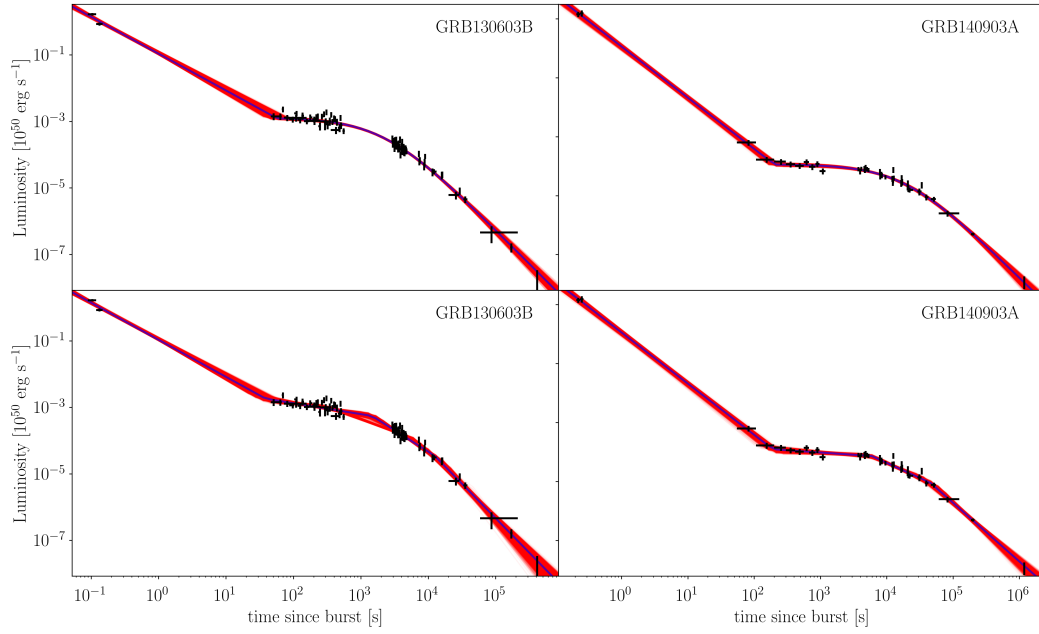
FIGURE 3.1: X-ray lightcurves for GRB130603B (left panels) and GRB140903A (right panels). Black points indicate data from *Swift* and *Chandra* satellites. The blue curve shows the maximum likelihood model for the millisecond magnetar model (top row) and four-component fireball model (bottom row). The dark red band is the superposition of 5000 models randomly drawn from the posterior distribution.

For both gamma-ray bursts we find that the millisecond magnetar model is favoured over the fireball model assuming both hypotheses are equally likely *a priori*.

3.4.1 Prior Odds

The odds $\mathcal{O}$ is the actual quantity that should be used for doing model selection (see discussion in Appendix 3.6). The odds is the product of the Bayes factor and the prior odds; see Eq. (3.13). Therefore, our analysis in the previous section where we used the Bayes Factor for model selection implicitly set the prior odds as $\Pi_M/\Pi_F = 1$. In this section, we improve on this by creating an *informed* prior on the probability that a long-lived magnetar exists following the gamma-ray burst.

If we assume all short gamma-ray burst progenitors are binary neutron star mergers, then the existence of a long-lived magnetar remnant is dependent on the masses of the progenitor and the nuclear equation of state. The equation of state dictates the maximum possible non-rotating mass of a neutron star, otherwise known as the Tolman-Oppenheimer-Volkoff mass M_{TOV} (Tolman, 1939; Oppenheimer & Volkoff, 1939). The most massive neutron star observed to date has a mass of $2.01 M_\odot$ (Antoniadis et al., 2013), which is therefore the smallest possible value of M_{TOV} given current observations of neutron stars. For a millisecond magnetar to be stable and not collapse to

a black hole, its mass must be less than $M_{\rm TOV}$. However, millisecond magnetars are born rapidly rotating and can often be supramassive neutron stars which have masses up to $\sim 1.2 \times M_{\rm TOV}$ (Cook et al., 1994). However, supramassive neutron stars collapse on timescales between $\sim 10 - 10^4$ s (Ravi & Lasky, 2014). As both GRB130603B and GRB140903A have observations lasting longer than $\sim 10^4$ s, if they are millisecond magnetars, they must be infinitely stable neutron stars with mass less than $M_{\rm TOV}$.

We estimate the fraction of binary neutron star mergers that result in an infinitely stable neutron star remnant as follows. Following Lasky et al. (2014), we calculate the post-merger mass distribution $P({\rm M})$ based off the statistically-determined mass distribution of galactic binary neutron star systems calculated by Kiziltan et al. (2013) $M = 1.32 \pm 0.11 M_{\odot}$. A calculation of the post-merger mass distribution then requires conversion of the gravitational mass to the rest mass. An approximate relation to make this conversion is, $M_{\rm rest} = M + 0.075 M^2$ (Timmes et al., 1996). Conservation of rest mass in the merger then leads to the post-merger mass distribution. In reality, the calculation needs to account for the mass ejected during merger. Numerical simulations of binary neutron star mergers indicate that the mass ejected is $\lesssim 0.01 M_{\odot}$ (e.g., Hotokezaka et al., 2013b; Giacomazzo & Perna, 2013). However, this is inconsistent with observations of the electromagnetic transient to GW170817, which requires a mass ejecta $\sim 0.03 M_{\odot}$ to explain the blue kilonova (e.g., Evans et al., 2017b), while an ejecta mass $\approx 0.07 M_{\odot}$ is required to explain both the blue and red kilonova observations (e.g., Metzger, 2017a). Accounting for the mass ejecta as indicated by the blue and red kilonova observations of GW170817 leads to the post-merger mass distribution of $P(M) = 2.38 \pm 0.14 M_{\odot}$, while ignoring the ejected mass gives $P(M) = 2.45 \pm 0.14 M_{\odot}$. We note that the post-merger mass distribution calculated in Lasky et al. (2014) is incorrectly written as an asymmetrical distribution due to a rounding error.

The prior odds for magnetar vs. fireball models is then the probability that the post-merger mass is less than the (unknown) maximum non-rotating mass $M_{\rm TOV}$. That is, the prior odds is

$$\frac{\Pi_{\rm M}}{\Pi_{\rm F}} = \int_0^{M_{\rm TOV}} P(M)\, dM. \tag{3.9}$$

We use Eq. (3.9) to evaluate the odds $\mathcal{O}_{\rm M/F}$ as a function of $M_{\rm TOV}$, which is shown in Fig. 3.2. The odds increases with $M_{\rm TOV}$ as the probability of forming an infinitely stable millisecond magnetar increases for higher $M_{\rm TOV}$. The black shaded region indicates an odds confidence interval and spans an odds of 0.5 to 2.0.

With an *informed* prior odds, selecting between the two models becomes highly dependent on $M_{\rm TOV}$ which is not known. Figure 3.2 shows that for $M_{\rm TOV} \gtrsim 2.01 M_{\odot}$ and $\gtrsim 2.3 M_{\odot}$ the odds $\mathcal{O}_{\rm M/F} \gtrsim 2$, indicating that the millisecond-magnetar model is at least twice as likely than the fireball model for GRB140903A and GRB130603B, respectively.
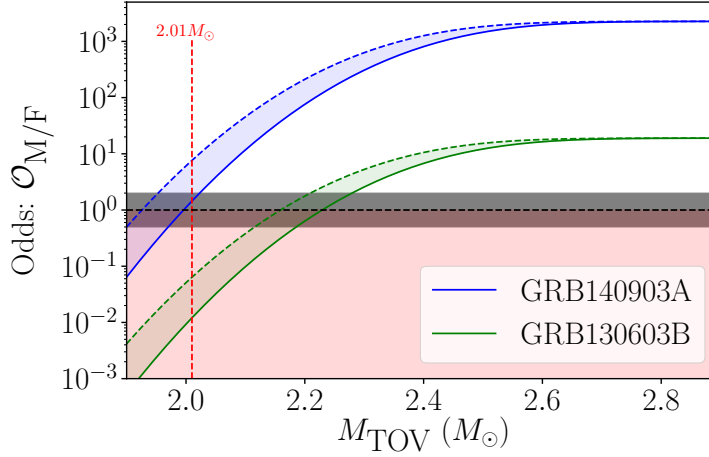
FIGURE 3.2: Odds $\mathcal{O}_{\mathrm{M/F}}$ as a function of M_{TOV}. The blue and green curves correspond to GRB140903A and GRB130603B, respectively, with the solid curves ignoring mass ejected in mergers, while dashed curves correspond to $0.07M_\odot$ consistent with the blue and red kilonova observations of GW170817 (e.g., Evans et al., 2017b; Metzger, 2017a). The blue and green shaded regions correspond to odds for ejecta masses between $0M_\odot$ and $0.07M_\odot$. The red shaded region indicates odds where the fireball model is favoured over the millisecond magnetar model. The dotted red curve corresponds to a $2.01M_\odot$ which is the smallest possible value of M_{TOV} given current observations of neutron stars. The black dotted line indicates $\mathcal{O} = 1$ while the black shaded region spans an odds of 0.5 to 2.

3.5 Conclusion

We analyse two short gamma-ray bursts, GRB130603B and GRB140903A and find that the millisecond-magnetar model is favoured over the fireball model with $\mathrm{BF}_{\mathrm{M/F}} \sim 20$ and ~ 2270 respectively, assuming the formation of a millisecond magnetar is just as likely as a fireball. When we use an *informed* prior odds based on the probability that a long-lived millisecond magnetar is born in the gamma-ray burst, model selection becomes strongly dependent on the maximum allowed non-rotating mass M_{TOV}, which is not known. However, we show that GRB140903A favours the millisecond-magnetar model for $M_{\mathrm{TOV}} \gtrsim 2.01 \ M_\odot$ which is also the most massive neutron star observed to date (Antoniadis et al., 2013). Therefore, for all possible equation of states, GRB140903A favours the millisecond-magnetar model. Similarly, GRB130603B favours the millisecond magnetar model for $M_{\mathrm{TOV}} \gtrsim 2.3 \ M_\odot$.

Our results show that for GR140903A and GRB130603B the millisecond-magnetar model is favoured over the fireball-shock model solely in the context of the X-ray afterglow data considered here for conservative assumptions on the value of M_{TOV}. This has significant implications for gamma-ray burst physics and the fate of the post-merger remnant of neutron star mergers. The millisecond-magnetar model implies a central neutron star engine that will spin down and emit gravitational waves, which may be detectable with current and future generation of gravitational-wave detectors (e.g., Stella et al., 2005; Dall'Osso & Stella, 2007; Dall'Osso et al., 2009;

Corsi & Mészáros, 2009; Dall'Osso et al., 2015a; Doneva et al., 2015; Lasky & Glampedakis, 2016; Lü et al., 2016a; Ho, 2016; Piro et al., 2017; Gao et al., 2017; Sarin et al., 2018; Lü et al., 2018; Dall'Osso et al., 2018). Motivated by the possibility of a long-lived neutron star post-merger remnant as supported by the kilonova observations (Yu et al., 2018; Ai et al., 2018) and an X-ray excess in the afterglow of GRB170817A (Piro et al., 2018), a search for gravitational-wave signals from a possible post-merger remnant from GW170817 was performed, with no detection as expected by theoretical constraints and current detector sensitivities (Abbott et al., 2017f, 2019c). The putative neutron star born in GRB170817A could also have collapsed to form a black hole instantly, which constrains $M_{\text{TOV}} \lesssim 2.16\ M_\odot$ (e.g, Margalit & Metzger, 2017; Ruiz et al., 2018; Rezzolla et al., 2018b).

In the future, we aim to extend this analysis to a population of short gamma-ray burst afterglows. Studying an entire population will allow a similar analysis to be performed as in Sec. 3.4 allowing us to probe the equation of state through this method.

3.6   Appendix

The foundation of this work is based on Bayesian inference. Given a model $\mathcal{M}$ with an associated set of parameters θ, Bayes theorem allows one to calculate the posterior distributions on the model parameters $p(\theta|d, \mathcal{M})$ given data d

$$p(\theta|d, \mathcal{M}) = \frac{\mathcal{L}(d|\theta, \mathcal{M})\pi(\theta|\mathcal{M})}{\mathcal{Z}(d|\mathcal{M})}, \tag{3.10}$$

where $\mathcal{L}(d|\theta, \mathcal{M})$ is the likelihood of the data given the model parameters, $\pi(\theta|\mathcal{M})$ reflects our prior knowledge of the model parameters, and $\mathcal{Z}(d|\mathcal{M})$ is the evidence

$$\mathcal{Z}(d|\mathcal{M}) = \int d\theta \mathcal{L}(d|\theta, \mathcal{M})\pi(\theta|\mathcal{M}). \tag{3.11}$$

The evidence plays no role when estimating the parameters for the model, however, it can be used to do a model comparison between two hypotheses, $\mathcal{M}_1$ and $\mathcal{M}_2$. In that case, the ratio of the two evidences is known as the Bayes factor

$$\text{BF}_{\mathcal{M}_1/\mathcal{M}_2} = \frac{\mathcal{Z}(d|\mathcal{M}_1)}{\mathcal{Z}(d|\mathcal{M}_2)}. \tag{3.12}$$

One can use the Bayes factor to distinguish between two different models or hypotheses using an odds.

$$\mathcal{O}_{1/2} = \frac{\mathcal{Z}_1}{\mathcal{Z}_2}\frac{\Pi_1}{\Pi_2}. \tag{3.13}$$

Here Π_1/Π_2 is referred to as the prior odds and describes our prior belief about the relative likelihood of one hypothesis over another. An odds can then be used for model comparison, an $\mathcal{O}_{1/2} > 1$ indicates that the first hypothesis is favoured over the second hypothesis, while $\mathcal{O}_{1/2} < 1$ indicates the second hypothesis is favoured over the first.

Chapter 4

X-ray guided gravitational-wave search for binary neutron star merger remnants

Abstract

X-ray observations of some short gamma-ray bursts indicate that a long-lived neutron star can form as a remnant of a binary neutron star merger. We develop a gravitational-wave detection pipeline for a long-lived binary neutron star merger remnant guided by these counterpart electromagnetic observations. We determine the distance out to which a gravitational-wave signal can be detected with Advanced LIGO at design sensitivity and the Einstein Telescope using this method, guided by X-ray data from GRB140903A as an example. Such gravitational waves can in principle be detected out to ~ 20 Mpc for Advanced LIGO and ~ 450 Mpc for the Einstein Telescope assuming a fiducial ellipticity of 10^{-2}. However, in practice we can rule out such high values of the ellipticity as the total energy emitted in gravitational waves would be greater than the total rotational energy budget of the system. We show how these observations can be used to place upper limits on the ellipticity using these energy considerations. For GRB140903A, the upper limit on the ellipticity is 10^{-3}, which lowers the detectable distance to ~ 2 Mpc and ~ 45 Mpc for Advanced LIGO and the Einstein Telescope, respectively.

4.1 Introduction

The era of gravitational-wave multi-messenger astrophysics has begun. On 17th August 2017, the Advanced Laser Interferometer Gravitational-wave Observatory (aLIGO) (Aasi et al., 2015) and Advanced Virgo (Acernese et al., 2015) made the first gravitational-wave observation of a binary neutron star

61

merger, known as GW170817 (Abbott et al., 2017). This event was also detected 1.74 seconds later as a short gamma-ray burst (SGRB) by the Fermi and Integral telescopes (Goldstein et al., 2017b), confirming that binary neutron star mergers can be the progenitors of SGRBs. There are competing hypotheses for the fate of the post-merger remnant. Some analyses of the electromagnetic observations support a hypermassive neutron star that collapsed to form a black hole in $\lesssim$ 1s (Metzger et al., 2018; Pooley et al., 2017; Margalit & Metzger, 2017). Others support the formation of a stable, rapidly spinning, long-lived magnetar (Yu et al., 2018).

In either case, a short- or long-lived post-merger remnant emits gravitational waves. The detection of such gravitational waves will have significant implications for the understanding of neutron-star physics including the nuclear equation of state. A search for short and intermediate duration gravitational-wave signals from a post-merger remnant of GW170817 did not return a significant result (Abbott et al., 2017f). This lack of detection was expected given theoretical models (Dall'Osso et al., 2015b; Lasky & Glampedakis, 2016; Doneva et al., 2015) and current aLIGO sensitivity. However, the proximity of GW170817, in conjunction with planned upgrades to aLIGO and Virgo sensitivity (Abbott et al., 2018) and improved algorithms, suggests, that we may be able to detect post-merger gravitational waves from GW170817-like remnants in the future.

In general, the merger of two neutron stars could result in four different outcomes, which depend on the mass and spin of the remnant and the equation of state - a stable neutron star, a supramassive neutron star, a hyper massive neutron star or the direct collapse to a black hole. A supramassive neutron star is initially supported against gravitational collapse by rigid-body rotation but will collapse to form a black hole on timescales of $10s - 10^4s$ (Ravi & Lasky, 2014). A hypermassive neutron star is supported against gravitational collapse through differential rotation but collapses to a black hole in $\leq$ 1s (see Baiotti & Rezzolla (2017) for a recent review).

In this paper, we focus on the scenario where a neutron star merger produces a supramassive or stable neutron star remnant. This rapidly spinning star spins down through a combination of electromagnetic and gravitational-wave radiation. The latter is likely produced by the non-zero stellar ellipticity in conjunction with the spin-flip instability (Cutler, 2002; Lasky & Glampedakis, 2016), unstable r-modes (Anderson & Kokkotas, 2001; Owen et al., 1998) or the secular Chandrasekhar-Friedmann-Schutz bar-mode instability (Lai & Shapiro, 1995; Shapiro & Zane, 1998; Coyne et al., 2016; Shibata et al., 2000; Corsi & Mészáros, 2009; Doneva et al., 2015).

The extended X-ray emission of many SGRBs has been observed by satellites such as *Swift* and Chandra, and used to determine parameters of the neutron star remnant (e.g., Rowlinson et al., 2013; Lü et al., 2015; Lasky et al., 2017). Rowlinson et al.(Rowlinson et al., 2010, 2013) showed that models of magnetic dipole radiation from spinning down millisecond magnetars

(Zhang & Mészáros, 2001; Dai & Lu, 1998) agree with X-ray afterglow observations of several SGRBs. GRB170817A had an extended emission of a different structure (e.g., Ruan et al., 2018; Troja et al., 2017).

In this paper, we present a method to search for gravitational waves from a long-lived post-merger neutron star remnant. In Sec. 4.2 we derive a model for the gravitational waves emitted from a rapidly spinning down millisecond magnetar while also describing the parameters and the parameter space. In Sec. 4.3 we discuss how we can utilize observations of X-ray afterglows from SGRBs to constrain parameters and run a targeted gravitational-wave search. We continue in Sec. 4.4 with a discussion of the detection statistics for our pipeline and conclude in Sec. 4.5 with a brief discussion on the extensions that will improve the analysis and physical theory.

4.2 Gravitational waveform from millisecond magnetars

A long-lived post-merger remnant spins down due to electromagnetic and gravitational-wave radiation. We start with the general torque equation.

$$\dot{\Omega} = -k\Omega^n, \tag{4.1}$$

where Ω and $\dot{\Omega}$ are the star's angular frequency and its time derivative, respectively, k is a constant of proportionality, and n is the braking index. The gravitational-wave frequency is a function of the star's spin frequency. Throughout this work, we assume the gravitational waves are emitted at twice the star's spin frequency, which is true for an orthogonal rotator. The following equations are therefore not valid for gravitational waves from r-mode emission; we discuss generalizations of our model in Sec. 4.5.

The braking index is related to the emission mechanism; $n = 3$ implies that the neutron star is spun down only through a dipole magnetic field in vacuum (Shapiro & Teukolsky, 1983), while $n = 5$ implies that the neutron star is spun down through gravitational-wave radiation (Yue et al., 2006; Bonazzola & Gourgoulhon, 1996). A braking index of $n = 7$ is conventionally associated with spin down through unstable r modes (e.g. Owen et al., 1998), although the true value can be less for different saturation mechanisms (Alford & Schwenzer, 2014, 2015). Inference of the braking index for two millisecond magnetars born in SGRBs give $n = 2.9 \pm 0.1$ and 2.6 ± 0.1 for GRB130603B and GRB140903A, respectively (Lasky et al., 2017).

Integrating Eq. (4.1) and solving for the gravitational-wave frequency gives the gravitational-wave frequency evolution

$$f_{\mathrm{gw}}(t) = f_{\mathrm{gw},0} \left(1 + \frac{t}{\tau} \right)^{\frac{1}{1-n}}, \tag{4.2}$$

where

$$\tau = \frac{\left(f_{\mathrm{gw},0} \pi \right)^{1-n}}{-k(1-n)}, \tag{4.3}$$

is the spin-down timescale and $f_{\mathrm{gw},0}$ is the gravitational-wave frequency at $t = 0$.

The dimensionless gravitational-wave strain amplitude for a non-axisymmetric, rotating body obeying Eq. (4.1) is given by

$$h_0(t) = \frac{4\pi^2 G I_{zz}}{c^4} \frac{\epsilon}{d} f_{\mathrm{gw},0}^2 \left(1 + \frac{t}{\tau} \right)^{\frac{2}{1-n}}. \tag{4.4}$$

Here, I_{zz} is the principle moment of inertia, ϵ is the ellipticity of the rotating body, d is the distance to the source, G is the gravitational constant, and c is the speed of light. The gravitational-wave strain at a detector $h(t)$ is a combination of the h_+ and $h_\times$ polarisations,

$$h(t) = h_0(t) \left[F_+ \frac{1 + \cos^2(\iota)}{2} \cos \Phi(t) + F_\times \cos(\iota) \sin \Phi(t) \right], \tag{4.5}$$

where, ι is the inclination angle, and

$$\Phi(t) = \Phi_0 + 2\pi \int_0^t dt' f_{\mathrm{gw}}(t'), \tag{4.6}$$

is the phase, with $\Phi_0 = \Phi(t = 0)$. In Eq. (4.5), F_+ and $F_\times$ are the antenna pattern functions (Jaranowski et al., 1998) for each of the polarisations. In reality, F_+ and $F_\times$ are functions of time. In this work, we have ignored this complication and assumed constant F_+ and $F_\times$ which we determine using the sky location of GRB140903A. This does not significantly affect our quantitative results, although it will need to be included when the full pipeline is developed to search for gravitational waves.

Substituting the gravitational-wave frequency evolution from Eq. (4.2) into Eq. (4.6) gives

$$\Phi(t) = \Phi_0 + 2\pi \tau f_{\mathrm{gw},0} \left(\frac{1-n}{2-n} \right) \left[\left(1 + \frac{t}{\tau} \right)^{\frac{2-n}{1-n}} - 1 \right]. \tag{4.7}$$

The full waveform model for a rapidly rotating neutron star spinning down due to gravitational wave radiation with an arbitrary braking index consists of Eq. (4.4), (4.5), and (4.7). We refer to this waveform model as the magnetar

waveform model, which is parameterized by the initial gravitational-wave frequency $f_{gw,0}$, the spin-down timescale τ, braking index n, inclination ι, initial phase Φ_0 and scaling parameters I_{zz}, ϵ, d.

In the following, we develop an algorithm for a matched-filter search for gravitational waves using the magnetar waveform model. We construct a template bank by choosing physical parameters for $f_{gw,0}$, τ, n, ι, and Φ_0 from a prior. We quantify in Sec. 4.4 that a template bank constructed from physically motivated but unconstrained priors is computationally expensive for detecting gravitational waves, but these priors can be further constrained using X-ray afterglow observations which reduce the computational cost of searches and increase the sensitivity. The scaling parameters do not require priors as they only affect the amplitude of the gravitational wave which is normalised in a matched-filter search. Throughout this work, we assume a fiducial moment of inertia, $I_{zz} = 10^{45}$ g cm^2, an optimal orientation $\iota = 0$, and a constant ellipticity ϵ. We note that the strain scales linearly with the moment of inertia, which may be a factor of a few larger than our fiducial value. In principle, we can choose to model the ellipticity as a function of time. However, over the long timescales considered here, the ellipticity is not expected to evolve significantly; the internal magnetic field that likely causes the stellar deformation gets wound up on the Alfvén timescale, which for these systems is $\ll$ 1s (e.g., Shapiro, 2000). Although it is possible to have an evolution of the ellipticity through other mechanisms such as stellar cooling, the effect is similar to the angle between the star's principal moment of inertia and its rotation axis evolving due to, for example, the spin-flip instability (see Sec. 4.5). We leave this generalization for future work.

4.2.1   Gravitational-wave energy budget

We also consider the energy budget of the gravitational wave emission to determine allowed regions of the parameter space. The total power emitted in gravitational waves is

$$\dot{E}_{\mathrm{gw}}(t) = -\frac{32G}{5c^5} I_{zz}^2 \epsilon^2 \Omega^6(t). \tag{4.8}$$

We substitute our gravitational-wave frequency evolution Eq. (4.2) for the evolution of the star's angular frequency and integrate to determine the energy emitted in gravitational waves for a constant braking index

$$E_{\mathrm{gw}}(t) = -\frac{32\pi^6 G}{5c^5} I_{zz}^2 f_{\mathrm{gw},0}^6 \epsilon^2 \tau \frac{n-1}{n-7} \left[\left(1 + \frac{t}{\tau}\right)^{\frac{7-n}{1-n}} - 1 \right]. \tag{4.9}$$

This energy evolution is different to a standard continuous-wave signal as the strain evolves as a function of time. The total energy emitted in gravitational waves must be less than the initial rotational energy, E_{rot} of the system

$$|E_{\mathrm{gw}}(t)| < E_{\mathrm{rot}}, \tag{4.10}$$

where

$$E_{\mathrm{rot}} = \frac{1}{2} I_{zz} f_{\mathrm{gw},0}^2 \pi^2. \tag{4.11}$$

We can use this condition to check if a given parameter space is physical. Figure 4.1 illustrates, for a post-merger remnant inferred from GRB140903A
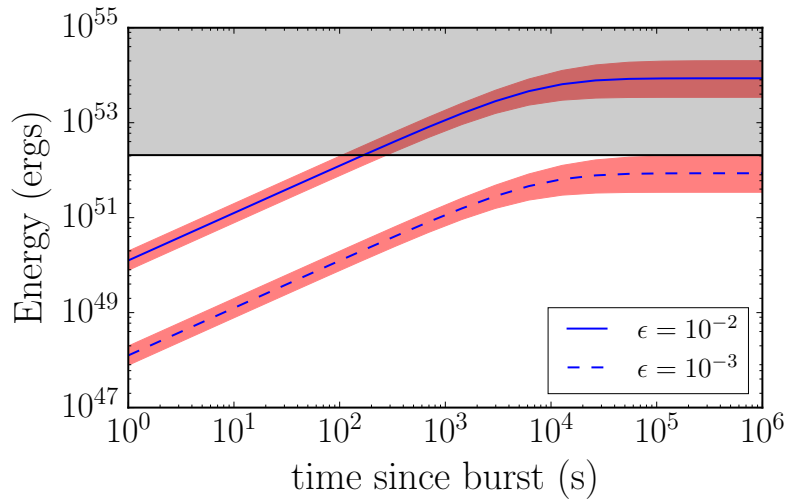
FIGURE 4.1: The energy budget of a post-merger remnant inferred from GRB140903A with ellipticity $\epsilon = 10^{-2}$ (solid curves) and 10^{-3} (dashed curves) with the red shaded region indicating the 2σ confidence interval. The grey shaded region above the solid black horizontal line is nonphysical as discussed in Sec. 4.2.1.

with a fiducial $I_{zz} = 10^{45}$ g cm^2, an ellipticity $\epsilon = 10^{-2}$ violates the energy-budget constraint. Based on these energy considerations the upper limit on ellipticity for GRB140903A is $\epsilon \approx 10^{-3}$. In reality, the moment of inertia for a long-lived post-merger remnant is likely higher than the fiducial value we use here, however all our limits can be scaled appropriately for different values of I_{zz}. In particular, the moment of inertia is inversely proportional to the inferred upper limit on ellipticity, because the rotational energy grows linearly with I_{zz}, but the gravitational-wave energy grows quadratically. Our fiducial moment of inertia therefore provides a conservative limit on the ellipticity.

4.2.2 Optimal matched filter statistic

The matched-filter signal-to-noise ratio ρ is given by (Cutler & Flanagan, 1994)

$$\rho = \frac{\langle h|u \rangle}{\sqrt{\langle u|u \rangle}},$$

(4.12)

where $h = s + n$ is the combination of signal s and noise n, u is the template, and $\langle a|b \rangle$ denotes the noise-weighted inner product (Cutler & Flanagan, 1994), defined by

$$\langle a|b \rangle = 4\Re \int_0^\infty \frac{\tilde{a}^*(f)\tilde{b}(f)}{S_h(f)} df.$$

(4.13)

Here $\tilde{a}$ denotes the Fourier transform of a, $\tilde{a}^\star$ its complex conjugate, and $S_h(f)$ is the noise power spectral density. The optimal matched-filter signal-to-noise ratio ρ_{opt} is achieved when the template matches the data precisely:

$$\rho_{\text{opt}} = \sqrt{\langle h|h \rangle}.$$

(4.14)

In this analysis, the threshold signal-to-noise ratio required to make a detection is $\rho_{\text{threshold}} = 4.4$, which is derived in Sec. 4.4. In Fig. 4.2 we show the region of parameter space where we could detect a signal from a post-merger remnant at the same distance as GW170817 (40 Mpc). We assume $I_{zz} = 10^{45}$ g cm^2, $\epsilon = 0.01$ (top panel) and $\epsilon = 0.001$ (bottom panel), $n = 2.71$ and $f_{\text{gw},0} = 2050$ Hz. We use these values of $f_{\text{gw},0}$ and n as they are the maximum likelihood parameters from GRB140903A using the method detailed in Sec. 4.3. The left-hand side of Fig. 4.2 shows it is theoretically possible for gravitational waves from such an object to be observable by aLIGO operating at design sensitivity (Abbott et al., 2018) if $\tau \gtrsim 4 \times 10^4$ s and $t_{\text{obs}} \gtrsim 4 \times 10^4$ s. The right-hand side shows that the Einstein Telescope (ET), a proposed third generation detector (Hild et al., 2011), can detect such a signal if $\tau \gtrsim 10^2$ s and $t_{\text{obs}} \gtrsim 10^2$ s for $\epsilon = 10^{-2}$. We note that GRB140903A has $\tau = 17207 \pm 1880$ s. However, as shown in Sec. 4.2.1 this large ellipticity is nonphysical for GRB140903A-like post-merger remnant in all of the parameter space required to detect a signal with aLIGO. A physically realistic ellipticity $\epsilon = 10^{-3}$ rules out any prospect of detection with aLIGO for a GRB140903A-like post-merger signal at 40 Mpc and requires $\tau \gtrsim 10^4$ s and $t_{\text{obs}} \gtrsim 10^4$ s for detecting the same signal with ET.

The optimal matched filter signal-to-noise ratio (Eq. 4.14) can also be used to estimate the distance out to which we can detect a signal. Figure 4.3 shows that with aLIGO at design sensitivity the furthest distance we can detect a signal with maximum likelihood parameters inferred from GRB140903A is 40 and 4 Mpc for $\epsilon = 10^{-2}$ and 10^{-3} respectively, while with ET the distances are 900 Mpc and 90 Mpc respectively. As we showed in Sec. 4.2.1, for the parameters inferred from GRB140903A only an ellipticity $\epsilon \leq 10^{-3}$ is physical,
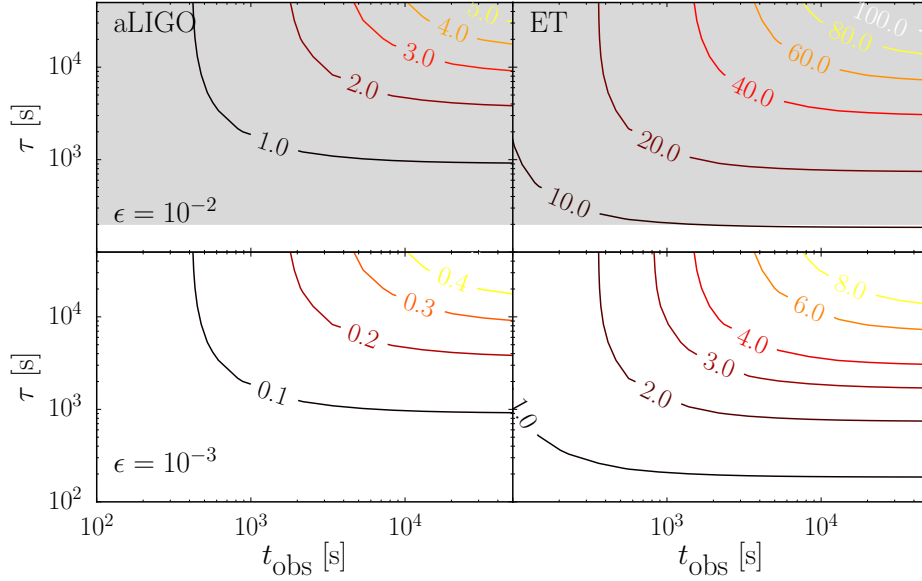
FIGURE 4.2: Optimal matched-filter signal-to-noise ratio ρ_{opt} for a typical SGRB post-merger signal at a distance of 40 Mpc as a function of the gravitational-wave observation time t_{obs} and the spin-down timescale of the system. The left panels shows ρ_{opt} for aLIGO with $\epsilon = 10^{-2}$ (top panel) and $\epsilon = 10^{-3}$ (bottom panel). The right panels show the same but for ET. The shaded region is nonphysical as the implied gravitational-wave energy emitted by the neutron star is greater than the available energy budget (see Sec. 4.2.1). A $\rho_{\mathrm{opt}} > 4.4$ is considered detectable.

post-merger remnants with longer spin-down timescale, τ, can be detected to larger distances assuming that $\epsilon \sim 10^{-3}$ is physical for those parameters.

The optimal matched filter is the maximum signal-to-noise ratio one can achieve in a matched filter search. In practice, this limit is unobtainable with current computational resources. As shown by Fig. 4.2 and Fig. 4.3, to achieve $\rho_{\mathrm{opt}} \geq 4.4$ and make a detection of gravitational waves, we need to observe a signal for at least $\sim 10^4$ seconds with aLIGO at design sensitivity. At large observation times, the volume of parameter space imposed by uniform priors becomes unfeasible for a realistic gravitational-wave search (see Sec. 4.4). In the following section, we demonstrate how to constrain the priors, and hence the search parameter space, using X-ray observations of SGRBs

4.3 X-ray afterglow

Short gamma-ray bursts are often followed by X-ray emission lasting up to many tens of thousands of seconds (Rowlinson et al., 2010, 2013; Lasky et al., 2017; Lü et al., 2015). Such an X-ray afterglow was not observed for
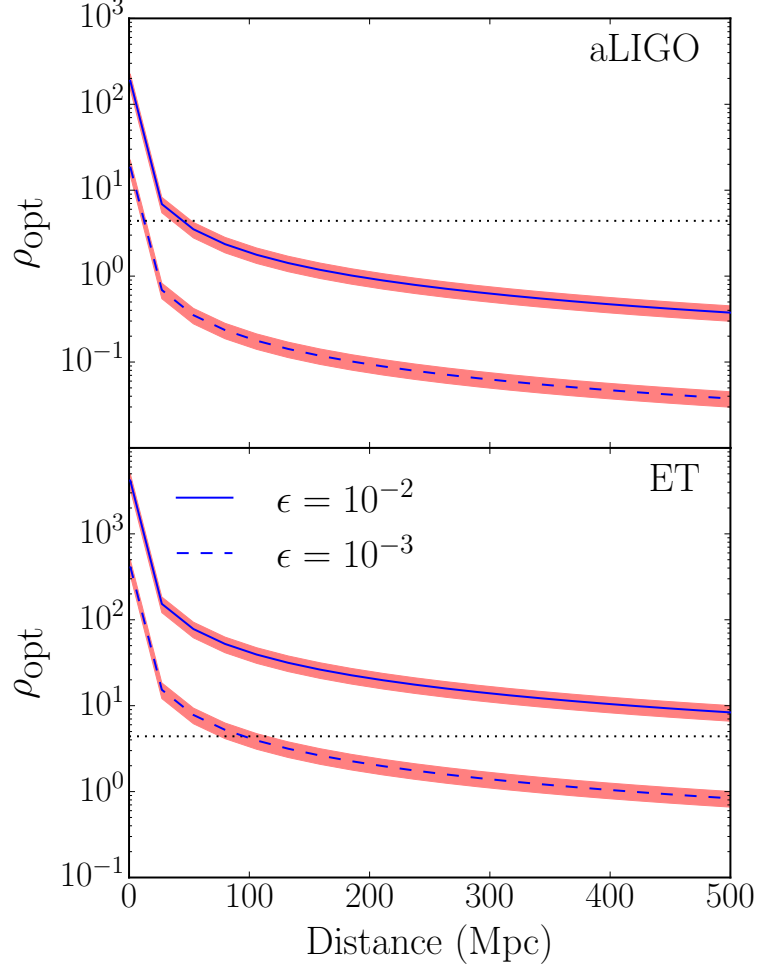
FIGURE 4.3: The optimal matched-filter signal-to-noise ratio ρ_{opt} as a function of distance for a millisecond magnetar inferred from GRB140903A for aLIGO (top panel) and ET (bottom panel) for two different ellipticities; $\epsilon = 10^{-2}$ (solid curves) and $\epsilon = 10^{-3}$ (dashed curves). The red shaded region indicates the 2σ confidence interval from the posteriors shown in Fig. 4.5. A threshold $\rho_{\mathrm{opt}} = 4.4$ is indicated by a black horizontal dotted line. Any value above this threshold is detectable by aLIGO at design sensitivity. All curves are constructed using an observation time of 5×10^{4} s.

GRB170817A. In Fig. 4.4 we show the X-ray afterglow of GRB140903A with data from the Neil Gehrels *Swift* and Chandra satellites (Troja et al., 2016). Rowlinson et al. (2013) modelled the X-ray afterglows of several SGRBs with
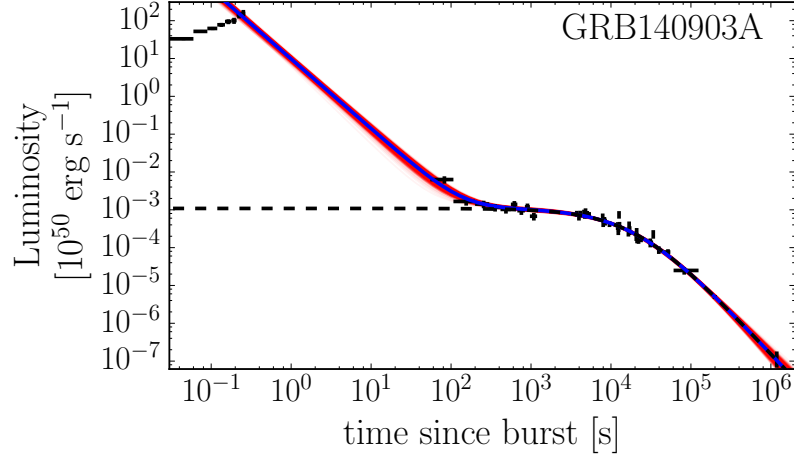
FIGURE 4.4: γ and X-ray lightcurves for GRB140903A. Black points are data from *Swift* and Chandra satellites. The blue curve shows the maximum likelihood model described in Sec. 4.3. The dark red band is the superposition of 800 models randomly drawn from the posterior distribution (shown in Fig. 4.5). The dashed black curve is the model for the luminosity from the nascent neutron star (Eq. 4.16).

two components. Firstly, an initial power-law decay,

$$L(t) = At^{-r}, \tag{4.15}$$

where L is the luminosity, A is the power-law amplitude, and r is the power-law exponent. Here, the decay exponent can be fixed to $r = \Gamma_\gamma + 1$, where Γ_γ is the photon index of the prompt emission, or allowed to vary. The second component is a luminosity law to model the energy injection from a millisecond magnetar that is spinning down through magnetic dipole radiation ($n = 3$) (Zhang & Mészáros, 2001; Dai & Lu, 1998). Lasky et al. (2017) extended this model to include other forms of radiation causing spin-down, which is derived by utilising the general torque equation (Eq. 4.1). The luminosity of the second component therefore comes directly from the nascent neutron star, and can be expressed as

$$L(t) = L_0 \left(1 + \frac{t}{\tau}\right)^{\frac{1+n}{1-n}}, \tag{4.16}$$

where, L_0 is the initial luminosity at the onset of the plateau phase and is related to the initial gravitational-wave frequency $f_{\mathrm{gw},0}$ by

$$L_0 = \frac{f_{\mathrm{gw},0}^2 \pi^2 I_{zz} \eta}{2\tau}, \tag{4.17}$$

where η encodes the efficiency of converting spin-down energy to X-rays. Our numerical model involves fitting Eq. (4.15) and (4.16) to the X-ray observations from *Swift* and Chandra. However, instead of fitting L_0 we fit our initial gravitational-wave frequency $f_{gw,0}$. We use a Markov Chain Monte Carlo algorithm (Foreman-Mackey et al., 2012) to fit the X-ray afterglow of SGRBs with our model using uniform priors for f_{gw}, n, τ, A, and r between $[\log_{10}(-1), \log_{10}(5)]$, $[\log_{10}(2), \log_{10}(6)]$, $[0, 6]$, $[\log_{10}(-10), \log_{10}(5)]$, and $[-2, 5]$ respectively. Fits we have made to GRB140903A are shown in Fig. 4.4. We determine the posterior distribution on our parameters $f_{gw,0}$, τ, and n which are shown in Fig. 4.5. In the following section, we discuss how these posteriors can be used as priors for a targeted search for the post-merger remnant associated with an SGRB.
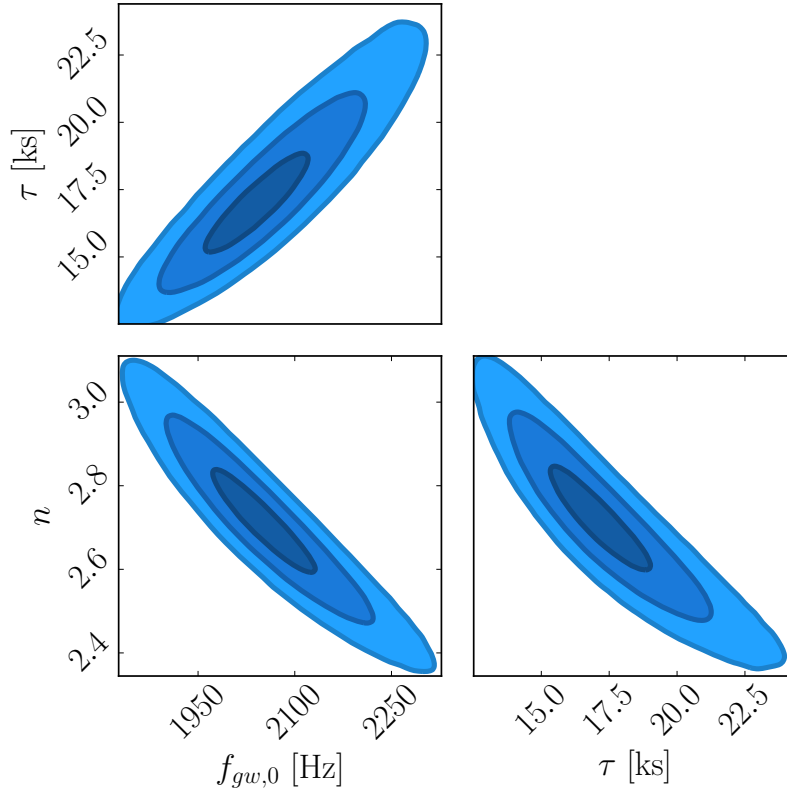
FIGURE 4.5: Posterior distribution for $f_{gw,0}$, n, and τ for GRB140903A. These posteriors are used as priors to build a GRB specific template bank. Shown are one-,two-, and three-sigma confidence levels. This figure is generated using the ChainConsumer software package (Hinton, 2016).

4.4 Gravitational-wave search pipeline

Here we describe a pipeline to search for gravitational waves from a spinning down millisecond magnetar. The algorithm can be summarised as follows:

1. Generate posterior distributions on the three waveform parameters $f_{\rm gw,0}$, n and τ using the X-ray afterglow observations of a specific SGRB as described in Sec. 4.3.

2. These posterior distributions, along with uniform priors on Φ_0 and $\cos \iota \in [0,1]$, serve as priors for our waveform model. Template waveforms are generated from points in these priors.

3. Templates are used to calculate the matched filter signal-to-noise ratio using LIGO data at the time of the SGRB.

The same pipeline can also be adopted with unconstrained uniform priors in step 1, in the case where no X-ray data is available. However, the number of templates required for a matched-filter search becomes computationally unfeasible. We quantify this throughout this section.

We calculate the fitting factor *FF* (Apostolatos, 1995), also commonly referred to as the overlap (e.g., Cornish, 2012). The fitting factor is the penalty in signal-to-noise ratio one suffers due to comparing templates that do not precisely match the signal: $FF = \rho/\rho_{\rm opt}$. We want to minimize this penalty while maximizing the signal-to-noise ratio.

To calculate the *FF* we randomly draw one value of each parameter from our priors and construct a model waveform using the waveform model described in Sec 4.2. We assume this is our true template, $h_{\rm T}$. We determine the optimal matched filter signal-to-noise ratio for this template using Eq. (4.14), We randomly draw from our priors excluding our 'true template' and create a random template, h_i, where i labels the ith drawn sample. We compute the matched filter signal-to-noise ratio (Eq. 4.12), ρ_i. We calculate ρ_i for N random templates. In the limit of infinite templates, $\max(\rho_{\rm i}) \to \rho_{\rm opt}$.

The maximum fitting factor is defined as

$$FF = \frac{\max(\rho_{\rm i})}{\rho_{\rm opt}}, \tag{4.18}$$

where $\max(\rho_{\rm i})$ is the maximum matched-filter signal-to-noise ratio from a population of N templates. In the limit of an infinite number of templates, $FF \to 1$, assuming our signal parameters are within our template parameter space. Creating a large number of templates is computationally expensive. We therefore want to minimise the number of templates we need. Additionally, we want to maximise our signal-to-noise ratio by creating templates for a longer duration.

In Fig. 4.6 we show the scaling of *FF* with the number of templates in the template bank for different $t_{\rm obs}$ and two different priors: an unconstrained uniform prior (left panel) where the priors on $f_{\rm gw,0}$, n and τ are $[500, 3000]$
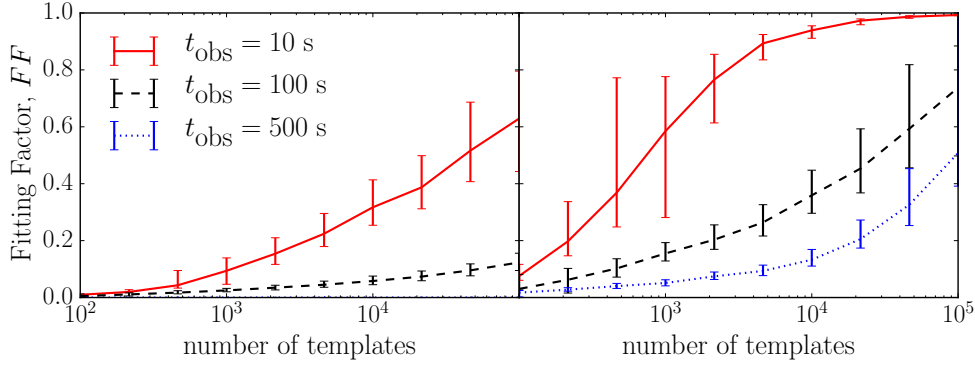
FIGURE 4.6: The fitting factor (*FF*) as a function of the number of templates with unconstrained parameter priors (left panel) and priors constrained by X-ray afterglow observations (right panel) for observation times $t_{\mathrm{obs}} = 10$ seconds (solid lines), $t_{\mathrm{obs}} = 100$ seconds (dashed lines), and $t_{\mathrm{obs}} = 500$ seconds (dotted lines). The error-bars indicate one sigma.

Hz, $[2.5, 5]$ and $[350, 35000]$ s, respectively, and the constrained posterior priors from using X-ray afterglow observations (right panel). The error bars indicate one sigma confidence levels, generated by repeating the analysis with 1000 different noise realizations.

Figure 4.6 shows that for 10^5 templates, $FF = 0.62$ for $t_{\mathrm{obs}} = 10$ s with uniform priors. A fitting factor $FF = 0.62$ implies that we lose 38% of the optimal matched-filter signal-to-noise ratio when running a matched-filter search. This recovery percentage is even worse for longer observation times, with $t_{\mathrm{obs}} = 100$ s having $FF = 0.12$ for uniform priors with 10^5 templates, indicating we lose 88% of the optimal matched-filter signal-to-noise ratio. Although *FF* scales up for an increasing number of templates, the amount of templates required to construct a search that could detect potential signals is unfeasible computationally for uniform priors. Furthermore, as shown in Sec. 4.2, real astrophysical signals likely require $t_{\mathrm{obs}} > 1000$ s, and *FF* at these t_{obs} is significantly worse. Fortunately, *FF* is comparatively better for constrained priors (right panel). For example, for $t_{\mathrm{obs}} = 100$ seconds with 10^5 templates, $FF = 0.72$ with constrained priors as opposed to 0.12 with uniform priors. In a real search we will likely require $t_{\mathrm{obs}} > 10^3$ seconds and 10^6 templates. We have not calculated the *FF* for these parameters as it is computationally expensive and requires an optimization step in the template generation to avoid using the high sampling frequencies throughout that are required at the beginning of the waveform. Furthermore, for aLIGO, detectable astrophysical signals require large τ values which are ruled out by the energy budget constraint; see Sec. 4.2.1. In addition, constructing searches with observation times significantly larger than τ gives worse results as one no longer accumulates significant signal-to-noise for $t \gg \tau$. Noting the scaling observed in *FF*, we expect $FF \approx 0.4$ for $t_{\mathrm{obs}} = 10^4$ seconds with 10^6 templates, an acceptable loss considering the gains from a longer signal duration.

We calibrate our pipeline by injecting signals into Gaussian noise coloured to match that of the expected strain sensitivity. This calibration is parameter dependent, so in a real search, we will need to do this for each SGRB. We use the posteriors from GRB140903A to create a fake signal. In Sec. 4.2 we used the optimal matched filter signal-to-noise ratio (Eq. 4.14) to determine an optimistic estimate for the distance out to which we can detect a signal (shown in Fig. 4.3). These distances are optimistic, and as we quantified with *FF*, we suffer a loss in signal-to-noise due to having imperfect templates.

We define a horizon distance as the distance to which a detector with a given sensitivity can observe events with a given significance in a real matched-filter search. We start with the matched filter signal-to-noise ratio ρ (Eq. 4.12) We determine a signal-to-noise ratio threshold $\rho_{\text{threshold}}$, which is the minimum signal-to-noise ratio to claim a detection with aLIGO at design sensitivity with a single detector. To determine this threshold, we calculate ρ using Eq. (4.12) with noise-only realisations ($s = 0$) and for N templates. We take the maximum ρ from N templates and do this for multiple realisations of noise retaining the maximum ρ each time. We determine the 99.7 percentile of our probability distribution on ρ with no signal, which indicates that 99.7 % of the time noise can mimic a signal (a false alarm). Any detection needs $\rho > \rho_{\text{threshold}}$ to be significant. For our pipeline, the 3σ $\rho_{\text{threshold}}$ is 4.4 with 10^4 templates and 1000 realisations of noise, however the choice of this false-alarm rate is arbitrary.

We also establish a false dismissal probability, which quantifies when a real signal present in the data cannot be disassociated from the noise. As a result, it fails to be identified. To determine a horizon distance, we find the distance where our false dismissal probability is less than 10 %, which is done by repeating the procedure for determining $\rho_{\text{threshold}}$, but injecting signals at fixed distances. We then determine at what distance less than 10 % signals have $\rho < \rho_{\text{threshold}}$.

Prior to this point, we have only considered a single detector; the signal-to-noise ratio grows approximately in quadrature for a network of N similar detectors and therefore having an aLIGO-Virgo triple detector network will increase the horizon distance accordingly. In the future, with a network of 3G detectors such as ET and Cosmic Explorer, a similar increase in signal-to-noise ratio can be expected. Other factors such as sky localization and time-varying F_+ and $F_\times$ will also affect the horizon distance. Considering these factors, in a real search we can expect our horizon distance for a GRB140903A inferred post-merger signal to be half the optimal matched-filter distance indicated by Fig. 4.3 as ~ 2 and ~ 45 Mpc for $\epsilon = 10^{-3}$ for aLIGO and ET respectively.

4.5 Conclusion

We have developed an algorithm to search for gravitational waves from a long-lived post-merger remnant of a binary neutron star merger. In Sec. 4.2, we derive a waveform model for gravitational waves emitted from a spinning down millisecond magnetar. We detail and analyze a matched filter detection pipeline using this waveform model. We find that using X-ray observations from SGRB afterglows results in a significant decrease in parameter space resulting in a much improved and targeted search for a post-merger remnant. These X-ray guided priors can also be applied in other post-merger search pipelines. Our analysis indicates for an ellipticity $\epsilon = 10^{-2}$ our pipeline can, in principle detect gravitational waves with aLIGO at design sensitivity out to ~ 20 Mpc for a fiducial moment of inertia 10^{45} g cm^2. If one ignores the energy-budget constraint, this fiducial value implies a conservative limit on the gravitational-wave strain and therefore horizon distance. In reality, the moment of inertia of the remnant may be a factor few larger than this fiducial value; as the strain scales linearly with the moment of inertia, this implies the horizon distance may also be a factor of a few larger. However, when including the energy-budget constraint, the horizon distance implied by a higher moment of inertia is lower due to the inverse relationship between the moment of inertia and the ellipticity.

It is the energy-budget constraint that ultimately sets the distance to which these post-merger remnants can be detected. A large region of the parameter space is implausible, which lowers the horizon distance to ~ 2 Mpc for GRB140903A-like post-merger signals. The Einstein Telescope can detect a similar signal out to ~ 45 Mpc. Post-merger signals with longer spin-down timescale τ will be detectable out to larger distances.

We are also investigating a more realistic model. The waveform model introduced here is simplified as the model assumes the neutron star is an orthogonal rotator. In this state, the principal eigenvector of the moment of inertia tensor is orthogonal to the star's rotation axis making the star an optimal emitter of gravitational waves. The neutron star is possibly driven to this orientation through the spin-flip instability (Cutler, 2002; Mestel et al., 1981; Jones, 1976b), but the timescales involved are uncertain (Dall'Osso et al., 2015b,a; Lasky & Glampedakis, 2016). As the system is driven to orthogonalization, it emits gravitational waves which we can include in our waveform model. We also have not accounted for time-varying F_+ and $F_\times$ terms.

Another extension is to constrain our parameter space further by including information obtained through parameter estimation on the binary neutron star inspiral gravitational-wave signal. Specifically, we can constrain the inclination of the source which should increase the pipeline sensitivity. The X-ray afterglow observations also suggest an evolution of the braking index with time with the system evolving from gravitational-wave dominated spin-down to magnetic dipole. This evolution of the braking index

is something we can include in our model.

Chapter 5

Interpreting the X-ray afterglows of gamma-ray bursts with radiative losses and millisecond magnetars.

Abstract

The spin-down energy of millisecond magnetars has been invoked to explain X-ray afterglow observations of a significant fraction of short and long gamma-ray bursts. Here, we extend models previously introduced in the literature, incorporating radiative losses with the spin down of a magnetar central engine through an arbitrary braking index. Combining this with a model for the tail of the prompt emission, we show that our model can better explain the data than millisecond-magnetar models without radiative losses or those that invoke spin down solely through vacuum dipole radiation. We find that our model predicts a subset of X-ray flares seen in some gamma-ray bursts. We can further explain the diversity of X-ray plateaus by altering the radiative efficiency and measure the braking index of newly-born millisecond magnetars. We measure the braking index of GRB061121 as $n = 4.85^{+0.11}_{-0.15}$ suggesting the millisecond-magnetar born in this gamma-ray burst spins down predominantly through gravitational-wave emission.

5.1 Introduction

Cosmological gamma-ray bursts are the most energetic explosions in the Universe. They are historically split into two categories: long and short based

primarily on their observed T90 duration, i.e., the duration where 90% of the energy is released. Long gamma-ray bursts (T90 $\gtrsim$ 2 s) are typically associated with the collapse of massive stars and often accompanied by core-collapse supernovae such as the case for long gamma-ray burst GRB111209A and SN2011kl (Greiner et al., 2015). Short gamma-ray bursts (T90 $\lesssim$ 2 s) are associated with the merger of two compact objects such as a binary neutron star. The association of a binary neutron star merger with a short gamma-ray burst was confirmed by the coincident detection of short gamma-ray burst GRB170817A and gravitational waves from the binary neutron star inspiral GW170817 (Abbott et al., 2017; Abbott et al., 2017d).

Regardless of the progenitor, both long and short-duration gamma-ray bursts are accompanied by lower energy extended emission referred to as an afterglow. Traditionally, the origin of this afterglow has been attributed to the interaction of the relativistic outflow with the surrounding environment (e.g., Mészáros & Rees, 1993b; Piran, 1999; Sari et al., 1998; Meszaros, 1999; Zhang, 2007). These external-shock fireball models have been largely successful in interpreting the afterglows of a large fraction of broadband afterglows of gamma-ray bursts. However, more recently and in particular since the launch of the *Neil Gehrels Swift Telescope* (Gehrels et al., 2004), X-ray afterglows of gamma-ray bursts have been observed in significantly more detail highlighting potential problems for the external-shock models. In particular, two observed features of X-ray afterglows are problematic to explain with the fireball model; the extended plateau seen in $\approx$ 50% (e.g., Rowlinson et al., 2013) of gamma-ray burst afterglows and the sharp drop in luminosity seen in $\approx$ 20% (e.g., Gao et al., 2016). These observational features are well interpreted within the framework of additional energy injection from a rapidly-spinning, highly magnetic neutron star, referred to as a millisecond magnetar. Determining whether the central engine is a black hole or a neutron star has important implications for the nuclear equation of state, the progenitors and rates for fast radio bursts, and the jet-launching mechanism for gamma-ray bursts (see Kumar & Zhang (2015) and references therein).

Millisecond magnetars were first proposed by Usov (1992); Dai & Lu (1998); Zhang & Mészáros (2001) as a central engine for gamma-ray bursts. The millisecond-magnetars spin-down energy provides an additional energy source that powers the X-ray afterglow. Such a model has been broadly successful in explaining the two aforementioned observational features (e.g., Fan & Xu, 2006; Rowlinson et al., 2010, 2013; Dall'Osso et al., 2011; Lü et al., 2015; Lasky et al., 2017); the plateau, which is sustained through the additional energy injection, and the sharp drop in luminosity, which is attributed to the collapse of these rapidly-spinning neutron stars into black holes (e.g., Rowlinson et al., 2010; Lasky et al., 2014; Sarin et al., 2020b).

Although broadly successful in explaining these two features, the millisecond-magnetar model fails to explain other observations. For example, the magnetar model can only explain the X-ray afterglow and has no detailed prescription for emission in other electromagnetic bands which is

instead attributed to the external shock (e.g., Dall'Osso et al., 2011). This emission from the external shock is believed to be subdominant in the X-ray afterglow when a millisecond magnetar is active. This seems plausible as, in a subset of short gamma-ray bursts that have observations of a sharp drop, one can see the previously subdominant emission from the external shock again (e.g., Rowlinson et al., 2013; Sarin et al., 2020b). Ultimately, a complete model is needed which predicts the emission across the electromagnetic spectrum. Work by Metzger & Piro (2014); Strang & Melatos (2019) towards this goal assume that the energy from the spin down of the millisecond magnetar is dissipated through a wind, similar to a pulsar-wind nebula. However, such models have not been fit in detail to observations.

The spin down of a magnetar can be characterised by its braking index. Early efforts in modelling the X-ray afterglow with the magnetar model involved assuming the magnetar was spinning down solely through magnetic dipole radiation (Zhang & Mészáros, 2001; Fan & Xu, 2006; Rowlinson et al., 2013; Lü et al., 2015). This assumption is in contrast to observations that suggest newly-born magnetars spin down through the emission of gravitational waves (Fan et al., 2013; Gao et al., 2016; Sarin et al., 2020b). Under the assumption that the braking index is arbitrary but constant through time, Lasky et al. (2017) measured the braking index of two gamma-ray bursts. More recently, Şaşmaz Muş et al. (2019) measured the evolution of the braking index through the coupling of the braking index to the evolution of the magnetic inclination angle (see e.g., Lander & Jones, 2018). However, perhaps more critically, these works assume a constant efficiency in converting between the spin-down energy of the magnetar central engine and the resulting X-ray afterglow luminosity, assuming that $\sim 10\%$ of the central engine spin-down energy is converted into an X-ray luminosity. Given the diversity of gamma-ray burst afterglows and their environments, it is difficult to conceive of all systems behaving in the same way through time and with the same efficiency.

The idea of a non-constant and/or distinct efficiency has been explored previously. Xiao et al. (2019) model the efficiency as dependent on the luminosity of the central engine itself i.e., $\eta_{\text{x-ray}} \propto L_{\text{magnetar}}$, where $\eta_{\text{x-ray}}$ is the efficiency and L_{magnetar} is the luminosity of the magnetar. This suggests that during the plateau phase, the efficiency stays constant as the luminosity of the millisecond magnetar is roughly constant, while at late times the efficiency drops following the drop in luminosity from the central engine. Another approach to account for efficiency is by considering the effect of radiative losses due to the deceleration of the shock in the interstellar medium (Cohen et al., 1998; Cohen & Piran, 1999). Dall'Osso et al. (2011) developed such a model where they considered the effect of radiative losses for a millisecond magnetar spinning down solely through vacuum dipole radiation, a model that has since been fit to several gamma-ray burst afterglows assuming the magnetar emission has an angular structure (Stratta et al., 2018).

Here, we extend the model from Dall'Osso et al. (2011) by including spin down through an arbitrary braking index and by incorporating the emission

from the tail of the prompt. We fit our model to a sample of well-studied long and short gamma-ray bursts that have been previously suggested to have millisecond magnetar central engines. We find that our model can explain some X-ray flares seen in the X-ray afterglow of some gamma-ray bursts, and is a better fit to the data than millisecond magnetar models used currently in the literature. In the process, we also measure the braking index of these millisecond magnetars. We introduce our model for a millisecond-magnetar spinning down through arbitrary braking indices and including radiative losses in Sec. 5.2. We then present our results for a small subset of long and short gamma-ray bursts in Sec. 5.3. We discuss the implications of our results and conclude in Sec. 5.4 and 5.5 respectively.

5.2   Model

We model the emission in the X-ray afterglow of the gamma-ray burst to be a combination of energy injection from a newly born millisecond magnetar interacting with the surrounding environment resulting in radiative loss (Cohen & Piran, 1999) and incorporating the emission from the tail of the prompt. As mentioned in Sec. 5.1, such a model without the inclusion of the emission from the tail of the prompt and assuming the magnetar spins down solely through vacuum dipole radiation was introduced by Dall'Osso et al. (2011). Our extension to this model starts by generalising the spin down of the magnetar through an arbitrary braking index such that $\dot{\Omega} \propto \Omega^n$. Here, Ω and $\dot{\Omega}$ are the neutron stars angular frequency and its derivative respectively, and n is the braking index. This generalisation allows one to write the luminosity of a millisecond magnetar spinning down through an arbitrary braking index (Lasky et al., 2017),

$$L_{\text{sd}}(t) = L_0 \left(1 + \frac{t}{\tau} \right)^{\frac{1+n}{1-n}}. \tag{5.1}$$

Here, L_{sd} is the spin-down luminosity of the magnetar, t is the time since burst, and τ is the spin-down timescale. The spin-down energy of the magnetar is subject to some radiative loss at the shock interface, which implies (Dall'Osso et al., 2011),

$$\frac{dE}{dt} = L_{\text{sd}} - \kappa \frac{E}{t}. \tag{5.2}$$

Here,

$$\kappa = 4\epsilon_e \frac{d \ln t^*}{d \ln t}, \tag{5.3}$$

is the radiative efficiency, ϵ_e is the fraction of total energy transferred to the electrons, and $d \ln t^* / d \ln t$ describes the dynamical evolution of the shock where t^* is the time in the reference frame of the central engine where the

energy is transferred into the shock. In Eq. (5.2), the first term on the right-hand side captures the energy injection from the spin down of the neutron star central engine, while the second term captures radiative losses at the shock interface. The lightcurve as seen by a distant observer is then,

$$L(t) = At^\Gamma + \mathcal{H}(t - t_0)\kappa \frac{E(t, t_0)}{t}. \tag{5.4}$$

Here, $E(t, t_0)$ is the solution to Eq. (5.2), t_0 is the time at which the observer starts to see the emission from radiative losses, A and Γ are the power-law amplitude and power-law exponent, respectively, which together describe the emission from the tail of the prompt. A lower limit on t_0 is the afterglow onset time, i.e., the time it takes the blast wave to reach the deceleration radius (e.g., Sari et al., 1998, 1999).

The tail of the prompt emission is the power-law decay in flux associated with the curvature effect. Photons emitted at the same time but at different latitudes within the jet opening angle will arrive at the distant observer at different times due to propagation effects, resulting in a steep temporal decay (e.g., Kumar & Panaitescu, 2000; Zhang et al., 2006). The tail of the prompt therefore marks the transition from the prompt emission phase to the afterglow emission. Furthermore, given typical X-ray afterglows do not show an early rise, the afterglow onset time and the associated rise in flux is likely hidden by the emission from the tail of the prompt. We note that previous works involving radiative losses did not include the tail of the prompt emission in their fit to minimise fitting parameters (Dall'Osso et al., 2011; Stratta et al., 2018). In later sections, we show that the inclusion of the tail of the prompt and radiative loss subject to energy injection from a newly-born neutron star can explain several interesting aspects of gamma-ray burst X-ray afterglows.

5.3 Results

We fit our model (Eq. 5.4) to the X-ray afterglow of a small sample of short and long-duration gamma-ray bursts observed by *Swift* using the nested sampler DYNESTY (Speagle, 2020) through the Bayesian inference library BILBY (Ashton et al., 2019) and a Gaussian likelihood. Our selection of gamma-ray bursts are chosen as their X-ray afterglow has a shallow decay phase indicative of central engine activity.

For our sample of gamma-ray bursts, we use the $0.3 - 10$ keV flux from the *Swift* database using the automatic binning strategies (Evans et al., 2009, 2010a). We convert the flux into luminosity using CIAO (Fruscione et al., 2006) performing k-corrections (e.g., Bloom et al., 2001). The gamma-ray bursts analysed, their associated redshifts and T90 durations are summarised in Table 5.1. For gamma-ray bursts without a measured redshift, we assume a

TABLE 5.1: Gamma-ray bursts analysed along with their associated T90 duration and redshift.

GRB	T90(s)	Redshift
GRB050319	152.5	3.24
GRB051221A	1.4	0.547
GRB060313	0.7	N/A
GRB060729	115.3	0.54
GRB061121	81.3	1.314
GRB070809	1.3	0.2187
GRB080430	16.2	0.767
GRB111020A	0.4	N/A

fiducial redshift $z = 0.75$ so that our model can be fit to luminosity data.

By including the effect of spindown through an arbitrary braking index we have introduced a new model for explaining X-ray afterglows of gamma-ray bursts. However, a pertinent question to consider: is the data better explained by the model? We answer this question through Bayesian model selection following the procedure in Sarin et al. (2019). We perform model selection for two models: a millisecond-magnetar model with an arbitrary braking index (Eq. 5.1) and the radiative losses model introduced here.

Our priors for the different models are listed in Table 5.2. We note that we used the same priors for all gamma-ray bursts except GRB051221A and GRB070809 which both have a narrower prior on t_0 to ensure the sampler converges to the correct mode. This tighter prior choice implies that the effect of radiative losses, and by extension the afterglow onset, occurs earlier in these short gamma-ray bursts. In reality, t_0 should be informed by considering the spectra of the gamma-ray burst itself. The transition from the tail of the prompt to the afterglow will be marked by a spectral change which then provides a tight constraint on t_0. However, given the difficulty in identifying a spectral change in gamma-ray burst data and the additional fitting required we use a more agnostic prior. The Bayes factors[1] for our analysis are shown in Table 5.3. Typically, a Bayes factor $\gtrsim 100$ is considered to be decisive (Kass & Raftery, 1995). The corner plots showing the one and two-dimensional posterior distributions for all gamma-ray bursts are available online (Sarin, 2020). We find that all eight gamma-ray bursts analysed favour the inclusion of radiative losses over the magnetar model. The weakest support comes from GRB070809 which has a weak preference for the radiative losses model. In other words, for this gamma-ray burst, the inclusion of the additional radiative losses physics does not provide a significantly better fit to the data. This weak preference may indicate that the effect of radiative losses is negligible in this gamma-ray burst or that more simply, there is insufficient data to probe the effects of this model. We return to this point in Sec 5.4.

---

[1]For clarity, we note that $BF_{a/b} = 2$ indicates model a is twice as likely as model b.

TABLE 5.2: Priors for the radiative losses model with spindown through an arbitrary braking index ($\mathcal{M}_{\text{rad-loss}}$). The priors for the millisecond magnetar model ($\mathcal{M}_{\text{mag}}$) are identical except for κ, t_0 and $\log_{10} E_0$ which are parameters not applicable to this model. We note that a LogUniform prior is a prior that is uniform in log-space.

Parameter [Units]	$\mathcal{M}_{\text{rad-loss}}$
$A\,[10^{50}\,\text{erg}]$	LogUniform$[10^{-10}, 10^{15}]$
Γ	Uniform$[-7, 1]$
$L_0\,[10^{50}\,\text{erg}]$	LogUniform$[10^{-5}, 1]$
$\tau\,[\text{s}]$	LogUniform$[10^2, 10^7]$
n	Uniform$[1.1, 7]$
κ	LogUniform$[10^{-3}, 4]$
$t_0\,[\text{s}]$	Uniform$[30, 400]$
$\log_{10} E_0$	Uniform$[-10, 2]$

TABLE 5.3: Gamma-ray bursts analysed along with the $\ln BF$ for the radiative losses (Eq. 5.4) model compared with the magnetar model (Eq. 5.1)

GRB	$\ln BF_{\mathcal{M}_{\text{rad-loss}}/\mathcal{M}_{\text{mag}}}$
GRB050319	3.1
GRB051221A	160.2
GRB060313	183.7
GRB060729	141.2
GRB061121	241.2
GRB070809	0.3
GRB080430	51.4
GRB111020A	93.9

5.3.1   X-ray flares

Flares are fast-rising then exponentially decaying features seen in several long and short gamma-ray bursts. While more prevalent in long-duration gamma-ray bursts, they have been observed in several short gamma-ray bursts as well, suggesting the mechanism behind them may be universal (e.g., Perna et al., 2006). However, they are also diverse and no one mechanism can successfully interpret the different characteristics (e.g., Kumar & Zhang, 2015).

A subset of flares are seen at the onset of the X-ray afterglow of a large fraction of gamma-ray bursts (O'Brien et al., 2006). Here, the onset of the afterglow marks the transition from the steep decay attributed to the tail of the prompt emission. A flare near this transition is difficult to explain with an external shock origin, and has been suggested to require central engine activity (Zhang et al., 2006), or specifically in the case of short gamma-ray bursts, magnetic reconnection events (Fan et al., 2005).

We find that our model can explain these flares as the breakout of excess energy in the relativistic blast wave at the onset of the afterglow. Here specifically, the flare is the product of the excess energy and transition to emission described by radiative losses with a millisecond magnetar central engine (i.e., the transition to the second term on the right-hand side in Eq. 5.4). The size of the flare is related to the amount of energy that is in the relativistic blast wave at the onset of radiative losses. The decay indices of the flare itself are determined by the radiative efficiency κ; in general, smaller κ produce more gradually decaying flares. Although this mechanism can successfully explain the diversity in size and decay index of flares seen in gamma-ray bursts, it likely cannot explain multiple flaring episodes. The excess energy will likely only generate one flare and such a flare will occur at the onset of the afterglow emission implying that other flares must be generated differently. Flares that occur later in the X-ray afterglow may also be products of radiative losses and excess energy but to explain such features the energy injection mechanism will need to be modified from the model we have used (Eq. 5.1).

In Figure 5.1, we show our fit to two short gamma-ray bursts, GRB060313 and GRB111020A which have flares near the transition of the tail of the prompt and the afterglow. Our model successfully explains the flare size and decay while also being a good fit for the rest of the data. In particular, GRB111020A has a bi-modality in the location of the flare. This is a product of the uncertainty in t_0 (i.e., the time where radiative losses turn on) given the sparsity of the data near the flare this parameter is poorly constrained, resulting in a bi-modality in when the flare occurs. Given the magnetar model without radiative losses (Eq. 5.1) cannot explain flares, it is not surprising that both these gamma-ray bursts strongly favour the radiative losses model (see Table 5.3).
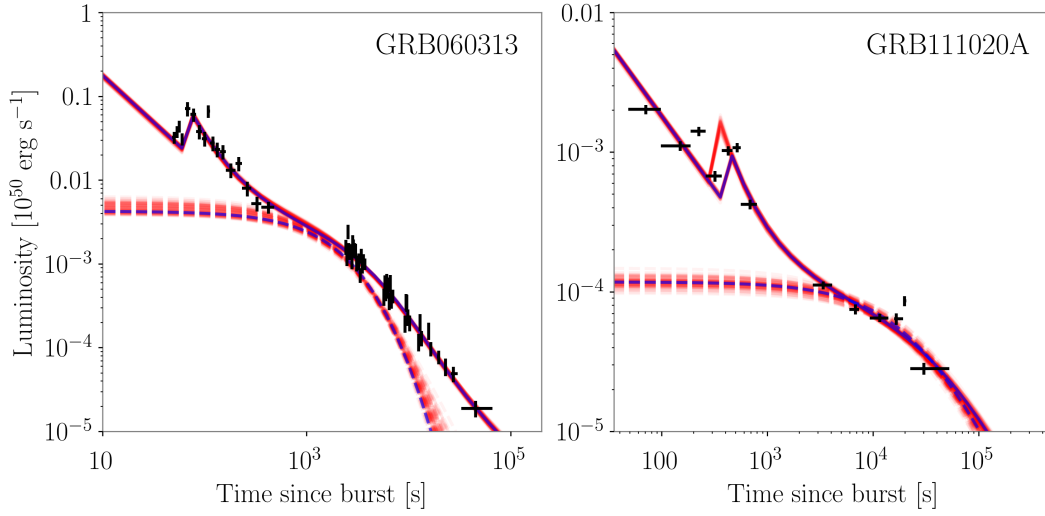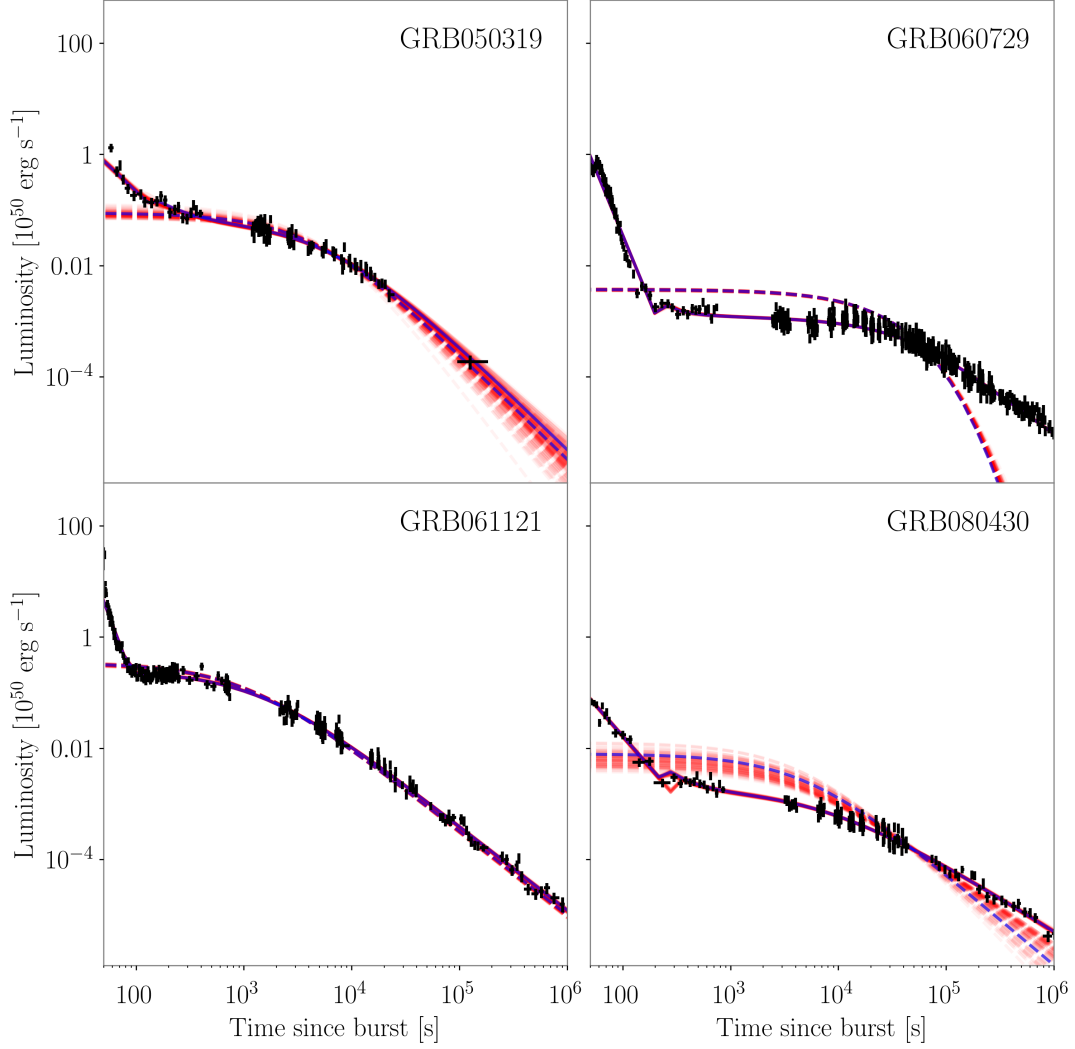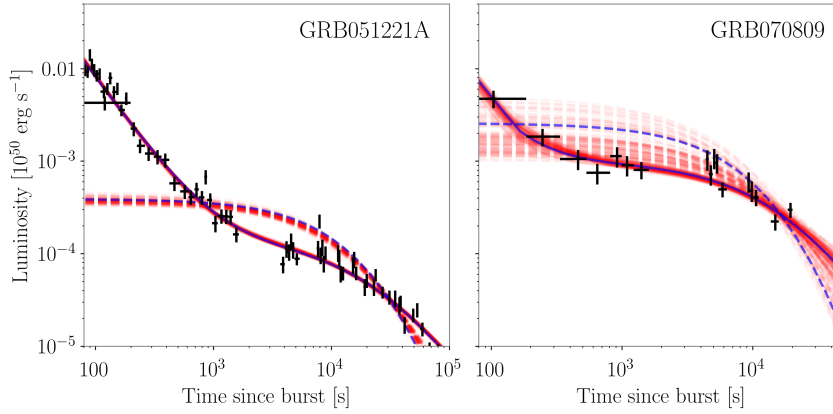
FIGURE 5.1: X-ray lightcurves for two short gamma-ray bursts. Black points indicate data from *Swift*. The blue curve shows the maximum likelihood model for the radiative losses model (Eq. 5.4). The dark red band is the superposition of 100 models randomly drawn from the posterior distribution. The flare seen in the onset of the plateau phase is naturally explained by the radiative losses model. We also show the underlying spin-down luminosity from the nascent magnetar in dashed lines.

5.3.2 Long gamma-ray bursts

Long gamma-ray bursts are associated with the collapse of massive stars. The afterglow of these bursts has been extensively studied, and for the vast majority of gamma-ray bursts, been largely in agreement with the predictions of the external shock model. A few gamma-ray bursts do, however, have sharp drops or plateaus indicative of a magnetar central engine (e.g., Troja et al., 2007; Lyons et al., 2010; Beniamini & Mochkovitch, 2017b), in particular, GRB050319, GRB060729, GRB061121, and GRB080430 (e.g., Dall'Osso et al., 2011; Xiao et al., 2019; Lü et al., 2019). These four gamma-ray bursts are well studied, partly due to their plentiful observations and have been fitted with the millisecond-magnetar model on numerous occasions (e.g., Dall'Osso et al., 2011; Xiao et al., 2019). Notably, the former included the effect of radiative losses with vacuum dipole radiation, while the latter assumed the X-ray luminosity is entirely from vacuum dipole radiation but the magnetar was spinning down through an arbitrary braking index.

We fit our model to these four aforementioned gamma-ray bursts, with our results shown in Figure 5.2. Since these gamma-ray bursts have plentiful observations, we are also able to constrain the inherent emission from the millisecond magnetar itself, which is shown as the dashed curves in Figure 5.2. We note that the inherent emission of the millisecond magnetar for GRB050319 and GRB061121 closely follows the observed lightcurve suggesting the impact of radiative losses is minimal. By contrast, GRB060729 and

GRB080430 show vast differences between the observed lightcurve and the inherent emission from the magnetar, suggesting radiative losses play a critical role. This impact of radiative losses is determined through κ, the radiative efficiency parameter, with lower values indicating radiative losses is more impactful. Why the impact of radiative losses is different in these gamma-ray bursts is an intriguing question, which we discuss in more detail in Sec 5.4. These gamma-ray bursts are all well fit by the radiative losses model and comparing Bayes factors (see Table 5.3), they strongly favour the inclusion of radiative losses over the magnetar model.

5.3.3   Short gamma-ray bursts

Short gamma-ray bursts are associated with the merger of compact objects. The multimessenger observations of GW170817 confirmed that binary neutron star mergers are the progenitors of some short gamma-ray bursts (Abbott et al., 2017d; Goldstein et al., 2017b). One of the motivations for determining whether millisecond magnetars exist in the aftermath of a short gamma-ray burst is to determine the maximum mass of neutron stars, and therefore the nuclear equation of state.

Unlike long gamma-ray bursts, short gamma-ray bursts from neutron star mergers have a well-defined progenitor mass distribution, motivated by the galactic double neutron star distribution (Kiziltan et al., 2013). However, the recent detection of GW190425 suggests the local binary neutron star distribution may be a poor representation of binary neutron stars mergers (Abbott et al., 2020a). Determining whether a short gamma-ray burst produced a black hole remnant or a millisecond magnetar can immediately inform the maximum mass. In reality, this is much more complicated as unless accompanied by gravitational waves from the inspiral, short gamma-ray bursts cannot alone provide a measurement for the maximum mass. For GW170817, the only coincident binary neutron star merger and short gamma-ray burst to date (GW190425 did not have any coincident electromagnetic observation (e.g., Coughlin et al., 2019; Hosseinzadeh et al., 2019)), there is still no strong consensus on the fate of the post-merger remnant (see Ai et al. (2019) for a review for the different possibilities).

We use our model to analyse the afterglow of two short gamma-ray bursts: GRB051221A and GRB070809. The former is a well-studied gamma-ray burst commonly associated with a millisecond magnetar central engine (Fan & Xu, 2006; Soderberg et al., 2006). However, it has been subject to significant debate with analysis by Lü et al. (2015) finding the afterglow to have a post-jet break index $\alpha \approx -1$ which is consistent with an external shock model or suggestive of magnetar spin down through gravitational-wave emission. We discuss this point in greater detail in Sec. 5.3.4. GRB070809 is another short gamma-ray burst with a plateau in the X-ray afterglow suggestive of a neutron star central engine. Furthermore, it was recently

FIGURE 5.2: X-ray lightcurves for four long gamma-ray bursts. Black points in-
dicate data from *Swift*. The blue curve shows the maximum likelihood model
for the radiative losses model (Eq. 5.4). The dark red band is the superposition
of 100 models randomly drawn from the posterior distribution. We also show
the underlying spin-down luminosity from the nascent magnetar in dashed lines.
For GRB050319 and GRB0601121 the observed emission closely follows the spin-
down luminosity of the nascent magnetar, while for GRB060729 and GRB080430
the observed luminosity is significantly different. This is direct consequence of
the different radiative efficiency κ for these gamma-ray bursts.

FIGURE 5.3: X-ray lightcurves for four long gamma-ray bursts. Black points indicate data from *Swift*. The blue curve shows the maximum likelihood model for the radiative losses model (Eq. 5.4). The dark red band is the superposition of 100 models randomly drawn from the posterior distribution. In dashed lines we show the underlying spin-down luminosity from the nascent magnetar.

identified to be associated with a blue kilonova counterpart (Jin et al., 2020) which naturally suggests a long-lasting neutron star central engine (e.g., Margalit & Metzger, 2017). We find that our model can successfully explain the observations of both gamma-ray bursts with our fits shown in Figure 5.3.

Comparing Bayes factors for both the model with radiative losses and without, we see that GRB051221A strongly favours the inclusion of radiative losses. Furthermore, while the observed lightcurve is consistent with a post-jet break index of $\alpha \approx -1$, the inherent emission from the millisecond magnetar is significantly different, implying a different braking index. We discuss this in more detail in Sec. 5.3.4. GRB070809 has a weak preference for the model including radiative losses. This may be indicative of the small effect of radiative losses for this gamma-ray burst, but given the relatively small amount of data, it is equally likely that the data cannot distinguish between the two models significantly. This is apparent when looking at the inherent emission from the millisecond magnetar for GRB070809.

5.3.4 Braking index

As discussed in Sec. 5.1, millisecond-magnetar models initially assumed the magnetar was spinning down solely through vacuum dipole radiation. This assumption was relaxed and used to measure the braking index of two millisecond magnetars born in GRB130603B and GRB140903A finding only the former to be consistent with $n = 3$ associated with vacuum dipole radiation (Lasky et al., 2017). Newly born millisecond magnetars are not expected to spin down solely through vacuum dipole radiation, instead, implying a significant amount of early gravitational-wave emission (e.g., Fan et al.,
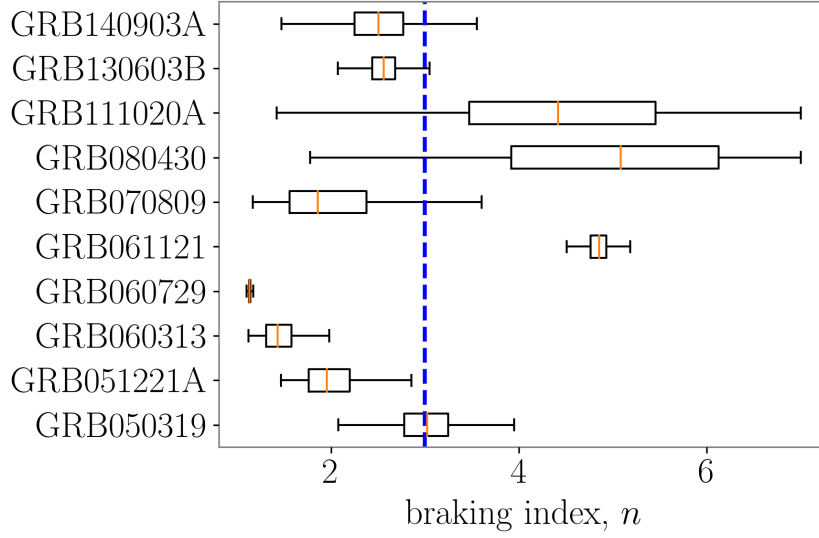
FIGURE 5.4: Measured millisecond magnetar braking indices for all gamma-ray bursts analysed in this paper and GRB140903A and GRB130603B with the radiative losses model (Eq. 5.4). The blue dashed line indicates $n = 3$, the braking index associated with vacuum dipole radiation.

2013; Gao et al., 2016; Sarin et al., 2020b). Furthermore, mechanisms such as twisted magnetosphere (e.g., Thompson et al., 2002), magnetic field axis evolution (e.g., Cutler, 2002) which are expected to be important in newly born millisecond magnetars (e.g., Lasky et al., 2017; Lander & Jones, 2018) all predict the braking index $n \lesssim 3$. Several more braking index measurements from gamma-ray bursts with putative millisecond magnetar central engines have been made (Xiao et al., 2019; Lü et al., 2019), however, none of these consider the effect of radiative losses.

In Fig 5.4, we show the braking index measurements with the radiative losses model for the eight gamma-ray bursts analysed in this paper. We also show the braking index measurement for the two aforementioned gamma-ray bursts, GRB130603B and GRB140903A which were measured previously (Lasky et al., 2017) but we revisit with the radiative losses model. In a simplistic view, the impact of radiative losses is to lower the braking index. The braking index is measured by the slope of the curve after the plateau phase ends, a shallower slope indicating a higher braking index. Inclusion of radiative losses means the shallower observations of the lightcurve can instead be explained by the radiative losses and therefore implies a steeper slope for the braking index.

For GRB051221A in particular, without the inclusion of radiative losses, we measure the braking index $n = 4.51^{+0.45}_{-0.38}$. Such a high braking index would imply a significant amount of energy released in gravitational waves at up to $\sim 10^5$ s post-formation. While not impossible, this is difficult to explain (e.g., Lasky & Glampedakis, 2016). However, by including radiative

losses, which is the preferred model, we measure $n = 1.96^{+0.38}_{-0.27}$ (68% confidence interval), alleviating this concern.

The braking index of GRB061121 is also intriguing, we measure $n = 4.85^{+0.11}_{-0.15}$ (68% confidence interval) with the radiative losses model which is consistent with the conclusion that the millisecond magnetar is spinning down predominantly through gravitational-wave emission. We do however caution that since this is a long gamma-ray burst, there may be additional effects, such as fall back accretion that may make such a measurement unreliable. At a redshift of $z = 1.314$, the gravitational-wave emission from such an object will not be observable individually in aLIGO or with third-generation telescopes such as the Einstein Telescope (e.g., Sarin et al., 2018). However, it does suggest that millisecond magnetars born in long gamma-ray bursts may spin down through gravitational-wave emission and that such a population of gravitational-wave sources may be observable as part of the stochastic gravitational-wave background.

5.4   Implications

The inclusion of radiative losses, the tail of the prompt, and the spin down through an arbitrary braking index can successfully explain several aspects of gamma-ray burst X-ray afterglows. The radiative efficiency κ controls the shape of the plateau and how much of the inherent emission from the central engine is directly visible to the observer. Higher values of κ imply the observed lightcurve closely follows the inherent emission from the millisecond magnetar, while smaller values of κ imply the effect of radiative losses is larger, and the observed lightcurve is visibly different from the emission from the millisecond magnetar. In general, we notice that gamma-ray bursts in a host galaxy with a higher density have smaller κ i.e., the impact of radiative losses is larger. This seems plausible as a denser medium likely means more radiative loss at the shock-interface. However, we leave the exploration of this correlation to future work with a larger selection of gamma-ray bursts.

Radiative losses can also explain the diversity in size and decay of X-ray flares seen at the onset of the afterglow. We have shown this for two gamma-ray bursts, GRB060313 and GRB111020A. In our model, the flare is a natural product of excess energy in the relativistic blast wave at the onset of the afterglow phase. Such a mechanism can only generate one flare, but we note that later flares may also be a product of radiative losses. However, modelling this will require a modification to the energy injection term we have used in this work.

In our model, κ encodes two terms; ϵ_e; the fraction of total energy transferred to electrons, and $d \ln t^* / d \ln t$, which describes the dynamical evolution of the shock. The dynamical evolution of the shock is difficult to constrain and requires detailed hydrodynamical modelling which would not be sufficiently fast making the fitting procedure computationally difficult. The former term is easier to probe, the afterglow emission from the external shock of a gamma-ray burst can provide a measurement for ϵ_e. Unfortunately, one cannot use the X-ray observations to make this measurement as owing to the putative magnetar, the external-shock emission is likely subdominant, and if not, it is difficult to decouple the emission from the central engine and one from the external shock. This motivates the need for a general model which includes the effect of both a millisecond magnetar and an external shock which we leave for future work. If one could measure ϵ_e independently, through the afterglow observation in another electromagnetic band, for example (Beniamini & van der Horst, 2017), this would allow the decoupling of the two terms in κ and direct measurement of the dynamical evolution of the shock. Under simple assumptions this could lead to a measurement of the decay index for the Lorentz factor and provide a complementary way of determining the structure of the jet. In this paper, we work only with the X-ray afterglow data and therefore cannot decouple the two parameters.

The radiative losses model introduced here can explain all the resolvable features in all eight gamma-ray bursts we have analysed. However, successfully fitting this model for all observed gamma-ray bursts is problematic. In particular, measuring t_0 is difficult, and given this parameter is co-variant with κ and E_0 makes analysing all gamma-ray bursts onerous. As mentioned previously, t_0 can be constrained by identifying the time of a spectral change which marks the transition from the prompt to the afterglow. In practice, this is difficult given the uncertainties on the data. Furthermore, given typical *Swift* slew times, it is often missed entirely. This problem of measuring t_0 can be alleviated if there are sufficient observations in the transition between the tail of the prompt and the plateau as for gamma-ray bursts analysed here. However, there are notable exceptions, such as GRB130603B which do not have such observations.

5.5 Conclusion

We have introduced a new model for the X-ray afterglow incorporating radiative losses at the shock interface with spin down of a magnetar central engine through an arbitrary braking index. By including this new model with emission from the tail of the prompt, we find we can naturally explain a variety of X-ray flares that produce an excess at the onset of the plateau phase. We find that radiative loss can explain both the diversity and sizes of such X-ray flares. In our model, these flares are the result of an energy breakout.

We also fit our model to a small subset of long and short gamma-ray bursts, the sample selected as they have extensive observations and have been previously suggested to have millisecond magnetar central engines. In the process, we measure the braking index of eight putative magnetars born in gamma-ray bursts. We find these braking indices to be lower than other works (e.g., Xiao et al., 2019; Lü et al., 2019), which did not take into account radiative losses and assumed that the X-ray luminosity is only generated through vacuum dipole radiation. We perform Bayesian model selection between our newly-derived model and one that does not take into account radiative losses, finding for all gamma-ray bursts analysed radiative losses can better explain the data.

We find that radiative loss can naturally explain the diversity of X-ray plateaus by altering the radiative efficiency κ which is a function of the hydrodynamical evolution of the shock and the fraction of total energy transferred to electrons. However, probing this further requires jointly fitting different electromagnetic bands with X-rays or developing a model that incorporates both the emission from the external shock and the emission from the central engine. We leave this extension, the exploration of the radiative efficiency, and application of this model to a larger catalogue of short and long gamma-ray bursts to future work.

Chapter 6

Gravitational waves or deconfined quarks: What causes the premature collapse of neutron stars born in short gamma-ray bursts?

Abstract

We infer the collapse times of long-lived neutron stars into black holes using the X-ray afterglows of 18 short gamma-ray bursts. We then apply hierarchical inference to infer properties of the neutron star equation of state and dominant spin-down mechanism. We measure the maximum non-rotating neutron star mass $M_{\mathrm{TOV}} = 2.31^{+0.36}_{-0.21} M_\odot$ and constrain the fraction of remnants spinning down predominantly through gravitational-wave emission to $\eta = 0.69^{+0.21}_{-0.39}$ with 68% uncertainties. In principle, this method can determine the difference between hadronic and quark equation of states. In practice, however, the data is not yet informative with indications that these neutron stars do not have hadronic equation of states at the 1σ level. These inferences all depend on the underlying progenitor mass distribution for short gamma-ray bursts produced by binary neutron star mergers. The recently announced gravitational-wave detection of GW190425 suggests this underlying distribution is different from the locally-measured population of double neutron stars. We show that M_{TOV} and η constraints depend on the fraction of binary mergers that form through a distribution consistent with the locally-measured population and a distribution that can explain GW190425. The more binaries that form from the latter distribution, the larger M_{TOV} needs to be to satisfy the X-ray observations. Our measurements above are marginalised over this unknown fraction. If instead, we assume GW190425 is not a binary neutron star merger, i.e the underlying

mass distribution of double neutron stars is the same as observed locally, we measure $M_{\mathrm{TOV}} = 2.26^{+0.31}_{-0.17} M_\odot$.

6.1   Introduction

The historic first detection of gravitational waves from a binary neutron star inspiral GW170817, ushered in a new era of gravitational-wave and electromagnetic multi-messenger astronomy (Abbott et al., 2017b,c; Savchenko et al., 2017; Goldstein et al., 2017a) and confirmed that binary neutron star mergers are the progenitors of some short gamma-ray bursts (see e.g., Abbott et al., 2017c). Short gamma-ray bursts are typically accompanied by lower energy broadband emission, commonly attributed to the interaction of the jet with the surrounding interstellar medium (e.g., Mészáros & Rees, 1993a; Piran, 1999; Sari et al., 1999; Granot et al., 1999; Mészáros, 2001b). However, the X-ray afterglow of some short gamma-ray bursts often exhibits two features that cannot be adequately explained by such an interaction; a plateau and steep decay hundreds to thousands of seconds after the burst (Zhang et al., 2006; Fan & Xu, 2006; Rowlinson et al., 2010, 2013; Lü et al., 2015). Although, there have been recent interpretations of sharp drops as a signature of a reverse shock (Beniamini & Mochkovitch, 2017a; Lamb et al., 2019). These features can be explained by a long-lived, rapidly-rotating, highly-magnetized neutron star (e.g., Dai & Lu, 1998; Zhang & Mészáros, 2001; Lasky et al., 2017; Sarin et al., 2019; Xue et al., 2019; Xiao et al., 2019; Strang & Melatos, 2019). A steep decay is attributed to the collapse of such a neutron star into a black hole (Troja et al., 2007; Rowlinson et al., 2010). Such supramassive neutron stars collapse because they are born above the non-rotating neutron star mass limit—the Tolman-Oppenheimer-Volkoff mass M_{TOV}—but collapse when they lose the additional centrifugal support required to prevent black hole formation. This is different to hypermassive neutron stars which collapse on shorter timescales (e.g., Lucca & Sagunski, 2019). In contrast, the observations of a plateau with no sharp drop are best interpreted as the signature of a stable long-lived neutron star, possible if the neutron star is born with mass below M_{TOV}.

Several authors have attempted to indirectly infer the neutron star equation of state given the aforementioned plateau and steep decay features. This is done through inferring the ratio of short gamma-ray bursts that produce supramassive or infinitely stable neutron stars (e.g., Lü et al., 2015), or by measuring the collapse time which is a function of the equation of state, the dominant spin-down mechanism, and the progenitor mass distribution (Lasky et al., 2014; Ravi & Lasky, 2014; Li et al., 2017b; Gao et al., 2016). The idea that the collapse time of these objects come from a distribution with the shorter than expected collapse time perhaps being an indication of gravitational-wave emission was suggested by Fan et al. (2013). Ravi & Lasky (2014) derived a theoretical collapse-time distribution

assuming supramassive neutron stars spindown predominantly through magnetic-dipole radiation, finding the four reliable collapse-time measurements at that time to be smaller, and seemingly at odds with the theoretical distribution. This discrepancy between the observed and theoretical distributions has been interpreted as evidence for two alternative hypotheses; the existence of deconfined quarks (Li et al., 2017b; Drago et al., 2016; Drago & Pagliara, 2018) or initial rapid spin-down through gravitational waves (Fan et al., 2013; Gao et al., 2016). The task of this paper is to determine which of these interpretations is correct.

We fit a collapsing neutron star model to the light-curves of all short gamma-ray burst X-ray afterglows observed by The Neil Gehrels *Swift* Telescope measuring the collapse time of 18 neutron stars born in short gamma-ray bursts. We perform Bayesian hierarchical inference to infer hyperparameters associated with the equation of state and dominant spin-down mechanism. This involves first, measuring the collapse time from the X-ray afterglow then inferring the parameters associated with the distribution of collapse times.

We measure $M_{\mathrm{TOV}} = 2.31^{+0.36}_{-0.21}M_\odot$; uncertainties here and throughout are 1σ unless otherwise stated. We constrain the fraction of neutron stars spinning down predominantly through gravitational-wave emission to $\eta = 0.69^{+0.21}_{-0.39}$, suggesting $\sim 70\%$ of these neutron stars spin down predominantly through gravitational waves. Although the gravitational waves emitted from these objects are likely not detectable individually, this constraint has important implications for the gravitational-wave stochastic background and the mechanisms which generate gravitational waves in these objects, such as the spin-flip or bar-mode instability. We also measure equation-of-state specific parameters which indicates that the data is best explained by quark star equation of states at the 1σ level.

These results all depend on the underlying binary neutron star mass distribution, which has been typically assumed to be the same as the galactic double neutron star mass distribution observed locally with radio. However, the gravitational-wave event GW190425 (Abbott et al., 2020a) is a massive binary neutron star merger with progenitor masses inconsistent with the local population. With a total mass $\sim 3.4M_\odot$, GW190425 may have formed dynamically rather than through isolated binary evolution or perhaps through case-BB common envelope phase (Abbott et al., 2020a). Conservatively, this suggests the neutron star binaries that merge to produce short gamma-ray bursts are a mixture of the locally observed binary neutron star mass distribution and a mass distribution that can explain GW190425.

We perform our analysis with a modified mass distribution that allows for a bimodal distribution consistent with all neutron stars in our galaxy. We parameterize this distribution with an unknown mixing fraction dictating the probability of neutron stars coming from the two aforementioned formation channels. Our results above are marginalised over this unknown mixing

fraction. If instead, we assume neutron star binaries that merge to produce short gamma-ray bursts are drawn equally from both distributions we measure $M_{\text{TOV}} = 2.30^{+0.38}_{-0.19} M_{\odot}$. If instead we assume a mixing fraction $\epsilon = 0$, i.e a distribution that can explain the progenitors of the locally observed binary neutron stars and GW170817 but one that cannot explain GW190425, then we measure $M_{\text{TOV}} = 2.26^{+0.31}_{-0.17} M_{\odot}$.

In this paper, we introduce our model for a collapsing magnetar and present the collapse-time probability distributions and lightcurves of 18 short gamma-ray bursts in Sec. 6.2. In Sec. 6.3 we derive our Bayesian hierarchical model. In Sec. 6.4 we show our results for the nuclear equation of state and spin-down mechanism and discuss the implications of our analysis. We discuss limitations and future extensions of our analysis and conclude in Sec. 6.5.

6.2   neutron star collapse times

Rapidly rotating, millisecond magnetars were first introduced as an alternative central engine for gamma-ray bursts (Dai & Lu, 1998; Zhang & Mészáros, 2001) and have been incredibly successful in interpreting the *Swift* X-ray afterglow observations of several short gamma-ray bursts (e.g., Fan & Xu, 2006; Rowlinson et al., 2010, 2013; Lü et al., 2015). The standard fireball-shock model governs the emission produced from the interaction of the jet with the surrounding interstellar medium. A model that has been modified in several ways to explain the plateau observations such as through the evolution of the microphysical parameters of the forward shock (Ioka et al., 2006), long-lived reverse shocks (Uhm & Beloborodov, 2007) and several other modifications (e.g., Toma et al., 2006; Oganesyan et al., 2019). However, these modifications cannot adequately explain the steep decay feature which is naturally included in the magnetar model as the signature of a neutron star collapsing into a black hole (e.g., Rowlinson et al., 2010).

Lasky et al. (2014) derived a model for the collapse time assuming these newly-born neutron stars spin down only through vacuum dipole radiation, which has been used to model the collapse time of several candidate neutron stars born in short gamma-ray bursts (e.g., Lü et al., 2016b). However, such modelling is fraught with difficulties with systematic uncertainties from k-corrections, restriction to modelling only for gamma-ray bursts with a measured redshift, and assumption of a vacuum dipole spin-down mechanism. The latter assumption is problematic as the braking index of two putative neutron stars born in GRB130603B and GRB140903A find only the former to be consistent with spindown through dipole radiation in vacuum.

The optimal approach is to directly measure the collapse time as the time

Parameter	Prior
A	$\log \text{Uniform}[10^{-20}, 10^2]$
Γ	$\text{Uniform}[-4, -1]$
L_0	$\log \text{Uniform}[10^{-20}, 10^{-9}]$
τ	$\log \text{Uniform}[10^2, 10^7]$
t_{col}	$\log \text{Uniform}[10^1, 10^7]$
n	$\text{Uniform}[2, 7]$

TABLE 6.1: Priors used to fit the collapsing magnetar model using Eq. 6.1.

of the sharp drop in the X-ray afterglow as done for GRB090515 (Rowlinson et al., 2010) and then extended to a full catalogue of short gamma-ray bursts (Rowlinson et al., 2013). Here we do a similar analysis with the extended model from Lasky et al. (2017) that allows for spin-down through arbitrary braking indices as opposed to the model used by Rowlinson et al. (2013) which was restricted to spindown with a fixed braking index. Our model for the luminosity evolution of a collapsing magnetar as derived in Lasky et al. (2017) is,

$$L(t) = At^\Gamma + \mathcal{H}(t - t_{\text{col}})L_0 \left(1 + \frac{t}{\tau}\right)^{\frac{1+n}{1-n}}. \tag{6.1}$$

Here, L is the luminosity, t is the time since burst, n is the braking index, A and Γ are the power-law amplitude and power-law exponent respectively, which together describe the emission from the tail of the prompt, L_0 is the initial luminosity at the onset of the plateau phase, τ is the spin-down timescale, and t_{col} is the collapse time. We note that since we fit to the flux data, the quantities here are in the detector frame and are later transformed into the source frame as we elaborate below. The second term in Eq. (6.1) is the magnetar model from Lasky et al. (2017), which models the luminosity evolution of a neutron star spinning down with an arbitrary braking index, with the step-function modification switching off this emission at a time t_{col}. We fit our model to all short gamma-ray bursts with X-ray afterglow data since the launch of *Swift* using the nested sampler DYNESTY (Speagle, 2020) through the Bayesian inference library BILBY (Ashton et al., 2019). Our Priors on the various parameters are listed in Table. 6.1.

In contrast to Rowlinson et al. (2013) who assumed an average redshift for gamma-ray bursts without redshift information, we fit directly to the flux lightcurve. Our inference allows us to measure the collapse time directly from the flux lightcurve which we then convert to the source frame by randomly drawing redshift samples from a probability distribution for z, $P(z)$. For gamma-ray bursts with a known redshift, $P(z)$ is defined as a Gaussian around the known redshift with mean and standard deviation obtained from the *Swift* database, while for gamma-ray bursts where the redshift is not known, we define $P(z)$ as uniform in co-moving volume between a redshift

$z = 0$ and $z = 2$. We obtained our flux data for all short gamma-ray bursts from the *Swift* database binned using the automatic binning strategies (Evans et al., 2010b).

We show our one-dimensional marginalized posterior for the source frame t_{col} in Fig. 6.1, with the top panel showing collapse-time measurements for short gamma-ray bursts with known redshift measurements, while the bottom panel shows the collapse-time measurements for gamma-ray bursts without a measured redshift. Our inference allows us to obtain posteriors for all six parameters for each gamma-ray burst. An interesting feature of the posterior is the top-hat structure. This is a product of the uncertainty in measuring the collapse time as the time of the sharp drop in X-ray flux and limited to the resolution of the data, i.e., t_{col} could be anywhere between two data points where the sharp drop occurs.
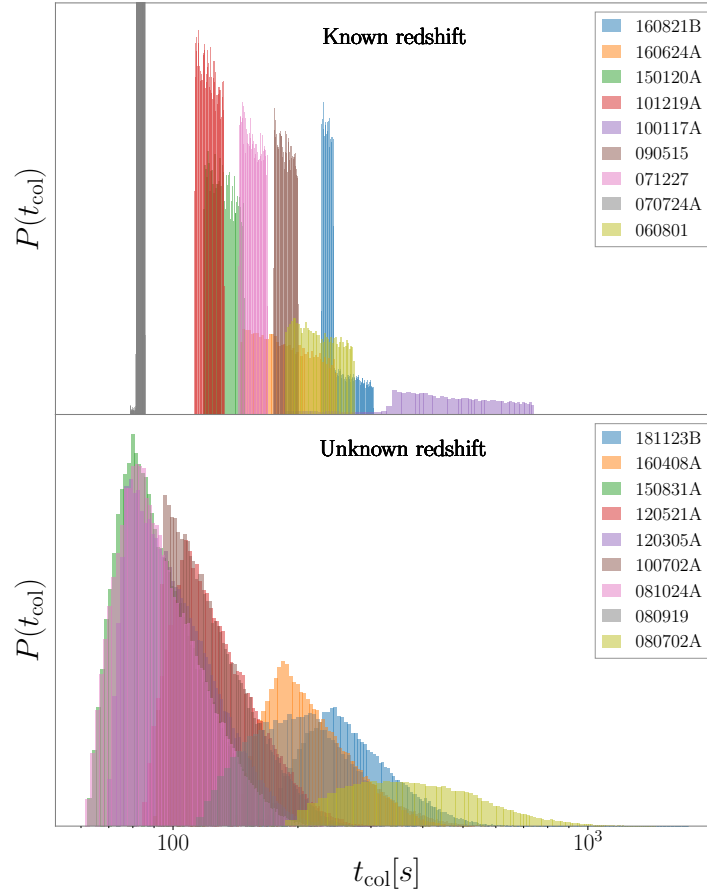
FIGURE 6.1: One-dimensional posterior distributions for the collapse times of all short gamma-ray bursts that have observations supporting a collapsing neutron star model. The top panel shows posteriors for short gamma-ray bursts with known redshifts, while the bottom panel shows posteriors for gamma-ray bursts with unknown redshifts.

Although a sharp drop in luminosity cannot be adequately explained

within the fireball-shock model, we perform Bayesian model selection between our collapsing magnetar model and an agnostic fireball-shock model as described in (Sarin et al., 2019) to ensure the data is best explained by a collapsing magnetar model. The Bayes factors comparing the fireball-shock and magnetar model for these 18 gamma-ray bursts are shown in Table 6.2. As these Bayes factors indicate, assuming both models are equally likely[1],

GRB	$\ln BF_{M/F}$
GRB181123B	12
GRB160821B	1874
GRB160624A	112
GRB160408A	28
GRB150831A	522
GRB150120A	3
GRB120521A	80
GRB120305A	419
GRB101219A	208
GRB100702A	1752
GRB100117A	756
GRB090515	732
GRB081024A	37
GRB080919	53
GRB080702A	6
GRB071227	430
GRB070724A	362
GRB060801	162

TABLE 6.2: Bayes factor $\ln BF_{M/F}$ for the collapsing magnetar model introduced here (Eq. 6.1) and fireball-shock model as introduced in (Sarin et al., 2019).

the collapsing magnetar model is significantly favoured over the fireball-shock model indicating that the X-ray afterglow observations here are best explained by the presence of a long-lived neutron star which collapses at some time. Of the set of gamma-ray bursts considered, GRB150120A and GRB080702 have the lowest Bayes factors, albeit still positive indicating preference for the collapsing magnetar model. To demonstrate our overall conclusions are not biased by these results, we repeat our hierarchical inference analysis without these two gamma-ray bursts and with leave-one-out cross validation: we find the same overall conclusions. We show fits to all short gamma-ray burst X-ray afterglows that are best-fit by our model (Eq. (6.1)) in Fig. 6.2.

---

[1] In reality, both models are not equally likely as the fireball is always believed to be present. Here, the correct metric to compare the two models is the Odds (see Sarin et al. (2019) for details), however model selection with the Odds requires knowing M_{TOV} and the neutron star mass distribution.
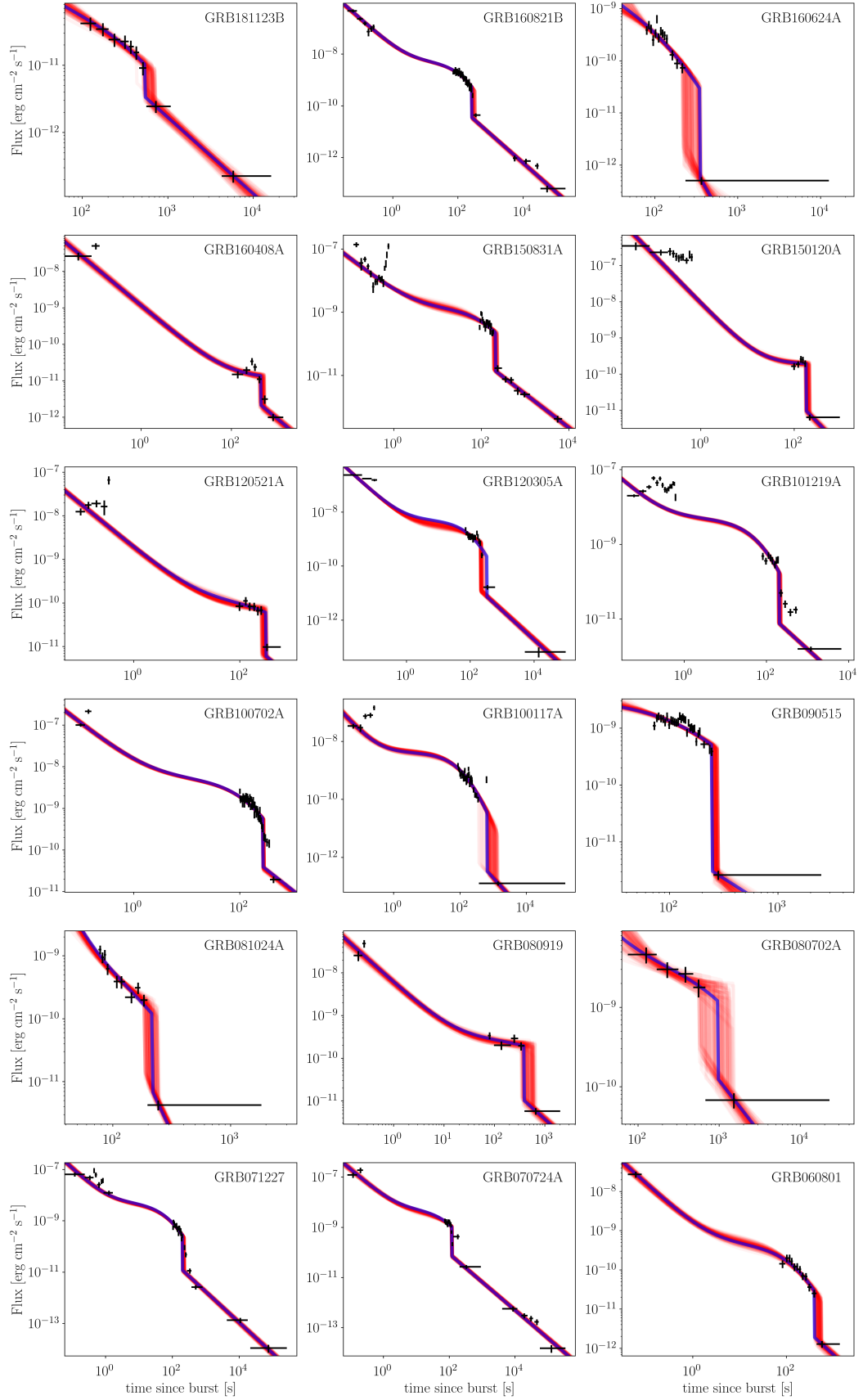
FIGURE 6.2: X-ray lightcurves for all gamma-ray bursts indicative of a collapsing neutron star. Black points indicate flux data from *Swift* binned using the Swift automated binning strategy. The blue curve shows the maximum likelihood model for the collapsing magnetar model (Eq. (6.1)). The dark red band is the superposition of 100 predicted lightcurves randomly drawn from the posterior distribution.

6.3 Methodology

While individual collapse-time measurements are insightful, particularly if accompanied by the detection of gravitational waves from the binary neutron star inspiral (e.g., Lasky et al., 2014), significant constraints on the nuclear equation of state and spin-down mechanism can be placed by considering the population. Hierarchical Bayesian inference is a formalism that can accurately measure population parameters. Here we write the formalism specifically for our problem; see MacKay (2002) for a general discussion and derivation.

As discussed in Sec. 6.1, there are two hypotheses in the literature to explain the inconsistency between the measured collapse times and the theoretical distribution (Ravi & Lasky, 2014). However, as we noted in Sec. 6.2, the model for the collapse time used in literature is derived assuming the neutron star is spinning down solely through vacuum dipole radiation. We extend this model to include spindown via arbitrary braking indices through the general torque equation

$$\dot{\Omega} = k\Omega^{\langle n \rangle}.\tag{6.2}$$

Here, Ω is the star's angular frequency, $\dot{\Omega}$ is its time derivative, and $\langle n \rangle$ is the *averaged* braking index. We emphasize that this *averaged* braking index is different from the braking index measured through the fitting of Eq. (6.1) to the X-ray afterglow as the braking index there is measured at later times after the spin-down timescale τ as the braking index likely evolves as the dynamics of the newly-born neutron star change (e.g., Şaşmaz Muş et al., 2019). One can see this more clearly by considering Fig. 6.2, given our model for the luminosity evolution (Eq. 6.1), the measurement of n comes after $t > \tau$, i.e., after the end of the plateau, as it dictates the shape of the power-law at the end of the plateau. The braking index is not measured earlier during the plateau, where it is quite likely different.

Using the general torque equation, one can derive a functional form of the evolution of the *averaged* spin period as a function of time

$$p(t) = p_0 \left(1 + \frac{t}{\tau}\right)^{\frac{\langle n \rangle - 1}{\langle n \rangle + 1}}.\tag{6.3}$$

Here, p_0 is the initial spin-period of the neutron star and $p(t)$ is the spin period as a function of time. The maximum gravitational mass, M_{max}, of a spinning neutron star for a given equation of state can be written as (Shapiro & Teukolsky, 1983),

$$M_{\text{max}} = M_{\text{TOV}} \left(1 + \alpha p^{\beta}\right)\tag{6.4}$$

Here, α and β are parameters fit to neutron star equilibrium sequences calculated for various values of the spin period, p. In Newtonian gravity, $\beta = -2$ and α is a function of the star's mass, radius and moment of inertia. Together,

α and β describe an equation of state and have been calculated for several equations of state (e.g., Lasky et al., 2014; Li et al., 2017b). To make our analysis cleaner, we nondimensionalize Eq. (6.4) by introducing a reference spin period, p_{ref}

$$M_{\mathrm{max}} = M_{\mathrm{TOV}} \left[1 + \bar{\alpha} \left(\frac{p}{p_{\mathrm{ref}}} \right)^{\beta} \right], \tag{6.5}$$

where $\bar{\alpha} = \alpha p_{\mathrm{ref}}^{\beta}$ is a dimensionless variable related to α. Substituting Eq. (6.3) into Eq. 6.5 and setting M_{max} to M_p and t to t_{col} gives

$$t_{\mathrm{col},i} = \frac{\tau_i}{p_{0,i}^{\gamma_i}} \left[\left(\frac{M_{p,i} - M_{\mathrm{TOV}}}{\alpha M_{\mathrm{TOV}}} \right)^{\frac{\gamma_i}{\beta}} - p_{0,i}^{\gamma_i} \right]. \tag{6.6}$$

Here

$$\gamma_i = \frac{\langle n \rangle_i + 1}{\langle n \rangle_i - 1}, \tag{6.7}$$

M_p is the mass of the post-merger remnant, p_{ref} is a reference spin period which we set to 1 ms without loss of generality. Parameters denoted with i are individual event parameters and those without are the population parameters we want to infer. Although M_{TOV} can be calculated explicitly by determining α and β, the relationship is not unique and as such we have conservatively assumed that these parameters are uncorrelated.

Of the parameters denoted with i, we measure τ from the X-ray afterglow, albeit poorly if the neutron star collapses before τ. Our initial parameter estimation on the X-ray afterglow also measures the braking index, n. However, as we emphasized above this n is different to $\langle n \rangle$. Instead, we model $\langle n \rangle$ as either being indicative of predominant spin down through gravitational-wave emission or through an unknown braking index which we measure. This implies that we model $\langle n \rangle$ to be randomly drawn from the distribution described by

$$\langle n \rangle = (1 - \eta) \mathcal{N}(\mu_{\langle n \rangle}, \sigma_1) + \eta \mathcal{N}(5, \sigma_2), \tag{6.8}$$

where $\mathcal{N}(\mu, \sigma)$ is a Gaussian distribution of mean μ and standard deviation σ, η is a mixing fraction between the two Gaussian distributions, $\mu_{\langle n \rangle}$ is the mean of the first Gaussian distribution and σ_1 and σ_2 are the standard deviations of the first and second Gaussian distributions. This implies that the population of *average* braking index is a mixture model of two Gaussian distributions, one centred on $\langle n \rangle = 5$ implying an *average* braking index where the spin down of the neutron star is dominated by gravitational-wave emission and another Gaussian distribution centred on $\mu_{\langle n \rangle}$ which we infer. We emphasize that this model is a choice and we believe it captures the necessary physics.

Equations (6.6) and (6.8) together describe our population model, parameterized by hyperparameters, $\Lambda = \{\bar{\alpha}, \beta, M_{\text{TOV}}, \mu_{\langle n \rangle}, \sigma_1, \sigma_2, \eta\}$. By Bayes' theorem the posterior distribution on these hyperparameters is

$$p_{\text{tot}}(\Lambda|\vec{d}) = \frac{\mathcal{L}_{\text{tot}}(\vec{d}|\Lambda)\pi(\Lambda)}{\int d\Lambda \mathcal{L}_{\text{tot}}(\vec{d}|\Lambda)\pi(\Lambda)}. \tag{6.9}$$

Here, $\vec{d}$ is the set of measurements of N events, $\pi(\Lambda)$ is our prior on the hyperparameters, and $\mathcal{L}_{\text{tot}}(\vec{d}|\Lambda)$ is the likelihood of the population data given our hyperparameters. The denominator is the hyper-evidence, which can be used for comparing two population models. Naively, looking at Eq. (6.9) we might not see any dependence of our posterior on the event parameters. This relationship can be made explicit by rewriting the likelihood as

$$\mathcal{L}_{\text{tot}}(\vec{d}|\Lambda) = \prod_i^N \int d\theta_i \mathcal{L}\left(d_i|\theta_i\right) \pi\left(\theta_i|\Lambda\right). \tag{6.10}$$

Here, θ_i is a vector of the ith event parameters ($\theta_i = \{A, \Gamma, L_0, \tau, t_{\text{col}}, n, M_p, p_0\}$), d_i is the data for the ith event, $\mathcal{L}\left(d_i|\theta_i\right)$ is the likelihood of the data d_i given event parameters θ_i and $\pi\left(\theta_i|\Lambda\right)$ is the prior on θ_i given our hyperparameters. These large sets of integrals in evaluating the hyper-likelihood make hierarchical inference prohibitively expensive, fortunately, a computational trick, referred to as "recycling" (e.g., Thrane & Talbot, 2019) replaces these integrals with sums over posterior samples from the initial step of parameter estimation on an individual event, in our case, the fitting of Eq. (6.1) to the X-ray afterglow.

Our formulation is still not complete as there are two event-specific parameters we do not measure when fitting Eq. (6.1) to the X-ray afterglow, the mass of the post-merger remnant M_p, and the initial spin-period, p_0. We therefore marginalize over these two parameters, which can be written explicitly as

$$\mathcal{L}_{\text{tot}}(\vec{d}|\Lambda) = \prod_i^N \iiint d\theta_i dM_{p,i} dp_{0,i} \mathcal{L}\left(d_i|\theta_i\right) \times$$
$$\pi\left(\theta_i|\Lambda\right) \pi\left(M_p|\Lambda\right) \pi\left(p_0|\Lambda\right), \tag{6.11}$$

where $\pi\left(M_p|\Lambda\right)$ and $\pi\left(p_0|\Lambda\right)$ are the prior distributions on M_p and p_0 given our hyperparameters. We assume a uniform prior on p_0 from $0.5 - 1.0$ ms, although we note that in reality the spin-period prior should be a function of the hyperparameters, in particular, α and β. However, given we are marginalising over this parameter, we have conservatively accounted for this covariance by propagating all of the uncertainty through to our measured parameters.

The prior on the post-merger remnant mass distribution, $\pi\left(M_p|\Lambda\right)$ is

much more complicated. Previously, several authors have calculated the distribution of M_p using the observed binary neutron star population in our galaxy (Lasky et al., 2014; Lü et al., 2015; Sarin et al., 2019). These galactic double neutron star systems measured with radio observations are empirically known to have a tight mass distribution described by a Gaussian of mean $\mu = 1.32 M_\odot$ and width $\sigma = 0.11 M_\odot$ (Kiziltan et al., 2013; Alsing et al., 2018). While the progenitors of GW170817 are consistent with the galactic double neutron star mass distribution (Farrow et al., 2019), the progenitors of GW190425 are not at a highly-significant level (Abbott et al., 2020a). This suggests GW190425 came from a different population, perhaps as a result of dynamical formation or unstable case-BB common-envelope evolution (Abbott et al., 2020a). In this case, one would expect the masses of the progenitors of GW190425 to be drawn from the population of neutron stars *not* in double neutron star systems and instead from a mass distribution consisting of all neutron stars.

Following Alsing et al. (2018), we use the galactic neutron star mass distribution, consisting both populations of double neutron stars and neutron stars in other systems, to be representative of the underlying mass distribution of progenitors for gravitational-wave mergers and short gamma-ray bursts. If GW190425 originated through a different evolutionary pathway than observed galactic double neutron star systems, then the relative fraction between the two populations is almost entirely unknown. Indeed, while it was originally thought the progenitor of GW170817 came from the same population as galactic double neutron stars (e.g., Farrow et al., 2019), even this should now be called into question. As a consequence, we leave the mixing fraction between the two populations as a free parameter. The full population of galactic neutron stars can be fit with a double-peaked Gaussian probability distribution (Alsing et al., 2018)

$$p(M) = (1 - \epsilon)\,\mathcal{N}\,(\mu_1, \sigma_1) + \epsilon \mathcal{N}\,(\mu_2, \sigma_2)\,, \tag{6.12}$$

The known galactic systems have $\mu_1 = 1.32 M_\odot$ and $\sigma_1 = 0.11$, $\mu_2 = 1.80 M_\odot$, $\sigma_2 = 0.21 M_\odot$, and mixing fraction $\epsilon = 0.35$.

In the left panel of Fig. 6.3 we show these mass distributions. The blue histogram shows the masses of neutron stars in galactic double neutron star systems, while the red histogram shows the masses of all other neutron stars. In black is the probability distribution given by Eq. (6.12) with values given above. In the right-hand panel of Fig. 6.3, we show in blue the corresponding histogram for the chirp masses of galactic double neutron stars; i.e., equivalent to the systems shown in blue in the left panel. The two vertical lines are the measured chirp masses for GW170817 in green and GW190425 in magenta; the uncertainties on these measurements are too small to be seen on this scale. The solid black curve shows the chirp-mass probability distribution corresponding to converting the probability distribution of Eq. (6.12) into chirp mass. The black dashed and dot-dashed curves show the same probability distribution, albeit with $\epsilon = 0.5$ and $\epsilon = 0.8$, respectively.
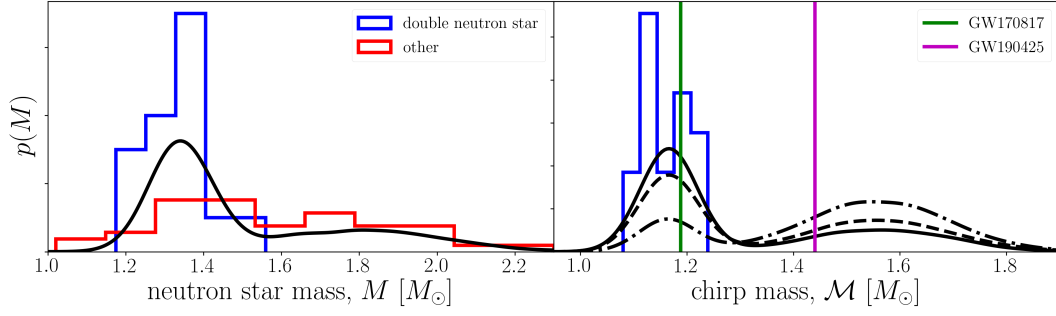
FIGURE 6.3: Neutron star mass distributions. Left panel: In blue are the measured neutron star masses for those in double neutron star systems, and in red are the masses of neutron stars in binaries with white dwarfs, main sequence stars, etc (Alsing et al., 2018). The black curve is the best-fit mass distribution to these from Alsing et al. (2018). Right panel: in blue are the same double neutron star systems, this time converted to chirp mass. In green and magenta are the chirp masses of the two gravitational-wave events GW170817 and GW190425, respectively. The solid black curve is the chirp-mass distribution associated with the solid black curve in the left panel. The dashed and dot-dashed black curves assume similar distributions to the solid-black curve, except the mixing fraction between the two binary populations is $\epsilon = 0.5$ and 0.8, respectively (cf. $\epsilon = 0.35$ for the solid black curve).

Inspecting Fig. 6.3 one can see that although the progenitors of GW190425 are inconsistent with the mass distribution inferred from galactic double neutron star systems, they are consistent with the mass distribution for all galactic neutron stars. Assuming our galaxy is typical, one, therefore, expects the progenitor mass distribution for all binary neutron star mergers to be similar to the distribution given by Eq. (6.12), albeit with an unknown mixing fraction ϵ.

For the remainder of the paper, we assume the progenitor mass distribution is given by Eq. (6.12) with $(\mu_1, \sigma_1) = (1.32, 0.11)$, $(\mu_2, \sigma_2) = (1.80, 0.21)$, and let ϵ be a free parameter which we infer through our hierarchical model. Following Sarin et al. (2019), one can derive the post-merger remnant mass distribution having the same functional form as Eq. (6.12) with $(\mu_1, \sigma_1) = (2.42, 0.09)$, $(\mu_2, \sigma_2) = (3.21, 0.25)$ assuming $\approx 0.07 M_\odot$ of dynamical ejecta is produced in the merger, consistent with observations of GW170817 (e.g., Evans et al., 2017a).

For the timescales we are interested in, neutron stars can only collapse if they are born with mass between M_{TOV} and approximately $1.2 \times M_{\text{TOV}}$ implying

$$\pi\left(M_p | \Lambda\right) = \begin{cases} f\left(\epsilon\right) & M_{\text{TOV}} \leq M_p \leq 1.2 M_{\text{TOV}} \\ 0 & \text{otherwise} \end{cases}, \qquad (6.13)$$

where $f\left(\epsilon\right) = \left(1 - \epsilon\right) \mathcal{N}\left(2.42, 0.09\right) + +\epsilon \mathcal{N}\left(3.21, 0.25\right)$. Our hierarchical

Parameter	Prior
M_{TOV}	Uniform$[2.01, 2.9]$
$\log_{10} \bar{\alpha}$	Uniform$[-3, 1]$
β	Uniform$[-6, -2]$
σ	Uniform$[1, 500]$
$\mu_{\langle n \rangle}$	Uniform$[1, 4]$
$\langle n \rangle_{\sigma,1}$	Uniform$[0.1, 1.5]$
$\langle n \rangle_{\sigma,2}$	Uniform$[0.1, 1.5]$
η	Uniform$[0, 1]$
ϵ	Uniform$[0, 1]$

TABLE 6.3: Priors for our hierarchical model described by Eqs. (6.11-6.13).

likelihood is completely defined by Eqs. (6.11-6.13), ready to be combined with suitable priors on our hierarchical model (Eq. 6.6). We perform hierarchical inference on our population of events using the nested sampler DYNESTY (Speagle, 2020) through the Bayesian inference library BILBY (Ashton et al., 2019). To make the analysis computationally feasible, we use an adaptation of the GPU-accelerated population inference code GWPOPULATION (Talbot et al., 2019) and CUPY (Okuta et al., 2017). Our priors for the rest of the hyperparameters are shown in Table. 6.3.

6.4 Equation of state and gravitational-wave constraints

We first show our measurement on the maximum allowed non-rotating mass M_{TOV}, as alluded to previously, this is a function of the unknown mixing fraction ϵ, between double neutron stars observed in our galaxy and the population that explains the progenitors of GW190425. Our measurement for M_{TOV} for mixing fraction, $\epsilon = 0$, and marginalised over all possible values of this mixing fraction are shown in Fig. 6.4 in the top panel. The bottom panel shows the two-dimensional posterior on M_{TOV} and ϵ. On the same plot, we plot vertical lines for different constraints on M_{TOV}. The black and blue lines correspond to the mass measurements of two pulsars, PSRJ0348+0432 and PSRJ0740+6620 as $2.01 \pm 0.04 M_{\odot}$ (Antoniadis et al., 2013) and $2.14 \pm 0.1 M_{\odot}$ (Cromartie et al., 2019) respectively, the existence of such massive neutron stars puts a lower limit on M_{TOV}. The other two vertical lines come from the observation of GW170817, in particular by combining the mass measurement from the gravitational-wave inspiral and by inferring fate of the post-merger remnant. However, there is still disagreement on the ultimate fate of the post-merger remnant of GW170817 with the interpretations of the electromagnetic observations ranging from a short-lived neutron star through to an infinitely stable neutron star. Such uncertainty on the fate of the post-merger

remnant results in the constraint on M_{TOV} ranging from $2.09 - 2.43 M_\odot$ (Ai et al., 2019). The green and red vertical lines correspond to the limits of this constraint. We note that the most widely accepted interpretation of the fate of the post-merger remnant of GW170817, a hypermassive neutron star that collapsed within 1.7 seconds into a black hole constrains $M_{\mathrm{TOV}} \lesssim 2.3 M_\odot$ (e.g., Margalit & Metzger, 2017; Shibata et al., 2019).

Assuming a mixing fraction $\epsilon = 0$, i.e a population consistent with local double neutron star systems but inconsistent with GW190425, we measure $M_{\mathrm{TOV}} = 2.26^{+0.31}_{-0.17} M_\odot$. As Fig. 6.4 shows, this is the most conservative measurement and comparable to other analyses measuring M_{TOV} (e.g., Lü et al., 2015; Gao et al., 2016) which assume the local binary neutron star population is a good representation of the binary neutron stars that merge. However, this mass distribution is inconsistent with GW190425. If instead we assume $\epsilon = 0.5$ we measure $M_{\mathrm{TOV}} = 2.30^{+0.38}_{-0.19} M_\odot$. We stress that with only two gravitational-wave observations of binary neutron star inspirals, it is impossible to constrain this mixing fraction. Instead, marginalizing over this unknown mixing fraction leads to $M_{\mathrm{TOV}} = 2.31^{+0.36}_{-0.21} M_\odot$. We can revisit this measurement after future gravitational-wave measurements constrain ϵ, allowing us to take a slice through our two-dimensional posterior for a fixed ϵ.

We also measure the braking index mixing fraction $\eta = 0.69^{+0.21}_{-0.39}$ which suggests that $\sim 70\%$ of neutron star post-merger remnants that collapse spin down predominantly through gravitational-wave emission. This has several consequences. Firstly, it is good for the prospect of detecting gravitational waves from these objects. Although not individually resolvable with current detectors and even future detectors unless sufficiently close (e.g., Sarin et al., 2018), they will contribute to the stochastic background (e.g., Regimbau & de Freitas Pacheco, 2006; Cheng et al., 2017), which may become detectable with third-generation gravitational-wave detectors (Cheng et al., 2017). We leave a calculation of the stochastic background for future work.

The fraction of remnants that spin down through gravitational-wave emission is also interesting for understanding the emission mechanism itself. It is intriguing to understand the physical difference between those remnants that do and do not spin down predominantly through gravitational-wave emission. For example, there are a number of physical mechanisms that cause large-amplitude gravitational waves such as the spin-flip instability (Cutler, 2002), inertial r modes (e.g., Andersson & Kokkotas, 2001), or the secular bar-mode instability (see e.g., Andersson, 2003). Whether each of these mechanisms operate in certain remnants but not others could be a result of different initial conditions such as the progenitor masses.

The spin-flip instability in newly born neutron stars may operate when the internal toroidal magnetic field winds up, causing the star to become a prolate spheroid. Internal dissipation then causes the star to become an orthogonal rotator in which the dominant moment of inertia axis is misaligned
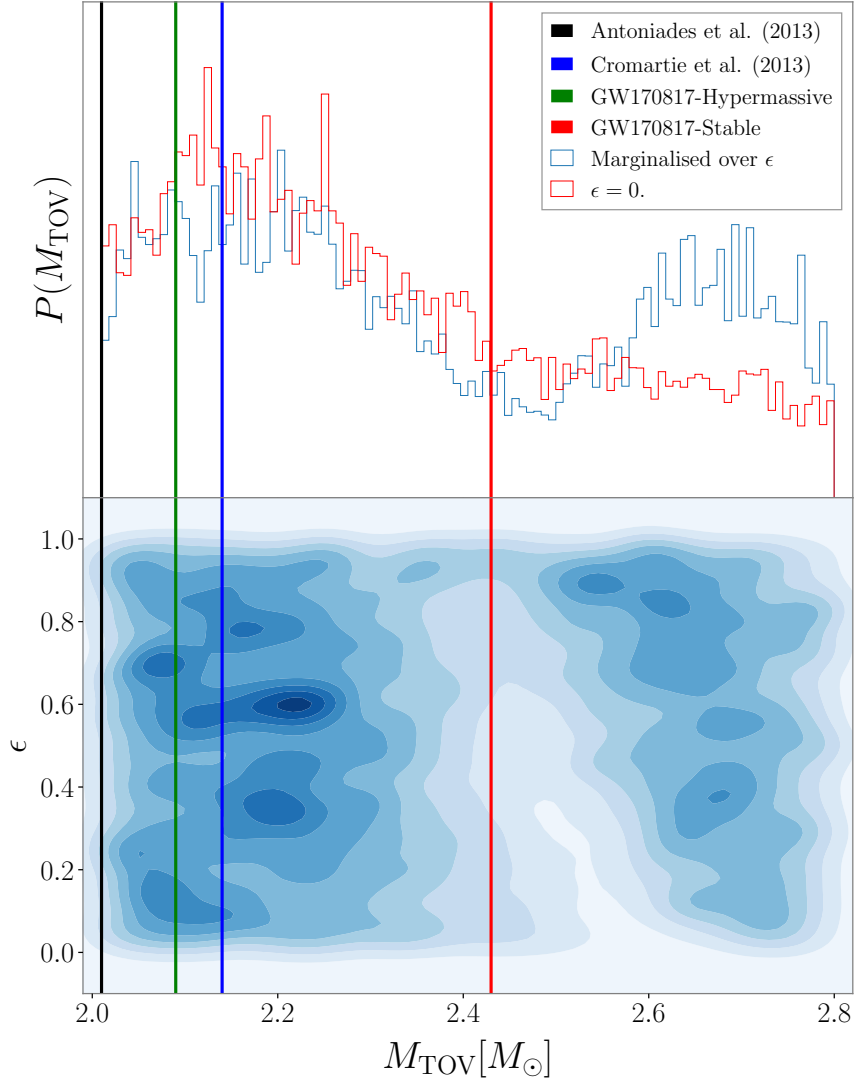
FIGURE 6.4: One (top panel) and two-dimensional (bottom panel) posterior distributions on M_{TOV} and $M_{\mathrm{TOV}} - \epsilon$. We also show a slice through the two-dimensional posterior for $\epsilon = 0$. i.e a mass distribution similar to the galactic double neutron star systems but inconsistent with the progenitors of GW190425. We measure $M_{\mathrm{TOV}} = 2.26^{+0.31}_{-0.17} M_\odot$ assuming a mixing fraction $\epsilon = 0$. which implies a mass distribution inconsistent with the progenitors of GW190425. We plot few other constraints for M_{TOV} based on pulsar observations (Antoniadis et al., 2013; Cromartie et al., 2019) and inferred fate of GW170817 (e.g., Ai et al., 2019). For clarity, we only plot the median of these measurements but we stress that several of these measurements have large uncertainties and the later constraint, based on the inferred fate of the post-merger remnant of GW170817 could realistically be anywhere between the two hypermassive (green) or stable (red) scenarios.

with the star's rotation axis. In this configuration, the star is a maximal emitter of gravitational waves. However, the birth magnetic field, temperature distribution, initial spin period can all play a large role in whether the spin-flip instability occurs or not (e.g., see Lander & Jones, 2018). Moreover, the

spin-flip instability can cause the star to initially become an orthogonal rotator, before re-aligning and becoming an aligned rotator. In such a situation, one would expect significant gravitational-wave emission early in the star's life which then gets suppressed significantly as the star again becomes aligned (Dall'Osso et al., 2018; Lander & Jones, 2020).

Both the secular bar mode and inertial r mode saturation amplitudes are highly uncertain, and likely depend on the star's temperature through bulk viscosity. For example, if the star does not cool sufficiently (10^{10} K), the bar-mode instability may be suppressed (e.g., Doneva et al., 2015) leading to a dearth of gravitational-wave emission. The secular bar-mode instability might also fail if the ratio of T/W, where T is the rotational kinetic energy and W is the gravitational potential energy, simply does not exceed the critical point for the instability due to, for example, the mass ratio of the merging neutron stars. While it is not clear what the active or dominant gravitational-wave emission mechanisms are in these nascent stars, it is clear that understanding the fraction that spin down through gravitational waves versus electromagnetic radiation could provide valuable insight into this interesting question.

We measure $\mu_{\langle n \rangle} = 3.12^{+0.69}_{-0.87}$ suggesting that the rest of the post-merger remnants that collapse spin-down through *on average* close to vacuum dipole radiation. Our measurement $\mu_{\langle n \rangle} \gtrsim 3$ could imply we are seeing a mixture of gravitational-wave and electromagnetic emission, i.e., while $\sim 70\%$ are consistent with $\langle n \rangle = 5$, the rest initially spin down through gravitational waves and later spin down through electromagnetic radiation. We use our posteriors to construct the probability density function for the *averaged* braking index which is shown in Fig. 6.5. This suggests that a large fraction of post-merger remnants that collapse spin-down predominantly through gravitational waves while the rest spin-down with an *average* braking index close to $\langle n \rangle = 3$, consistent with vacuum dipole radiation. We show the full two-dimensional posterior distribution on all these parameters in the Appendix 6.6.

In Fig. 6.6 we show the two-dimensional posterior distribution of α and β, see Eq. (6.4). Here, hadronic equation of states are marked with blue dots while quark star equation of states are marked with red crosses. The shade of blue in the posterior indicates the confidence level of our posterior and grey is the 95% prior. Our posterior is consistent with both quark and hadronic equations of state at the two-sigma level, with current constraints slightly favouring quark-like equations of states over purely hadronic. The specific equation of states as well as their corresponding α, β parameters are listed in Table 6.4 but we emphasise that given the current size of the population we are not interested in individual equation of states, but rather the large difference in $\alpha - \beta$ parameter space between quark and hadronic equation of states. The relationship between α and β has been explored in the past with Ai et al. (2019) exploring the constraints on these parameters for different equation of states with observations of GW170817 and Gao et al. (2020)
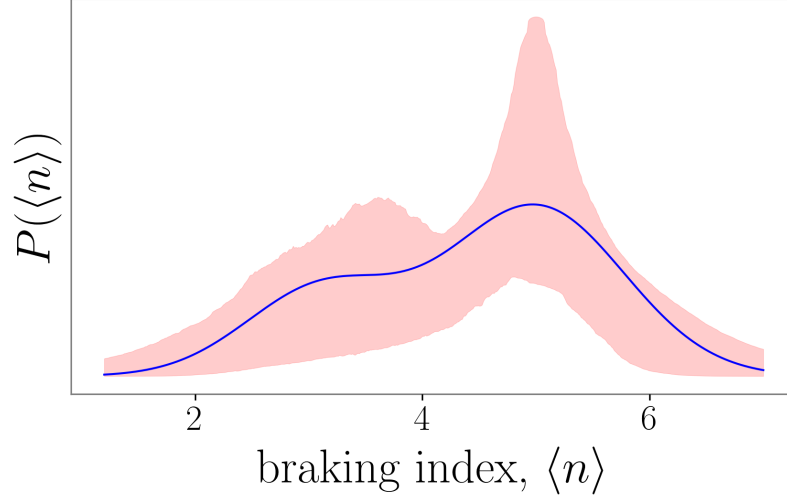
FIGURE 6.5: *Average* braking index distribution. The blue curve indicates the median value of the posterior while the red curves are two-sigma confidence intervals.

Equation of state	α	β
GM1	$1.58 \times 10^{-10} p^{-\beta}$	-2.84
APR	$0.303 \times 10^{-10} p^{-\beta}$	-2.95
BSk20	$3.39 \times 10^{-10} p^{-\beta}$	-2.68
BSk21	$2.81 \times 10^{-10} p^{-\beta}$	-2.75
CIDDM	$2.58 \times 10^{-16} p^{-\beta}$	-4.93
CDDM1	$3.938 \times 10^{-16} p^{-\beta}$	-5.0
CDDM2	$2.22 \times 10^{-16} p^{-\beta}$	-5.18
MIT2	$1.67 \times 10^{-15} p^{-\beta}$	-4.58
MIT3	$3.35 \times 10^{-15} p^{-\beta}$	-4.60
PMQS1	$4.39 \times 10^{-15} p^{-\beta}$	-4.51
PMQS2	$5.90 \times 10^{-15} p^{-\beta}$	-4.51
PMQS3	$9.00 \times 10^{-15} p^{-\beta}$	-4.48

TABLE 6.4: Equation of states and their corresponding α and β parameters, all equation of states parameters are from Li et al. (2017b).

deriving a general relationship for α and β by parameterising in terms of how much more mass can be added for a given spin period. If these supramassive neutron stars are quark stars, this might suggest that either these newly-born neutron stars are born via the merger of two quark stars, or that the merger of two hadronic neutron stars results in a phase transition from a hadronic to quark equation of state. Both of these options have implications for nuclear theory, with the latter phase transition being perhaps detectable in the near-future with aLIGO (e.g., Chatziioannou & Han, 2020).
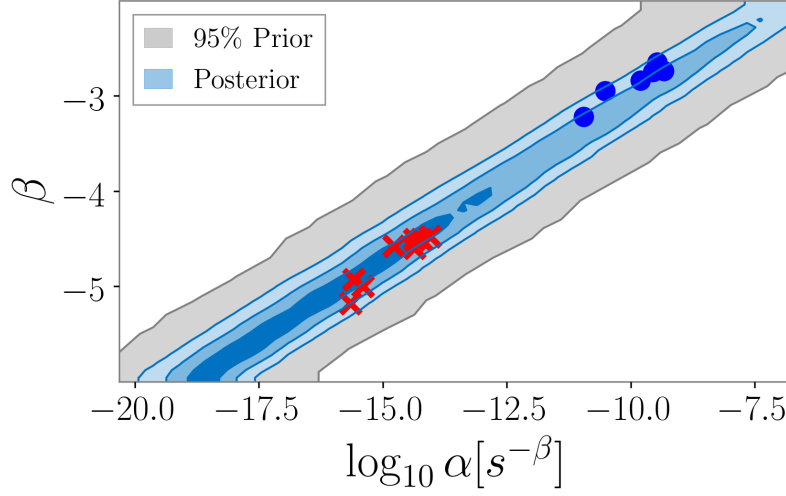
FIGURE 6.6: Two-dimensional posterior distribution of α and β with hadronic equation of states marked by circles and quark star equation of states marked by crosses. The shades of blue correspond to one-two-three sigma confidence intervals.

In the future, with more events and a better informed binary neutron star mass distribution we will revisit these measurements.

6.5 Conclusion

We have shown how observations of the X-ray afterglows of short gamma-ray bursts can be used to infer the presence of long-lived binary neutron star post-merger remnants that later collapse to form black holes. This implicitly requires that long-lived neutron star post-merger remnants can produce a short gamma-ray burst, which is still heavily debated see (e.g., Giacomazzo & Perna, 2013; Beniamini et al., 2020a; Ciolfi, 2020b) We have also shown that, given a population of these putative collapsing neutron stars, hierarchical Bayesian inference provides a framework for measuring the population properties. In particular, we use the observations of 18 short gamma-ray bursts to measure the maximum allowed non-rotating mass $M_{\text{TOV}} = 2.31^{+0.36}_{-0.21} M_{\odot}$ marginalised over the unknown mixing fraction between the mass distribution describing both single and double neutron stars observed in our galaxy, the former being consistent with the progenitors of GW190425. If instead, we assume $\epsilon = 0$ (i.e., a mass distribution that is inconsistent with the progenitors of GW190425 but a good representation of locally observed double neutron star systems), we measure $M_{\text{TOV}} = 2.26^{+0.31}_{-0.17} M_{\odot}$. Future measurements of gravitational waves from binary neutron stars will allow an independent measurement of ϵ allowing us to revisit our measurement and therefore provide a tighter constraint on M_{TOV}.

Although broad, our measurement for M_{TOV} marginalised over the unknown mixing fraction is comparable to inferences of M_{TOV} made with short gamma-ray bursts (e.g., Lü et al., 2015). However, such measurements will need to be revisited as they assume the galactic double neutron star distribution is a good representation of binary neutron star merger progenitors. The observation of GW190425 suggests this is not the case. Our measurement is also comparable to inferences of a sharp cut-off in the galactic neutron star mass distribution (Alsing et al., 2018) and inference based on the uncertain nature of the post-merger remnant of GW170817 (Ai et al., 2019).

We measure equation-of-state specific parameters, $\log_{10}\alpha = -14.89^{+3.94}_{-2.72}\text{s}^{-\beta}$ and $\beta = -4.67^{+1.32}_{-0.92}$. Together these measurements suggest deconfined quark equation of states are slightly favoured over hadronic, however, the data is not conclusive with both sets of equations of states being consistent with the population at the two-sigma level.

We also measure the fraction of post-merger remnants that spin-down through gravitational waves implying a braking index, $n = 5$ as $\eta = 0.69^{+0.21}_{-0.39}$, suggesting that $\sim 70\%$ of neutron star post-merger remnants born in short gamma-ray bursts which collapse do so due to spin down predominantly through the emission of gravitational waves.

There are some limitations to our analysis. In particular, we do not consider any selection effects, which for a population such as ours are two-fold. First, intrinsically brighter short gamma-ray bursts are assumed to be observed on-axis and as such the emission produced by the interaction of the burst with the surrounding environment is brighter than the putative neutron star post-merger remnant. This implies that for on-axis short gamma-ray bursts, the window to infer the presence of a sharp drop due to the collapse of a long-lived neutron star is shorter as the initial emission from the jet has to drop to a level such that the emission from the neutron star can be observed. Second, *Swift* typically takes up to ~ 100 seconds to slew and observe an X-ray afterglow implying it will not see the collapse of some long-lived neutron stars that collapse before ~ 100 seconds. However, to complicate this further, this is the time measured in the detector frame which is red-shifted by an amount often not known. We aim to formulate and incorporate these selection effects in the future, however, we note that both these effects currently do not influence our results. We have verified this with injection studies with up to 20 events in our population and the bias caused by these effects is below our measurement uncertainty and will only become important as the population grows.

As described in Sec. 6.3 we numerically marginalized over the unknown individual masses and spin periods of the putative post-merger remnants in our population. These marginalisations add uncertainty to our measurements as they propagate the uncertainty from not knowing these parameters

into our inferred population parameters. In the future, with a possible co-incident detection of gravitational waves from a binary neutron star inspiral and an X-ray afterglow, we can avoid these marginalization's or have a more informative prior, which will lead to a much more informative measurement.

In conclusion, we have shown that X-ray afterglow observations of short gamma-ray bursts can be used to constrain properties of post-merger remnants, with the population properties offering critical insight into the nuclear equation of state and gravitational-wave emission from newly born neutron stars. In light of GW190425, we measure $M_{\text{TOV}} = 2.31^{+0.36}_{-0.21} M_\odot$ marginalised over all possible values of the mixing fraction describing the mass distribution of double and single neutron star systems in our galaxy, the latter being consistent with the progenitors of GW190425. If instead, we assume a mixing fraction $\epsilon = 0$, i.e a mass distribution consistent with the double neutron star systems in our galaxy but one that rules out GW190425 having neutron star progenitors, we measure $M_{\text{TOV}} = 2.26^{+0.31}_{-0.17} M_\odot$.

6.6 Appendix
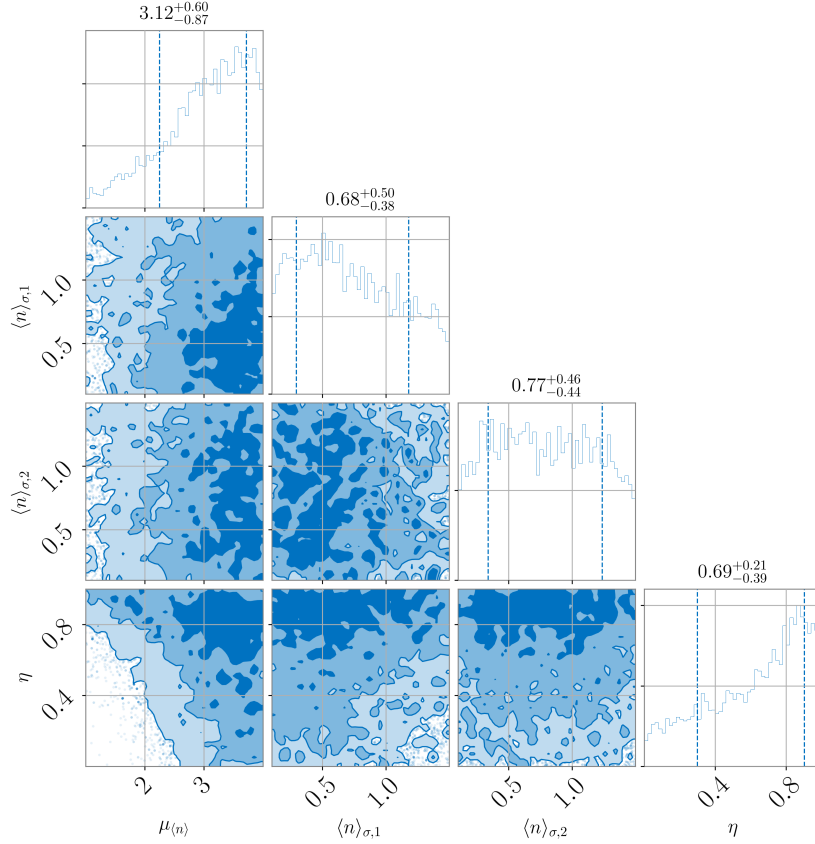
FIGURE 6.7: Corner plot showing the one and two-dimensional posterior distributions on $\mu_{\langle n \rangle}$, $\langle n \rangle_{\sigma,1}$, $\langle n \rangle_{\sigma,2}$ and η. The shades of blue correspond to one-two-three sigma confidence intervals.

Chapter 7

CDF-S XT1: The off-axis afterglow of a neutron star merger at z=2.23

Abstract

CDF-S XT1 is a fast-rising non-thermal X-ray transient detected by *Chandra* in the Deep-Field South Survey. Although various hypotheses have been suggested, the origin of this transient remains unclear. Here, we show that the observations of CDF-S XT1 are well explained as the X-ray afterglow produced by a relativistic structured jet viewed off-axis. We measure properties of the jet, showing that they are similar to those of GRB170817A, albeit at cosmological distances. We measure the observers viewing angle to be $\theta_{\mathrm{obs}} = 10° \pm 3°$ and the core of the ultra-relativistic jet to be $\theta_{\mathrm{core}} = 4.4° \pm 0.9°$, where the uncertainties are the 68% credible interval. The inferred properties and host galaxy combined with Hubble, radio, and optical non detections favour the hypothesis that CDF-S XT1 is the off-axis afterglow of a binary neutron star merger. We find that other previously suggested hypotheses are unable to explain all properties of CDF-S XT1. At a redshift of $z = 2.23$, this is potentially the most distant observed neutron star merger to date and the first orphan afterglow of a short gamma-ray burst. We discuss the implications of a binary neutron star merger at such a high redshift for the star-formation rate in the early Universe, the nucleosynthesis of heavy elements, and the prospect of identifying other off-axis afterglows.

7.1   Introduction

Gamma-ray bursts are highly energetic explosions caused by either the collapse of a massive star or the merger of a neutron star binary. While the mechanism behind the prompt gamma-ray emission is still uncertain (e.g., Pe'er, 2015), the weaker broadband afterglow emission observed extensively in X-rays, optical and radio has been studied in significant detail. This broadband afterglow is widely believed to be synchrotron radiation produced from the interaction of a relativistic jet with the surrounding interstellar medium (e.g., Sari et al., 1999).

It has long been accepted that gamma-ray bursts are collimated into an ultra-relativistic jet (e.g., Kumar & Zhang, 2015), a point spectacularly confirmed by very-long baseline interferometry of GRB170817A (e.g., Mooley et al., 2018a), the gamma-ray burst that accompanied the first gravitational-wave observation of a binary neutron star merger (Abbott et al., 2017d,c). In general, as the jet ploughs into the surrounding interstellar medium, the initial high velocity of the material implies the emission is relativistically beamed and can only be seen for an observer close to the emission axis. As that material slows, the beaming cone broadens, and off-axis observers begin to see the burst afterglow. This relativistic beaming necessarily implies the existence of *orphan* afterglows, where the observer misses the early prompt emission but sees the afterglow as the jet broadens.

Orphan afterglows are notoriously difficult to find. Despite numerous searches in multiple diverse data sets, there are only three putative long gamma-ray burst orphan afterglow candidates, one observed in radio (Marcote et al., 2019) and two in optical (Ho et al., 2020). In 2014, the Chandra Deep-Field South Survey detected a fast-rising transient known as CDF-S XT1 (Bauer et al., 2017). CDF-S XT1 is associated with a host galaxy in the CANDELS survey (Grogin et al., 2011) with a photometric redshift of $z = 2.23^{+0.98}_{-1.84}$ (2σ). With a non-thermal spectrum, a photon index $\gamma \approx 1.43$ (Bauer et al., 2017) (i.e., a declining spectrum), and non-detections in optical and radio, the transient properties are unlike many other high-energy transients (Bauer et al., 2017). Since its discovery, various hypotheses have been suggested to explain the observations and properties of CDF-S XT1. Hypotheses such as a supernova-shock breakout (Bauer et al., 2017; Alp & Larsson, 2020), a tidal disruption event of a white dwarf with an intermediate-mass black hole (Bauer et al., 2017; Peng et al., 2019), and the trapped emission from a millisecond magnetar (Sun et al., 2019) have all been explored previously to varying success.

In this Letter, we show that CDF-S XT1 observations can instead be well interpreted as the X-ray afterglow produced by a relativistic jet viewed off-axis. In Sec. 7.2 we describe our new method for fitting the raw photon count data with detailed structured jet models. In Sec. 7.3 we discuss the

results and present evidence for the observations being explained as the X-ray afterglow of a gamma-ray burst viewed off axis. In Sec. 7.4 we utilise the multi-wavelength non detections and the spectrum to build evidence for CDF-S XT1 being the X-ray afterglow of a short gamma-ray burst produced by the merger of a neutron star binary. In Sec. 7.5 we discuss the weaknesses of the alternative interpretations. We conclude and discuss the implications of our results in Sec. 7.6.

7.2 Method

CDF-S XT1 was observed on October 1, 2014. The first photon arrived 1.68×10^4 s into the observation period (Bauer et al., 2017). During the subsequent ~ 100 s, the photon count rate sharply increased, before decreasing over the next $\sim 10^5$ s. We develop a new method for analysing the data of CDF-S XT1 to fit the data with various models and infer parameters of the burst including the time of the prompt emission, density of the interstellar medium, the opening angle and energetics of the relativistic jet, and the observer viewing angle. We use individual photon arrival times from the source region of CDF-S XT1 as defined in Bauer et al. (2017) with a 0.26″ spatial extraction region. We use the Chandra Interactive Analysis of Observations (CIAO) (Fruscione et al., 2006) software package to extract 115 source photons in the $0.3 - 7$ keV energy range. Given the location of the transient and the point-spread function, this observation is unlikely to suffer from pileup (two incident photons count as one, or get rejected) (Bauer et al., 2017). There are no other photons in this region across the entire observation.

The first photon has been the source of debate, with Sun et al. (2019) considering that photon to be consistent with the background. We analyse the entire $\approx 5 \times 10^4$ s observation epoch to determine whether this photon is consistent with the background. We calculate the background rate from an off-source region to be 3×10^{-5} cts s^{-1}. Given this rate, the probability that one background photon arrives within ~ 50 s of all the other photons is 1×10^{-4}, suggesting that it is unlikely this photon is consistent with the background. Conversely, given our fitting allows us to estimate the source rate, the probability that this photon is from the source is $\gtrsim 74\%$.

We use the raw photon time of arrivals from *Chandra* that are binned with a constant bin size of $\Delta T = 3.2$ s across the entire observation period. We perform Bayesian inference using a Poisson likelihood on this binned data. Our likelihood is,

$$\mathcal{L}(\vec{d}|\vec{\theta}) = \prod_i \frac{r_i \Delta T e^{-r \Delta T}}{k_i!}, \tag{7.1}$$

where r_i is the rate of photons in the ith bin, k_i is the number of photons in that bin, and ΔT is the bin size. We calculate the rate in the ith bin using,

$$r_i = \frac{\sigma_i \int_{0.3\,\text{keV}}^{7.0\,\text{keV}} F(t_i, \vec{\theta}, \nu) d\nu}{E_i} + \Lambda_{\text{background}}, \tag{7.2}$$

where σ_i is the effective area of the detector, E_i is the averaged energy of the photons in the given area, $F(t_i, \vec{\theta}, \nu)$ is the flux density of our model at time t_i at a given frequency ν with associated vector of parameters $\vec{\theta}$, and $\Lambda_{\text{background}}$ is the background rate. We note that this expression is an approximation and calculation of the true rate requires modelling the detector response and point-spread function. However, the uncertainties caused by this approximation are small compared to model uncertainties. We calculate the flux density using the smooth power-law structured jet model in AFTER-GLOWPY (Ryan et al., 2019) with inverse Compton emission and jet spreading. We note that we also perform inference without these effects and our conclusions do not change. The smooth power-law structured jet model defines the energy distribution of the jet as,

$$E(\theta_{\text{obs}}) = E_0 \left(1 + \frac{\theta_{\text{obs}}^2}{\beta \theta_{\text{core}}^2}\right)^{-\beta/2}. \tag{7.3}$$

Here β, is the exponent dictating the slope of the power-law jet structure. The Lorentz factor of the jet follows $E_{\theta_{\text{obs}}}^{1/2}$, with an initial Lorentz factor Γ_0. There is an additional parameter, θ_{wing} which is a truncation angle outside of which the energy is initially zero. This structured jet interacts with the surrounding interstellar medium accelerating a fraction of electrons, ξ_n, with a fraction of the total thermal energy, ϵ_e and fraction of the thermal energy in the magnetic field, ϵ_b. The synchrotron radiation produced by these electrons is responsible for the emission we observe. We set the flux before the onset of the burst T_{start} to zero. We sample over the redshift by putting a uniform prior on z between $0.39 - 3.21$ corresponding to the 95% credible interval from the host galaxy photometric redshift. We use Planck-15 cosmology to convert the redshift into a luminosity distance to the source (Planck Collaboration et al., 2016).

To reduce the computational cost, we use a larger binning size of $\Delta T = 64\,\text{s}$ compared to the raw data. We verify there is no systematic bias introduced by this larger bin size by repeating the calculation with different bin sizes with AFTERGLOWPY. We infer consistent parameters across $\Delta T = 64, 128, 256\,\text{s}$. We note that bin sizes larger than 256s destroy the structure of the data and change the results. To ensure there is no bias introduced by not using the raw data, we also train a neural network algorithm to compute the flux density, calibrating it to the output of AFTERGLOWPY. This trained model can be evaluated approximately three orders of magnitude faster than

AFTERGLOWPY making the analysis tractable with the raw data, but it introduces a systematic uncertainty due to the nature of machine learning. We infer consistent posteriors (at $1 - \sigma$) with the neural network model on the raw data binned at $\Delta T = 3.2\,\mathrm{s}$ and the larger bin sizes with AFTERGLOWPY. We have also verified that our machine learning model is accurate by performing tests on untrained data, simulating signals generated with AFTERGLOWPY and recovering them with consistent parameters with the trained neural network model using the infrastructure described here. We will present details of the neural network model in future work.

7.3 An off-axis gamma-ray burst

Several properties of CDF-S XT1 are consistent with a gamma-ray burst afterglow, including the event rate (Bauer et al., 2017; Sun et al., 2019). Firstly, the energetics and high redshift ($z = 2.23^{+0.98}_{-1.84}$) demands a highly energetic transient, with upwards of 10^{50} erg of energy. The non-thermal spectrum immediately rules out any thermal transient such as a supernova, while the fast rise and slow decay rule out a persistent non-thermal source. These properties, in particular the rise and slow decay are indicative of an off-axis gamma-ray burst afterglows (Granot et al., 2002). Moreover, the declining spectrum and rising lightcurve is likely due to misaligned evolution i.e., $\theta_{\mathrm{obs}} > \theta_{\mathrm{core}}$ (e.g., Ryan et al., 2019).

To investigate the above interpretation in detail, we first consider the X-ray data. We apply our method described in Sec. 7.2 and fit the X-ray data of CDF-S XT1. We infer the parameters of the system using BILBY (Ashton et al., 2019) and the PYMULTINEST sampler (Feroz et al., 2009). In Tab. 7.1 we list the full set of parameters $\vec{\theta}$, their descriptions, their associated priors used in the analysis, and their posteriors with 68% posterior credible interval.

In Fig. 7.1, we plot the raw X-ray photon counts detected by Chandra in the $0.3 - 7.0\,\mathrm{keV}$ band. For visualisation purposes, we bin the photon arrival times with a bin size of $128\,\mathrm{s}$. Times in Fig. 7.1 are referenced to our estimated burst start time. In red, we show model-predicted counts from 100 random draws of the posterior distribution. In the same Figure, we also show a schematic view of the physics creating the various features of the light curve. In particular, the jet slowing and subsequent broadening of the beaming cone give rise to the sharp increase in photon count seen approximately $100\,\mathrm{s}$ after the burst.

We measure the observer angle to be $\theta_{\mathrm{obs}} = 10° \pm 3°$ and the core of the jet to be $\theta_{\mathrm{core}} = 4.4° \pm 0.9°$. This implies that CDF-S XT1 was observed from outside the jet-core naturally explaining the lack of prompt gamma-ray emission due to relativistic beaming.

TABLE 7.1: Parameters associated with the smooth power-law structured jet model along with a brief description, the prior used in our analysis and the posterior. We note that the posterior values quoted here are from analysis with the neural network model run on data binned at $\Delta T = 3.2$s.

Parameter [unit]	Description	Prior	Posterior
T_{start} [s]	burst start time into the observation	Uniform$[10, 16800]$	16784^{+9}_{-13}
z	redshift	Uniform$[0.39, 3.21]$	$1.7^{+0.8}_{-0.7}$
Γ_0	initial Lorentz factor	Uniform$[1, 1000]$	420^{+300}_{-240}
$\Lambda_{\text{background}}$ [counts/s]	background rate	log Uniform$[10^{-6}, 10^{-4}]$	$10^{-4} \pm 10^{-5}$
θ_{obs} [°]	observers viewing angle	Cosine$[0, 0.7]$	$10° \pm 3°$
$\log_{10}(E_{\text{iso}}/\text{erg})$	isotropic-equivalent energy	Uniform$[10^{44}, 10^{54}]$	52.2 ± 0.5
θ_{core} [°]	half-width of jet core	Uniform$[0.01, 0.1]$	$4.4° \pm 0.9°$
θ_{wing} [°]	wing truncation angle of the jet	Uniform$[0.01, 0.7]$	$10° \pm 3°$
β	power for power-law structure	Uniform$[0.5, 10]$	4.7 ± 1.7
$\log_{10}(n_{\text{ism}}/\text{cm}^{-3})$	number density of ISM	Uniform$[-5, 2]$	$1.8^{+0.6}_{-0.8}$
p	electron distribution power-law index	Uniform$[2, 3]$	2.2 ± 0.1
$\log_{10}\epsilon_e$	thermal energy fraction in electrons	Uniform$[-5, 0]$	-0.7 ± 0.3
$\log_{10}\epsilon_b$	thermal energy fraction in magnetic field	Uniform$[-5, 0]$	-0.8 ± 0.5
ξ_N	fraction of accelerated electrons	Uniform$[0, 1]$	0.8 ± 0.2

We derive the start time of the burst to be $T_{\text{start}} = 16784^{+9}_{-13}$ s into the observation which implies that the afterglow peaks approximately 150 s after the predicted time of the prompt emission. Within our off-axis interpretation, this peak timescale t_{peak} is dictated by the timescale for the edge of the ultra-relativistic core to start becoming visible to the off-axis observer i.e., for $\Gamma(\theta_{\text{obs}} - \theta_{\text{wing}}) \sim 1$. A back-of-the-envelope estimate for this peak timescale is (e.g., Nakar & Piran, 2021)

$$t_p \approx 130 \, \text{d} \left(\frac{E}{10^{51} \, \text{erg}} \frac{10^{-3} \, \text{cm}^{-3}}{n_{\text{ism}}} \right)^{1/3} \left(\frac{\theta_{\text{obs}} - \theta_{\text{wing}}}{15°} \right)^2 .$$

From our estimated parameters, this gives $t_p \sim 700$ s, which is comparable to the observations.

We note that this peak timescale is different to the peak timescale seen for GRB170817A, which came 160 d following the prompt. That peak time was the jet break time. For CDF-S XT1 this can be estimated by (e.g., Granot et al., 2018)

$$t_{\text{break}} = 70 \, \text{d} E_{51}^{1/3} n_0^{-1/3} \theta_{\text{obs}}^2 .$$

From our estimated parameters this is $t_{\text{break}} \sim 4$ days, which is significantly shorter than the t_{break} of GRB170817A. However, this discrepancy in timescales is not inconsistent and can be ascribed to the smaller viewing angle θ_{obs} and the higher interstellar medium density n_{ism} for CDF-S XT1.

Our inferred estimates for the isotropic energy is also consistent with a back-of-the-envelope estimate. The reported fluence for CDF-S XT1 is $4.2^{+3.5}_{-0.2} \times 10^{-9}$erg cm^{-2} (Bauer et al., 2017). At a redshift of $z = 2.23$, this implies a jet with energy $\sim 10^{50}$ erg, which is comparable to the estimated jet
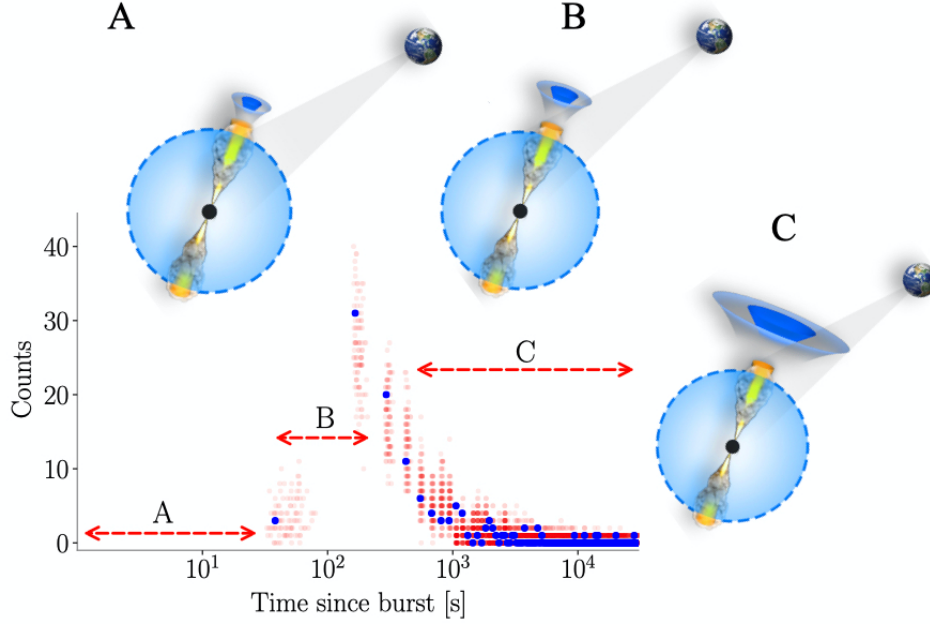
FIGURE 7.1: **CDF-S XT1 data and model light curves**. X-ray counts as a function of time binned at $\Delta T = 128$s intervals in blue, and posterior predictions for the off-axis short gamma-ray burst model in red. The schematic illustrates the physical process responsible for the different observational epochs. In epoch A, the observer sees no emission as the ultra-relativistic jet (blue cone) and mildly relativistic wings (grey cone) are beamed away from Earth's line of sight. As the structured jet slows, its beaming cone broadens such that the mildly relativistic wings are now in Earth's line of sight. At this point, the observer on Earth starts to see X-ray photons from the source (epoch B). As the jet slows down further it continues to broaden at which point the jet core becomes visible to the observer on Earth and the photon rate peaks (epoch C). The subsequent gradual decay is a product of further slowing down of the jet and subsequent broadening of the jet.

energy from our analysis. Comparing the energetics CDF-S XT1 to X-ray afterglows seen in other gamma-ray bursts, the total energy radiated in X-rays of CDF-S XT1 would be lower by two orders of magnitude compared to the dimmest X-ray afterglows we see unless CDF-S XT1 is at $z \gtrsim 2$. Although, since CDF-S XT1 is observed off-axis, some difference in brightness is to be expected.

Although Figure 7.1 shows the fit on a 128 s binned timescale, we infer similar parameters across all bin sizes i.e., our conclusion is robust to the choice of binning. Similarly, even accounting for the redshift uncertainty, our results and conclusion are quantitatively similar: CDF-S XT1 is consistent with being an orphan afterglow of an off-axis gamma-ray burst. We note that the posterior values mentioned above and those listed in Tab. 7.1 are marginalised over the redshift uncertainty. We sample over the redshift to account for this uncertainty in our estimated parameters and ensure that our results are not affected by assuming a fixed redshift. Our posterior on the

redshift is effectively the prior and therefore when discussing the results we work with the assumption that CDF-S XT1 occurred at $z = 2.23$, i.e., the most likely redshift of the host galaxy.

To probe the nature of CDF-S XT1, the source region was searched in several other electromagnetic bands. In optical, the Very Large Telescope (VLT) observed the location of the transient 80 minutes after the arrival of the first photon, and again 18 days later, setting stringent *r*-band upper limits (Treister et al., 2014; Bauer et al., 2017). The Hubble Space Telescope (HST) searched the source region 111 days after the first X-ray observations, setting the most sensitive limits for the source region in the *F110W* filter (Bauer et al., 2017). In radio, the Australian Telescope Compact Array (ATCA) observed the source region seven days after the first X-ray photons, setting limits at different radio frequencies (Burlon et al., 2014). In gamma rays, neither *Swift* nor *Fermi* had coverage in the direction of CDF-S XT1 for the few hours surrounding the event (Bauer et al., 2017). None of these observations found a counterpart to CDF-S XT1. To correctly identify the nature of CDF-S XT1, we must be able to explain these non-detections. Gamma-ray burst afterglow models make reliable predictions about emission across all of these bands. Therefore these non-detections can be used to verify our proposed off-axis gamma-ray burst hypothesis.

We evaluate the predicted flux density light curves in optical at 640 nm and 1179 nm, and radio at 5 GHz, corresponding to the VLT *r*-band, HST *F110W*-band, and ATCA observations, respectively. We show these lightcurves, as well as the upper limits in optical and radio in Fig. 7.2 at a fixed redshift $z = 2.23$ corresponding to the median value of the host galaxy photometric redshift for easier comparison. The left and middle panels show the optical light curves for 100 different samples randomly drawn from our posterior distribution as predicted in the VLT *r*-band and the HST *F110W*-band, while the right panel shows the corresponding flux density in the radio band. The black arrows indicate the upper limits set by VLT, HST and ATCA in the left, middle and right panels, respectively.

We estimate the total extinction from its association with the neutral hydrogen column density, which we infer from the spectra. We infer a total extinction of $A_V = 5.96^{+6.98}_{-3.22}$ at a redshift $z = 2.23$, largely due to the strong redshift dependence of the inferred hydrogen column density (Bauer et al., 2017). In Fig. 7.2, These observed upper limits are above the corresponding optical and radio light curve predictions, consistent with the non-detections in these electromagnetic bands. We note that in Fig. 7.2 we have used the median value of $A_V = 5.96$ as the total extinction in the *r*-band. The *F110W*-band and radio do not suffer such high extinction due to the behaviour of interstellar extinction curves at these wavelengths. Given our uncertainty on the extinction, we estimate that there is a less than 10^{-4} % probability that the optical afterglow in *r*-band would have been detectable. It is worth noting that our inferred extinction values are significantly higher than those inferred for other gamma-ray bursts. This is a product of our choice of the dust-to-gas

ratio (Güver & Özel, 2009) and the strong redshift dependence of the inferred hydrogen column density.
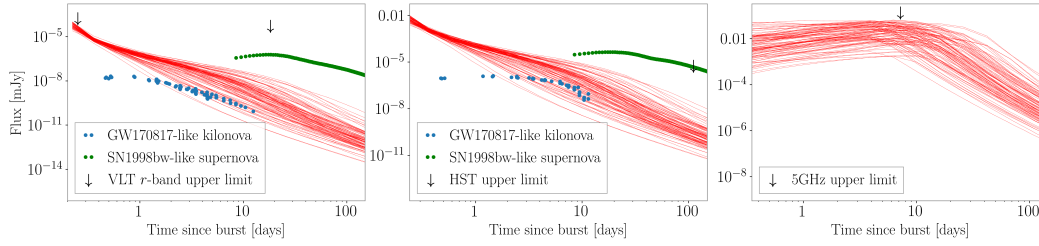
FIGURE 7.2: Optical and radio upper limits are above predictions from our model. Flux density in optical ($\lambda = 640$nm; left panel, and $\lambda = 1179$nm; middle panel) and radio (5GHz; right panel), with arrows representing VLT, HST and ATCA upper limits, respectively (Bauer et al., 2017). Each red curve is a predicted light curve, calculated by drawing parameters randomly from our posterior probability distribution. The arrows correspond to upper limits derived from VLT, HST and ATCA observations respectively (Treister et al., 2014; Burlon et al., 2014). The blue points are data from the kilonova associated with GW170817 but scaled assuming a redshift of $z = 2.23$. Likewise, the green points are the data for supernova SN1998bw but scaled to a redshift of $z = 2.23$. Our posterior predictive models are consistent with the interpretation of this event as a compact object coalescence, but not necessarily with that of a supernova.

In gamma rays, neither *Swift* nor *Fermi* had coverage in the direction of CDF-S XT1 for the few hours surrounding the event (Bauer et al., 2017). Our inferred parameters from fitting the X-ray data and the large redshift implied from the identification of the host galaxy imply no prompt emission would have been detected from this system even with gamma-ray coverage. Furthermore, the inferred parameters can explain the non-detections in other electromagnetic bands. This analysis above suggests CDF-S XT1 is potentially the first orphan afterglow detected in X rays and one of the most distant orphan afterglow candidates ever.

7.4 A compact object merger?

Having established that CDF-S XT1 is potentially an orphan X-ray afterglow of a gamma-ray burst we now turn to answer whether CDF-S XT1 is an orphan afterglow of a long or short gamma-ray burst? In other words, was this the orphan afterglow due to the collapse of a massive star, or the merger of a neutron star binary? Here, we investigate the various properties of CDF-S XT1 and the multi-wavelength observations to answer this question.

A short gamma-ray burst would likely be accompanied by an optical/infrared kilonova, such as AT2017gfo for GW170817 (e.g., Abbott et al., 2017c) and several other short gamma-ray bursts. Similarly, a long

gamma-ray burst should be accompanied by a core-collapse supernova, such as the case for GRB980425 accompanied by SN1998bw (e.g., Clocchiatti et al., 2011) and GRB111209A accompanied by SN2011kl (e.g., Greiner et al., 2015). In the left and middle panels of Fig. 7.2 we show the prediction for a GW170817-like kilonova (blue points) and a SN1998bw-like supernova (green points) if either had accompanied CDF-S XT1 at $z = 2.23$. We pick SN1998bw as it is a relatively dim supernova to accompany a long gamma-ray burst, and largely due to its proximity, the best observed. In particular, we take data from AT2017gfo and scale it to a distance of $z = 2.23$. The VLT upper limits being above the blue points indicates that the kilonova associated with GW170817 would not have been seen by VLT had it been at a redshift of $z = 2.23$. Moreover, that the red predictive curves are consistent with the GW170817-like kilonova indicate too that, if CDF-S XT1 was a short gamma-ray burst with associated kilonova, one would not have expected to see it with VLT observations.

The green dots on the left and middle panels of Fig. 7.2 take the r and i-band observations from SN1998bw, respectively, and scale them to a distance of $z = 2.23$. We note that SN1998bw was not observed by HST and the i-band observations are likely a lower estimate of what SN1998bw would have looked like realistically with HST. SN1998bw was a relatively dim supernova compared to other supernovae that accompany long gamma-ray bursts (e.g., Clocchiatti et al., 2011). That the green dots are close to the HST upper limit implies an SN1998bw-like supernova would have been marginally detectable. Had a brighter supernova been associated with CDF-S XT1, it would have been potentially observed by the HST. This deep constraint from HST rules out most potential supernovae up to a redshift $z \sim 2$ (Richardson et al., 2014). A similar point could be made for the VLT observations if this system does not suffer from severe extinction. If a supernova accompanied CDF-S XT1, it would have had to be relatively dim to not be observed by HST. We note that there have been observations of long gamma-ray bursts without an accompanying supernova, however, these are likely due to observational selection effects (Lyutikov, 2013). This non-detection of a supernova adds weight to the hypothesis that the progenitor of CDF-S XT1 was the merger of a neutron star binary rather than the collapse of a massive star.

The star-formation rate ($1.15 \pm 0.04 \ M_\odot \mathrm{yr}^{-1}$) of the putative host galaxy CANDELS 28573 and the off-set (0.13") are also consistent with other short gamma-ray bursts (Bauer et al., 2017; Sun et al., 2019). We note that the uncertainty in the location of the transient is smaller than the size of a typical galaxy, such that the effect of the incompleteness of galaxy catalogues does not significantly affect this association. Furthermore, given the implied high redshift, a requirement based on energetics, the effect of the supernova kick also does not add significant uncertainty to affect this association. We note that our inferred interstellar medium density suggests that the gamma-ray burst was not significantly offset from the host. The mass of the host galaxy is on the smaller end for short gamma-ray bursts, while the star formation

rate is comparable. However, the limited number of known short gamma-ray bursts beyond redshift $z \approx 2$ implies this is not a statistically robust statement (Sun et al., 2019).

Our inferred interstellar-medium density $\log_{10}(n_{\text{ism}}/\text{cm}^{-3}) = 1.8^{+0.6}_{-0.8}$ is more akin to long gamma-ray bursts than short (Fong et al., 2015). However, approximately 5 to 20% of short gamma-ray bursts (Fong et al., 2015) have $n_{\text{ism}} \gtrsim 1\,\text{cm}^{-3}$. Moreover, systematic studies of interstellar-medium densities to date typically fix the energy fraction in the magnetic field and electrons, which systematically underestimates n_{ism}. We do not fix these parameters but instead marginalise over this uncertainty.

Finally, we consider the implied spectrum of CDF-S XT1. Gamma-ray bursts show an empirical correlation between the isotropic gamma-ray energy and the rest-frame peak energy in gamma-rays. For long gamma-ray bursts this is known as the Amati correlation (Amati, 2006), which differs from that measured for short gamma-ray bursts with observed redshifts. Therefore, identifying the consistency with the Amati relation offers another way to probe whether the gamma-ray burst is long or short (e.g., Amati, 2006; Minaev & Pozanenko, 2020).

We use our inferred isotropic energy from the afterglow and the full range of observed prompt emission gamma-ray efficiencies (Fong et al., 2015) to determine the isotropic energy in gamma rays emitted from CDF-S XT1, finding $\log_{10}(E_{\gamma,\text{iso}}/\text{erg}) = 50 \pm 0.6$. We use the relation between the X-ray photon index and rest-frame peak energy (Virgili et al., 2012) to infer the rest-frame peak energy, $E_{\text{peak,z}} = 830^{+1200}_{-500}$ keV. We note that this relation is derived from photon indices from the tail of the prompt emission or the early X-ray afterglow of on-axis gamma-ray bursts, and so may not apply for CDF-S XT1. However, data for many gamma-ray bursts shows a consistent photon index between the tail of the prompt and late-time X-ray afterglow (e.g., Wang et al., 2015).

To ameliorate this potential issue, we also estimate the $E_{\text{peak,z}}$, through the three-parameter correlation between the X-ray ($E_{\text{x-ray,iso}}$), gamma-ray ($E_{\gamma,\text{iso}}$) isotropic energies and E_{peak}, derived from a large sample of gamma-ray bursts (Margutti et al., 2013). We emphasise that both these analyses are agnostic to whether a gamma-ray burst is from the collapse of a massive star or the merger of a neutron star binary. However, we note that while these analyses hold for on-axis gamma-ray bursts, they potentially may not for an off-axis gamma-ray burst. In Fig. 7.3, we show that the inferred parameters for CDF-S XT1 using both the Virgilli (orange) and Margutti (blue) correlations are inconsistent with observed long gamma-ray bursts and the Amati relation. However, these parameters are consistent with several observed short gamma-ray bursts. This adds significant weight to the hypothesis that CDF-S XT1 is the orphan afterglow of a short gamma-ray burst produced in the merger of a neutron star binary.
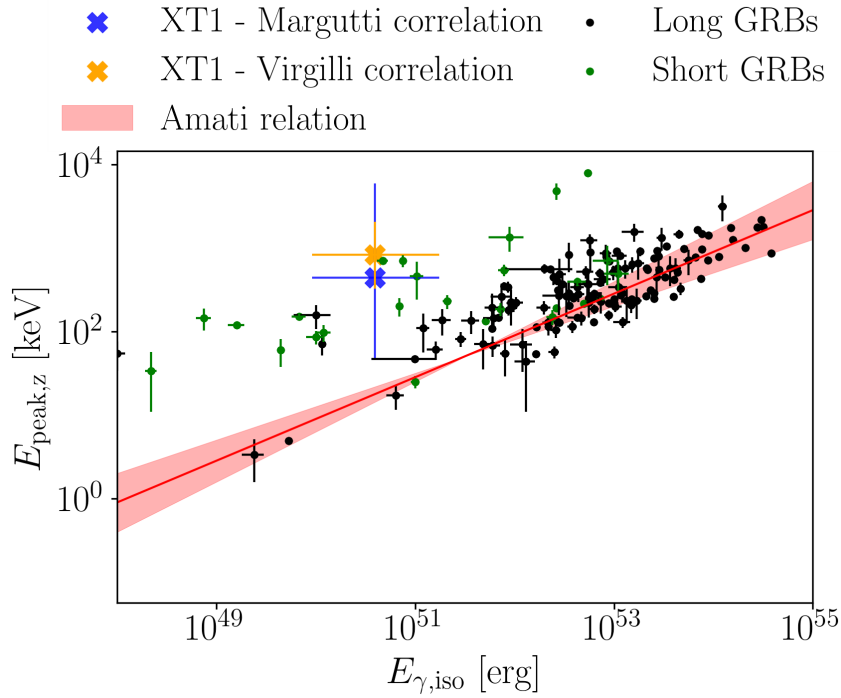
FIGURE 7.3: The observed isotropic gamma-ray energy and peak rest-frame energy of a sample of observed long (black) and short (green) gamma-ray bursts (Minaev & Pozanenko, 2020). The empirical Amati relation and associated uncertainty is shown in red. In blue, we show the observed isotropic gamma-ray energy of CDF-S XT1 obtained by using the three-parameter correlation from Margutti et al. (2013), while in orange we show the same parameters but obtained using the Virgilli correlation (Virgili et al., 2012), the error bars correspond to the 68% credible interval. The uncertainty on these parameters is obtained by propagating uncertainties in the spectral slope, the inferred kinetic energy and the distribution of gamma-ray radiative efficiencies (e.g., Fong et al., 2015; Wang et al., 2015) and the correlation itself. CDF-S XT1 is inconsistent with the Amati relation, while being consistent with observed short gamma-ray bursts, adding weight to our argument that CDF-S XT1 is the X-ray afterglow of a binary neutron star merger. Note that the Amati relation is derived from a significantly larger sample of observed gamma-ray bursts than shown here (Minaev & Pozanenko, 2020).

7.5 Alternative interpretations

Three alternate explanations were offered for this transient in the discovery paper (Bauer et al., 2017) and explored briefly elsewhere (Sun et al., 2019; Peng et al., 2019; Alp & Larsson, 2020). Here we critically assess each of these scenarios, providing a summary of the different scenarios and their failure to explain observations in Tab. 7.2.

It has been argued that CDF-S XT1 could be a supernova-shock breakout from a core-collapse supernova (Bauer et al., 2017; Alp & Larsson, 2020) in

TABLE 7.2: Class of systems and emission mechanisms and whether they can explain the different observational constraints on CDF-S XT1. Note that to preserve structure of the manuscript within the thesis format, this table is different to the version that appears in (Sarin et al., 2021a).

Emission mechanism	Spectrum	Luminosity	Optical constraints	Host-galaxy
Tidal disruption event	?	x	✓	✓
Jetted tidal disruption event	?	x	?	✓
Supernova-shock breakout	x	x	x	✓
LGRB orphan afterglow	x	✓	?	✓
SGRB orphan afterglow	✓	✓	✓	✓
Kilonova with energy injection	?	✓	?	✓

which the shock wave from the supernova blasts out of the progenitor star's surface. While the timescale and steep-rise/gradual decay of the light curve is consistent with such phenomena, the spectrum is not. Supernova shock-breakouts are thermal transients and the radiation they produce is typically soft X rays or ultra-violet depending on the temperature of the system (e.g., Tominaga et al., 2011). For typical shock breakouts, the dominant emission is expected at $0.01 - 1\,$keV i.e., a thermal spectrum, inconsistent with the non-thermal spectrum of CDF-S XT1. Although, the supernova shock breakout observed in SN2008D, was distinctly non-thermal (e.g., Soderberg et al., 2008). Furthermore, the peak luminosity from typical supernova-shock breakouts (Tominaga et al., 2011) of $10^{44} - 10^{45}\,$erg is inconsistent with the inferred peak luminosity of CDF-S XT1 at $z \gtrsim 0.4$. To explain the observations of CDF-S XT1 at $z = 2.23$, a supernova-shock breakout would have to be more energetic than the most energetic shock-breakout observed by two orders of magnitude. Importantly, a supernova-shock breakout will also be accompanied by a supernova. However, the upper limits set by HST observations confidently rule out a supernova at redshift $z \lesssim 2$ (Richardson et al., 2014). The combination of these constraints suggests that the supernova-shock breakout scenario is a poor explanation of the observations: the supernova-shock breakout would have to be exceptionally bright but accompanied by a relativity dim supernova and explain the hard spectrum. While we cannot definitively rule out a supernova-shock breakout, the event would be like nothing else we have seen before.

It has been suggested that CDF-S XT1 could be caused by a tidal disruption event (Bauer et al., 2017; Peng et al., 2019). The fast rise and hard X-ray flux of CDF-S XT1 imply that the only viable part of the parameter space for a tidal disruption event that can explain the observations is a compact white dwarf around an intermediate-mass black hole of around $10^3 - 10^4 M_\odot$ (Bauer et al., 2017; Peng et al., 2019). However, such a scenario is problematic because the Eddington limit for such a system is $2 - 3$ orders of magnitude below what is required given the associated redshift (Bauer et al., 2017). This discrepancy in energy could be explained by a strongly beamed, jetted tidal disruption event. One would expect such a scenario to

also be observed in radio and optical as is the case for other jetted tidal disruptions (Cenko et al., 2012) which also have longer decay timescales. However, we do not observe radio and optical counterparts and a long decay timescale is inconsistent with the decay of CDF-S XT1. The only proposed way to generate sufficient magnetic fields to create a jetted tidal disruption event is by anchoring the magnetic field to a black hole (Tchekhovskoy et al., 2014) or through a highly magnetised star from a recent merger (e.g., Mandel & Levin, 2015). In both cases, the timescale for the rise and decay of the light curve would be significantly longer than that observed in CDF-S XT1 and inconsistent with the observations.

Finally, a more exotic scenario was developed to explain both CDF-S XT1 and CDF-S XT2 in a unified framework as being the emission from a millisecond magnetar combined with the kilonova from the ejecta of a neutron star merger (Sun et al., 2019). In this scenario, CDF-S XT1 was a neutron star merger that produced a remnant neutron star that acted as a central engine injecting energy into the surrounding ejecta. To explain the lack of detection in optical, such a system would need to be unusually dim given the additional energy injection, which is possible for comparatively lower ejecta masses than for the kilonova associated with GW170817. However, the ejecta cannot be too small either, as such a system would then not be optically thick and not explain the rise seen in the light curve of CDF-S XT1. It is important to note that the typical timescale for such a system to become optically thin is $\sim 9\,\mathrm{hr}$ (Metzger & Piro, 2014), which would imply such a model is inconsistent with CDF-S XT1. However, there is substantial latitude in the timescale given the uncertain opacity of the ejecta. Furthermore, the spectrum from such a model would be a combination of the non-thermal spectrum from the spin-down of the nascent neutron star and quasi-thermal spectrum from the ejecta, which is at odds with the non-thermal spectrum inferred for CDF-S XT1. Moreover, this model requires the formation of an infinitely stable neutron star We note that to explain the observations of CDF-S XT1 with such a model, Sun et al. (2019) considered the first photon of the observation as being consistent with the background—in Sec. 7.2 we argue that the first photon was from CDF-S XT1, implying their fit to CDF-S XT1 is inconsistent with the data.

Even with an afterglow interpretation, there are other ways to interpret the data. Within our interpretation, to explain the relatively fast rise and subsequent decay, the data requires the jet to be truncated near the observer. The angle at which the jet truncates is set by θ_{wing}, which we keep as a free parameter. This implies that the jet energy drops sharply at an angle close to the observer. Such a sharp drop is implicitly built into other jet models such as the top-hat (e.g., Ryan et al., 2019). We analyse the data by not allowing such a sharp drop in energy by fixing $\theta_{\mathrm{wing}} = f \times \theta_{\mathrm{core}}$ where f is some factor such that the jet energy is ≈ 0, i.e., we do not truncate the jet. Such a model is perhaps more plausible than one with a sharp drop, although without detailed

hydrodynamical simulations or extensive observations of off-axis gamma-ray bursts one cannot know for certain what the true jet structure is. We note that past hydrodynamical simulations do produce sharp drops in jet energy (e.g., Aloy et al., 2005).

If instead, we demand a jet structure that does not truncate, we would need to explain the rise time with the pre-deceleration behaviour of an on-axis relativistic jet. Fixing $f = 8$, and fitting to the data, we find that the data can be explained by having a weakly relativistic jet with Lorentz factor $\Gamma_0 = 46^{+30}_{-20}$ and the observer being on-axis. In such a scenario, the rise and decay can be explained by the deceleration of a low Lorentz factor ($\lesssim 100$) jet. Such a relativistic jet may not produce prompt gamma-rays due to the pair production threshold for gamma-ray production, also known as the compactness problem. However, the threshold for prompt gamma-ray emission is not well understood. Such gamma-ray bursts are also known as failed gamma-ray bursts or dirty fireballs (e.g., Huang et al., 2002; Rhoads, 2003). We note, however, that this solution is not preferred by the data, with a Bayesian odds, assuming both hypotheses are equally likely, of $\mathcal{O} = 3.3$ in favour of truncating the jet. That is, the solution suggesting the jet truncates near the observer is ~ 3 times more favourable than not.

7.6 Implications and Conclusions

Considering the limitations of the other three models posed in the literature (see Sec. 7.5 and Tab. 7.2 for a summary) and the success of the orphan afterglow interpretation presented here in explaining the various constraints, we believe CDF-S XT1 is the orphan afterglow of an off-axis gamma-ray burst. This makes CDF-S XT1 potentially one of the first orphan afterglows ever detected, considering the uncertain nature of other candidates (e.g., Cenko et al., 2012; Marcote et al., 2019; Ho et al., 2020; Sarin et al., 2021b). The method developed here is ideally suited for detecting orphan afterglows from other X-ray surveys.

Our inferred parameters, the host galaxy properties, optical upper limits, and inconsistency with the empirical Amati relation imply that CDF-S XT1 is more likely to be the afterglow of a short gamma-ray burst afterglow than a long, implying the most likely progenitor model is that of a binary neutron star coalescence similar to the first multimessenger gravitational-wave detection GW170817 (Abbott et al., 2017b,c). This has far-reaching implications. Most notably, at a potential redshift of $z = 2.23$, this is likely one of the most distant short gamma-ray burst ever observed (GRB090426, with a redshift of $z = 2.61$, was initially classified as a short gamma-ray burst (Antonelli et al., 2009), but is now likely considered a long gamma-ray burst (Levesque et al., 2010)).

Observing neutron star mergers so early in the Universe has implications for our understanding of stellar evolution. The best-fit redshift for CDF-S XT1 places it before the peak of star formation, implying the binary that merged to produce the gamma-ray burst must have formed and merged on a relatively short timescale. Population synthesis studies estimate that the rate for short gamma-ray bursts peaks in the redshift range $z = 0.6$–1 (Wiggins et al., 2018), similar to observations of short gamma-ray bursts with known redshifts (Fong et al., 2015). The existence of CDF-S XT1 and its potential progenitor being the merger of a neutron star binary suggests that the rate of the merger of these systems at high redshifts is not negligible, which has important implications for understanding binary stellar evolution and for detecting gravitational waves from mergers of these objects. Furthermore, it may imply that there are significant short delay-time binary neutron star mergers, which may mean that a relatively high fraction of binary mergers occurs in dense stellar environments such as globular clusters, or that common-envelope evolution is more efficient at reducing the orbital separation than previously realised. This also has implications for the offset of short gamma-ray bursts from their host galaxy, particularly at higher redshifts.

A neutron star merger progenitor hypothesis for CDF-S XT1 also has implications for heavy element nucleosynthesis. The multimessenger observations of GW170817 confirmed that binary neutron star mergers are the production sites of heavy r-process elements such as gold, which are difficult to produce in ordinary supernovae. However, owing to the relative lack of expected mergers at high redshifts, they are not believed to be the only source (Siegel et al., 2019). If instead there are more neutron star mergers at high redshifts than otherwise expected, this could imply that these systems play a more critical role in the chemical evolution of the Universe.

Chapter 8

Low-efficiency long GRBs: A case study with AT2020blt

Abstract

The Zwicky Transient Facility recently announced the detection of an optical transient AT2020blt at redshift $z = 2.9$, consistent with the afterglow of a gamma-ray burst. No prompt emission was observed. We analyse AT2020blt with detailed models, showing the data are best explained as the afterglow of an on-axis long gamma-ray burst, ruling out other hypotheses such as a cocoon and a low-Lorentz factor jet. We search *Fermi* data for prompt emission, setting deeper upper limits on the prompt emission than in the original detection paper. Together with KONUS-*Wind* observations, we show that the gamma-ray efficiency of AT2020blt is likely lower than 98.4% of observed gamma-ray bursts. We speculate that AT2020blt and AT2021any belong to the low-efficiency tail of long gamma-ray burst distributions that are beginning to be readily observed because of the capabilities of new facilities like the Zwicky Transient Facility.

8.1   Introduction

The interaction of an ultra-relativistic jet launched in a gamma-ray burst with the surrounding interstellar medium is known to produce broadband synchrotron radiation referred to as an afterglow. Observed extensively in X rays, optical and radio, these phenomena are observationally confirmed to be linked to the collapse of massive stars and compact object mergers (e.g., Cano et al., 2017; Abbott et al., 2017d).

Afterglows of gamma-ray bursts are predominantly observed following-up the prompt emission trigger. There are a few exceptional cases such as iPTF11gg (Cenko et al., 2012), iPTF14yb (Cenko et al., 2015), FIRSTJ141918 (Marcote et al., 2019), and AT2020blt (Ho et al., 2020). These transients were either independently detected from the prompt emission and later associated to a gamma-ray counterpart that were missed in low-latency (Cenko et al., 2015), initially believed to be observed off-axis, in which case the high-energy prompt emission was missed due to relativistic beaming (Marcote et al., 2019), or later shown to not be afterglows at all (Lee et al., 2020).

The transient AT2020blt (Ho et al., 2020) is a fast-fading optical transient at $z = 2.9$ observed by the Zwicky Transient Facility without any high-energy trigger from gamma-ray satellites. This transient has characteristic features akin to afterglows from gamma-ray bursts and broadband observations in X rays, optical, and radio (Singer et al., 2020; Ho et al., 2020). However, the non-detection of prompt gamma-ray emission is puzzling. Ho et al. (2020) suggest that this non-detection may be due to one of three reasons: 1) The prompt emission expected in gamma-rays was weak or missed due to occultation by the Earth. 2) The transient was the afterglow from an off-axis gamma-ray burst where the prompt gamma-rays were missed because of relativistic beaming. 3) AT2020blt was the afterglow of a dirty fireball, i.e., a gamma-ray burst with a low Lorentz factor ($\Gamma \lesssim 100$), such that the optically-thick environment absorbed the gamma-ray photons.

Prompt gamma-ray emission observed for both long and short gamma-ray bursts is likely produced by internal dissipation in an ultra-relativistic jet (e.g., Kumar, 1999). To produce a gamma-ray burst, the jet must be ultra-relativistic to avoided the compactness problem (Ruderman, 1975), i.e., that gamma-ray photons are above the pair production threshold and should only be observable if the jet is moving ultra-relativistically. This theoretical constraint has led to the placement of lower limits on the initial bulk Lorentz factor of $\Gamma_0 \gtrsim 100$ (e.g., Lithwick & Sari, 2001). The existence of relativistic jets following gamma-ray bursts has also been shown observationally, for e.g., through multi-wavelength observations of GRB 170817A (e.g., Mooley et al., 2018a; Lamb et al., 2018).

As an ultra-relativistic jet passes through the stellar/ejecta envelope, it creates a cocoon of shocked material. If the jet stalls within this envelope then such a *choked* jet will dissipate energy into the surrounding bubble of matter, forming a quasi-spherical *cocoon*, that will produce minimal prompt gamma-ray emission (e.g., Gottlieb et al., 2018). The interaction of the jet and/or cocoon with the interstellar medium is ultimately responsible for producing the broadband afterglow we see following almost all gamma-ray bursts.

The broadband observations of GRB 170817A confirmed that a relativistic jet successfully broke out of the ejecta and that the jet was likely structured i.e., the energy and Lorentz factor of the jet had some angular dependence. Although the exact jet structure is unknown, various phenomenological models such as a Gaussian or power-law structure can successfully explain the broadband afterglow observations of GRB 170817A (e.g., Troja et al., 2017; Lamb et al., 2018; Ryan et al., 2019). We note that although a jet without any angular dependence is possible (e.g., Aloy et al., 2005), it is unlikely as both the jet-launching mechanism and jet-breakout will likely produce some jet structure (e.g., Nakar, 2019).

In this letter, we investigate why there was no detection of prompt gamma-rays from AT2020blt by analysing the multi-wavelength data from Ho et al. (2020) with detailed afterglow models. In Sec. 8.2, we use the multi-wavelength observations and physical arguments to estimate when the associated gamma-ray burst happened. Using this estimated time, we fit the data with a structured-jet model and cocoon model. We introduce our structured-jet and cocoon models in Sec. 8.3 and perform Bayesian model selection to identify the more likely scenario. We explore the dirty fireball hypothesis by estimating the Lorentz factor in Sec. 8.4. We perform a sub-threshold search in *Fermi* data and discuss the efficiency of the unobserved prompt gamma-ray emission in Sec. 8.5. We discuss the implications of our results and conclude in Sec. 8.6. Our analysis suggests that AT2020blt is likely an on-axis low efficiency long gamma-ray burst. The lack of gamma-ray radiation can be attributed to the low radiative efficiency of AT2020blt. We find that the non detection in gamma rays with KONUS-*Wind* implies AT2020blt has a radiative efficiency $\lesssim 2.8\%$, weaker than 98.4% of the gamma-ray burst population.

8.2 Estimating the burst time

AT2020blt was first observed in the *r* band on 28 January 2020, by the Zwicky Transient Facility (Bellm et al., 2019). Follow-up observations provided detections in *g* and *i* bands along with detections in radio and X rays (Ho et al., 2020; Singer et al., 2020). No coincident gamma-ray trigger was found (Ridnaia et al., 2020; Ho et al., 2020). The lack of a gamma-ray trigger implies that we do not know the burst time t_0, which is critical for discerning physics and testing the various hypotheses in detail.

Ho et al. (2020) estimated the burst time by fitting a broken power-law simultaneously to the *r*, *g* and *i* band data assuming constant colour offsets. This allowed them to estimate t_0 as January 28.18. However, by fitting for t_0 with a broken power-law, Ho et al. (2020) have estimated the peak time of an afterglow t_{peak}. For a typical on-axis relativistic jet, this peak time is likely not significantly different to t_0. However, for a mildly relativistic jet viewed

on-axis, t_{peak} can be up to a few days after t_0 (e.g., Sari & Piran, 1999), while for an off-axis system, the peak time could be several months after t_0 (e.g., Granot et al., 2002).

To investigate the reason for the lack of observed prompt gamma-ray emission with detailed afterglow models, we must first estimate the burst time more robustly. For a relativistic outflow viewed on-axis the peak timescale in optical is the deceleration timescale (e.g., Sari & Piran, 1999)

$$t_{\text{dec}} \approx 90 \, \text{s} \, (1+z) \left(\frac{E_k}{10^{50} \, \text{erg}} \frac{10^{-2} \, \text{cm}^{-3}}{n_{\text{ism}}} \right)^{1/3} \left(\frac{\Gamma_0}{100} \right)^{-8/3}. \tag{8.1}$$

Here, E_k is the kinetic energy of the outflow, z is the redshift, n_{ism} is the interstellar medium density, and Γ_0 is the initial Lorentz factor of the outflow. For an on-axis observer, the optical lightcurve is well modelled as a rising power-law till t_{dec} (e.g., Sari & Piran, 1999).

The location of AT2020blt was observed prior to the first detection on January 27th with an r band upper limit of > 21.36 mag. We use this non-detection combined with a rising power-law on the observed flux

$$F = A \, (t - t_0)^m, \tag{8.2}$$

which describes the pre-deceleration physics, to estimate t_0. We use broad uninformative priors on t_0, t_{dec} and fix A to ensure the pre-deceleration power-law smoothly connects with the observations. The prior on m is informed by physics and depends on whether the forward or reverse shock dominates, or on the thickness of the shells launched in the burst. To minimise the effect of the prior, we choose a broad uniform prior from $0.5 - 7.5$, which covers all possible scenarios (e.g., Zhang, 2018). We note that typical observed pre-deceleration behaviour follows $m \approx 3$ (e.g., Zhang, 2018). We examine whether the pre-deceleration power law would produce a signal above the upper limit on 27 January, ruling out the parameter space that violates this constraint.

The above analysis implies that if AT2020blt is observed on-axis (i.e., the assumption of pre-deceleration is correct) then we measure $t_0 = 58875.53^{+0.33}_{-0.60}$ MJD i.e., Jan $27.53^{+0.33}_{-0.60}$. This initial analysis can already offer some clues into the nature of AT2020blt. For shallow indices $m \lesssim 3$, as would be expected for a cocoon or a relativistic jet where the forward shock dominates the pre-deceleration physics, a start time before ~ 27 January can not explain the non-detection. While for steeper indices $m \gtrsim 3$ (i.e., where reverse shock emission dominates), the range of t_0 is significantly broader, potentially as early as ~ 26 January. We show our posterior on t_0 and m in Fig 8.1.

The above deceleration analysis can also be extended to an off-axis observer. We emphasise that this latter physics is a consequence of relativistic
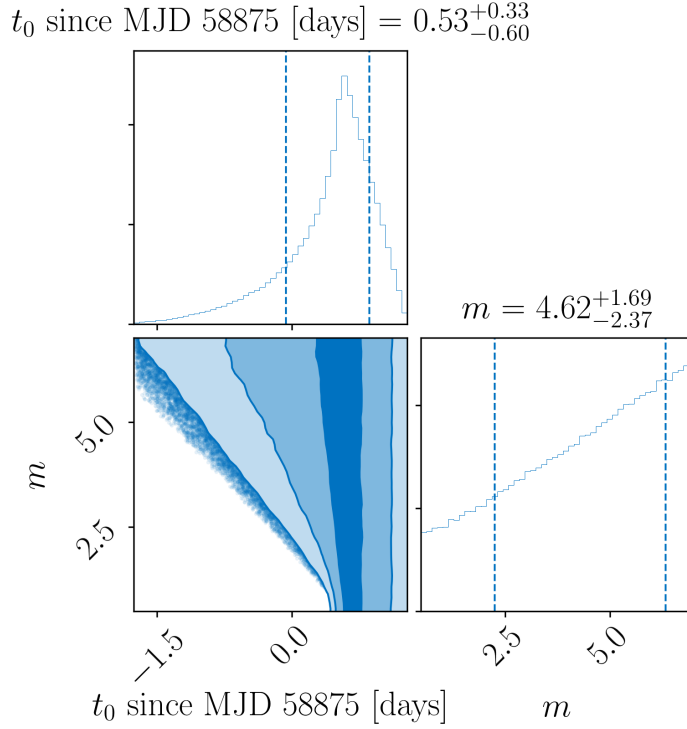
FIGURE 8.1: Posterior distribution for the burst time t_0 since MJD 58875 i.e., 27 January 2020 and m the pre-deceleration index. The uncertainties are the 68% credible interval.

beaming and not deceleration. A relativistic jet viewed off-axis will also rise with $m \gtrsim 3$. However, if the jet has an extended structure such that a significant fraction of the jet energy covers the observers' line of sight, the rise will be much shallower (e.g., Nakar, 2019). This suggests that if AT2020blt was an off-axis afterglow, the observer must satisfy $\theta_{\mathrm{obs}} > 1/\Gamma$ at the time of the non-detection or for the gamma-ray burst to occur after the non-detection on 27 January. These two conditions combined with the steep late-time decay of AT2020blt suggests an off-axis interpretation is unfeasible.

8.3 Afterglow constraints

If AT2020blt is the afterglow of a typical gamma-ray burst, the absence of observed gamma-ray emission immediately points towards two hypotheses: either the observer was off-axis, and therefore the prompt gamma-ray emission was missed due to relativistic beaming (e.g., Granot et al., 2002), or the jet did not successfully break through the ejecta and cocoon emission was responsible for producing the afterglow (e.g., Nakar & Piran, 2017). We first test both these hypotheses by fitting the broadband afterglow to a power-law structured jet and cocoon model. We note that to decrease computational

cost, we only fit to the optical data, and later apply the constraints from the X-ray and radio observations.

The power-law jet model is an angular structured jet with an energy distribution defined as,

$$E(\theta_{\text{observer}}) = E_{\text{iso}} \left(1 + \frac{\theta_{\text{observer}}^2}{\beta \theta_{\text{core}}^2} \right)^{-\beta/2}. \qquad (8.3)$$

Here, β is the exponent dictating the slope of the power-law jet structure, θ_{observer} is the observers viewing angle, θ_{core} is the half-width opening angle of the jet core. The Lorentz factor of the jet is proportional to $E(\theta_{\text{observer}})^{1/2}$ and E_{iso} is the on-axis isotropic equivalent energy. The cocoon model is a spherical outflow with velocity stratification with an energy distribution,

$$E(u) = E_0 \left(\frac{u}{u_{\text{max}}} \right)^{-k}. \qquad (8.4)$$

Here, u is the dimensionless four-velocity, E_0 is the kinetic energy of the fastest material, and k is the power-law index. Both the cocoon and structured jet outflows interact with the surrounding interstellar medium accelerating a fraction of electrons, ξ_n, with a fraction of the total energy, ϵ_e, and the fraction of the energy in the magnetic field, ϵ_b. The radiation produced by these electrons is responsible for the observed broadband afterglow.

We fit the multi-wavelength flux data of AT2020blt (including the upper-limits) using the power-law structured jet and cocoon model described above implemented in AFTERGLOWPY (Ryan et al., 2019) and a Gaussian likelihood. We include both synchrotron and inverse Compton emission and account for potential host galaxy extinction. We estimate the uncertainty on each data point as the quadrature sum of the measurement uncertainty reported by Ho et al. (2020) and an estimated systematic uncertainty which we model. Our prior on this systematic uncertainty is uniform from $10^{-4} - 10^{-3}$ mJy. The values being motivated by the flux data. We infer the parameters of the system using BILBY (Ashton et al., 2019) and the DYNESTY sampler (Speagle, 2020). Our fits to the broadband data are shown in Fig 8.2.

We find that the cocoon model does not explain the *r*-band data at late times well, while the structured-jet model can successfully explain all the observations. In particular, the last data point is a two sigma outlier from the posterior prediction for the cocoon model. Furthermore, given the pre-deceleration power-law exponent of a cocoon is $m \lesssim 3$, to explain the observations with a cocoon the associated gamma-ray burst must have occurred after the non-detection on 27 January. This requires the cocoon emission to rise rapidly to explain the observations on 28 January, which is difficult (e.g., Nakar & Piran, 2017).

More quantitatively, we perform Bayesian model selection between the
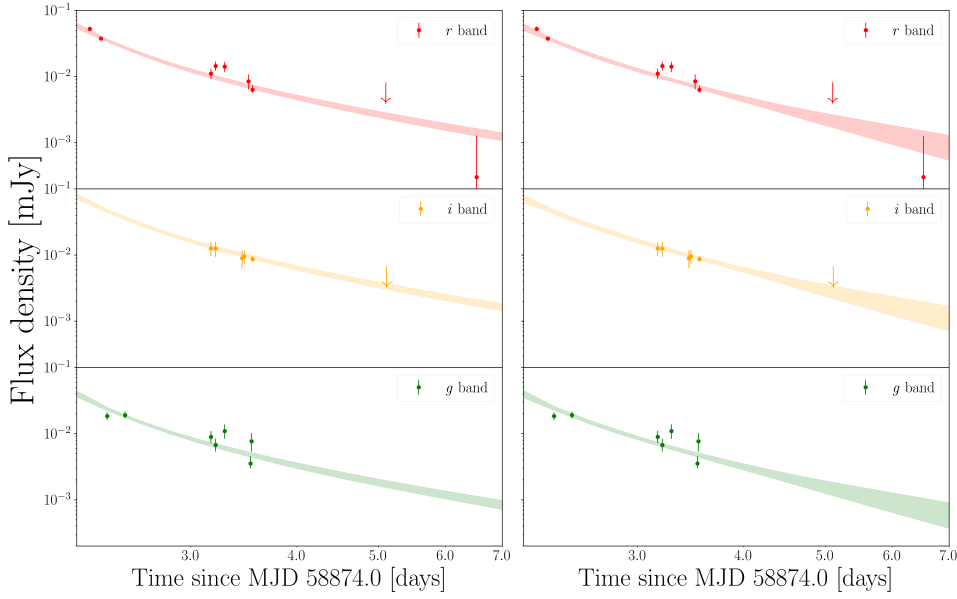
FIGURE 8.2: Data for AT2020blt in *r*, *i* and *g* bands from the top to bottom panels, with arrows indicating upper limits. In the left panel we show the 95% credible interval predicted lightcurves from our posterior samples for the cocoon model. Similarly, the right panels show the 95% credible interval predicted lightcurves for the power-law jet model. The errors on the data are the measurement uncertainty reported by Ho et al. (2020) combined with our modelled uncertainty for each model.

two hypotheses. Assuming both models are equally likely a priori, the structured-jet model is ~ 4 times more likely than the cocoon interpretation, favouring the hypothesis that an ultra-relativistic structured jet broke out of the ejecta and later interacted with the surrounding environment to produce AT2020blt.

Although we focus here on the power-law structured jet model for simplicity, we find a similar overwhelming preference for other jet models, including a Gaussian structured jet and a top-hat jet with Bayes factors of ~ 4 and ~ 6 in favour of the jet hypothesis respectively. We emphasise that these Bayes factors are predicated on the assumption that AT2020blt was a gamma-ray burst i.e., we are comparing the cocoon and structured jet hypotheses given AT2020blt is a gamma-ray burst. In Sec. 8.6, we speculate that it is possible, although unlikely, that AT2020blt may have a different origin, in which case this analysis would not be valid.

As we are also modelling the noise, another way to compare the model fit is by the size of the estimated noise. We find $\sigma = 7.7 \times 10^{-4}$ and $\sigma = 8.2 \times 10^{-4}$ for the power-law structured jet and cocoon models respectively, i.e., to fit the data with the cocoon model, we need the data to be noisier, suggesting that the structured-jet model is favoured over the cocoon.
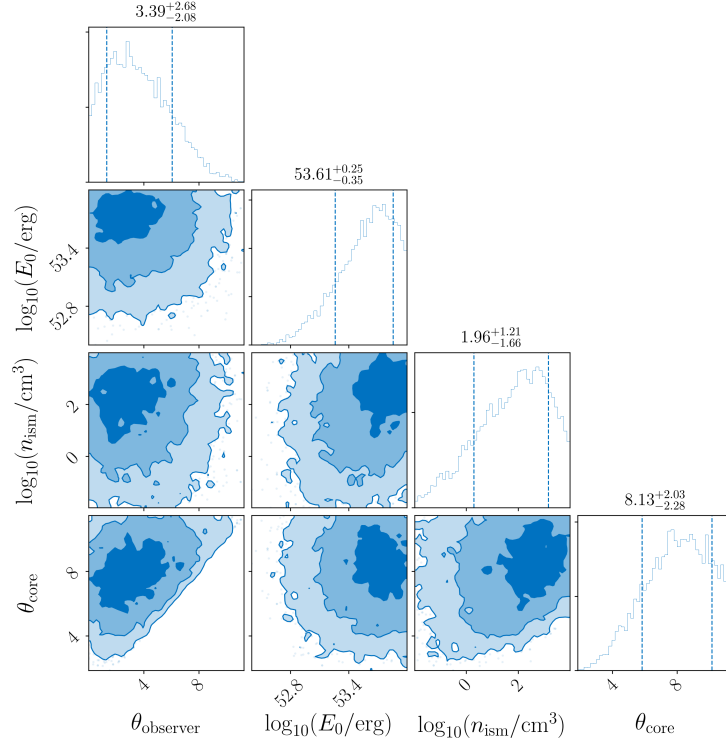
FIGURE 8.3: Posterior distributions for the structured jet model observers viewing angle $\theta_{\mathrm{observer}}$, the half-width jet core θ_{core}, the on-axis isotropic equivalent energy E_{iso}, and the ambient interstellar medium density n_{ism} for AT2020blt.

The inability to explain the observations with a cocoon while successfully explaining the observations with a structured jet suggests AT2020blt had a successful jet breakout, as typical for most observed gamma-ray bursts. Therefore, the lack of observed prompt gamma-ray emission could be a consequence of relativistic beaming, i.e., that we observed AT2020blt outside the ultra-relativistic core. We test this hypothesis by fitting the structured jet models above with a broad uniform prior on t_0 from 1 January 2019 to January 27.54 2020 (i.e., the first non-detection) and enforcing that the observer is located off-axis. We find that we can not fit the data well, with a Bayes factor of $\sim 8 \times 10^{16}$ in favour of the on-axis hypothesis. This is likely due to the sharp rise required to explain the non-detection and first observation around 28 January and the subsequent steep decay, which is difficult with an observer located off-axis (e.g., Granot et al., 2002; Nakar, 2019).

In Fig. 8.3, we show the one and two-dimensional posterior distributions for the observers viewing angle $\theta_{\mathrm{observer}}$, the half-width jet core θ_{core}, the isotropic equivalent energy E_{iso}, and the ambient interstellar medium density n_{ism}. Our measurement of the ultra-relativistic core of the jet is $\theta_{\mathrm{core}} = 8.13°^{+2.03°}_{-2.28°}$, while $\theta_{\mathrm{observer}} = 3.39°^{+2.68°}_{-2.08°}$, implying that we observed AT2020blt on-axis much like most other gamma-ray bursts. The credible intervals are 68% unless specified otherwise. We also measure the on-axis isotropic equivalent energy $\log_{10}(E_{\mathrm{iso}}/\mathrm{erg}) = 53.61^{+0.25}_{-0.35}$, and the ambient interstellar medium density $\log_{10}(n_{\mathrm{ism}}/\mathrm{cm}^{-3}) = 1.96^{+1.21}_{-1.66}$ consistent with

the population of other gamma-ray bursts (e.g., Wang et al., 2015; Fong et al., 2015).

These measurements suggest that AT2020blt is consistent with being the afterglow of a relatively typical long gamma-ray burst where the observer is located within the ultra-relativistic core. This implies that the non-detection of prompt gamma-ray emission cannot be due to relativistic beaming i.e., we did not observe AT2020blt off-axis.

Our results confirm that assuming AT2020blt was related to the gamma-ray burst phenomena, the data of AT2020blt is best explained as the afterglow produced by an on-axis jet that successfully broke out of the ejecta. This implies that we can rule out the non-detection of prompt gamma-ray emission due to relativistic beaming or that the jet that produced AT2020blt did not successfully break out of the ejecta. We now explore whether the jet launched in AT2020blt could produce prompt gamma-ray emission.

8.4 Lorentz factor

As discussed above, gamma-ray production requires a relativistic jet to alleviate the compactness problem (Ruderman, 1975). Naturally, this implies that if a jet breaks out of the ejecta and it is not sufficiently relativistic (for potential explanations of non-relativistic jets see e.g., Huang et al. (2002)), the jet will not produce detectable prompt gamma-ray emission.

In Sec. 8.3, we showed that AT2020blt is on-axis and likely successfully launched a jet that broke out of the ejecta. Here, we explore if the jet was above the prompt emission threshold through back-of-the-envelope estimates and detailed fitting.

The threshold for producing prompt gamma-ray emission is typically assumed to be $\Gamma_0 \gtrsim 100$, with jets with Lorentz factors below this threshold referred to as 'dirty' fireballs or failed gamma-ray bursts (Huang et al., 2002; Rhoads, 2003). However, indirect measurements of the Lorentz factor as low as $\Gamma_0 \sim 20$ have been made for jets following some successful gamma-ray bursts (e.g., Ghirlanda et al., 2018) with weak prompt emission. Accurately defining the gamma-ray prompt emission threshold requires knowing the radius at which prompt emission is produced, through what mechanism, and the fraction of photons above the pair production threshold in the co-moving frame. We do not know any of these constraints. However, all of these unknowns serve to lower the threshold Γ_0 value for producing prompt gamma-ray emission. As such, we take the conservative value of $\Gamma_0 \sim 100$ as the gamma-ray emission threshold, with $\Gamma_0 \sim 20$ serving as the absolute lower limit.

We estimate the Lorentz factor by fitting the same power-law structured jet model described earlier with a finite deceleration radius allowing us to estimate the Lorentz factor. Our posterior on the Lorentz factor is $\Gamma_0 = 502^{+297}_{-294}$. The probability of having the Lorentz factor lower than the prompt emission threshold ($\Gamma_0 \lesssim 100$) is $\lesssim 7\%$ and $\lesssim 1\%$ for $\Gamma_0 \lesssim 20$. However, we note that because AT2020blt is missing early time data, our result is strongly dependent on the prior we assume for Γ_0. For the analysis above, we place a uniform prior on Γ_0 between $1 - 1000$. To mitigate this dependency on the prior, we also estimate the Lorentz factor through back-of-the-envelope arguments.

The Lorentz factor can be estimated by measuring the afterglow onset time, also referred to as the deceleration timescale t_{dec}. For an on-axis observer, the deceleration timescale is the peak of the optical lightcurve, with the relativistic jet starting to decelerate on this timescale. This allows us to place a lower limit on Γ_0. The Lorentz factor is related to the deceleration timescale and weakly to the interstellar medium density and jet energy. We can approximate this relationship by (e.g., Sari & Piran, 1999; Nakar, 2007)

$$\Gamma_0 \approx 40 \left(\frac{E_{k,\mathrm{iso},50}}{n_{\mathrm{ism}}} \right)^{1/8} \left(\frac{100(1+z)}{t_{\mathrm{peak}} - t_0} \right)^{3/8}. \tag{8.5}$$

Here, $E_{k,\mathrm{iso},50}$ is the isotropic equivalent kinetic energy in units of 10^{50} erg, which we measure from the fitting of the afterglow, and z is the redshift. We do not observe this peak in AT2020blt but our analysis from Sec. 8.2 provides a conservative estimate of $t_{\mathrm{peak}} = 58876.10^{+0.13}_{-0.22}$ MJD. With this estimate for t_{peak} we can use Eq. 8.5 and the derived values of E_{iso} and n_{ism} from Sec. 8.3 to set a lower limit on the Lorentz factor. We emphasise that the derived estimates of E_{iso} and n_{ism} are robust to the choice of the prior. This back of the envelope estimate suggests, conservatively $\Gamma_0 \gtrsim 15$, indicating that AT2020blt should have successfully produced prompt gamma-ray emission.

We note that if AT2020blt was a 'dirty' fireball or failed gamma-ray burst, the threshold for producing gamma-rays would be higher. This is due to gamma-ray photons being produced when the jet is still optically thick and subsequently reabsorbed into the outflow, raising the kinetic energy of the outflow (e.g., Lamb & Kobayashi, 2016). A scaling for this threshold is $\Gamma_0 \sim 16(E_{k,50})^{0.15}$, which is weakly dependent on the efficiency in turning the gamma-ray energy into kinetic. For our estimated kinetic energy from Sec. 8.3, this implies $\Gamma_0 \sim 56$ for producing gamma-ray emission, above our conservative estimate. However, our estimated Lorentz factor above is conservative and if AT2020blt is not a dirty fireball then this analysis does not hold. We therefore work with the observationally supported threshold where a jet with $\Gamma_0 \sim 20$ produced a successful gamma-ray burst.

Our analysis indicates that AT2020blt is most likely not the afterglow from a 'dirty' fireball and that the jet that broke out of the ejecta was likely above

the threshold for producing prompt gamma-ray emission.

The lack of observed gamma-rays is therefore puzzling. As we show in Sec. 8.3, we observed AT2020blt on-axis, and therefore, relativistic beaming cannot explain the non-detection of prompt gamma-rays. Furthermore, our analysis indicates that AT2020blt can not be from a cocoon. Having ruled both these hypotheses out, we now turn to look at the prompt emission efficiency itself.

8.5 Prompt emission efficiency

Despite over three decades of observations, we still do not understand how prompt gamma-ray emission is produced. Given this uncertainty, we do not have a robust generative model to predict the energetics of the prompt gamma-ray emission. Given the lack of a model, a common approach in the field is to compare the energetics of the prompt and afterglow phases and compute a radiative efficiency n_γ

$$n_\gamma = \frac{E_{\gamma,\mathrm{iso}}}{E_{k,\mathrm{iso}} + E_{\gamma,\mathrm{iso}}}, \tag{8.6}$$

where $E_{\gamma,\mathrm{iso}}$ is the observed isotropic energy in gamma-rays. This efficiency has been calculated for a large catalogue of long and short gamma-ray bursts (Wang et al., 2015; Fong et al., 2015) using various techniques that have their own associated problems, most notably, fixing the energy in the magnetic-field ϵ_b, rather than marginalising over the uncertainty in this parameter. The efficiencies have a broad distribution ranging from ~ 1 to $\sim 90\%$. In principle, the radiative efficiency can offer a clue into the prompt emission mechanism. However, this is fraught with uncertainties due to detector selection effects, uncertain physics and modelling (e.g., Lloyd-Ronning & Zhang, 2004; Zhang et al., 2007).

Ho et al. (2020) searched for sub-threshold triggers in *Fermi* (Meegan et al., 2009b) and KONUS-*Wind* (Aptekar et al., 1995) finding no potential counterpart. Based on IPN observations, Ho et al. (2020) placed an upper limit on the gamma-ray energy of $E_\gamma \lesssim 7 \times 10^{52}$ erg by taking a nominal fluence threshold of 10^{-6} erg/cm^2. Given our estimate for the kinetic energy through the afterglow fitting (see Sec. 8.3) this implies $n_\gamma \lesssim 4.5\%$. However, this threshold is conservative. A search for coincident gamma-rays from KONUS-*Wind* has instead set a deeper upper limit on the fluence of 6.1×10^{-7} erg/cm^2 (Ridnaia et al., 2020). With our estimate of the kinetic energy, this implies $n_\gamma \lesssim 2.8\%$ for gamma-rays not to be observed by KONUS-*Wind* or a gamma-ray energy $E_\gamma \lesssim 1.2 \times 10^{52}$ erg.

To augment this upper limit, we perform a sub-threshold search of *Fermi*
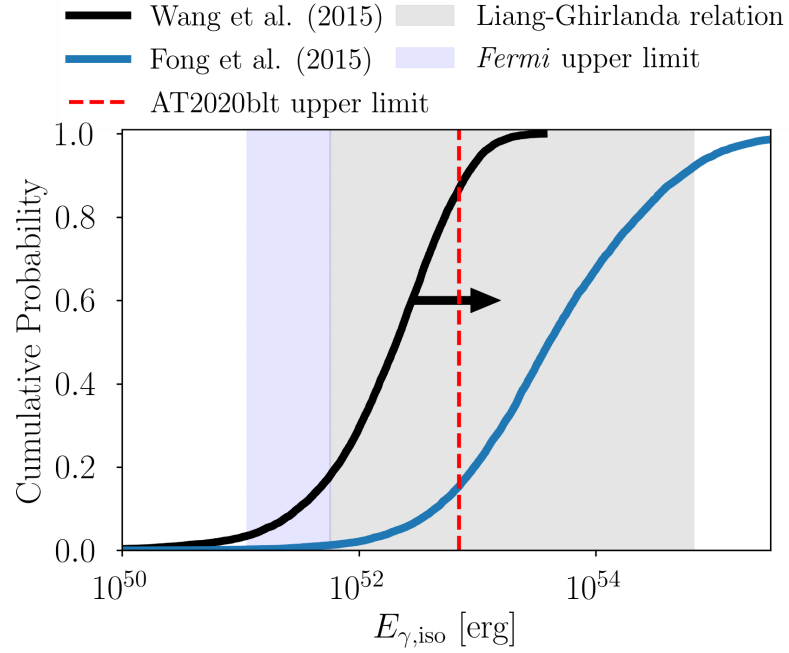
FIGURE 8.4: Cumulative probability distributions of the isotropic equivalent energy in gamma-rays $E_{\text{fl,iso}}$ of AT2020blt. The blue curve shows the cumulative distribution of energies for AT2020blt as inferred from a catalogue of short gamma-ray burst efficiencies (Fong et al., 2015), while the black curve shows the cumulative distribution from a catalogue of long gamma-ray burst efficiencies (Wang et al., 2015). The black arrow indicates that the distribution derived in Wang et al. (2015) is likely a lower limit. The red line indicates the conservative upper limit for AT2020blt based on IPN. observations set by Ho et al. (2020), while the blue shaded region shows the upper limit from a sub-threshold search we perform with *Fermi*. The grey band is the prediction for the gamma-ray energy from Liang-Ghirlanda relation.

data (Goldstein et al., 2019). Unlike KONUS-*Wind* which did not have any interruptions to observations, *Fermi* observations were periodically interrupted due to occultation by Earth and *Fermi* passing through the South Atlantic Anomaly. However, the constraints *Fermi* provides are more sensitive, with an upper limit on $E_{\gamma,\text{iso}}$ from $1 - 6 \times 10^{51}$ erg depending on the spectrum of the source and spectral template used in the search. Taking the lower value implies that for AT2020blt to not produce detectable prompt emission, the radiative efficiency must have been lower than 0.3%, challenging several prompt emission models such as photospheric emission (e.g., Lazzati et al., 2013) and magnetic field dissipation (e.g., Zhang & Yan, 2011), but plausible for internal shock models (e.g., Kumar, 1999).

In Fig. 8.4, we show these upper limits on the isotropic energy in gamma-rays for AT2020blt. The blue and black curves are the cumulative distribution of gamma-ray burst energies for AT2020blt calculated using the efficiencies derived from the Fong et al. (2015), and Wang et al. (2015) catalogues. We note that as Wang et al. (2015) fix $\epsilon_b = 10^{-5}$, the efficiency derived in their sample are systematically biased to low values and serve as a lower limit on the observed population. The non-detection by KONUS-*Wind* and *Fermi* implies that if AT2020blt produced prompt emission, the isotropic energy released in gamma-rays must have been lower than $\sim 6 \times 10^{51}$ erg, an efficiency weaker than $\sim 99.8\%$ of the observed distribution of gamma-ray bursts (Fong et al., 2015). In the gray shaded region, we show the predicted isotropic gamma-ray energy through the Liang-Ghirlanda relation, $E_\gamma \sim 10^{52}(\Gamma_0/182)^4$ (e.g., Liang et al., 2010; Ghirlanda et al., 2018). Here, we use our posterior, $\Gamma_0 = 502^{+297}_{-294}$ obtained by fitting the afterglow (see Sec. 8.3). Given the non-detection by *Fermi* and KONUS-*Wind*, AT2020blt likely did not follow the Liang-Ghirlanda relation, which may suggest a different origin for this transient. However, it is worth noting that there are notable exceptions to the Liang-Ghirlanda relation, such as GRB090510 (Ghirlanda et al., 2010).

Our results suggest that if AT2020blt is a typical gamma-ray burst, given the afterglow modelling indicates that this event was on-axis, the prompt emission must have been low-luminosity to not be detected by *Fermi* and KONUS-*Wind* or missed by *Fermi* and weaker than 98.4% of the population. This low efficiency is not necessarily a problem for prompt emission models (e.g., Kumar, 1999) and might even support certain varieties of internal shock models. However, it is inconsistent with a large fraction of observed gamma-ray bursts (e.g., Wang et al., 2015; Fong et al., 2015). It is also plausible that AT2020blt is a failed gamma-ray burst, but to confirm this hypothesis, we need to accurately determine the threshold for generating gamma-ray emission. If the threshold is $\Gamma_0 \sim 20$ (motivated by observations of successful gamma-ray bursts) then our most conservative analysis suggests AT2020blt is not a failed gamma-ray burst. However, if the threshold is higher, then there is some part of the parameter space where the jet launched in AT2020blt could fail to produce gamma-ray emission.

8.6 Implications and conclusion

Gamma-ray bursts have been observed extensively for over three decades, with their lower energy broadband afterglows almost always observed in the follow-up to a gamma-ray trigger. The Zwicky Transient Facility is quickly changing this dynamic, with three afterglow-like transients already detected without a gamma-ray trigger (Ho et al., 2020, 2021), with a further four independent detections of an optical counterpart to a gamma-ray burst. Here,

we have investigated the observations of AT2020blt in detail to ultimately determine why no prompt gamma-ray emission was observed?

In Sec. 8.3, we showed that AT2020blt is best interpreted as the afterglow produced by a successful on-axis structured jet. We ruled out the hypotheses that AT2020blt was the afterglow of a cocoon or an off-axis gamma-ray burst, with a cocoon and off-axis jet model unsuccessful in explaining the observations. In Sec. 8.4, we showed that the jet launched in AT2020blt was likely above the prompt emission generation threshold, i.e., the jet was relativistic enough to alleviate the compactness problem, potentially ruling out the hypothesis that AT2020blt was the afterglow of a dirty fireball. Moreover, given the rate of afterglow-like transients and gamma-ray bursts are roughly consistent, such phenomena can potentially already be ruled out (e.g., Cenko et al., 2015; Ho et al., 2020). In Sec. 8.5, we found that the non-detections of prompt gamma-ray emission in *Fermi* and KONUS-*Wind* imply that the prompt gamma-ray emission in AT2020blt was weaker than 99.8% of other gamma-ray bursts (e.g., Fong et al., 2015) or 98.4% if the gamma-ray burst occurred when only KONUS-*Wind* was observing.

The prompt emission we observed for GRB 170817A was likely produced through a different mechanism to other gamma-ray bursts, with cocoon-shock breakouts as one of the leading candidates (e.g., Gottlieb et al., 2018). However, given the large redshift of AT2020blt, a similar signature would have likely been undetectable (e.g., Nakar & Sari, 2012). We also predicted the prompt emission energy through the Liang-Ghirlanda relation. If AT2020blt was consistent with this relation, the prompt emission should have been detected by both *Fermi* and KONUS-*Wind*, implying the gamma-ray energy generated in AT2020blt must be lower than the predictions by the Liang-Ghirlanda relation. However, we note that there are other gamma-ray burst exceptions to this relation, particularly GRB 090510 (Ghirlanda et al., 2010), which like AT2020blt, had weaker gamma-ray emission than expected.

Given our inadequate knowledge of prompt emission generation, the only meaningful study about the prompt emission we can do is investigate the prompt emission efficiency. Depending on the upper limits used, the radiative efficiency of AT2020blt is inconsistent with $\gtrsim$ 98.4% of the population (Fong et al., 2015). This low-efficiency strongly favours internal shocks as the likely prompt emission generation mechanism (e.g., Kumar, 1999).

In addition to AT2020blt, the Zwicky Transient Facility also detected AT2021any, another potential afterglow-like transient at $z = 2.514$ (Ho et al., 2021; Ho & Zwicky Transient Facility Collaboration, 2021) which was observed to be rapidly fading after $\sim$ 22mins and detected without an identified gamma-ray counterpart despite coverage from multiple gamma-ray telescopes (Ho et al., 2021). Given that AT2021any was rapidly fading after $\sim$ 22mins, it was also likely observed on-axis and the non-detection of gamma-ray emission could imply it also has a low prompt emission

efficiency that is inconsistent with the population. We note that the data for AT2021any is not yet available and therefore we can not perform the detailed analyses for AT2021any we presented here.

The radiative efficiencies of AT2020blt and AT2021any are potentially inconsistent with (or at least in the tails of) the observed population of gamma-ray bursts. The capabilities of the Zwicky Transient Facility, in particular, the high cadence and large survey volume (e.g., Bellm et al., 2019) provide an opportunity to detect afterglow transients without a gamma-ray counterpart. This implies that the detection of transients such as AT2020blt and AT2021any are independent of gamma-ray observatories' observational biases. Therefore, it is conceivable that AT2020blt and AT2021any are the afterglows produced by the low-luminosity gamma-ray bursts that have so far been missed entirely (or less frequently observed) due to a Malmquist bias associated with gamma-ray observatories. Future all-sky gamma-ray detectors can avoid this bias and test whether these transients are genuinely part of the cosmological gamma-ray burst population or a distinct new class. Furthermore, new optical telescopes like the Vera Rubin observatory (e.g., Ivezić et al., 2019) will be capable of finding more transients like AT2020blt to deeper magnitudes and provide stringent constraints on various parameters to test the nature of these transients.

We also note that the inconsistency of the radiative efficiencies of AT2020blt and AT2021any with the observed population may be a product of inadequate modelling. Inferring prompt emission efficiencies requires robustly determining the kinetic energy in the afterglow, which requires a good understanding of the jet structure (at least for off-axis sources). Furthermore, in previous analyses, the estimations have often been done by fixing the energy fraction in the magnetic field, ϵ_b, which significantly underestimates uncertainties at best or leads to biases at worst. This motivates the need for detailed afterglow modelling on individual gamma-ray bursts and entire populations with a detailed treatment of observational selection effects (e.g., Mandel et al., 2019).

It is also worth considering—albeit cautiously—whether AT2020blt and AT2021any are afterglows of typical gamma-ray burst progenitors at all. Instead, they may be the product of a different phenomenon or a subclass of typical gamma-ray burst progenitors that can launch a mildly relativistic, ultra-low efficiency jet that interacts with the interstellar medium to produce an afterglow-like transient but does not necessarily produce prompt gamma-ray emission. If the Zwicky Transient Facility and later the Vera Rubin observatory continues to find afterglow-like transients without prompt emission, it would be intriguing to consider the host galaxy properties and the population properties of such transients. Although, as we discussed previously, it is more likely that AT2020blt and AT2021any are simply afterglows of gamma-ray bursts we previously missed due to observational biases. By virtue of opening a new window into these phenomena, it is likely that the Zwicky Transient Facility and in the future, Vera Rubin observatory will continue to

find afterglow-like transients without high energy counterparts.

Chapter 9

Conclusion

This thesis explored the observational signatures associated with nascent neutron stars, particularly their connection to X-ray afterglows of gamma-ray bursts. I have also discussed work on interpreting the nature of enigmatic transients, CDF-S XT1 and AT2020blt. In this final chapter, I examine the implications of these works and explore some of the next big questions in the field of multi-messenger astrophysics directly relevant to the material presented in this thesis. I discuss what is needed to answer these questions and briefly mention some planned future work that will address these questions.

9.1   What are the implications of this work?

9.1.1   Chapter 3: *X-ray afterglows of short gamma-ray bursts: Magnetar or Fireball?*

Currently, a critical unanswered question is whether a neutron star can be a viable engine for short gamma-ray bursts. Most numerical simulations indicate that if the engine is a neutron star, the jet-launching site is polluted by neutrinos (e.g., Murguia-Berthier et al., 2014, 2017; Ciolfi, 2018; Ciolfi et al., 2019). This pollution prevents the outflow from becoming sufficiently relativistic as to produce gamma-ray emission. This is also referred to as the baryon-loading problem (e.g., Shemi & Piran, 1990). Although these neutrinos eventually dissipate, theoretical work (see e.g., Beniamini et al., 2017) indicates that this will not happen on timescales that could explain the 1.74 s delay between the gravitational-wave and gamma-ray burst emission in GW170817. However, see recent simulations by Mösta et al. (2020) with detailed neutrino transport that indicate neutrino pollution is avoided on much shorter timescales.

While theoretical support is missing, observationally, the plateau features seen in the X-ray afterglows of gamma-ray bursts are commonly interpreted

by invoking energy injection from a nascent neutron star (millisecond magnetar model) (e.g., Rowlinson et al., 2010, 2013; Lü et al., 2015; Lasky et al., 2017). However, some of these observations are also interpreted within the fireball model of gamma-ray burst afterglows. Here the plateau is instead a product of the jet structure, dynamics and geometry. This debate is perhaps best evidenced for GRB140903A, where the X-ray data has been interpreted with the fireball model (Troja et al., 2016) and millisecond magnetar model (Lasky et al., 2017; Zhang et al., 2017).

In Chapter 3, I described a Bayesian framework to determine whether the neutron star or fireball interpretation is correct. For GRB140903A, a nascent neutron star interpretation is favoured for all possible equations of state. However, the conclusion for another gamma-ray burst, GRB130603B, is more tentative and depends on the unknown maximum mass of neutron stars $M_{\rm TOV}$. If $M_{\rm TOV} \lesssim 2.3 M_\odot$ then the data of GRB130603B favours the fireball model, and if $M_{\rm TOV} \gtrsim 2.3 M_\odot$ then the central engine of GRB130603B is a nascent neutron star. The same Bayesian framework was used in Chapter 6 on an extensive catalogue of short gamma-ray burst X-ray afterglows with sharp drops in luminosity. Here, the evidence favouring nascent neutron star engines is more overwhelming, with 18 more systems favouring the hypothesis that nascent neutron stars powered the X-ray afterglows. This large sample of gamma-ray bursts that favour a nascent neutron star hypothesis highlights the importance of considering the energy injection when inferring properties about gamma-ray bursts through the fitting of the afterglow. Moreover, this Bayesian analysis is the ideal framework for interpreting the nature of orphan X-ray transients such as CDF-S XT2 (Xue et al., 2019) and the newly reported XRT21403 (Ai & Zhang, 2021).

More importantly, these analyses provide observational evidence that newborn neutron stars can launch ultra-relativistic jets, i.e., nascent neutron stars are viable engines of short gamma-ray bursts. This evidence hints at a gap in our current theoretical understanding. This observational verification, if correct, may imply that the delay between the merger and gamma-ray burst in GW170817 is not some representative quantity but merely a consequence of the remnant's magnetic field alongside the jet formation and propagation timescale. This hints towards a distribution of delay times between merger and gamma-ray burst that is intrinsically connected to the remnants magnetic field alongside the jet formation and propagation timescales. An alternative scenario may be that neutrinos dissipate on much quicker timescales at the jet-launching site than current predictions from numerical simulations. The lack of these neutrinos at the jet-launching site will likely impact the kilonova light curve by allowing heavier r-process elements to be synthesised. This may make a visible difference to the colour of the kilonova if the observer is looking down the polar region, potentially introducing some further viewing angle dependence on the kilonova light curve. Although, it is worth noting that such an observer may not be able to discern the kilonova signature from the early afterglow. More numerical

simulations of kilonova ejecta with varying baryon loads interacting with the relativistic jet may shed light on this behaviour.

9.1.2 Chapter 4: *X-ray guided gravitational-wave search for binary neutron star merger remnants*

Our current (albeit limited) understanding of M_{TOV} and the binary neutron star mass distribution indicates that up to 79% of binary neutron stars will form a long-lived neutron star remnant (e.g., Margalit & Metzger, 2019; Ai et al., 2020). While it could be debated if these neutron stars are viable engines of short gamma-ray bursts, it is beyond doubt that these neutron stars spin down through a combination of electromagnetic and gravitational-wave radiation (e.g., Andersson & Kokkotas, 2001; Cutler, 2002; Corsi & Mészáros, 2009; Dall'Osso et al., 2015a; Lasky & Glampedakis, 2016; Lander & Jones, 2018, 2020).

In Chapter 4, I developed a new waveform model for the gravitational-wave signature from a nascent neutron star. As a part of the LIGO Scientific Collaboration (LSC), we used this model to search for the gravitational-wave signature from the remnant of GW170817 (Abbott et al., 2017f, 2019c). No signal was detected, but this was expected given current detector sensitivities, gravitational-wave strain of the source, and the energy-budget constraint I calculated in Chapter 4. This model is also used in LSC searches for long-duration transients (e.g., Abbott et al., 2019a).

In Chapter 4, I also demonstrated that one could improve the sensitivity of gravitational-wave searches by up to $\sim 50\%$ by using coincident X-ray observations. For a neutron star remnant similar in properties to the putative remnant of GRB140903A, the gravitational-wave signal could be detectable out to $\sim 2\,\mathrm{Mpc}$ and $\sim 45\,\mathrm{Mpc}$ for Advanced LIGO and the Einstein Telescope, respectively.

9.1.3 Chapter 5: *Interpreting the X-ray afterglows of gamma-ray bursts with radiative losses and millisecond magnetars.*

The millisecond magnetar model was first introduced by Dai & Lu (1998); Zhang & Mészáros (2001). In this model, some fraction of the nascent neutron star's spin-down energy (typically assumed to be a constant 10%) is extracted and turned into X-ray radiation. This model has been incredibly successful in explaining several X-ray afterglows of gamma-ray bursts, if one assumes these nascent neutron stars spin down solely through magnetic dipole radiation (e.g., Fan & Xu, 2006; Rowlinson et al., 2010; Lü et al., 2015). However,

the assumption of a constant efficiency and only magnetic dipole radiation is likely incorrect. Much work has gone into accounting for these two generalisations (e.g., Lasky et al., 2017; Xiao & Dai, 2019). However, another complication with these models is that there is no description of the mechanism that turns the extracted energy into X-ray photons.

In Chapter 5, I expanded on the work by Cohen & Piran (1999); Dall'Osso et al. (2011); Stratta et al. (2018) and developed a new model for the X-ray afterglows of gamma-ray bursts, incorporating radiative losses with the spin-down energy of a nascent neutron star and the tail of the prompt emission. In this model, the X-ray afterglow is produced through radiative losses at the interface between the jet and the interstellar medium. Here, energy at the shock interface is continuously boosted by the spin-down of the nascent neutron star. Fitting this model to a subset of gamma-ray bursts, I showed that this new model is a better explanation of the data than models previously used in the literature. Furthermore, the model can naturally explain X-ray flares as the breakout of excess energy at the shock interface. Similarly, the dynamical evolution of the shock, which is unique to a gamma-ray burst, provides a natural explanation for the observed diversity of X-ray afterglows.

In principle, the excess energy at the shock interface can also explain extended prompt emission seen in some gamma-ray bursts. Although, I note that this has not yet been demonstrated. This analysis also led to the measurement of the braking index of several putative nascent neutron stars. In particular, GRB061121, which has a braking index of $n = 4.85^{+0.11}_{-0.15}$, suggesting the neutron star born in this long gamma-ray burst spins down predominantly through gravitational-wave emission. At a redshift of $z = 1.3$, the gravitational-wave signature of this neutron star is undetectable, even with third-generation detectors. However, this gamma-ray burst and other measurements (Sarin et al., 2020b) suggest the prospect of detecting the stochastic gravitational-wave background of nascent neutron stars with third-generation detectors is bright (Cheng et al., 2017).

9.1.4   Chapter 6: *Gravitational waves or deconfined quarks: What causes the premature collapse of neutron stars born in short gamma-ray bursts?*

The leading interpretation of the sharp drop in luminosity seen in $\approx 30\%$ of all short gamma-ray bursts (e.g., Rowlinson et al., 2013; Gao et al., 2016) is the spin down of a nascent supramassive neutron star that later collapses into a black hole (e.g., Troja et al., 2007; Rowlinson et al., 2010; Lasky et al., 2014; Ravi & Lasky, 2014; Li et al., 2016; Gao et al., 2016; Drago et al., 2016). However, a detailed look into the distribution of observed collapse times indicated an inconsistency between the observed and expected distribution (Fan

et al., 2013; Ravi & Lasky, 2014). This inconsistency has previously been interpreted as evidence for deconfined quark matter (Li et al., 2016; Drago et al., 2016) or spin-down through gravitational-wave emission (Fan et al., 2013; Gao et al., 2016).

In Chapter 6, I introduced a Bayesian hierarchical study utilising the entire population of neutron star collapse times to constrain properties of the nuclear equation of state and the dynamics of nascent neutron stars. The analysis led to several results. Firstly, I measured the maximum neutron star mass as $M_{\mathrm{max}} = 2.31^{+0.36}_{-0.21}M_{\odot}$, which indicates that a significant fraction of binary neutron star mergers will form neutron stars. This may also imply that the secondary component of GW190814 is a neutron star, which has vast implications on our understanding of binary stellar evolution and nuclear physics (e.g., Abbott et al., 2020b; Fattoyev et al., 2020; Biswas et al., 2021). I also measured the fraction of remnants that spin-down predominantly through gravitational-wave emission to be $69^{+21}_{-39}\%$. This measurement highlights that gravitational waves are a dominant source of energy loss in these systems while also implying that mechanisms such as the bar-mode or spin-flip instabilities are likely active in these nascent objects. These mechanisms, if truly active, have significant implications on the dynamics of these young neutron stars (e.g., Dall'Osso et al., 2018; Lander & Jones, 2020; Sarin & Lasky, 2020). I also found tentative evidence for the presence of temperature-dependent phase transitions, with these nascent neutron stars potentially composed of freely moving deconfined quarks. If correct, this would imply that the behaviour of nuclear matter in these young stars is different to old neutron stars we see merge in gravitational waves or observe in our Galaxy. With more observations, the method developed in this work will become a powerful complementary tool for constraining the equation of state, particularly at higher densities and temperatures than methods involving the gravitational-wave inspiral or through X-ray observations of Galactic neutron stars.

Alongside these results, the analysis indicates that most supramassive neutron stars collapse on timescales $\lesssim 100\,$s. This has important implications for the follow-up of binary neutron star mergers. Typically, *Swift* takes up to $\sim 100\,$s to slew following a gamma-ray trigger. This implies that for the vast majority of mergers, *Swift* will likely miss the sharp drop in luminosity that is one of the smoking-gun observations of a supramassive neutron star. This could lead to the misidentification of the merger remnant of binary neutron star mergers. For GW170817, *Swift* first observed $\sim 3000\,$s after the merger making it conceivable that the remnant of GW170817 was a supramassive neutron star that collapsed on shorter timescales. Furthermore, suppose these nascent neutron stars are spinning down predominantly through gravitational-wave emission (as the results above indicate), then it is increasingly difficult (if not impossible) to use energetic arguments based on the kilonova (e.g., Margalit & Metzger, 2017) or radio observations (e.g., Schroeder et al., 2020) to infer the fate of a binary neutron star merger.

9.1.5   Chapter 7: *CDF-S XT1: The off-axis afterglow of a neutron star merger at $z = 2.23$*

CDF-S XT1 is an intriguing fast X-ray transient identified in the Chandra Deep-Field South Survey at redshift $z = 2.23$ (Bauer et al., 2017). The nature of this transient is unclear, with hypotheses ranging from a supernova shock breakout, tidal disruption event, and trapped emission from a magnetar all suggested in the literature (Bauer et al., 2017; Peng et al., 2019; Sun et al., 2019; Alp & Larsson, 2020).

In Chapter 7, I showed evidence that the X-ray data of CDF-S XT1 is well described as the X-ray afterglow of an off-axis gamma-ray burst. By considering the spectrum, host galaxy properties, Hubble, Very Large Array, and Australian Telescope Compact Array observations, I showed that CDF-S XT1 is best interpreted as the orphan afterglow of a short gamma-ray burst at a redshift $z = 2.23$. This interpretation makes CDF-S XT1 one of the most distant binary neutron star mergers and the first orphan afterglow of a short gamma-ray burst.

To observe a binary neutron star merger so early in the Universe necessitates a non-negligible population of short delay time binary mergers. This is also indicated by the relatively small offset of CDF-S XT1 from the host galaxy and the high inferred interstellar medium density. This immediately implies that classifying between short and long gamma-ray bursts by considering the host-galaxy offsets alone should be done cautiously (e.g., Beniamini & Piran, 2019). The short delay time to merger has two critical implications on the chemical enrichment of the Universe. First, if the rate of binary neutron star mergers at high redshifts is non-negligible, then one may not need another source to explain the chemical enrichment of the Universe at high redshifts (e.g., Siegel et al., 2019). Second, if short delay mergers are common, this could alleviate the issue with galactic Eu/Fe measurements, which otherwise suggest that the chemical enrichment of the Universe can not be explained by neutron star mergers alone (e.g., Beniamini & Piran, 2019; Wanajo et al., 2021). Furthermore, such short delay time mergers may also explain the apparent discrepancy between the binary masses of GW190425 and the binary neutron stars observed locally in radio (Galaudage et al., 2021).

Another implication of CDF-S XT1 is on the formation of the neutron star binaries itself. A merger before the peak of star formation has important implications for our understanding of stellar evolution. The short delay from formation to merger may imply that CDF-S XT1 and likely other mergers are formed dynamically in dense stellar environments such as globular clusters. It may also suggest that common-envelope evolution is more efficient at reducing the orbital separation than previously realised. Either of these scenarios has significant implications for gravitational-wave observations from binary neutron star mergers.

Lastly, the methodology developed in this work is ideally suited for searching for off-axis gamma-ray bursts with other telescopes such as eROSITA (Merloni et al., 2012), the Zwicky Transient Facility (Bellm et al., 2019) and the Vera Rubin Observatory (Ivezić et al., 2019).

9.1.6 Chapter 8: *Low-efficiency long GRBs: A case study with AT2020blt*

Most gamma-ray burst afterglows are identified in the follow-up to a high energy gamma-ray trigger. There are a few exceptional cases such as iPTF11gg (Cenko et al., 2012), iPTF14yb (Cenko et al., 2015), FIRSTJ141918 (Marcote et al., 2019), and AT2020blt (Ho et al., 2020) where an afterglow-like transient was identified independently. These transients were later shown to be associated with a gamma-ray burst missed in low-latency (e.g., Cenko et al., 2015), or not afterglows of gamma-ray bursts (Lee et al., 2020). Ho et al. (2020) recently announced the discovery of AT2020blt, an afterglow-like transient at a redshift $z = 2.9$. Despite deep upper limits, there is no prompt emission detected. Ho et al. (2020) proposed three hypotheses for the lack of prompt emission: 1) AT2020blt was observed off-axis. 2) AT2020blt was the afterglow of a failed gamma-ray burst. 3) The prompt emission was weak and missed by gamma-ray detectors.

In Chapter 8, I looked at the multi-wavelength data of AT2020blt with detailed afterglow models, finding that the data is best explained as the afterglow of an on-axis long gamma-ray burst. The lack of observed gamma-ray emission indicates that AT2020blt has a radiative efficiency $\eta_\gamma \lesssim 0.3\%$, weaker than the majority ($\gtrsim 98.4\%$) of observed gamma-ray bursts.

The implications of AT2020blt and other candidates detected by the Zwicky Transient Facility (ZTF) on gamma-ray burst physics are profound. Firstly, given observational selection effects that plague gamma-ray detectors and the capabilities of ZTF and future observatories like the Vera Rubin, it will become increasingly common to have detections of afterglow-like transients without a high energy counterpart. This will offer a different window into these transients, shed new light on their physics and finally reveal the cosmological distribution of gamma-ray bursts. Second, the low radiative efficiencies of AT2020blt and potentially AT2021any (another ZTF afterglow-like transient) appear to be inconsistent with the observed population of long gamma-ray bursts. This inconsistency hints at a sub-population or a new distinct population of very low-efficiency gamma-ray burst or gamma-ray burst-like systems. If these systems do generate prompt gamma-ray emission, then the low efficiency implies that the mechanism must be internal shocks (Kumar, 1999). Other mechanisms such as magnetic field dissipation (Zhang & Yan, 2011) and photospheric emission (Lazzati et al., 2013) are unable to explain efficiencies this low. Although gamma-ray bursts with higher radiative efficiencies have been detected, hinting that

these other mechanisms may also be active, these measurements may be systematically biased (e.g., Beniamini et al., 2016). This may solve the long debated efficiency crisis of gamma-ray burst prompt emission (Beloborodov, 2000; Ioka et al., 2006; Fan & Piran, 2006; Wang et al., 2015; Beniamini et al., 2016) and mean that internal shocks are the dominant prompt emission mechanism.

9.2   What are the next big questions in the field?

Having discussed the implications of the work presented in this thesis, I now look to the future. In particular, I describe what, in my opinion, are the next big questions in this field and what is necessary both theoretically and observationally to address them.

9.2.1   Nuclear equation of state

Insights from short gamma-ray bursts or inferences into the fate of the remnant of GW170817 suggest the maximum mass of neutron stars to be $M_{\text{TOV}} \lesssim 2.3 M_\odot$ (e.g., Gao et al., 2016; Ruiz et al., 2016; Margalit & Metzger, 2017; Shibata et al., 2019; Schroeder et al., 2020). Together with the binary neutron star mass distribution (which in itself could be considered a big question), the maximum mass dictates what fraction of binary neutron star mergers produce a neutron star. If these remnant neutron stars are not viable engines of short gamma-ray bursts, then this fraction of binary mergers will not produce short gamma-ray bursts. This will produce an eventual discrepancy between the binary neutron star merger rate and the short gamma-ray burst rate. Furthermore, if short gamma-ray bursts are more common than binary neutron star mergers, this discrepancy will need to be explained by neutron star-black hole mergers. However, to produce electromagnetic radiation, neutron star-black hole mergers have to disrupt the neutron star, which imposes significant constraints on the spin and mass distributions of the black holes. This has significant implications on binary stellar evolution and neutron star black hole formation. It is worth noting that none of the candidate neutron star-black hole mergers detected by the LSC (Abbott et al., 2021) would have disrupted the neutron star and produced electromagnetic radiation (e.g., Foucart, 2020).

The maximum mass is a key (but not the only) property of the nuclear equation of state. Independently, gravitational-wave observations of neutron stars (e.g., Abbott et al., 2019b, 2020a) and X-ray observations of neutron stars in our Galaxy (e.g., Riley et al., 2019, 2021) are providing a complementary and powerful probe into the behaviour of nuclear matter through measurements of the mass and radius. These approaches typically rely on

phenomenological models that often ignore phase transitions and physical states like hyperons or deconfined quark matter. An issue that may already be beginning to be resolved through detailed modelling incorporating these effects (e.g., Raaijmakers et al., 2021; Li et al., 2021). However, evidence already suggests that the behaviour of nuclear matter is different in hot, young neutron stars due to temperature-dependent phase transitions (e.g., Li et al., 2016; Drago et al., 2016; Sarin et al., 2020b). These objects are likely the only place in the Universe where the behaviour of the hottest and densest nuclear matter can be tested, tying the low-density regime probed by terrestrial experiments where quantum chromodynamics is relatively well understood to the most extreme conditions in the Universe.

9.2.2 Jet-launching mechanism, jet structure, prompt-emission mechanism

Observations of GRB170817A confirmed the long-held suspicion that gamma-ray burst jets are structured (e.g., Alexander et al., 2018; Lamb et al., 2018; Troja et al., 2017; Mooley et al., 2018a; Ryan et al., 2019). While several phenomenological models have been fit to the multi-wavelength data, the exact structure is unknown. Understanding the structure of jets has important implications. First, the jet structure and, critically, the jet-opening angle are vital ingredients for calculating the rates of short and long gamma-ray bursts, which has important implications for understanding the chemical enrichment of the Universe and its star-formation history. Second, it enables the precise determination of the expected number of coincident short gamma-ray bursts and neutron star mergers expected to be observed by LIGO/Virgo and the next generation of gravitational waves detectors. Third, it can be used to probe the jet-launching mechanism, and therefore probe the engine that powered the jet, which is vital for understanding the aftermath of the gamma-ray burst. However, it is worth questioning whether the jet structure is the same for every merger/collapsar. Is there a cosmological population of jet structures? Is the structure intrinsically connected to the binary/progenitor parameters or a product of the interaction with the envelope/ejecta? Is the structure different for short gamma-ray bursts produced in neutron star-black hole mergers? Is the structure different between short and long gamma-ray bursts?

GRB170817A also raises doubts about the nature of prompt gamma-ray emission. Various lines of evidence indicate that we viewed GW170817 off-axis (e.g., Abbott et al., 2017b; Mooley et al., 2018a,b; Mandel, 2018), and that the prompt emission was generated off-axis (e.g., Ioka & Nakamura, 2019; Matsumoto et al., 2019), potentially through a cocoon-shock breakout (e.g., Gottlieb et al., 2018). However, it is worth questioning whether this is the only mechanism and perhaps internal dissipation also occurs outside the relativistic core (e.g., Lazzati et al., 2017). Moreover, it is also

worth questioning whether previously discovered faint short gamma-ray bursts were viewed off-axis (Burgess et al., 2017; Troja et al., 2018) with the prompt-emission generated in a similar way to GRB170817A. Furthermore, it is worth considering whether this mechanism, combined with the typical prompt-emission mechanism, can explain extended emission seen in some short gamma-ray bursts (e.g., Irwin & Chevalier, 2016) or explain the incompatibility of gamma-ray spectra with synchrotron or photospheric emission (e.g., Bégué et al., 2017).

9.2.3   What role do neutron star binary mergers play in the chemical enrichment of the Universe?

Observations of GW170817 confirmed that neutron star mergers are one of the primary sources of r-process elements (e.g., Abbott et al., 2017c; Kasen et al., 2017; Smartt et al., 2017; Cowperthwaite et al., 2017; Evans et al., 2017a). However, apart from Strontium (Watson et al., 2019), it is not well understood which elements were synthesised, and near-future kilonova observations will likely suffer from similar uncertainty. Depending on how frequent and plentiful binary neutron star mergers are, they can potentially explain all the required r-process elements in the Universe (e.g., Wanajo et al., 2021). Although, it is likely that other channels also play a role (e.g., Siegel et al., 2019). However, this analysis is complicated further when considering the impact of the merger remnant. It is well understood that the lifetime and nature of the remnant can dramatically alter the r-process elements synthesised and their yields (e.g., Perego et al., 2017b; Metzger, 2017b; Margalit & Metzger, 2017, 2019; Bernuzzi, 2020). A fraction of mergers (dictated by the nuclear equation of state and the binary neutron star mass distribution) with a long-lived nascent neutron star will be unable to form elements past the first r-process peak (e.g., Lippuner et al., 2017). In contrast, heavier neutron star mergers that form short-lived neutron stars will form third peak r-process elements. It is not yet understood what impact this complication has on the chemical enrichment of our Universe.

9.2.4   Other transients

Since the launch of *Swift*, nascent neutron stars have been invoked to explain the internal and external plateaus seen in the X-ray afterglows of gamma-ray bursts (e.g., Fan & Xu, 2006; Troja et al., 2007; Rowlinson et al., 2010, 2013). However, are all internal and external plateaus due to nascent neutron stars. Or are they products of reverse shocks (e.g., Lamb & Kobayashi, 2019; van Eerten, 2018), high-latitude emission (e.g., Ascenzi et al., 2019; Oganesyan et al., 2019), fall-back accretion (Desai et al., 2019), or a combination of such mechanisms? If they are all due to nascent neutron stars, what mechanism

produces X-ray photons? Furthermore, what physics of the nascent neutron star is dominant and directly impacts the lightcurve (e.g., Şaşmaz Muş et al., 2019; Strang & Melatos, 2019; Suvorov & Kokkotas, 2020; Sarin et al., 2020a)?

Nascent neutron stars have also been invoked as the central engine for other transients, such as CDF-S XT2 (Xue et al., 2019) and XRT21403 (Ai & Zhang, 2021). These transients raise more questions. For example, are these simply nascent neutron stars born in off-axis gamma-ray bursts? Or are they ones that did not successfully launch a jet or failed to produce prompt gamma-ray emission? Similarly, young neutron stars are also believed to be the progenitors of fast radio bursts (e.g., Metzger et al., 2017b; Margalit et al., 2019, 2020b) and the central engines of superluminous supernovae (e.g., Margalit et al., 2018; Nicholl et al., 2017b, 2020). If correct, this raises more questions, e.g., what is the interplay between the supernova ejecta and the spin-down energy? What is the minimum age of the neutron star before a fast radio burst can be produced? Is the fast radio burst population dominated by neutron stars born in binary neutron star mergers, accretion induced collapse of white dwarfs or supernovae?

9.2.5   What is needed to address these questions?

All these questions can only be answered through a combination of theory, observation and interpretation of data. In the following, I discuss specific advancements, several already planned to address the questions raised above.

One of the cleanest ways to probe the behaviour of nuclear matter in hot nascent neutron stars is to directly detect gravitational waves from the post-merger remnant (e.g., Bauswein et al., 2012; Bauswein & Janka, 2012; Hotokezaka et al., 2013a; Read et al., 2013; Takami et al., 2014; Bauswein & Stergioulas, 2019; Most et al., 2019). However, detection of gravitational waves from a post-merger remnant requires sensitivity in the kHz regime (e.g., Martynov et al., 2019). Until third-generation gravitational-wave detectors are active, the sensitivity of gravitational-wave detectors will not be sufficient to detect post-merger gravitational waves to meaningful distances (e.g., Abbott et al., 2017f; Martynov et al., 2019; Easter et al., 2019). Recently, dedicated high-frequency detectors such as NEMO (Ackley et al., 2020) have been proposed. These dedicated instruments could be operational by the early to mid-2030s preceding broadband third-generation gravitational-wave detectors with comparable high-frequency sensitivity. This high-frequency sensitivity is critical for enabling studies into the behaviour of nuclear matter (e.g., Ackley et al., 2020). On shorter timescales, a better understanding of the binary neutron star mass distribution through population synthesis or future gravitational-wave observations will allow for statistical measurements of the maximum mass and the equation of state (e.g., Sarin et al., 2020b; Hernandez Vivanco et al., 2019).

Insights into gamma-ray burst physics requires more detailed and contemporaneous multi-wavelength observations of these events. Probing the jet structure will likely require significantly more detections of off-axis gamma-ray burst observations. In this regard, current facilities like ZTF, Gravitational-wave Optical Transient Observer (GOTO) and *Swift* will be significantly benefited by upcoming facilities like Vera Rubin and the Space Variable Objects Monitor (Götz et al., 2009). Future planned observatories, like THESEUS (e.g., Ciolfi et al., 2021; Ghirlanda et al., 2021) will also provide significant opportunity for discovery. Of particular importance will be the identification and rapid multi-wavelength follow-up of gamma-ray and gravitational-wave triggers. Low latency or wide-field surveys are necessary for the former, while the latter will require low-latency or potentially negative latency triggers from the LVK (Ligo-Virgo-Kagra collaboration). Rapid follow-up is essential, as a dominant fraction of binary neutron star merger remnants will collapse on timescales shorter than $100\,\mathrm{s}$ (Sarin et al., 2020b). Similarly, it is essential that observatories like Vera Rubin, ZTF and others follow up binary neutron star mergers rapidly and, often, independently identify kilonova and afterglow candidates without a gamma-ray and/or gravitational-wave trigger. After identification, an effort also needs to be made to gather spectral information to identify the elements synthesised and the source redshift. Such independent observations alongside watershed events like GW170817 will offer crucial insights into the chemical evolution of the Universe and the impact of nascent neutron stars on kilonovae and other transients.

Alongside all these observational advancements, to address these questions we need better theoretical models. In particular, we need to develop models which tie well-defined features of the gravitational wave and/or electromagnetic signature with the central engine/progenitor (e.g., Nicholl et al., 2021). Furthermore, alongside these theoretical developments, these transients need to be probed as a population with techniques such as hierarchical inference to get insights into these explosions that are greater than the sum of the individual events.

9.3   Future work

Modern advances in time-domain astronomy are revolutionising the way we view the night sky. With the emergence of new, more sensitive telescopes and deeper surveys, we are rapidly approaching an exciting new era. Simultaneously, these advances are now complemented by the rapidly growing field of gravitational-wave astronomy that is opening a new window into our Universe. These advances enable us to study gamma-ray bursts, supernovae, fast radio bursts, and other transients in unprecedented detail. Nascent neutron stars are likely involved in these explosions in some form or another.

Understanding these explosions offers the only way to probe these exotic objects that harbour the hottest and densest observable matter and the largest magnetic fields in the Universe. Understanding these objects and these explosions will allow us to develop significant insight into the deaths of massive stars, the dynamics of young neutron stars, and the chemical evolution and expansion of our Universe. The work presented in this thesis is a step towards this goal. Below I list a combination of major and minor projects that address the big questions raised above and provide another step in improving our understanding of the biggest explosions and their central engines.

9.3.1 Observational fingerprint of nascent neutron stars

The analysis and framework described in Chapter 3 implicitly assumes that the X-ray afterglow is either the product of the interaction of the relativistic jet with the surrounding interstellar medium or a signature of a nascent neutron star. In reality, it is likely a mixture of these two emission mechanisms. The model described in Chapter 5 provides a stepping stone towards building a complete model for the afterglows of gamma-ray bursts. In the future, I will expand on this work to self-consistently incorporate emission from the nascent neutron star, relativistic jet and ejecta, including all three dominant sources of radiation for the first time. Such a model will enable me to confront observations of gamma-ray bursts, magnetar-driven supernovae and kilonovae and infer properties of the system with techniques such as Bayesian inference. I will also extend the model to include the dynamical evolution of the nascent neutron star. In particular, the evolution of the angle between the magnetic and rotation axes. Observing the distribution and evolution of this angle will provide considerable insight into the early lives of these objects and their evolution into the neutron stars we see in our Galaxy today (e.g., Lander & Jones, 2018).

9.3.2 Fundamental physics of nascent neutron stars

In Chapter 6, I described a novel method for probing the equation of state in nascent neutron stars. Tentative evidence already suggests that the equation of state in this regime is different to colder neutron stars probed through X-ray observations of isolated neutron stars in our Galaxy or through the gravitational-wave inspiral. In the future, I will extend the method developed in Chapter 6 to directly study the relationship between the mass and radius of nascent neutron stars born in gamma-ray bursts and supernovae. Such analyses will probe the behaviour of hot supranuclear matter, conditions unlike any other in the Universe.

Simultaneously, I will utilise models such as the model introduced in Chapter 5 and others in development to confront observations of a population of short gamma-ray bursts. This analysis, combined with insight into the binary neutron star mass distribution from gravitational-wave measurements, will yield a statistical measurement of the maximum mass of neutron stars. I will also use such a model on long gamma-ray bursts observations and supernovae. Combining these measurements will allow me to determine the relative rate for forming nascent neutron stars. As these objects are the likely progenitors of fast radio bursts, these relative rates will have important implications on identifying the progenitors of fast radio bursts and their relative fractions. Furthermore, by combining the most dominant formation channels for these objects, I will determine the spin-down mechanisms that govern nascent neutron stars and probe how these objects evolve into the magnetars we see in our Galaxy today.

9.3.3   Jet structure of gamma-ray bursts

The extensive observations of the afterglow of GRB170817A offered, for the first time, a chance to study the jet structure of a gamma-ray burst in considerable detail. However, individual events can only take you so far, and significantly more information can be extracted by combining observations of multiple gamma-ray bursts (e.g., Lamb et al., 2021). In the future, I aim to statistically combine a large population of short and long gamma-ray bursts to determine a data-driven structure of the jet using techniques such as Bayesian hierarchical inference. Given the $\sim$ 1500 gamma-ray burst afterglows already observed by X-ray telescopes such as the *Swift* Telescope and the large and ever-growing catalogue of optical afterglows detected by, e.g., ZTF, this combined analysis will determine the structure of the jet at an unprecedented level. Connecting this data-driven model with numerical simulations (e.g., Murguia-Berthier et al., 2017; Salafia et al., 2020; Gottlieb et al., 2021), I will probe the jet-launching mechanism and probe what gives gamma-ray burst jets their structure. This analysis will also shed critical insight into the dynamics of these explosions, their surrounding environment and the progenitors of both long and short gamma-ray bursts.

9.3.4   Leveraging observations of the mergers of neutron star binaries

In the very near future, multi-messenger observations like GW170817 will be rare. Fortunately, we have and continue to see a significant number of binary neutron star mergers as short gamma-ray bursts. The early prompt emission from a significant fraction of gamma-ray bursts will be missed due to relativistic beaming. However, the afterglow, especially in the era of wide-field

optical surveys like ZTF, GOTO and the upcoming Vera Rubin Observatory, will be seen for an extensive range of observers viewing angles.

In Chapter 7, I introduced the methodology required to robustly identify orphan afterglows within a Bayesian framework and infer properties of the system with detailed gamma-ray burst models. In the future, I will apply this method to transients observed by various observatories such as ZTF, GOTO, *Swift* and eROSITA to identify any afterglow-like transients. Given preliminary estimates of the beaming-corrected gamma-ray burst rate $\sim 500 \text{yr}^{-1} \text{ Gpc}^{-3}$ (e.g., Berger, 2014), it is likely there will be several detections of afterglow-like transients without gamma-ray counterparts in the near future. By combining the observations of multiple afterglow-like transients, in particular, any that are orphan, I aim to determine the beaming-corrected rate of gamma-ray bursts throughout the Universe. The rate of these explosions throughout the Universe has important implications for its chemical enrichment and star formation history. Furthermore, identifying the beaming-corrected rate of short gamma-ray bursts and inferring properties of their surrounding environment is critical for understanding how binary neutron stars form. In particular, the efficiency of the common-envelope phase and the delay-time distribution. Both effects have implications on the prospect of detecting gravitational waves from the early inspiral of binary neutron stars with the Laser Interferometer Space Antenna (LISA) and the potential of detecting binary neutron star mergers at high redshift with the next generation of gravitational-wave detectors.

Bibliography

Aasi, J., Abbott, B. P., Abbott, R., et al. 2015, Classical and Quantum Gravity, 32, 074001, doi: 10.1088/0264-9381/32/7/074001

Aasi, J., et al. 2015, Classical and Quantum Gravity, 32, 074001. http://stacks.iop.org/0264-9381/32/i=7/a=074001

Abbott, B. P., Abbott, R., Abbott, T. D., et al. 2016, Living Reviews in Relativity, 19, 1, doi: 10.1007/lrr-2016-1

—. 2017a, Classical and Quantum Gravity, 34, 044001, doi: 10.1088/1361-6382/aa51f4

—. 2020a, ApJ, 892, L3, doi: 10.3847/2041-8213/ab75f5

Abbott, B. P., Abbott, R., Abbott, T. D., Abraham, S., & et al. 2019a, Phys. Rev. D, 99, 104033, doi: 10.1103/PhysRevD.99.104033

Abbott, B. P., Abbott, R., Abbott, T. D., et al. 2017b, Phys. Rev. Lett., 119, 161101, doi: 10.1103/PhysRevLett.119.161101

—. 2017c, Astrophys. J., 848, L12, doi: 10.3847/2041-8213/aa91c9

—. 2017d, Astrophys. J., 848, L13, doi: 10.3847/2041-8213/aa920c

—. 2017e, Nature, 551, 85, doi: 10.1038/nature24471

—. 2017f, ApJ, 851, L16, doi: 10.3847/2041-8213/aa9a35

—. 2019b, Phys. Rev. X, 9, 011001, doi: 10.1103/PhysRevX.9.011001

—. 2019c, ApJ, 875, 160, doi: 10.3847/1538-4357/ab0f3d

Abbott, B. P., et al. 2017, Phys. Rev. Lett., 119, 161101, doi: 10.1103/PhysRevLett.119.161101

—. 2018, Living Reviews in Relativity, 21, 3, doi: 10.1007/s41114-018-0012-9

Abbott, R., Abbott, T. D., Abraham, S., Acernese, F., & et al. 2020b, ApJ, 896, L44, doi: 10.3847/2041-8213/ab960f

—. 2021, ApJ, 915, L5, doi: 10.3847/2041-8213/ac082e

Acernese, F., Agathos, M., Agatsuma, K., et al. 2015, Classical and Quantum Gravity, 32, 024001, doi: 10.1088/0264-9381/32/2/024001

Ackermann, M., Asano, K., Atwood, W. B., et al. 2010, ApJ, 716, 1178, doi: 10.1088/0004-637X/716/2/1178

Ackley, K., Adya, V. B., Agrawal, P., et al. 2020, arXiv e-prints, arXiv:2007.03128. https://arxiv.org/abs/2007.03128

Agathos, M., Zappa, F., Bernuzzi, S., et al. 2020, Phys. Rev. D, 101, 044006, doi: 10.1103/PhysRevD.101.044006

Aguilera-Miret, R., Viganò, D., Carrasco, F., Miñano, B., & Palenzuela, C. 2020, Phys. Rev. D, 102, 103006, doi: 10.1103/PhysRevD.102.103006

Ahumada, T., Singer, L. P., Anand, S., Coughlin, M. W., & et al. 2021, arXiv e-prints, arXiv:2105.05067. https://arxiv.org/abs/2105.05067

Ai, S., Gao, H., Dai, Z.-G., et al. 2018, ApJ, 860, 57, doi: 10.3847/1538-4357/aac2b7

Ai, S., Gao, H., & Zhang, B. 2019, arXiv e-prints, arXiv:1912.06369. https://arxiv.org/abs/1912.06369

—. 2020, ApJ, 893, 146, doi: 10.3847/1538-4357/ab80bd

Ai, S., & Zhang, B. 2021, arXiv e-prints, arXiv:2105.14592. https://arxiv.org/abs/2105.14592

Akgün, T., Reisenegger, A., Mastrano, A., & Marchant, P. 2013, MNRAS, 433, 2445, doi: 10.1093/mnras/stt913

Alexander, K. D., Margutti, R., Blanchard, P. K., et al. 2018, ApJ, 863, L18, doi: 10.3847/2041-8213/aad637

Alford, M. G., & Schwenzer, K. 2014, ApJ, 781, 26, doi: 10.1088/0004-637X/781/1/26

—. 2015, MNRAS, 446, 3631, doi: 10.1093/mnras/stu2361

Aloy, M. A., Janka, H. T., & Müller, E. 2005, A&A, 436, 273, doi: 10.1051/0004-6361:20041865

Alp, D., & Larsson, J. 2020, arXiv e-prints, arXiv:2004.09519. https://arxiv.org/abs/2004.09519

Alsing, J., Silva, H. O., & Berti, E. 2018, MNRAS, 478, 1377, doi: 10.1093/mnras/sty1065

Amati, L. 2006, MNRAS, 372, 233, doi: 10.1111/j.1365-2966.2006.10840.x

Anderson, N., & Kokkotas, K. D. 2001, International Journal of Modern Physics D, 10, 381, doi: 10.1142/S0218271801001062

Andersson, N. 2003, Classical and Quantum Gravity, 20, R105, doi: 10.1088/0264-9381/20/7/201

Andersson, N., & Kokkotas, K. D. 2001, International Journal of Modern Physics D, 10, 381, doi: 10.1142/S0218271801001062

Andrews, J. J., & Mandel, I. 2019, ApJ, 880, L8, doi: 10.3847/2041-8213/ab2ed1

Antonelli, L. A., D'Avanzo, P., Perna, R., et al. 2009, A&A, 507, L45, doi: 10.1051/0004-6361/200913062

Antoniadis, J., Freire, P. C. C., Wex, N., et al. 2013, Science, 340, 448, doi: 10.1126/science.1233232

Antonucci, F., Astone, P., D'Antonio, S., Frasca, S., & Palomba, C. 2008, Classical and Quantum Gravity, 25, 184015, doi: 10.1088/0264-9381/25/18/184015

Apostolatos, T. A. 1995, Physical Review D, 52, 605, doi: 10.1103/PhysRevD.52.605

Aptekar, R. L., Frederiks, D. D., Golenetskii, S. V., et al. 1995, Space Sci. Rev., 71, 265, doi: 10.1007/BF00751332

Arcavi, I., Hosseinzadeh, G., Howell, D., et al. 2017, Nature, 551, 64, doi: 10.1038/nature24291

Archibald, R. F., Gotthelf, E. V., Ferdman, R. D., et al. 2016, ApJ, 819, L16, doi: 10.3847/2041-8205/819/1/L16

Ascenzi, S., Oganesyan, G., Salafia, O. S., et al. 2020, A&A, 641, A61, doi: 10.1051/0004-6361/202038265

Ascenzi, S., Coughlin, M. W., Dietrich, T., et al. 2019, MNRAS, 486, 672, doi: 10.1093/mnras/stz891

Ashton, G., Hübner, M., Lasky, P. D., et al. 2019, ApJS, 241, 27

Astone, P., Colla, A., D'Antonio, S., Frasca, S., & Palomba, C. 2014, Phys. Rev. D, 90, 042002, doi: 10.1103/PhysRevD.90.042002

Baiotti, L., Hawke, I., & Rezzolla, L. 2007, Classical and Quantum Gravity, 24, S187, doi: 10.1088/0264-9381/24/12/S13

Baiotti, L., Hawke, I., Rezzolla, L., & Schnetter, E. 2005, Phys. Rev. Lett., 94, 131101, doi: 10.1103/PhysRevLett.94.131101

Baiotti, L., & Rezzolla, L. 2017, Reports on Progress in Physics, 80, 096901, doi: 10.1088/1361-6633/aa67bb

Baiotti, L., & Rezzolla, L. 2017, Reports on Progress in Physics, 80, 096901. http://stacks.iop.org/0034-4885/80/i=9/a=096901

Bannister, K. W., Deller, A. T., Phillips, C., et al. 2019, Science, 365, 565, doi: 10.1126/science.aaw5903

Barnes, J., Zhu, Y. L., Lund, K. A., et al. 2020, arXiv e-prints, arXiv:2010.11182. https://arxiv.org/abs/2010.11182

Bauer, F. E., Treister, E., Schawinski, K., et al. 2017, MNRAS, 467, 4841, doi: 10.1093/mnras/stx417

Baumgarte, T. W., Shapiro, S. L., & Shibata, M. 2000, ApJ, 528, L29, doi: 10.1086/312425

Bauswein, A., Bastian, N.-U. F., Blaschke, D. B., et al. 2019, Phys. Rev. Lett., 122, 061102, doi: 10.1103/PhysRevLett.122.061102

Bauswein, A., Baumgarte, T. W., & Janka, H.-T. 2013, Phys. Rev. Lett., 111, 131101, doi: 10.1103/PhysRevLett.111.131101

Bauswein, A., Blacker, S., Lioutas, G., et al. 2020, arXiv e-prints, arXiv:2010.04461. https://arxiv.org/abs/2010.04461

Bauswein, A., Goriely, S., & Janka, H. T. 2013, ApJ, 773, 78, doi: 10.1088/0004-637X/773/1/78

Bauswein, A., & Janka, H. T. 2012, Phys. Rev. Lett., 108, 011101, doi: 10.1103/PhysRevLett.108.011101

Bauswein, A., Janka, H. T., Hebeler, K., & Schwenk, A. 2012, Phys. Rev. D, 86, 063001, doi: 10.1103/PhysRevD.86.063001

Bauswein, A., Janka, H. T., & Oechslin, R. 2010, Phys. Rev. D, 82, 084043, doi: 10.1103/PhysRevD.82.084043

Bauswein, A., & Stergioulas, N. 2019, arXiv e-prints. https://arxiv.org/abs/1901.06969

Bauswein, A., Stergioulas, N., & Janka, H.-T. 2016, European Physical Journal A, 52, 56

Bégué, D., Burgess, J. M., & Greiner, J. 2017, ApJ, 851, L19, doi: 10.3847/2041-8213/aa9d85

Bellm, E. C., et al. 2019, PASP, 131, 018002, doi: 10.1088/1538-3873/aaecbe

Beloborodov, A. M. 2000, ApJ, 539, L25, doi: 10.1086/312830

Beloborodov, A. M. 2008, in American Institute of Physics Conference Series, Vol. 1054, Cool Discs, Hot Flows: The Varying Faces of Accreting Compact Objects, ed. M. Axelsson, 51–70, doi: 10.1063/1.3002509

—. 2017, ApJ, 843, L26, doi: 10.3847/2041-8213/aa78f3

—. 2020, ApJ, 896, 142, doi: 10.3847/1538-4357/ab83eb

Beniamini, P., Barniol Duran, R., Petropoulou, M., & Giannios, D. 2020a, arXiv e-prints, arXiv:2001.00950. https://arxiv.org/abs/2001.00950

Beniamini, P., Duque, R., Daigne, F., & Mochkovitch, R. 2020b, MNRAS, 492, 2847, doi: 10.1093/mnras/staa070

Beniamini, P., Duran, R. B., Petropoulou, M., & Giannios, D. 2020c, ApJ, 895, L33, doi: 10.3847/2041-8213/ab9223

Beniamini, P., Giannios, D., & Metzger, B. D. 2017, MNRAS, 472, 3058, doi: 10.1093/mnras/stx2095

Beniamini, P., & Mochkovitch, R. 2017a, A&A, 605, A60, doi: 10.1051/0004-6361/201730523

—. 2017b, A&A, 605, A60, doi: 10.1051/0004-6361/201730523

Beniamini, P., Nava, L., & Piran, T. 2016, MNRAS, 461, 51, doi: 10.1093/mnras/stw1331

Beniamini, P., & Piran, T. 2019, MNRAS, 487, 4847, doi: 10.1093/mnras/stz1589

Beniamini, P., & van der Horst, A. J. 2017, MNRAS, 472, 3161, doi: 10.1093/mnras/stx2203

Berger, E. 2014, ARA&A, 52, 43, doi: 10.1146/annurev-astro-081913-035926

Berger, E., Fong, W., & Chornock, R. 2013, ApJ, 774, L23, doi: 10.1088/2041-8205/774/2/L23

Bernardini, M. G., Margutti, R., Chincarini, G., Guidorzi, C., & Mao, J. 2011, A&A, 526, A27, doi: 10.1051/0004-6361/201015703

Bernuzzi, S. 2020, arXiv e-prints, arXiv:2004.06419. https://arxiv.org/abs/2004.06419

Bernuzzi, S., Nagar, A., Dietrich, T., & Damour, T. 2015, Phys. Rev. Lett., 114, 161103, doi: 10.1103/PhysRevLett.114.161103

Bernuzzi, S., Breschi, M., Daszuta, B., et al. 2020, MNRAS, 497, 1488, doi: 10.1093/mnras/staa1860

Biswas, B., Nandi, R., Char, P., Bose, S., & Stergioulas, N. 2021, MNRAS, 505, 1600, doi: 10.1093/mnras/stab1383

Blandford, R. D., & Znajek, R. L. 1977, MNRAS, 179, 433

Bloom, J. S., Frail, D. A., & Sari, R. 2001, AJ, 121, 2879, doi: 10.1086/321093

Bochenek, C. D., Ravi, V., Belov, K. V., et al. 2020, Nature, 587, 59, doi: 10.1038/s41586-020-2872-x

Bonazzola, S., & Gourgoulhon, E. 1996, Astronomy & Astrophysics, 06, 675. http://arxiv.org/abs/astro-ph/9602107

Bose, S., Chakravarti, K., Rezzolla, L., Sathyaprakash, B. S., & Takami, K. 2018, Phys. Rev. Lett., 120, 031102

Brady, P. R., Creighton, T., Cutler, C., & Schutz, B. F. 1998, Phys. Rev. D, 57, 2101, doi: 10.1103/PhysRevD.57.2101

Braithwaite, J. 2009, MNRAS, 397, 763, doi: 10.1111/j.1365-2966.2008.14034.x

Bucciantini, N., Metzger, B. D., Thompson, T. A., & Quataert, E. 2012, MN-RAS, 419, 1537, doi: 10.1111/j.1365-2966.2011.19810.x

Burgess, J. M., Greiner, J., Begue, D., et al. 2017, arXiv e-prints, arXiv:1710.05823. https://arxiv.org/abs/1710.05823

Burlon, D., Bannister, K., Hancock, P., et al. 2014, The Astronomer's Telegram, 6583, 1

Burns, E., Svinkin, D., Hurley, K., Wadiasingh, Z., & et al. 2021, ApJ, 907, L28, doi: 10.3847/2041-8213/abd8c8

Burrows, D. N., Grupe, D., Capalbi, M., et al. 2006, ApJ, 653, 468, doi: 10.1086/508740

Burrows, D. N., Romano, P., Falcone, A., Kobayashi, S., & et al. 2005, Science, 309, 1833, doi: 10.1126/science.1116168

Cano, Z., Wang, S.-Q., Dai, Z.-G., & Wu, X.-F. 2017, Advances in Astronomy, 2017, 8929054, doi: 10.1155/2017/8929054

Çıkıntoğlu, S., Şaşmaz Muş, S., & Ekşi, K. Y. 2020, MNRAS, 496, 2183, doi: 10.1093/mnras/staa1556

Cenko, S. B., Krimm, H. A., Horesh, A., et al. 2012, ApJ, 753, 77, doi: 10.1088/0004-637X/753/1/77

Cenko, S. B., Urban, A. L., Perley, D. A., et al. 2015, ApJ, 803, L24, doi: 10.1088/2041-8205/803/2/L24

Chandrasekhar, S. 1970, Phys. Rev. Lett., 24, 611, doi: 10.1103/PhysRevLett.24.611

Chase, E. A., O'Connor, B., Fryer, C. L., et al. 2021, arXiv e-prints, arXiv:2105.12268. https://arxiv.org/abs/2105.12268

Chatterjee, S., Law, C. J., Wharton, R. S., et al. 2017, Nature, 541, 58, doi: 10.1038/nature20797

Chattopadhyay, D., Stevenson, S., Hurley, J. R., Rossi, L. J., & Flynn, C. 2020, MNRAS, 494, 1587, doi: 10.1093/mnras/staa756

Chatziioannou, K., Clark, J. A., Bauswein, A., et al. 2017, Phys. Rev. D, 96, 124035, doi: 10.1103/PhysRevD.96.124035

Chatziioannou, K., & Han, S. 2020, Phys. Rev. D, 101, 044019, doi: 10.1103/PhysRevD.101.044019

Cheng, Q., Zhang, S.-N., & Zheng, X.-P. 2017, Phys. Rev. D, 95, 083003, doi: 10.1103/PhysRevD.95.083003

Chornock, R., Berger, E., Kasen, D., et al. 2017, ApJ, 848, L19, doi: 10.3847/2041-8213/aa905c

Ciolfi, R. 2018, International Journal of Modern Physics D, 27, 1842004, doi: 10.1142/S021827181842004X

—. 2020a, MNRAS, 495, L66, doi: 10.1093/mnrasl/slaa062

—. 2020b, arXiv e-prints, arXiv:2001.10241. https://arxiv.org/abs/2001.10241

Ciolfi, R., Kastaun, W., Giacomazzo, B., et al. 2017, Phys. Rev. D, 95, 063016, doi: 10.1103/PhysRevD.95.063016

Ciolfi, R., Kastaun, W., Kalinani, J. V., & Giacomazzo, B. 2019, Phys. Rev. D, 100, 023005, doi: 10.1103/PhysRevD.100.023005

Ciolfi, R., & Rezzolla, L. 2012, ApJ, 760, 1, doi: 10.1088/0004-637X/760/1/1

Ciolfi, R., Stratta, G., Branchesi, M., Gendre, B., & et al. 2021, arXiv e-prints, arXiv:2104.09534. https://arxiv.org/abs/2104.09534

Clark, C. J., Pletsch, H. J., Wu, J., et al. 2016a, ApJ, 832, L15, doi: 10.3847/2041-8205/832/1/L15

Clark, J. A., Bauswein, A., Stergioulas, N., & Shoemaker, D. 2016b, Class. Quantum Grav., 33, 085003

Clocchiatti, A., Suntzeff, N. B., Covarrubias, R., & Candia, P. 2011, ApJ, 141, 163, doi: 10.1088/0004-6256/141/5/163

Cohen, E., & Piran, T. 1999, ApJ, 518, 346, doi: 10.1086/307272

Cohen, E., Piran, T., & Sari, R. 1998, ApJ, 509, 717, doi: 10.1086/306523

Cook, G. B., Shapiro, S. L., & Teukolsky, S. A. 1994, ApJ, 424, 823, doi: 10.1086/173934

Cordes, J. M., & Chatterjee, S. 2019, ARA&A, 57, 417, doi: 10.1146/annurev-astro-091918-104501

Cornish, N. J. 2012, Philosophical Transactions of the Royal Society of London Series A, 371, 20110540, doi: 10.1098/rsta.2011.0540

Cornish, N. J., & Littenberg, T. B. 2015, Classical and Quantum Gravity, 32, 135012, doi: 10.1088/0264-9381/32/13/135012

Corsi, A., & Mészáros, P. 2009, ApJ, 702, 1171, doi: 10.1088/0004-637X/702/2/1171

Costa, E., Frontera, F., Heise, J., Feroci, M., & et al. 1997, Nature, 387, 783, doi: 10.1038/42885

Coughlin, M. W., Ahumada, T., Anand, S., et al. 2019, The Astrophysical Journal, 885, L19, doi: 10.3847/2041-8213/ab4ad8

Coulter, D. A., Foley, R. J., Kilpatrick, C. D., et al. 2017, Science, 358, 1556, doi: 10.1126/science.aap9811

Cowperthwaite, P. S., Berger, E., Villar, V. A., Metzger, B. D., & Nicholl, M. o. 2017, ApJ, 848, L17, doi: 10.3847/2041-8213/aa8fc7

Coyne, R., Corsi, A., & Owen, B. J. 2016, Physical Review D, 93, 104059, doi: 10.1103/PhysRevD.93.104059

Cromartie, H. T., Fonseca, E., Ransom, S. M., et al. 2019, Nature Astronomy, 439, doi: 10.1038/s41550-019-0880-2

Şaşmaz Muş, S., Çıkıntoğlu, S., Aygün, U., Ceyhun Andaç, I., & Ekşi, K. Y. 2019, ApJ, 886, 5, doi: 10.3847/1538-4357/ab498c

Cunningham, V., Cenko, S. B., Ryan, G., Vogel, S. N., & et al. 2020, ApJ, 904, 166, doi: 10.3847/1538-4357/abc2cd

Cutler, C. 2002, Phys. Rev. D, 66, 084025, doi: 10.1103/PhysRevD.66.084025

Cutler, C., & Flanagan, I. E. 1994, Physical Review D, 49, 2658, doi: 10.1103/PhysRevD.49.2658

Dai, Z. G., & Lu, T. 1998, A&A, 333, L87. https://arxiv.org/abs/astro-ph/9810402

Dai, Z. G., Wang, X. Y., Wu, X. F., & Zhang, B. 2006, Science, 311, 1127, doi: 10.1126/science.1123606

Dall'Osso, S., Giacomazzo, B., Perna, R., & Stella, L. 2015a, ApJ, 798, 25, doi: 10.1088/0004-637X/798/1/25

—. 2015b, The Astrophysical Journal, 798, 25, doi: 10.1088/0004-637X/798/1/25

Dall'Osso, S., Shore, S. N., & Stella, L. 2009, MNRAS, 398, 1869, doi: 10.1111/j.1365-2966.2008.14054.x

Dall'Osso, S., & Stella, L. 2007, Ap&SS, 308, 119, doi: 10.1007/s10509-007-9323-0

Dall'Osso, S., Stella, L., & Palomba, C. 2018, MNRAS, 480, 1353, doi: 10.1093/mnras/sty1706

Dall'Osso, S., Stratta, G., Guetta, D., et al. 2011, A&A, 526, A121, doi: 10.1051/0004-6361/201014168

Darbha, S., & Kasen, D. 2020, ApJ, 897, 150, doi: 10.3847/1538-4357/ab9a34

De Pietri, R., Feo, A., Font, J. A., et al. 2018, Phys. Rev. Lett., 120, 221101, doi: 10.1103/PhysRevLett.120.221101

—. 2020, Phys. Rev. D, 101, 064052, doi: 10.1103/PhysRevD.101.064052

de Ugarte Postigo, A., Thöne, C. C., Rowlinson, A., et al. 2014, A&A, 563, A62, doi: 10.1051/0004-6361/201322985

Demorest, P. B., Pennucci, T., Ransom, S. M., Roberts, M. S. E., & Hessels, J. W. T. 2010, Nature, 467, 1081, doi: 10.1038/nature09466

Desai, D., Metzger, B. D., & Foucart, F. 2019, MNRAS, 485, 4404, doi: 10.1093/mnras/stz644

Dietrich, T., Radice, D., Bernuzzi, S., et al. 2018, Class. Quantum Grav., 35, 24LT01, doi: 10.1088/1361-6382/aaebc0

Dionysopoulou, K., Alic, D., & Rezzolla, L. 2015, Phys. Rev. D, 92, 084064, doi: 10.1103/PhysRevD.92.084064

Doneva, D. D., Kokkotas, K. D., & Pnigouras, P. 2015, Phys. Rev. D, 92, 104040, doi: 10.1103/PhysRevD.92.104040

Drago, A., Lavagno, A., Metzger, B. D., & Pagliara, G. 2016, Phys. Rev. D, 93, 103001, doi: 10.1103/PhysRevD.93.103001

Drago, A., & Pagliara, G. 2018, ApJ, 852, L32, doi: 10.3847/2041-8213/aaa40a

Duez, M. D., Liu, Y. T., Shapiro, S. L., Shibata, M., & Stephens, B. C. 2006a, Phys. Rev. D, 73, 104015, doi: 10.1103/PhysRevD.73.104015

—. 2006b, Phys. Rev. Lett., 96, 031101, doi: 10.1103/PhysRevLett.96.031101

Duez, M. D., & Zlochower, Y. 2019, Reports on Progress in Physics, 82, 016902, doi: 10.1088/1361-6633/aadb16

Easter, P. J., Ghonge, S., Lasky, P. D., et al. 2020, arXiv e-prints, arXiv:2006.04396. https://arxiv.org/abs/2006.04396

Easter, P. J., Lasky, P. D., Casey, A. R., Rezzolla, L., & Takami, K. 2019, arXiv e-prints. https://arxiv.org/abs/1811.11183

Echeverria, F. 1989, Phys. Rev. D, 40, 3194, doi: 10.1103/PhysRevD.40.3194

Eichler, D., Livio, M., Piran, T., & Schramm, D. N. 1989, Nature, 340, 126, doi: 10.1038/340126a0

Evans, P. A., Beardmore, A. P., Page, K. L., et al. 2009, MNRAS, 397, 1177, doi: 10.1111/j.1365-2966.2009.14913.x

Evans, P. A., Willingale, R., Osborne, J. P., et al. 2010a, A&A, 519, A102, doi: 10.1051/0004-6361/201014819

—. 2010b, A&A, 519, A102, doi: 10.1051/0004-6361/201014819

Evans, P. A., et al. 2017a, Science, 358, 1565, doi: 10.1126/science.aap9580

Evans, P. A., Cenko, S. B., Kennea, J. A., et al. 2017b, Science, 358, 1565, doi: 10.1126/science.aap9580

Falcke, H., & Rezzolla, L. 2014, A&A, 562, A137, doi: 10.1051/0004-6361/201321996

Fan, Y., & Piran, T. 2006, MNRAS, 369, 197, doi: 10.1111/j.1365-2966.2006.10280.x

Fan, Y.-Z., Piran, T., & Xu, D. 2006, Journal of Cosmology and Astroparticle Physics, 1, 013, doi: 10.1088/1475-7516/2006/09/013

Fan, Y. Z., & Wei, D. M. 2005, MNRAS, 364, L42, doi: 10.1111/j.1745-3933.2005.00102.x

Fan, Y.-Z., Wu, X.-F., & Wei, D.-M. 2013, Phys. Rev. D, 88, 067304, doi: 10.1103/PhysRevD.88.067304

Fan, Y.-Z., & Xu, D. 2006, MNRAS, 372, L19, doi: 10.1111/j.1745-3933.2006.00217.x

Fan, Y.-Z., Yu, Y.-W., Xu, D., et al. 2013, The Astrophysical Journal, 779, L25, doi: 10.1088/2041-8205/779/2/L25

Fan, Y. Z., Zhang, B., & Wei, D. M. 2005, ApJ, 628, 298, doi: 10.1086/430693

Farrow, N., Zhu, X.-J., & Thrane, E. 2019, ApJ, 876, 18, doi: 10.3847/1538-4357/ab12e3

Fattoyev, F. J., Horowitz, C. J., Piekarewicz, J., & Reed, B. 2020, Phys. Rev. C, 102, 065805, doi: 10.1103/PhysRevC.102.065805

Ferdman, R. D., Stairs, I. H., Kramer, M., Breton, R. P., & et al. 2013, ApJ, 767, 85, doi: 10.1088/0004-637X/767/1/85

Fernández, R., & Metzger, B. D. 2013, MNRAS, 435, 502, doi: 10.1093/mnras/stt1312

—. 2016, Annual Review of Nuclear and Particle Science, 66, 23, doi: 10.1146/annurev-nucl-102115-044819

Fernández, R., Tchekhovskoy, A., Quataert, E., Foucart, F., & Kasen, D. 2019, MNRAS, 482, 3373, doi: 10.1093/mnras/sty2932

Feroz, F., Gair, J. R., Hobson, M. P., & Porter, E. K. 2009, Classical and Quantum Gravity, 26, 215003, doi: 10.1088/0264-9381/26/21/215003

Feroz, F., Hobson, M. P., & Bridges, M. 2009, MNRAS, 398, 1601, doi: 10.1111/j.1365-2966.2009.14548.x

Ferrario, L., Melatos, A., & Zrake, J. 2015, Space Sci. Rev., 191, 77, doi: 10.1007/s11214-015-0138-y

Fong, W., & Berger, E. 2013, ApJ, 776, 18, doi: 10.1088/0004-637X/776/1/18

Fong, W., Berger, E., Margutti, R., & Zauderer, B. A. 2015, ApJ, 815, 102, doi: 10.1088/0004-637X/815/2/102

Fong, W., Berger, E., Metzger, B. D., et al. 2014, ApJ, 780, 118, doi: 10.1088/0004-637X/780/2/118

Fong, W., Blanchard, P. K., Alexander, K. D., et al. 2019, ApJ, 883, L1, doi: 10.3847/2041-8213/ab3d9e

Fong, W., Laskar, T., Rastinejad, J., et al. 2020, arXiv e-prints, arXiv:2008.08593. https://arxiv.org/abs/2008.08593

Foreman-Mackey, D., Hogg, D. W., Lang, D., & Goodman, J. 2012, Publications of the Astronomical Society of the Pacific, 125, 306, doi: 10.1086/670067

Foucart, F. 2020, Frontiers in Astronomy and Space Sciences, 7, 46, doi: 10.3389/fspas.2020.00046

Foucart, F., O'Connor, E., Roberts, L., et al. 2016, Phys. Rev. D, 94, 123016, doi: 10.1103/PhysRevD.94.123016

Frail, D. A., Kulkarni, S. R., Sari, R., Djorgovski, S. G., & et al. 2001, ApJ, 562, L55, doi: 10.1086/338119

Friedman, J. L., & Ipser, J. R. 1987, ApJ, 314, 594, doi: 10.1086/165088

Friedman, J. L., & Schutz, B. F. 1978, ApJ, 222, 281, doi: 10.1086/156143

Fruscione, A., et al. 2006, in Society of Photo-Optical Instrumentation Engineers (SPIE) Conference Series, Vol. 6270, Observatory Operations: Strategies, Processes, and Systems, 62701V, doi: 10.1117/12.671760

Fujibayashi, S., Sekiguchi, Y., Kiuchi, K., & Shibata, M. 2017, ApJ, 846, 114, doi: 10.3847/1538-4357/aa8039

Gaensler, B. M. 2014, GRB Coordinates Network, 16533, 1

Galaudage, S., Adamcewicz, C., Zhu, X.-J., Stevenson, S., & Thrane, E. 2021, ApJ, 909, L19, doi: 10.3847/2041-8213/abe7f6

Gao, H., Ai, S.-K., Cao, Z.-J., et al. 2020, Frontiers of Physics, 15, 24603, doi: 10.1007/s11467-019-0945-9

Gao, H., Cao, Z., & Zhang, B. 2017, ApJ, 844, 112, doi: 10.3847/1538-4357/aa7d00

Gao, H., Zhang, B., & Lü, H.-J. 2016, Phys. Rev. D, 93, 044065

Gehrels, N., Chincarini, G., Giommi, P., et al. 2004, ApJ, 611, 1005, doi: 10.1086/422091

Ghirlanda, G., Ghisellini, G., & Nava, L. 2010, A&A, 510, L7, doi: 10.1051/0004-6361/200913980

Ghirlanda, G., Salvaterra, R., Toffano, M., Ronchini, S., & et al. 2021, arXiv e-prints, arXiv:2104.10448. https://arxiv.org/abs/2104.10448

Ghirlanda, G., Nappo, F., Ghisellini, G., et al. 2018, A&A, 609, A112, doi: 10.1051/0004-6361/201731598

Giacomazzo, B., & Perna, R. 2013, ApJ, 771, L26, doi: 10.1088/2041-8205/771/2/L26

Giacomazzo, B., Rezzolla, L., & Stergioulas, N. 2011, Phys. Rev. D, 84, 024022, doi: 10.1103/PhysRevD.84.024022

Giannios, D. 2006, A&A, 455, L5, doi: 10.1051/0004-6361:20065578

Goldstein, A., Veres, P., Burns, E., et al. 2017a, ApJ, 848, L14, doi: 10.3847/2041-8213/aa8f41

Goldstein, A., et al. 2017b, The Astrophysical Journal, 848, L14, doi: 10.3847/2041-8213/aa8f41

Goldstein, A., Hamburg, R., Wood, J., et al. 2019, arXiv e-prints, arXiv:1903.12597. https://arxiv.org/abs/1903.12597

Gottlieb, O., Nakar, E., & Bromberg, O. 2021, MNRAS, 500, 3511, doi: 10.1093/mnras/staa3501

Gottlieb, O., Nakar, E., Piran, T., & Hotokezaka, K. 2018, MNRAS, 479, 588, doi: 10.1093/mnras/sty1462

Götz, D., Paul, J., Basa, S., Wei, J., & et al. 2009, in American Institute of Physics Conference Series, Vol. 1133, Gamma-ray Burst: Sixth Huntsville Symposium, ed. C. Meegan, C. Kouveliotou, & N. Gehrels, 25–30, doi: 10.1063/1.3155898

Granot, J., Gill, R., Guetta, D., & De Colle, F. 2018, MNRAS, 481, 1597, doi: 10.1093/mnras/sty2308

Granot, J., Panaitescu, A., Kumar, P., & Woosley, S. E. 2002, ApJ, 570, L61, doi: 10.1086/340991

Granot, J., Piran, T., & Sari, R. 1999, The Astrophysical Journal, 10, 679, doi: 10.1086/306884

Greiner, J., Mazzali, P. A., Kann, D. A., Krühler, T., & et al. 2015, Nature, 523, 189, doi: 10.1038/nature14579

Grogin, N. A., et al. 2011, ApJS, 197, 35, doi: 10.1088/0067-0049/197/2/35

Güver, T., & Özel, F. 2009, MNRAS, 400, 2050, doi: 10.1111/j.1365-2966.2009.15598.x

Hajela, A., Margutti, R., Kathirgamaraju, A., et al. 2020, Research Notes of the American Astronomical Society, 4, 68, doi: 10.3847/2515-5172/ab9229

Hajela, A., Margutti, R., Alexander, K. D., et al. 2019, ApJ, 886, L17, doi: 10.3847/2041-8213/ab5226

Herbrik, M., & Kokkotas, K. D. 2017, MNRAS, 466, 1330, doi: 10.1093/mnras/stw3098

Hernandez Vivanco, F., Smith, R., Thrane, E., et al. 2019, Phys. Rev. D, 100, 103009, doi: 10.1103/PhysRevD.100.103009

Hild, S., et al. 2011, Classical and Quantum Gravity, 28, 094013. http://stacks.iop.org/0264-9381/28/i=9/a=094013

Hinton, S. R. 2016, The Journal of Open Source Software, 1, 00045, doi: 10.21105/joss.00045

Ho, A. Y. Q., Perley, D. A., Yao, Y., & Andreoni, I. 2021, Transient Name Server AstroNote, 20, 1

Ho, A. Y. Q., & Zwicky Transient Facility Collaboration. 2021, GRB Coordinates Network, 29313, 1

Ho, A. Y. Q., Perley, D. A., Beniamini, P., et al. 2020, ApJ, 905, 98, doi: 10.3847/1538-4357/abc34d

Ho, W. C. G. 2016, MNRAS, 463, 489, doi: 10.1093/mnras/stw2016

Horesh, A., Hotokezaka, K., Piran, T., Nakar, E., & Hancock, P. 2016, ApJ, 819, L22, doi: 10.3847/2041-8205/819/2/L22

Hosseinzadeh, G., Cowperthwaite, P. S., Gomez, S., et al. 2019, The Astrophysical Journal, 880, L4, doi: 10.3847/2041-8213/ab271c

Hotokezaka, K., Kiuchi, K., Kyutoku, K., et al. 2013a, Phys. Rev. D, 87, 024001, doi: 10.1103/PhysRevD.87.024001

Hotokezaka, K., Kyutoku, K., Tanaka, M., et al. 2013b, The Astrophysical Journal, 778, doi: 10.1088/2041-8205/778/1/L16

Hotokezaka, K., Nakar, E., Gottlieb, O., et al. 2019, Nature Astronomy, 3, 940, doi: 10.1038/s41550-019-0820-1

Hotokezaka, K., & Piran, T. 2015, MNRAS, 450, 1430, doi: 10.1093/mnras/stv620

Howell, E. J., Ackley, K., Rowlinson, A., & Coward, D. 2019, MNRAS, 485, 1435, doi: 10.1093/mnras/stz455

Howitt, G., Stevenson, S., Vigna-Gómez, A., et al. 2020, MNRAS, 492, 3229, doi: 10.1093/mnras/stz3542

Huang, Y. F., Dai, Z. G., & Lu, T. 2002, MNRAS, 332, 735, doi: 10.1046/j.1365-8711.2002.05334.x

Ioka, K., & Nakamura, T. 2019, MNRAS, 487, 4884, doi: 10.1093/mnras/stz1650

Ioka, K., Toma, K., Yamazaki, R., & Nakamura, T. 2006, A&A, 458, 7, doi: 10.1051/0004-6361:20064939

Ipser, J. R., & Lindblom, L. 1991, ApJ, 373, 213, doi: 10.1086/170039

Irwin, C. M., & Chevalier, R. A. 2016, MNRAS, 460, 1680, doi: 10.1093/mnras/stw1058

Ivezić, Ž., et al. 2019, ApJ, 873, 111, doi: 10.3847/1538-4357/ab042c

Jaranowski, P., Królak, A., & Schutz, B. F. 1998, Physical Review D, 58, 063001, doi: 10.1103/PhysRevD.58.063001

Jin, Z.-P., Covino, S., Liao, N.-H., et al. 2020, Nature Astronomy, 4, 77, doi: 10.1038/s41550-019-0892-y

Jones, D. I., & Andersson, N. 2002, MNRAS, 331, 203, doi: 10.1046/j.1365-8711.2002.05180.x

Jones, P. B. 1976a, Ap&SS, 45, 369, doi: 10.1007/BF00642671

—. 1976b, The Astrophysical Journal, 45, 369, doi: 10.1007/BF00642671

Kaplan, J. D., Ott, C. D., O'Connor, E. P., et al. 2014, ApJ, 790, 19, doi: 10.1088/0004-637X/790/1/19

Kasen, D., & Bildsten, L. 2010, ApJ, 717, 245, doi: 10.1088/0004-637X/717/1/245

Kasen, D., Fernández, R., & Metzger, B. D. 2015, MNRAS, 450, 1777, doi: 10.1093/mnras/stv721

Kasen, D., Metzger, B., Barnes, J., Quataert, E., & Ramirez-Ruiz, E. 2017, Nature, 551, 80, doi: `10.1038/nature24453`

Kass, R. E., & Raftery, A. E. 1995, Journal of the American Statistical Association, 90, 773. `http://www.jstor.org/stable/2291091`

Kastaun, W., & Galeazzi, F. 2015, Phys. Rev. D, 91, 064027, doi: `10.1103/PhysRevD.91.064027`

Katz, J. I. 1994, ApJ, 432, L107, doi: `10.1086/187523`

—. 2016, ApJ, 826, 226, doi: `10.3847/0004-637X/826/2/226`

—. 2018, MNRAS, 481, 2946, doi: `10.1093/mnras/sty2459`

Kawaguchi, K., Shibata, M., & Tanaka, M. 2020, ApJ, 889, 171, doi: `10.3847/1538-4357/ab61f6`

Kiuchi, K., Cerdá-Durán, P., Kyutoku, K., Sekiguchi, Y., & Shibata, M. 2015, Phys. Rev. D, 92, 124034, doi: `10.1103/PhysRevD.92.124034`

Kiuchi, K., Kyutoku, K., Sekiguchi, Y., & Shibata, M. 2018, Phys. Rev. D, 97, 124039

Kiuchi, K., Kyutoku, K., Sekiguchi, Y., Shibata, M., & Wada, T. 2014, Phys. Rev. D, 90, 041502, doi: `10.1103/PhysRevD.90.041502`

Kiziltan, B., Kottas, A., De Yoreo, M., & Thorsett, S. E. 2013, ApJ, 778, 66, doi: `10.1088/0004-637X/778/1/66`

Klimenko, S., Vedovato, G., Drago, M., et al. 2016, Phys. Rev. D, 93, 042004, doi: `10.1103/PhysRevD.93.042004`

Kramer, M., Stairs, I. H., Manchester, R. N., McLaughlin, M. A., & et al. 2006, Science, 314, 97, doi: `10.1126/science.1132305`

Krishnan, B., Sintes, A. M., Papa, M. A., et al. 2004, Phys. Rev. D, 70, 082001, doi: `10.1103/PhysRevD.70.082001`

Krüger, C. J., Ho, W. C. G., & Andersson, N. 2015, Phys. Rev. D, 92, 063009, doi: `10.1103/PhysRevD.92.063009`

Kulkarni, S. R., Ofek, E. O., Neill, J. D., Zheng, Z., & Juric, M. 2014, ApJ, 797, 70, doi: `10.1088/0004-637X/797/1/70`

Kulkarni, S. R., Frail, D. A., Wieringa, M. H., et al. 1998, Nature, 395, 663, doi: `10.1038/27139`

Kumar, P. 1999, ApJ, 523, L113, doi: `10.1086/312265`

Kumar, P., & Granot, J. 2003, ApJ, 591, 1075, doi: `10.1086/375186`

Kumar, P., & Panaitescu, A. 2000, ApJ, 541, L51, doi: `10.1086/312905`

Kumar, P., & Zhang, B. 2015, Phys. Rep., 561, 1, doi: 10.1016/j.physrep.2014.09.008

Kyutoku, K., Kiuchi, K., Sekiguchi, Y., Shibata, M., & Taniguchi, K. 2018, Phys. Rev. D, 97, 023009, doi: 10.1103/PhysRevD.97.023009

Lackey, B. D., Nayyar, M., & Owen, B. J. 2006, Phys. Rev. D, 73, 024021, doi: 10.1103/PhysRevD.73.024021

Lai, D., & Shapiro, S. L. 1995, ApJ, 442, 259, doi: 10.1086/175438

Lamb, G. P., Kann, D. A., Fernández, J. J., et al. 2021, arXiv e-prints, arXiv:2104.11099. https://arxiv.org/abs/2104.11099

Lamb, G. P., & Kobayashi, S. 2016, ApJ, 829, 112, doi: 10.3847/0004-637X/829/2/112

—. 2019, MNRAS, 489, 1820, doi: 10.1093/mnras/stz2252

Lamb, G. P., Levan, A. J., & Tanvir, N. R. 2020, ApJ, 899, 105, doi: 10.3847/1538-4357/aba75a

Lamb, G. P., Mandel, I., & Resmi, L. 2018, MNRAS, 481, 2581, doi: 10.1093/mnras/sty2196

Lamb, G. P., Tanvir, N. R., Levan, A. J., et al. 2019, ApJ, 883, 48, doi: 10.3847/1538-4357/ab38bb

Lander, S. K., & Jones, D. I. 2018, MNRAS, 481, 4169, doi: 10.1093/mnras/sty2553

—. 2020, MNRAS, 494, 4838, doi: 10.1093/mnras/staa966

Lasky, P. D. 2015, PASA, 32, e034, doi: 10.1017/pasa.2015.35

Lasky, P. D., & Glampedakis, K. 2016, MNRAS, 458, 1660, doi: 10.1093/mnras/stw435

Lasky, P. D., Haskell, B., Ravi, V., Howell, E. J., & Coward, D. M. 2014, Phys. Rev. D, 89, 047302, doi: 10.1103/PhysRevD.89.047302

Lasky, P. D., Leris, C., Rowlinson, A., & Glampedakis, K. 2017, The Astrophysical Journal, 843, L1, doi: 10.3847/2041-8213/aa79a7

Lasky, P. D., & Melatos, A. 2013, Phys. Rev. D, 88, 103005, doi: 10.1103/PhysRevD.88.103005

Lasky, P. D., Zink, B., Kokkotas, K. D., & Glampedakis, K. 2011, ApJ, 735, L20, doi: 10.1088/2041-8205/735/1/L20

Lazzati, D., López-Cámara, D., Cantiello, M., et al. 2017, ApJ, 848, L6, doi: 10.3847/2041-8213/aa8f3d

Lazzati, D., Morsony, B. J., Margutti, R., & Begelman, M. C. 2013, ApJ, 765, 103, doi: 10.1088/0004-637X/765/2/103

Lee, K. H., Bartos, I., Privon, G. C., Rose, J. C., & Torrey, P. 2020, arXiv e-prints, arXiv:2007.00563. https://arxiv.org/abs/2007.00563

Lehner, L., Liebling, S. L., Palenzuela, C., et al. 2016, Classical and Quantum Gravity, 33, 184002, doi: 10.1088/0264-9381/33/18/184002

Levesque, E. M., Bloom, J. S., Butler, N. R., et al. 2010, MNRAS, 401, 963, doi: 10.1111/j.1365-2966.2009.15733.x

Li, A., Miao, Z., Han, S., & Zhang, B. 2021, ApJ, 913, 27, doi: 10.3847/1538-4357/abf355

Li, A., Zhang, B., Zhang, N.-B., et al. 2016, Phys. Rev. D, 94, 083010, doi: 10.1103/PhysRevD.94.083010

Li, A., Zhu, Z.-Y., & Zhou, X. 2017a, ApJ, 844, 41, doi: 10.3847/1538-4357/aa7a00

—. 2017b, ApJ, 844, 41, doi: 10.3847/1538-4357/aa7a00

Li, L.-X., & Paczyński, B. 1998, ApJ, 507, L59, doi: 10.1086/311680

Li, S.-Z., Liu, L.-D., Yu, Y.-W., & Zhang, B. 2018, ApJ, 861, L12, doi: 10.3847/2041-8213/aace61

Liang, E.-W., Yi, S.-X., Zhang, J., et al. 2010, ApJ, 725, 2209, doi: 10.1088/0004-637X/725/2/2209

Lin, J., & Lu, R.-J. 2019, ApJ, 871, 160, doi: 10.3847/1538-4357/aaf72f

Lin, Y.-Q., Dai, Z.-G., & Gu, W.-M. 2019, arXiv e-prints. https://arxiv.org/abs/1903.07878

Lippuner, J., Fernández, R., Roberts, L. F., et al. 2017, MNRAS, 472, 904, doi: 10.1093/mnras/stx1987

Lipunov, V. M., Gorbovskoy, E., Kornilov, V. G., et al. 2017, ApJ, 850, L1, doi: 10.3847/2041-8213/aa92c0

Lithwick, Y., & Sari, R. 2001, ApJ, 555, 540, doi: 10.1086/321455

Littenberg, T. B., & Cornish, N. J. 2015, Phys. Rev. D, 91, 084034, doi: 10.1103/PhysRevD.91.084034

Lloyd-Ronning, N. M., & Zhang, B. 2004, ApJ, 613, 477, doi: 10.1086/423026

Lorimer, D. R., Bailes, M., McLaughlin, M. A., Narkevic, D. J., & Crawford, F. 2007, Science, 318, 777, doi: 10.1126/science.1147532

Lü, H.-J., Lan, L., & Liang, E.-W. 2019, ApJ, 871, 54, doi: 10.3847/1538-4357/aaf71d

Lü, H.-J., Zhang, B., Lei, W.-H., Li, Y., & Lasky, P. D. 2015, ApJ, 805, 89, doi: 10.1088/0004-637X/805/2/89

Lü, H.-J., Zhang, H.-m., Zhong, S.-q., et al. 2016a, The Astrophysical Journal, 835, 181, doi: 10.3847/1538-4357/835/2/181

—. 2016b, The Astrophysical Journal, 835, 181, doi: 10.3847/1538-4357/835/2/181

Lü, H.-J., Zhang, H.-M., Zhong, S.-Q., et al. 2017, ApJ, 835, 181, doi: 10.3847/1538-4357/835/2/181

Lü, H.-J., Zou, L., Lan, L., & Liang, E.-W. 2018, MNRAS, 480, 4402, doi: 10.1093/mnras/sty2176

Lu, W., & Kumar, P. 2018, MNRAS, 477, 2470, doi: 10.1093/mnras/sty716

Lu, W., Kumar, P., & Zhang, B. 2020, MNRAS, 498, 1397, doi: 10.1093/mnras/staa2450

Lucca, M., & Sagunski, L. 2019, arXiv e-prints, arXiv:1909.08631. https://arxiv.org/abs/1909.08631

Lyons, N., O'Brien, P. T., Zhang, B., et al. 2010, MNRAS, 402, 705, doi: 10.1111/j.1365-2966.2009.15538.x

Lyubarsky, Y. 2014, MNRAS, 442, L9, doi: 10.1093/mnrasl/slu046

Lyutikov, M. 2013, ApJ, 768, 63, doi: 10.1088/0004-637X/768/1/63

MacKay, D. J. C. 2002, Information Theory, Inference & Learning Algorithms (New York, NY, USA: Cambridge University Press)

Mandel, I. 2018, ApJ, 853, L12, doi: 10.3847/2041-8213/aaa6c1

Mandel, I., Farr, W. M., & Gair, J. R. 2019, MNRAS, 486, 1086, doi: 10.1093/mnras/stz896

Mandel, I., & Levin, Y. 2015, ApJ, 805, L4, doi: 10.1088/2041-8205/805/1/L4

Marcote, B., Nimmo, K., Salafia, O. S., et al. 2019, ApJ, 876, L14, doi: 10.3847/2041-8213/ab1aad

Marcote, B., Paragi, Z., Hessels, J. W. T., et al. 2017, ApJ, 834, L8, doi: 10.3847/2041-8213/834/2/L8

Margalit, B., Beniamini, P., Sridhar, N., & Metzger, B. D. 2020a, ApJ, 899, L27, doi: 10.3847/2041-8213/abac57

Margalit, B., Berger, E., & Metzger, B. D. 2019, ApJ, 886, 110, doi: 10.3847/1538-4357/ab4c31

Margalit, B., & Metzger, B. D. 2017, ApJ, 850, L19, doi: 10.3847/2041-8213/aa991c

—. 2018, ApJ, 868, L4, doi: `10.3847/2041-8213/aaedad`

—. 2019, ApJ, 880, L15, doi: `10.3847/2041-8213/ab2ae2`

Margalit, B., Metzger, B. D., & Beloborodov, A. M. 2015, Phys. Rev. Lett., 115, 171101, doi: `10.1103/PhysRevLett.115.171101`

Margalit, B., Metzger, B. D., & Sironi, L. 2020b, MNRAS, 494, 4627, doi: `10.1093/mnras/staa1036`

Margalit, B., Metzger, B. D., Thompson, T. A., Nicholl, M., & Sukhbold, T. 2018, MNRAS, 475, 2659, doi: `10.1093/mnras/sty013`

Margutti, R., Zaninoni, E., Bernardini, M. G., Chincarini, G., & et al. 2013, MNRAS, 428, 729, doi: `10.1093/mnras/sts066`

Marshall, F. E., Guillemot, L., Harding, A. K., Martin, P., & Smith, D. A. 2016, ApJ, 827, L39, doi: `10.3847/2041-8205/827/2/L39`

Martin, D., Perego, A., Arcones, A., et al. 2015, ApJ, 813, 2, doi: `10.1088/0004-637X/813/1/2`

Martynov, D., Miao, H., Yang, H., et al. 2019, arXiv e-prints. `https://arxiv.org/abs/1901.03885`

Mastrano, A., Lasky, P. D., & Melatos, A. 2013, MNRAS, 434, 1658, doi: `10.1093/mnras/stt1131`

Matsumoto, T., Nakar, E., & Piran, T. 2019, MNRAS, 483, 1247, doi: `10.1093/mnras/sty3200`

Meegan, C., Lichti, G., Bhat, P. N., et al. 2009a, ApJ, 702, 791, doi: `10.1088/0004-637X/702/1/791`

—. 2009b, ApJ, 702, 791, doi: `10.1088/0004-637X/702/1/791`

Melatos, A. 1997, MNRAS, 288, 1049, doi: `10.1093/mnras/288.4.1049`

—. 2000, MNRAS, 313, 217, doi: `10.1046/j.1365-8711.2000.03031.x`

Melatos, A., & Priymak, M. 2014, ApJ, 794, 170, doi: `10.1088/0004-637X/794/2/170`

Merloni, A., Predehl, P., Becker, W., et al. 2012, arXiv e-prints, arXiv:1209.3114. `https://arxiv.org/abs/1209.3114`

Mestel, L., Nittmann, J., Wood, W. P., & Wright, G. A. E. 1981, Monthly Notices of the Royal Astronomical Society, 195, 979, doi: `10.1093/mnras/195.4.979`

Mestel, L., & Takhar, H. S. 1972, MNRAS, 156, 419, doi: `10.1093/mnras/156.4.419`

Meszaros, P. 1999, AIP Conference Proceedings, 526, 514, doi: 10.1063/1.1361591

Mészáros, P. 2001a, Progress of Theoretical Physics Supplement, doi: 10.1143/PTPS.143.33/1875854

—. 2001b, Progress of Theoretical Physics Supplement, doi: 10.1143/PTPS.143.33/1875854

Mészáros, P., & Rees, M. J. 1993a, The Astrophysical Journal, 405, 278, doi: 10.1086/172360

—. 1993b, The Astrophysical Journal, 405, 278, doi: 10.1086/172360

Mészáros, P., & Rees, M. J. 1997, ApJ, 476, 232, doi: 10.1086/303625

Mészáros, P., Rees, M. J., & Wijers, R. A. M. J. 1998, ApJ, 499, 301, doi: 10.1086/305635

Metzger, B. D. 2017a, arXiv e-prints, arXiv:1710.05931. https://arxiv.org/abs/1710.05931

—. 2017b, Living Reviews in Relativity, 20, 3, doi: 10.1007/s41114-017-0006-z

Metzger, B. D., Berger, E., & Margalit, B. 2017a, ApJ, 841, 14, doi: 10.3847/1538-4357/aa633d

—. 2017b, ApJ, 841, 14, doi: 10.3847/1538-4357/aa633d

Metzger, B. D., & Fernández, R. 2014, MNRAS, 441, 3444, doi: 10.1093/mnras/stu802

Metzger, B. D., & Fernandez, R. 2021, arXiv e-prints, arXiv:2106.02052. https://arxiv.org/abs/2106.02052

Metzger, B. D., Margalit, B., & Sironi, L. 2019, MNRAS, 485, 4091, doi: 10.1093/mnras/stz700

Metzger, B. D., Martínez-Pinedo, G., Darbha, S., et al. 2010, MNRAS, 406, 2650, doi: 10.1111/j.1365-2966.2010.16864.x

Metzger, B. D., & Piro, A. L. 2014, Monthly Notices of the Royal Astronomical Society, 439, 3916, doi: 10.1093/mnras/stu247

Metzger, B. D., & Piro, A. L. 2014, MNRAS, 439, 3916, doi: 10.1093/mnras/stu247

Metzger, B. D., Piro, A. L., & Quataert, E. 2008, MNRAS, 390, 781, doi: 10.1111/j.1365-2966.2008.13789.x

Metzger, B. D., Thompson, T. A., & Quataert, E. 2018, ApJ, 856, 101, doi: 10.3847/1538-4357/aab095

Miao, H., Yang, H., & Martynov, D. 2018, Phys. Rev. D, 98, 044044, doi: 10.1103/PhysRevD.98.044044

Miller, A., Astone, P., D'Antonio, S., et al. 2018, Phys. Rev. D, 98, 102004, doi: 10.1103/PhysRevD.98.102004

Miller, J., Barsotti, L., Vitale, S., et al. 2015, Phys. Rev. D, 91, 062005, doi: 10.1103/PhysRevD.91.062005

Minaev, P. Y., & Pozanenko, A. S. 2020, MNRAS, 492, 1919, doi: 10.1093/mnras/stz3611

Mooley, K. P., Deller, A. T., Gottlieb, O., et al. 2018a, Nature, 561, 355, doi: 10.1038/s41586-018-0486-3

Mooley, K. P., Nakar, E., Hotokezaka, K., et al. 2018b, Nature, 554, 207, doi: 10.1038/nature25452

Most, E. R., Papenfort, L. J., Dexheimer, V., et al. 2019, Phys. Rev. Lett., 122, 061101, doi: 10.1103/PhysRevLett.122.061101

Mösta, P., Ott, C. D., Radice, D., et al. 2015, Nature, 528, 376, doi: 10.1038/nature15755

Mösta, P., Radice, D., Haas, R., Schnetter, E., & Bernuzzi, S. 2020, arXiv e-prints, arXiv:2003.06043. https://arxiv.org/abs/2003.06043

Murguia-Berthier, A., Montes, G., Ramirez-Ruiz, E., De Colle, F., & Lee, W. H. 2014, ApJ, 788, L8, doi: 10.1088/2041-8205/788/1/L8

Murguia-Berthier, A., Ramirez-Ruiz, E., Montes, G., et al. 2017, ApJ, 835, L34, doi: 10.3847/2041-8213/aa5b9e

Nakar, E. 2007, Phys. Rep., 442, 166, doi: 10.1016/j.physrep.2007.02.005

—. 2019, arXiv e-prints, arXiv:1912.05659. https://arxiv.org/abs/1912.05659

Nakar, E., & Piran, T. 2017, ApJ, 834, 28, doi: 10.3847/1538-4357/834/1/28

—. 2021, ApJ, 909, 114, doi: 10.3847/1538-4357/abd6cd

Nakar, E., & Sari, R. 2012, ApJ, 747, 88, doi: 10.1088/0004-637X/747/2/88

Narayan, R., Paczynski, B., & Piran, T. 1992, ApJ, 395, L83, doi: 10.1086/186493

Nativi, L., Bulla, M., Rosswog, S., et al. 2020, arXiv e-prints, arXiv:2010.08989. https://arxiv.org/abs/2010.08989

Nedora, V., Bernuzzi, S., Radice, D., et al. 2019, ApJ, 886, L30, doi: 10.3847/2041-8213/ab5794

Nicholl, M., Berger, E., Kasen, D., et al. 2017a, ApJ, 848, L18, doi: `10.3847/2041-8213/aa9029`

Nicholl, M., Margalit, B., Schmidt, P., et al. 2021, arXiv e-prints, arXiv:2102.02229. `https://arxiv.org/abs/2102.02229`

Nicholl, M., Williams, P. K. G., Berger, E., et al. 2017b, ApJ, 843, 84, doi: `10.3847/1538-4357/aa794d`

Nicholl, M., Blanchard, P. K., Berger, E., et al. 2020, Nature Astronomy, 4, 893, doi: `10.1038/s41550-020-1066-7`

O'Brien, P. T., Willingale, R., Osborne, J., Goad, M. R., & et al. 2006, ApJ, 647, 1213, doi: `10.1086/505457`

O'Connor, B., Troja, E., Dichiara, S., et al. 2021, MNRAS, 502, 1279, doi: `10.1093/mnras/stab132`

Oechslin, R., & Janka, H. T. 2006, MNRAS, 368, 1489, doi: `10.1111/j.1365-2966.2006.10238.x`

Oganesyan, G., Ascenzi, S., Branchesi, M., et al. 2020, ApJ, 893, 88, doi: `10.3847/1538-4357/ab8221`

—. 2019, arXiv e-prints, arXiv:1904.08786. `https://arxiv.org/abs/1904.08786`

Okuta, R., Unno, Y., Nishino, D., Hido, S., & Loomis, C. 2017, in Proceedings of Workshop on Machine Learning Systems (LearningSys) in The Thirty-first Annual Conference on Neural Information Processing Systems (NIPS). `http://learningsys.org/nips17/assets/papers/paper_16.pdf`

Oliver, M., Keitel, D., Miller, A. L., Estelles, H., & Sintes, A. M. 2019a, MNRAS, 485, 843, doi: `10.1093/mnras/stz439`

Oliver, M., Keitel, D., & Sintes, A. M. 2019b, Phys. Rev. D, 99, 104067, doi: `10.1103/PhysRevD.99.104067`

Omand, C. M. B., Kashiyama, K., & Murase, K. 2018, MNRAS, 474, 573, doi: `10.1093/mnras/stx2743`

Oppenheimer, J. R., & Volkoff, G. M. 1939, Physical Review, 55, 374, doi: `10.1103/PhysRev.55.374`

Owen, B. J., Lindblom, L., Cutler, C., et al. 1998, Phys. Rev. D, 58, 084020, doi: `10.1103/PhysRevD.58.084020`

Paczynski, B., & Rhoads, J. E. 1993, ApJ, 418, L5, doi: `10.1086/187102`

Page, D., Prakash, M., Lattimer, J. M., & Steiner, A. W. 2011, Physical Review Letters, 106, 081101, doi: `10.1103/PhysRevLett.106.081101`

Parthasarathy, A., Shannon, R. M., Johnston, S., et al. 2019, MNRAS, 489, 3810, doi: `10.1093/mnras/stz2383`

Paschalidis, V., Etienne, Z. B., & Shapiro, S. L. 2012, Phys. Rev. D, 86, 064032, doi: `10.1103/PhysRevD.86.064032`

Pe'er, A. 2015, Advances in Astronomy, 2015, 907321, doi: `10.1155/2015/907321`

Peng, Z.-K., Yang, Y.-S., Shen, R.-F., et al. 2019, ApJ, 884, L34, doi: `10.3847/2041-8213/ab481b`

Perego, A., Bernuzzi, S., & Radice, D. 2019, arXiv e-prints. `https://arxiv.org/abs/1903.07898`

Perego, A., Radice, D., & Bernuzzi, S. 2017a, ApJ, 850, L37, doi: `10.3847/2041-8213/aa9ab9`

Perego, A., Rosswog, S., Cabezón, R. M., et al. 2014, MNRAS, 443, 3134, doi: `10.1093/mnras/stu1352`

Perego, A., Yasin, H., & Arcones, A. 2017b, Journal of Physics G Nuclear Physics, 44, 084007, doi: `10.1088/1361-6471/aa7bdc`

Perna, R., Armitage, P. J., & Zhang, B. 2006, ApJ, 636, L29, doi: `10.1086/499775`

Pian, E., D'Avanzo, P., Benetti, S., et al. 2017, Nature, 551, 67, doi: `10.1038/nature24298`

Piran, T. 1999, Phys. Rep., 314, 575, doi: `10.1016/S0370-1573(98)00127-6`

Piro, A. L., Giacomazzo, B., & Perna, R. 2017, ApJ, 844, L19, doi: `10.3847/2041-8213/aa7f2f`

Piro, A. L., & Thrane, E. 2012, ApJ, 761, 63, doi: `10.1088/0004-637X/761/1/63`

Piro, L., Troja, E., Zhang, B., et al. 2018, ArXiv e-prints. `https://arxiv.org/abs/1810.04664`

—. 2019, MNRAS, 483, 1912, doi: `10.1093/mnras/sty3047`

Planck Collaboration, et al. 2016, A&A, 594, A13, doi: `10.1051/0004-6361/201525830`

Platts, E., Weltman, A., Walters, A., et al. 2019, Phys. Rep., 821, 1, doi: `10.1016/j.physrep.2019.06.003`

Pooley, D., Kumar, P., & Wheeler, J. C. 2017, ArXiv e-prints. `https://arxiv.org/abs/1712.03240`

Popov, S. B., & Postnov, K. A. 2013, arXiv e-prints, arXiv:1307.4924. https://arxiv.org/abs/1307.4924

Porth, O., Komissarov, S. S., & Keppens, R. 2013, MNRAS, 431, L48, doi: 10.1093/mnrasl/slt006

Punturo, M., Abernathy, M., Acernese, F., et al. 2010, Class. Quantum Grav., 27, 194002, doi: 10.1088/0264-9381/27/19/194002

Raaijmakers, G., Greif, S. K., Hebeler, K., et al. 2021, arXiv e-prints, arXiv:2105.06981. https://arxiv.org/abs/2105.06981

Radice, D., Galeazzi, F., Lippuner, J., et al. 2016, MNRAS, 460, 3255, doi: 10.1093/mnras/stw1227

Radice, D., Perego, A., Hotokezaka, K., et al. 2018a, ApJ, 869, L35, doi: 10.3847/2041-8213/aaf053

Radice, D., Perego, A., Zappa, F., & Bernuzzi, S. 2018b, ApJ, 852, L29, doi: 10.3847/2041-8213/aaa402

Ravi, V. 2019, Nature Astronomy, 3, 928, doi: 10.1038/s41550-019-0831-y

Ravi, V., & Lasky, P. D. 2014, MNRAS, 441, 2433, doi: 10.1093/mnras/stu720

Ravi, V., Catha, M., D'Addario, L., et al. 2019, Nature, 572, 352, doi: 10.1038/s41586-019-1389-7

Raynaud, R., Guilet, J., Janka, H.-T., & Gastine, T. 2020, Science Advances, 6, eaay2732, doi: 10.1126/sciadv.aay2732

Rea, N., et al. 2013, ApJ, 770, 65, doi: 10.1088/0004-637X/770/1/65

Read, J. S., Baiotti, L., Creighton, J. D. E., et al. 2013, Phys. Rev. D, 88, 044042, doi: 10.1103/PhysRevD.88.044042

Regimbau, T., & de Freitas Pacheco, J. A. 2006, A&A, 447, 1, doi: 10.1051/0004-6361:20053702

Ren, J., Lin, D.-B., Zhang, L.-L., et al. 2020, ApJ, 901, L26, doi: 10.3847/2041-8213/abb672

Rezzolla, L., Baiotti, L., Giacomazzo, B., Link, D., & Font, J. A. 2010, Classical and Quantum Gravity, 27, 114105, doi: 10.1088/0264-9381/27/11/114105

Rezzolla, L., Most, E. R., & Weih, L. R. 2018a, ApJ, 852, L25, doi: 10.3847/2041-8213/aaa401

—. 2018b, ApJ, 852, L25, doi: 10.3847/2041-8213/aaa401

Rhoads, J. E. 2003, ApJ, 591, 1097, doi: 10.1086/368125

Ricci, R., Troja, E., Bruni, G., et al. 2020, MNRAS, doi: 10.1093/mnras/staa3241

Richardson, D., Jenkins, Robert L., I., Wright, J., & Maddox, L. 2014, AJ, 147, 118, doi: 10.1088/0004-6256/147/5/118

Ridnaia, A., Golenetskii, S., Aptekar, R., et al. 2020, GRB Coordinates Network, 27039, 1

Riles, K. 2013, Progress in Particle and Nuclear Physics, 68, 1, doi: 10.1016/j.ppnp.2012.08.001

Riley, T. E., Watts, A. L., Bogdanov, S., Ray, P. S., & et al. 2019, ApJ, 887, L21, doi: 10.3847/2041-8213/ab481c

Riley, T. E., Watts, A. L., Ray, P. S., Bogdanov, S., & et al. 2021, arXiv e-prints, arXiv:2105.06980. https://arxiv.org/abs/2105.06980

Rossi, A., Rothberg, B., Palazzi, E., Kann, D. A., & et al. 2021, arXiv e-prints, arXiv:2105.03829. https://arxiv.org/abs/2105.03829

Rossi, E., Lazzati, D., & Rees, M. J. 2002, MNRAS, 332, 945, doi: 10.1046/j.1365-8711.2002.05363.x

Rosswog, S., & Liebendörfer, M. 2003, MNRAS, 342, 673, doi: 10.1046/j.1365-8711.2003.06579.x

Rosswog, S., Liebendörfer, M., Thielemann, F. K., et al. 1999, A&A, 341, 499. https://arxiv.org/abs/astro-ph/9811367

Rowlinson, A., O'Brien, P. T., Metzger, B. D., Tanvir, N. R., & Levan, A. J. 2013, MNRAS, 430, 1061, doi: 10.1093/mnras/sts683

Rowlinson, A., O'Brien, P. T., Tanvir, N. R., et al. 2010, MNRAS, 409, 531, doi: 10.1111/j.1365-2966.2010.17354.x

Ruan, J. J., Nynka, M., Haggard, D., Kalogera, V., & Evans, P. 2018, The Astrophysical Journal, 853, L4, doi: 10.3847/2041-8213/aaa4f3

Ruderman, M. 1975, Annals of the New York Academy of Sciences, 262, 164, doi: https://doi.org/10.1111/j.1749-6632.1975.tb31430.x

Ruffert, M., & Janka, H. T. 1998, A&A, 338, 535. https://arxiv.org/abs/astro-ph/9804132

Ruffert, M., Janka, H.-T., & Schaefer, G. 1996, A&A, 311, 532

Ruiz, M., Lang, R. N., Paschalidis, V., & Shapiro, S. L. 2016, ApJ, 824, L6, doi: 10.3847/2041-8205/824/1/L6

Ruiz, M., Shapiro, S. L., & Tsokaros, A. 2018, Phys. Rev. D, 97, 021501, doi: 10.1103/PhysRevD.97.021501

—. 2021, arXiv e-prints, arXiv:2102.03366. https://arxiv.org/abs/2102.03366

Ryan, G., van Eerten, H., Piro, L., & Troja, E. 2019, arXiv e-prints, arXiv:1909.11691. https://arxiv.org/abs/1909.11691

Salafia, O. S., Barbieri, C., Ascenzi, S., & Toffano, M. 2020, A&A, 636, A105, doi: 10.1051/0004-6361/201936335

Sari, R., & Piran, T. 1999, ApJ, 520, 641, doi: 10.1086/307508

Sari, R., Piran, T., & Halpern, J. P. 1999, ApJ, 519, L17, doi: 10.1086/312109

Sari, R., Piran, T., & Narayan, R. 1998, ApJ, 497, L17, doi: 10.1086/311269

Sarin, N. 2020, Posteriors, https://github.com/nikhil-sarin/GRB_radiative_losses_results, GitHub, doi: https://zenodo.org/badge/latestdoi/285225484

Sarin, N., Ashton, G., Lasky, P. D., et al. 2021a, arXiv e-prints, arXiv:2105.10108. https://arxiv.org/abs/2105.10108

Sarin, N., Hamburg, R., Burns, E., et al. 2021b, arXiv e-prints, arXiv:2106.01556. https://arxiv.org/abs/2106.01556

Sarin, N., & Lasky, P. D. 2020, arXiv e-prints, arXiv:2012.08172. https://arxiv.org/abs/2012.08172

Sarin, N., Lasky, P. D., & Ashton, G. 2019, ApJ, 872, 114, doi: 10.3847/1538-4357/aaf9a0

—. 2020a, MNRAS, 499, 5986, doi: 10.1093/mnras/staa3090

—. 2020b, Phys. Rev. D, 101, 063021, doi: 10.1103/PhysRevD.101.063021

Sarin, N., Lasky, P. D., Sammut, L., & Ashton, G. 2018, Phys. Rev. D, 98, 043011, doi: 10.1103/PhysRevD.98.043011

Savchenko, V., Ferrigno, C., Kuulkers, E., et al. 2017, ApJ, 848, L15, doi: 10.3847/2041-8213/aa8f94

Schroeder, G., Margalit, B., Fong, W.-f., et al. 2020, ApJ, 902, 82, doi: 10.3847/1538-4357/abb407

Sekiguchi, Y., Kiuchi, K., Kyutoku, K., & Shibata, M. 2011a, Phys. Rev. Lett., 107, 211101, doi: 10.1103/PhysRevLett.107.211101

—. 2011b, Phys. Rev. Lett., 107, 051102, doi: 10.1103/PhysRevLett.107.051102

Sekiguchi, Y., Kiuchi, K., Kyutoku, K., Shibata, M., & Taniguchi, K. 2016, Phys. Rev. D, 93, 124046, doi: 10.1103/PhysRevD.93.124046

Shapiro, S. L. 2000, The Astrophysical Journal, 544, 397. http://stacks.iop.org/0004-637X/544/i=1/a=397

Shapiro, S. L., & Teukolsky, S. A. 1983, Black holes, white dwarfs, and neutron stars: The physics of compact objects

Shapiro, S. L., & Zane, S. 1998, The Astrophysical Journal Supplement Series, 117, 531, doi: 10.1086/313124

Shemi, A., & Piran, T. 1990, ApJ, 365, L55, doi: 10.1086/185887

Shibata, M., Baumgarte, T. W., & Shapiro, S. L. 2000, ApJ, 542, 453, doi: 10.1086/309525

Shibata, M., Duez, M. D., Liu, Y. T., Shapiro, S. L., & Stephens, B. C. 2006, Phys. Rev. Lett., 96, 031102, doi: 10.1103/PhysRevLett.96.031102

Shibata, M., Fujibayashi, S., & Sekiguchi, Y. 2021, Phys. Rev. D, 103, 043022, doi: 10.1103/PhysRevD.103.043022

Shibata, M., & Taniguchi, K. 2006, Phys. Rev. D, 73, 064027, doi: 10.1103/PhysRevD.73.064027

Shibata, M., Zhou, E., Kiuchi, K., & Fujibayashi, S. 2019, Phys. Rev. D, 100, 023015, doi: 10.1103/PhysRevD.100.023015

Shternin, P. S., Yakovlev, D. G., Heinke, C. O., Ho, W. C. G., & Patnaude, D. J. 2011, MNRAS, 412, L108, doi: 10.1111/j.1745-3933.2011.01015.x

Siegel, D. M., Barnes, J., & Metzger, B. D. 2019, Nature, 569, 241, doi: 10.1038/s41586-019-1136-0

Siegel, D. M., & Ciolfi, R. 2016, The Astrophysical Journal, 819, 15, doi: 10.3847/0004-637x/819/1/15

Siegel, D. M., Ciolfi, R., Harte, A. I., & Rezzolla, L. 2013, Phys. Rev. D, 87, 121302

Siegel, D. M., & Metzger, B. D. 2017, Phys. Rev. Lett., 119, 231102, doi: 10.1103/PhysRevLett.119.231102

—. 2018, ApJ, 858, 52, doi: 10.3847/1538-4357/aabaec

Singer, L. P., Ahumada, T., Ho, A. Y. Q., Zwicky Transient Facility (ZTF), & Global Relay Of Observatories Watching Transients Happen (Growth) Collaboration. 2020, GRB Coordinates Network, 26968, 1

Smartt, S. J., Chen, T. W., Jerkstrand, A., et al. 2017, Nature, 551, 75, doi: 10.1038/nature24303

Soares-Santos, M., Holz, D. E., Annis, J., et al. 2017, ApJ, 848, L16, doi: 10.3847/2041-8213/aa9059

Soderberg, A. M., Berger, E., Page, K. L., Schady, P., & et al. 2008, Nature, 453, 469, doi: 10.1038/nature06997

Soderberg, A. M., Berger, E., Kasliwal, M., et al. 2006, ApJ, 650, 261, doi: `10.1086/506429`

Speagle, J. S. 2020, MNRAS, 493, 3132, doi: `10.1093/mnras/staa278`

Spitler, L. G., Cordes, J. M., Hessels, J. W. T., et al. 2014, ApJ, 790, 101, doi: `10.1088/0004-637X/790/2/101`

Spitler, L. G., Scholz, P., Hessels, J. W. T., et al. 2016, Nature, 531, 202, doi: `10.1038/nature17168`

Stamatikos, M., Malesani, D., Page, K. L., & Sakamoto, T. 2014, GRB Coordinates Network, 16520, 1

Stark, R. F., & Piran, T. 1985, Phys. Rev. Lett., 55, 891, doi: `10.1103/PhysRevLett.55.891`

Stella, L., Dall'Osso, S., Israel, G. L., & Vecchio, A. 2005, ApJ, 634, L165, doi: `10.1086/498685`

Strang, L. C., & Melatos, A. 2019, MNRAS, 487, 5010, doi: `10.1093/mnras/stz1648`

Strang, L. C., Melatos, A., Sarin, N., & Lasky, P. D. 2021

Stratta, G., Dainotti, M. G., Dall'Osso, S., Hernandez, X., & De Cesare, G. 2018, ApJ, 869, 155, doi: `10.3847/1538-4357/aadd8f`

Sun, H., Li, Y., Zhang, B.-B., et al. 2019, ApJ, 886, 129, doi: `10.3847/1538-4357/ab4bc7`

Sun, L., & Melatos, A. 2019, Phys. Rev. D, 99, 123003, doi: `10.1103/PhysRevD.99.123003`

Sur, A., & Haskell, B. 2020, arXiv e-prints, arXiv:2010.15574. `https://arxiv.org/abs/2010.15574`

Suvorov, A. G., & Kokkotas, K. D. 2020, ApJ, 892, L34, doi: `10.3847/2041-8213/ab8296`

Suvorova, S., Sun, L., Melatos, A., Moran, W., & Evans, R. J. 2016, Phys. Rev. D, 93, 123009, doi: `10.1103/PhysRevD.93.123009`

Takami, K., Rezzolla, L., & Baiotti, L. 2014, Phys. Rev. Lett., 113, 091104, doi: `10.1103/PhysRevLett.113.091104`

—. 2015, Phys. Rev. D, 91, 064001, doi: `10.1103/PhysRevD.91.064001`

Talbot, C., Smith, R., Thrane, E., & Poole, G. B. 2019, arXiv e-prints, arXiv:1904.02863. `https://arxiv.org/abs/1904.02863`

Tanaka, M., Kato, D., Gaigalas, G., & Kawaguchi, K. 2020, MNRAS, 496, 1369, doi: `10.1093/mnras/staa1576`

Tanvir, N. R., Levan, a. J., Fruchter, a. S., et al. 2013, Nature, 500, 547, doi: `10.1038/nature12505`

Tanvir, N. R., Levan, A. J., González-Fernández, C., et al. 2017, ApJ, 848, L27, doi: `10.3847/2041-8213/aa90b6`

Tauris, T. M., Kramer, M., Freire, P. C. C., Wex, N., & et al. 2017, ApJ, 846, 170, doi: `10.3847/1538-4357/aa7e89`

Tchekhovskoy, A., Metzger, B. D., Giannios, D., & Kelley, L. Z. 2014, MNRAS, 437, 2744, doi: `10.1093/mnras/stt2085`

Tendulkar, S. P., Bassa, C. G., Cordes, J. M., et al. 2017, ApJ, 834, L7, doi: `10.3847/2041-8213/834/2/L7`

The Chime/Frb Collaboration, Andersen, B. C., Bandura, K. M., Bhardwaj, M., et al. 2020, Nature, 587, 54, doi: `10.1038/s41586-020-2863-y`

Thompson, C., & Duncan, R. C. 1995, MNRAS, 275, 255, doi: `10.1093/mnras/275.2.255`

—. 1996, ApJ, 473, 322, doi: `10.1086/178147`

Thompson, C., Lyutikov, M., & Kulkarni, S. R. 2002, ApJ, 574, 332, doi: `10.1086/340586`

Thompson, T. A., Chang, P., & Quataert, E. 2004, ApJ, 611, 380, doi: `10.1086/421969`

Thrane, E., & Coughlin, M. 2013, Phys. Rev. D, 88, 083010, doi: `10.1103/PhysRevD.88.083010`

—. 2015, Phys. Rev. Lett., 115, 181102, doi: `10.1103/PhysRevLett.115.181102`

Thrane, E., Kandhasamy, S., Ott, C. D., et al. 2011, Phys. Rev. D, 83, 083004, doi: `10.1103/PhysRevD.83.083004`

Thrane, E., & Talbot, C. 2019, PASA, 36, e010, doi: `10.1017/pasa.2019.2`

Timmes, F. X., Woosley, S. E., & Weaver, T. A. 1996, ApJ, 457, 834, doi: `10.1086/176778`

Tolman, R. C. 1939, Physical Review, 55, 364, doi: `10.1103/PhysRev.55.364`

Toma, K., Ioka, K., Yamazaki, R., & Nakamura, T. 2006, ApJ, 640, L139, doi: `10.1086/503384`

Tominaga, N., Morokuma, T., Blinnikov, S. I., et al. 2011, ApJS, 193, 20, doi: `10.1088/0067-0049/193/1/20`

Totani, T., & Panaitescu, A. 2002, ApJ, 576, 120, doi: `10.1086/341738`

Treister, E., Bauer, F., & Schawinski, K. 2014, The Astronomer's Telegram, 6603, 1

Troja, E., Piro, L., van Eerten, H., et al. 2017, Nature, 551, 71, doi: `10.1038/nature24290`

Troja, E., Sakamoto, T., Cenko, S. B., et al. 2016, ApJ, 827, 102, doi: `10.3847/0004-637X/827/2/102`

Troja, E., van Eerten, H., Zhang, B., et al. 2020, arXiv e-prints, arXiv:2006.01150. `https://arxiv.org/abs/2006.01150`

Troja, E., Cusumano, G., O'Brien, P. T., et al. 2007, ApJ, 665, 599, doi: `10.1086/519450`

Troja, E., Ryan, G., Piro, L., et al. 2018, Nature Communications, 9, 4089, doi: `10.1038/s41467-018-06558-7`

Troja, E., van Eerten, H., Ryan, G., et al. 2019, MNRAS, 489, 1919, doi: `10.1093/mnras/stz2248`

Tsang, K. W., Dietrich, T., & Van Den Broeck, C. 2019, arXiv e-prints, arXiv:1907.02424. `https://arxiv.org/abs/1907.02424`

Uhm, Z. L., & Beloborodov, A. M. 2007, The Astrophysical Journal, 665, L93, doi: `10.1086/519837`

Usov, V. V. 1992, Nature, 357, 472, doi: `10.1038/357472a0`

Valenti, S., Sand, D. J., Yang, S., et al. 2017, ApJ, 848, L24, doi: `10.3847/2041-8213/aa8edf`

van Eerten, H. 2018, International Journal of Modern Physics D, 27, 1842002, doi: `10.1142/S0218271818420026`

van Putten, M. H. P. M., & Della Valle, M. 2019, MNRAS, 482, L46, doi: `10.1093/mnrasl/sly166`

Villar, V. A., Guillochon, J., Berger, E., et al. 2017, ApJ, 851, L21, doi: `10.3847/2041-8213/aa9c84`

Virgili, F. J., Qin, Y., Zhang, B., & Liang, E. 2012, MNRAS, 424, 2821, doi: `10.1111/j.1365-2966.2012.21411.x`

von Kienlin, A., Meegan, C., & Goldstein, A. 2017, GRB Coordinates Network, Circular Service, 21520

Wanajo, S., Hirai, Y., & Prantzos, N. 2021, Neutron star mergers as the astrophysical site of the r-process in the Milky Way and its satellite galaxies. `https://arxiv.org/abs/2106.03707`

Wanajo, S., Sekiguchi, Y., Nishimura, N., et al. 2014, ApJ, 789, L39, doi: `10.1088/2041-8205/789/2/L39`

Wang, X.-G., Zhang, B., Liang, E.-W., et al. 2015, ApJS, 219, 9, doi: 10.1088/0067-0049/219/1/9

Watson, D., Hansen, C. J., Selsing, J., Koch, A., & et al. 2019, Nature, 574, 497, doi: 10.1038/s41586-019-1676-3

Wiggins, B. K., Fryer, C. L., Smidt, J. M., et al. 2018, ApJ, 865, 27, doi: 10.3847/1538-4357/aad2d4

Xiao, D., & Dai, Z.-G. 2019, ApJ, 878, 62, doi: 10.3847/1538-4357/ab12da

Xiao, D., Zhang, B.-B., & Dai, Z.-G. 2019, ApJ, 879, L7, doi: 10.3847/2041-8213/ab2980

Xing, Z., Centrella, J. M., & McMillan, S. L. W. 1994, Phys. Rev. D, 50, 6247, doi: 10.1103/PhysRevD.50.6247

Xue, Y. Q., Zheng, X. C., Li, Y., et al. 2019, Nature, 568, 198

Yang, H., Paschalidis, V., Yagi, K., et al. 2018, Phys. Rev. D, 97, 024049, doi: 10.1103/PhysRevD.97.024049

Yu, Y.-W., Liu, L.-D., & Dai, Z.-G. 2018, ApJ, 861, 114, doi: 10.3847/1538-4357/aac6e5

Yu, Y.-W., Zhang, B., & Gao, H. 2013, ApJ, 776, L40, doi: 10.1088/2041-8205/776/2/L40

Yue, Y. L., Xu, R. X., & Zhu, W. W. 2006, Advances in Space Research, 40, 1491, doi: 10.1016/j.asr.2007.08.016

Zappa, F., Bernuzzi, S., Radice, D., Perego, A., & Dietrich, T. 2018, Phys. Rev. Lett., 120, 111101, doi: 10.1103/PhysRevLett.120.111101

Zhang, B. 2007, Advances in Space Research, 40, 1186, doi: 10.1016/j.asr.2007.01.016

—. 2013, ApJ, 763, L22, doi: 10.1088/2041-8205/763/1/L22

—. 2014, ApJ, 780, L21, doi: 10.1088/2041-8205/780/2/L21

—. 2017, ApJ, 836, L32, doi: 10.3847/2041-8213/aa5ded

—. 2018, The Physics of Gamma-Ray Bursts, doi: 10.1017/9781139226530

—. 2020a, Nature, 587, 45, doi: 10.1038/s41586-020-2828-1

—. 2020b, ApJ, 890, L24, doi: 10.3847/2041-8213/ab7244

Zhang, B., Fan, Y. Z., Dyks, J., et al. 2006, The Astrophysical Journal, 642, 354, doi: 10.1086/500723

Zhang, B., Fan, Y. Z., Dyks, J., et al. 2006, ApJ, 642, 354, doi: 10.1086/500723

Zhang, B., & Mészáros, P. 2001, ApJ, 552, L35, doi: 10.1086/320255

—. 2002, ApJ, 571, 876, doi: 10.1086/339981

—. 2004, International Journal of Modern Physics A, 19, 2385, doi: 10.1142/S0217751X0401746X

Zhang, B., & Yan, H. 2011, ApJ, 726, 90, doi: 10.1088/0004-637X/726/2/90

Zhang, B., Liang, E., Page, K. L., et al. 2007, ApJ, 655, 989, doi: 10.1086/510110

Zhang, S., Jin, Z.-P., Wang, Y.-Z., & Wei, D.-M. 2017, ApJ, 835, 73, doi: 10.3847/1538-4357/835/1/73

Zhang, S., Jin, Z.-P., Wang, Y.-Z., & Wei, D.-M. 2017, The Astrophysical Journal, 835, 73, doi: 10.3847/1538-4357/835/1/73

Zhang, S. N., Xiong, S. L., Li, C. K., et al. 2020, The Astronomer's Telegram, 13696, 1

Zhou, P., Zhou, X., Chen, Y., et al. 2020, arXiv e-prints, arXiv:2005.03517. https://arxiv.org/abs/2005.03517

Zhu, Y. L., Lund, K., Barnes, J., et al. 2020, arXiv e-prints, arXiv:2010.03668. https://arxiv.org/abs/2010.03668

Zrake, J., & MacFadyen, A. I. 2013, ApJ, 769, L29, doi: 10.1088/2041-8205/769/2/L29